OFFICE OF CIVILIAN RADIOACTIVE WASTE MANAGEMENT
ANALYSIS/MODEL COVER SHEET

Complete Only Applicable Items

1. QA: QA

Page: 1 of: 240

2. ☒ Analysis Check all that apply

Type of Analysis	☐ Engineering ☐ Performance Assessment ☒ Scientific
Intended Use of Analysis	☐ Input to Calculation ☒ Input to another Analysis or Model ☒ Input to Technical Document

Describe use:
Provides chemistry of water entering drifts for other AMRs and UZ and NFE PMRs.

3. ☒ Model Check all that apply

Type of Model	☒ Conceptual Model ☐ Mathematical Model ☒ Process Model	☐ Abstraction Model ☐ System Model
Intended Use of Model	☐ Input to Calculation ☒ Input to another Model or Analysis ☒ Input to Technical Document	

Describe use:
Provides THC models for abstraction and use by PA, and for use in analysis of Drift Scale Test, and for supporting the UZ and NFE PMRs.

4. Title:
Drift-Scale Coupled Processes (DST and THC Seepage) Models

5. Document Identifier (including Rev. No. and Change No., if applicable):
MDL-NBS-HS-000001 REV01

6. Total Attachments:
11

7. Attachment Numbers - No. of Pages in Each:
I-2, II-4, III-2, IV-4, V-3, VI-3, VII-3, VIII-3, IX-3, X-3, XI-7

	Printed Name	Signature	Date
8. Originator	Eric Sonnenthal		2/5/01
	Nicolas Spycher		2/5/01
9. Checker	P.E. Persoff		2/5/01
10. Lead/Supervisor	G.S. Bodvarsson	Bo Bodvarsson	2/5/01
11. Responsible Manager	G.S. Bodvarsson	Bo Bod	2/5/01

12. Remarks:

Section 6.7 was written by Patrick Dobson. Tim Kneafsey designed and performed the experiment described in Section 6.7. Charles Haukwa created the initial permeability realizations for Section 6.5. Jennifer Hinds provided information from the 3-D UZ Site-Scale Flow and Transport Model.

Editorial corrections:
Page 146, Figure 53 - remove "Total" from caption. J&H 2/9/01
Page 200, Figure 94 - change "Tptpmn" to "Tptpll" in caption J&H 2/9/01
Page 29 - Add clause "have been used within the range of validation" J&H 2/9/01
Page 30 - Remove last sentence in first paragraph J&H 2/9/01
Page 49 - Remove "separate" from second line of A-1 J&H 2/9/01
Page 49 - In A-4, change Figures numbers 28 and 29 to 39 and 40 J&H 2/9/01
Page 50 - In A-8 change "for" to "of" J&H 2/9/01
Page 54 - In C-1 remove "of" J&H 2/9/01
Pages 239, 240 - Removed "C" from DI J&H 3/5/01

AP-3.10Q.3

Rev. 02/25/2000

OFFICE OF CIVILIAN RADIOACTIVE WASTE MANAGEMENT
ANALYSIS/MODEL REVISION RECORD
Complete Only Applicable Items

1. Page: 2 of: 240

2. Analysis or Model Title:
Drift-Scale Coupled Processes (DST and THC Seepage) Models

3. Document Identifier (including Rev. No. and Change No., if applicable):
MDL-NBS-HS-000001 REV01

4. Revision/Change No.	5. Description of Revision/Change
REV00	Initial Issue
REV01	Incorporating additional data from DST for model validation. Incorporating sensitivity studies, including effect of backfill versus no backfill. Additional Models/Updates: REV01 DST THC Model Tptpmn THC No-Backfill Model Tptpmn THC Heterogeneous Model Tptpll THC Model Plug-Flow Reactor Model Validation

CONTENTS

CONTENTS (Continued)

CONTENTS (Continued)

CONTENTS (Continued)

Page

FIGURES

FIGURES (Continued)

Page

FIGURES (Continued)

FIGURES (Continued)

FIGURES (Continued)

Page

FIGURES (Continued)

FIGURES (Continued)

Page

FIGURES (Continued)

FIGURES (Continued)

FIGURES (Continued)

Page

FIGURES (Continued)

Page

INTENTIONALLY LEFT BLANK

TABLES

TABLES (Continued)

Page

ACRONYMS

2D, 2-D	two-dimensional, two dimensions
3D, 3-D	three-dimensional, three dimensions
ACC	Accession Number
AMR	Analysis/Model Report
AP	Administrative Procedure
aq	aqueous
CDTT	Cross Drift Thermal Test
CRWMS	Civilian Radioactive Waste Management System
DIRS	Document Input Reference System
DOE	Department of Energy
DST	Drift Scale Test
DTN	Data Tracking Number
EDA	Enhanced Design Alternative
ESF	Exploratory Studies Facility
LBNL	Lawrence Berkeley National Laboratory
M&O	Management and Operating Contractor
NFE	Near-Field Environment
OCRWM	Office of Civilian Radioactive Waste Management
PA	Performance Assessment
PMR	Process Model Report
PTn	Paintbrush Tuff nonwelded unit
Q	Qualified
QARD	Quality Assurance Requirements and Description
QIP	Quality Implementing Procedure
SEM	Scanning Electron Microscope
SHT	Single Heater Test
SN	Scientific Notebook
SR	Site Recommendation
STN	Software Tracking Number
TBV	To Be Verified
TCw	Tiva Canyon welded unit
TH	Thermal-Hydrological
THC	Thermal-Hydrological-Chemical

ACRONYMS (Continued)

Tptpll	Topopah Spring Lower lithophysal unit
Tptpln	Topopah Spring Lower nonlithophysal unit
Tptpmn	Topopah Spring Middle nonlithophysal unit
Tptpul	Topopah Spring Upper lithophysal unit
TSPA	Total System Performance Assessment
TSPA-SR	Total System Performance Assessment-Site Recommendation
TSw	Topopah Spring welded unit
TWP	Technical Work Plan
U.S.	United States
UZ	Unsaturated Zone
YMP	Yucca Mountain Site Characterization Project

1. PURPOSE

The purpose of this Analysis/Model Report (AMR) is to document the Near-Field Environment (NFE) and Unsaturated Zone (UZ) models used to evaluate the potential effects of coupled thermal-hydrologic-chemical (THC) processes on unsaturated zone flow and transport. This is in accordance with the *Technical Work Plan* (TWP) *for Unsaturated Zone Flow and Transport Process Model Report*, Addendum D, Attachment D-4 (Civilian Radioactive Waste Management System (CRWMS) Management and Operating Contractor (M&O) 2000 [153447]) and *Technical Work Plan for Nearfield Environment Thermal Analyses and Testing* (CRWMS M&O 2000 [153309]). These models include the Drift Scale Test (DST) THC Model and several THC seepage models. These models provide the framework to evaluate THC coupled processes at the drift scale, predict flow and transport behavior for specified thermal loading conditions, and predict the chemistry of waters and gases entering potential waste-emplacement drifts. The intended use of this AMR is to provide input for the following:

- Performance Assessment (PA)
- Abstraction of Drift-Scale Coupled Processes AMR (ANL-NBS-HS-000029)
- UZ Flow and Transport Process Model Report (PMR)
- Near-Field Environment (NFE) PMR

The work scope for this activity is presented in the TWPs cited above, and summarized as follows: Continue development of the repository drift-scale THC seepage model used in support of the TSPA in-drift geochemical model; incorporate heterogeneous fracture property realizations; study sensitivity of results to changes in input data and mineral assemblage; validate the DST model by comparison with field data; perform simulations to predict mineral dissolution and precipitation and their effects on fracture properties and chemistry of water (but not flow rates) that may seep into drifts; submit modeling results to the TDMS and document the models. The model development, input data, sensitivity and validation studies described in this AMR are required to fully document and address the requirements of the TWPs.

The DST THC Model, constructed for the DST, is used to investigate THC processes during the DST. The spatial scale and temperatures for the DST are similar to that for current designs of the potential repository. This, combined with the relatively long time that it has been operating (3 years as of December 2000) makes it by far the best experiment for validation of drift-scale THC coupled process models (i.e., the THC seepage models). Measured data from the DST are used to evaluate and validate the conceptual and numerical models. The iterative approach of evaluating, refining, and comparing the DST numerical model against measured data is performed throughout the DST study. The THC seepage models provide an analysis of the effects of THC processes in the near-field host rock around the potential emplacement drifts on the seepage water chemistry and gas-phase composition. This analysis includes a complete description of the pertinent mineral-water processes in the host rock and their effect on the NFE. The seepage models are used to evaluate the effects of mineral dissolution and precipitation, the effects of CO_2 exsolution and transport in the region surrounding emplacement drifts, the potential for forming calcite, silica, or other mineral assemblage "precipitation caps," and the resulting changes to porosity, permeability, and seepage. Sensitivity studies are documented on the effect on THC processes of varying fracture permeability heterogeneity, reaction rates, absence of backfill, repository emplacement horizon lithology, and geochemical systems considered. Evaluation of the THC model parameters and methodology, including sensitivity analyses, are also presented through comparison to a plug-flow reactor laboratory experiment.

For the THC seepage models, systematic sensitivity studies involving changing numerous input values over a wide range were not conducted because these are beyond the scope of this project. As a result, quantification of the model uncertainty is not feasible. Variations in input parameters considered in the THC seepage models are mostly related to model improvements and changes in drift design, but nonetheless allow some qualitative assessment of the model sensitivity to input parameters.

The following designations have been assigned to the models and their variations presented in this AMR:

- DST THC Model Rev00: DST THC Model and simulations for Rev00 of this AMR (Section 6.2).
- DST THC Model Rev01: DST THC Model and simulations for Rev01 of this AMR (Section 6.2).
- Tptpmn THC Backfill Model: THC Seepage Model for Rev00 of this AMR. Considers heat load in Topopah Spring Tuff middle non-lithophysal unit (Tptpmn) with backfill placed above waste packages (Section 6.3).
- Tptpmn THC No-Backfill Model: THC Seepage Model for Rev01 of this AMR. Considers heat load in the Tptpmn without backfill (Section 6.4).
- Tptpmn THC Heterogeneous Model: THC Seepage Model for Rev01 of this AMR. Considers heat load in the Tptpmn with initial heterogeneous fracture permeability variations and without backfill. Same grid and THC parameters as in the Tptpmn no-backfill model (Section 6.5).
- Tptpll THC Model: THC Seepage model for Rev01 of this AMR. Heat load in Topopah Spring Tuff lower lithophysal unit (Tptpll) without backfill (Section 6.6).

The first two models are collectively referred to as the DST THC Model, and the latter four as THC seepage models. These models are fully described in Section 6.

Rev00 of this report presented THC simulations of the Drift Scale Test (the above mentioned DST THC Model Rev00) and a THC seepage model (the above mentioned Tptpmn THC Backfill Model). These models and their results were not changed in Rev01, except for a correction to Figure 29 of Rev00 (Figure 40 in Rev01). All THC simulations for Rev00 were performed using TOUGHREACT V2.2 (interim “Q” version) [153219].

As listed above, this Rev01 includes results for the DST THC Model Rev01, and three additional models (Tptpmn THC No-Backfill Model, Tptpmn THC Heterogeneous Model, and the Tptpll THC Model). These new simulations include better constrained input thermodynamic data for silicate minerals (Section 4.1.4.2), which, together with other conceptual changes described later in the report, narrow the differences that were observed in Rev00 between simulations including

Main Menu

EXIT

and excluding aluminosilicate minerals. Also, the Rev01 simulations make use of TOUGHREACT V2.3 [153101] which, among other improvements described later, considers a much stronger coupling of fracture permeability to fracture porosity (Section 6.1.6).

Caveats and Limitations

The THC Backfill and No-Backfill models were developed with data for specific hydrogeologic units, the Tptpmn and Tptpll. Although many aspects of the model are applicable to other host rock units of the potential repository, differences in the mineralogy, geochemistry, and thermohydrological properties must be considered before the results can be directly applied elsewhere in the potential repository. One limitation of the model is that it is a continuum model with average properties or realizations of idealized permeability fields, and therefore is meant to represent overall changes in space and time. Thus, it must be applied with caution at any specific location.

The DST THC Model is a 2-D representation with homogeneous properties of a 3-D experiment in heterogeneous fractured rock. Therefore, the model is meant to capture overall changes as a function of space and time, but cannot be expected to match data exactly at any one point in time.

The THC models in this AMR must be recognized as idealizations of the real world that represent specific physical processes in the real world. Input data summarized in Section 4 characterize the physical properties of the rock but are not intended to include every detail. In particular, the infiltration of water is laterally uniform over the model top boundary. As a result of such simplifications, the model results describe overall changes in space and time within the model domain, but must be applied with caution when considered as predictions of future conditions at any specific location.

INTENTIONALLY LEFT BLANK

2. QUALITY ASSURANCE

The activities documented in this AMR were evaluated under Administrative Procedure (AP)-2.21Q, *Quality Determinations and Planning for Scientific, Engineering, and Regulatory Compliance Activities* and were determined to be subject to the requirements of the United States Department of Energy (U.S. DOE) Office of Civilian Radioactive Waste Management (OCRWM) *Quality Assurance Requirements and Description* (QARD) (DOE 2000 [149540]). These evaluations are documented in the Technical Work Plan (CRWMS M&O 2000 [153447], Addendum D, Attachment D-9) and in the Technical Work Plan (CRWMS M&O 2000 [153309], Attachment V). Electronic management of information was evaluated in accordance with AP-SV.1Q, *Control of the Electronic Management of Information*, (CRWMS M&O 2000), and controlled under YMP-LBNL-QIP-SV.0, *Management of YMP-LBNL Electronic Data.* This evaluation is documented in CRWMS M&O 2000 [153447], Addendum D, Attachment D-8.

This AMR reports on a natural barrier that has been included in the Q-List (YMP 2000 [149733]) as an item important to waste isolation. The AMR contributes to the analyses and modeling data used to support performance assessment. The conclusions of this AMR do not affect the repository design or permanent items as discussed in QAP-2-3, *Classification of Permanent Items*.

The modeling activities documented in this AMR were conducted in accordance with the quality assurance program of the Civilian Radioactive Waste Management System Management and Operating Contractor (CRWMS M&O), using OCRWM APs and Yucca Mountain Site Characterization Project (YMP) Quality Implementing Procedures (QIPs) for the Lawrence Berkeley National Laboratory (LBNL). This AMR was developed under the *Technical Work Plan for Unsaturated Zone Flow and Transport Process Model Report*, Addendum D, Attachment D-4 (CRWMS M&O 2000 [153447]) and *Technical Work Plan for Nearfield Environment Thermal Analyses and Testing* (CRWMS M&O 2000 [153309]). These Technical Work Plans were developed in accordance with AP-2.21Q, and this AMR was developed in accordance with procedure AP-3.10Q, *Analyses and Models*.

INTENTIONALLY LEFT BLANK

3. COMPUTER SOFTWARE AND MODEL USAGE

The major software codes and software routines used in this study are listed in Table 1. These software (with the exception of TOUGHREACT V2.3 [153101]) have been baselined in accordance with AP-SI.1Q, *Software Management*, are appropriate for the intended use, and were obtained from the Software Configuration Management (SCM).

have been used within the range of validation,
2/9/01

Table 1. Computer Software and Routines

Software Name and Version	Software Tracking Number (STN)	DIRS Reference Number	Computer Used*
TOUGHREACT V2.2	10154-2.2-00	153219	1 and 2
TOUGHREACT V2.3	10396-2.3-00	153101	1 and 2
SOLVEQ/CHILLER V1.0	10057-1.0-00	153217	3
SUPCRT92 V1.0	10058-1.0-00	153218	3 and 4
TOUGH2 V1.4	10007-1.4-01	146496	1 and 2
AMESH V1.0	10045-1.0-00	153216	1 and 2
GSLIB V1.0SISIMV1.204	10397-1.0SISIMV1.204-00	153100	1
Routine Name and Version			
flipk V1.0	10320-1.0-00	152883	1
switch V1.0	10322-1.0-00	152899	3
regress V1.0	10321-1.0-00	152900	3
mk_incon V1.0	10350-1.0-00	152901	1
kreg V1.0	10318-1.0-00	152902	1
kswitch V1.0	10319-1.0-00	153087	1
exclude.f V1.0	10316-1.0-00	153089	1
assign.f V1.0	10315-1.0-00	153090	1
merggrid2.f V1.0	10314-1.0-00	153091	1
mk_circ2 V1.0	10312-1.0-00	153092	1
mk_rect2 V1.0	10313-1.0-00	153093	1
2kgridv1a.for V1.0	10382-1.0-00	153067	3
mk_grav2.f V1.0	10379-1.0-00	153068	1
sav1d_dst2d.f V1.0	10381-1.0-00	153083	1
mrgdrift.f V1.0	10380-1.0-00	153082	1
avgperm.f V1.0	10378-1.0-00	153085	1 and 2

*NOTES: Platform with Operating System and Computer ID:
1:SUN UltraSparc with Unix SunOS; Computer ID - LBNL DOE# 6332537
2:DEC-Alpha with Unix OSf1; Computer ID - LBNL DOE# 6409291
3:PC with MS Windows: Computer ID - LBNL DOE# 6362008
4:MAC with MACOS; Computer ID - LBNL DOE # 6324051

TOUGHREACT V2.2 [153219] and V2.3 [153101] are the primary codes used in the DST THC and THC Seepage models. The code SOLVEQ/CHILLER V1.0 [153217] was utilized to perform supporting computations for the models. SUPCRT92 V1.0 [153218] generates thermodynamic databases for use by SOLVEQ/CHILLER V1.0 [153217], TOUGHREACT V2.2 [153219] and TOUGHREACT V2.3 [153101]. The code TOUGH2 V1.4 [146496] was used to generate boundary conditions. The code AMESH V1.0 [153216] was used to generate grids for the two models, and GSLIB V1.0SISIMV1.204 [153100] was used to perform geostatistical analysis of permeability. ~~EQ3/6 V7.2b [126891] is cited in this AMR as a source of thermodynamic data, but was not used as software to directly support this AMR.~~ JEH 2/9/01

The unqualified software code, TOUGHREACT V2.3 [153101], is currently being qualified; a Software Activity Plan (10396-SAP-2.3-00) for use of unqualified software, a SUR, and a copy of the code have been submitted to SCM according to Subsection 5.11 (Interim Use of Unqualified Software to Support Site Recommendation (SR) Products) of AP-SI.1Q.

An unqualified version of TOUGHREACT V2.2 [153219] was used for the DST THC Model Rev00 and the Tptpmn THC Backfill Model and has since been qualified per AP-SI.1Q. Comparison runs were executed to verify the results produced by the unqualified version of the code and have been documented with SCM under Software Activity Number (SAN) LBNL-1999-141. There were some, justifiable differences between the unqualified and qualified code output due to corrections to the gas diffusion coefficient for CO_2, and the capillary pressure scaling resulting from porosity-permeability changes. These modifications had a limited effect on the simulation results with no change in the general trends in the gas and water chemistry or significant changes in the resultant flow fields. More recent modifications to the drift design (no-backfill), revisions to input thermodynamic and kinetic data, and superseding code upgrades in TOUGHREACT V2.3 [153101] caused greater differences in model results, as documented here, than differences between the qualified and unqualified TOUGHREACT V2.2 [153219].

This AMR documents the DST THC and THC Seepage Models as listed in Section 1. The input and output files for the model runs presented in this AMR are listed in Attachment XI. This AMR also utilizes properties from the Calibrated Properties Model and boundary conditions from the UZ Flow and Transport Model. These models are documented in separate AMRs.

4. INPUTS

4.1 DATA AND PARAMETERS

The Q-status of all inputs is shown in the Document Input Reference System (DIRS) database. Because this AMR documents models of coupled phenomena, a wide variety of input data are required. This section provides documentation for data that are input to the AMR. Furthermore, data that are input to the model simulations, but which are calculated from other input data or derived based on certain assumptions are also presented in this section. The type of data is clearly identifiable by the associated reference. Data input to the AMR are referred to by Data Tracking Number (DTN) or by reference, whereas the bases for developed data are described and have an associated output DTN. This format allows for all data of similar use in the AMR to be kept in single location for readability of the document and simplicity for downstream users. We further divide all input data into three categories, which are listed in Table 2.

1. Hydrologic properties data and geochemical data, including both measured and derived values, are specific to the Yucca Mountain site (and therefore appropriate for this application) and are all traceable by DTN to the TDMS.

2. All models discussed in this AMR require additional input data not specific to Yucca Mountain. Appropriate values for such data, including thermodynamic and kinetic data for mineral phases, are taken from the open literature. Such data are noted by the cited reference.

3. Geometric input such as drift geometry or mineral reactive surface areas are taken from design documents or calculated by making reasonable approximations. These data are considered as part of the assumptions, since the design of the potential repository has not been finalized.

4.1.1 Hydrological and Thermal Properties

4.1.1.1 DST THC and Tptpmn THC Models

The modeling analyses for these models utilized data from the lower, mean, and upper bound calibrated hydrological property sets for the present day climate (see DTNs in Table 2). Thermal parameters were obtained from the calibrated property set for the mean infiltration rate, and are identical for all property sets. These data are included in the DTNs in Table 2 for the calibrated property sets. The data sets include calibrated properties such as fracture and matrix permeabilities and van Genuchten parameters as well as uncalibrated properties such as porosity, heat capacity, and thermal conductivity. DTNs for infiltration rates and model boundary water temperatures are also included in Table 2. Specific hydrological and thermal parameters for the in-drift components of the Tptpmn THC models are given in Section 4.1.7.2.

4.1.1.2 Tptpll THC Model

Input hydrological and thermal properties for the Tptpll THC Model are the same as described in Section 4.1.1.1 except for the following differences: Fracture permeabilities of the Topopah Spring Tuff geologic units (except model layer tsw31) and the fracture porosity and air entry pressure for the Tptpll unit are higher, reflecting a new calibration that included recent air permeability and tracer test data from the Tptpll geologic unit (row 2, Table 2). Also, the fracture permeability of all other units, except the Tptpmn, were updated for consistency with the most recent data (Table 2).

4.1.2 Mineralogical Data

4.1.2.1 DST THC and Tptpmn THC Models

This section describes mineralogical data that are specific to the geologic units encountered in borehole USW SD-9 (the borehole closest to the DST) and in host rocks of Alcove 5 of the Exploratory Studies Facility (ESF) where the DST is located. These data were used in the DST THC Model (Rev00 and Rev01) and the Tptpmn THC models (backfill and no-backfill). These input data consist of the volume fractions (of each given mineral) per total solid volume and the reactive surface areas for these minerals. These two forms of the reactive surface area are used to describe minerals in the matrix of the rock (cm^2/g mineral) or those on the surface of fractures (m^2/m^3 of total medium, including pore space), respectively. These data are given in Attachments I (volume fractions) and III (reactive surface areas) for minerals initially present in the model hydrological units. The DTNs for data from which these properties were derived are given in Table 2, and include borehole USW SD-9 mass percent minerals as determined by x-ray diffraction (3-D Mineralogical Model: LA9908JC831321.001 [113495]). The calculation of the mineral volume fractions and reactive surface areas requires significant additional information, such as mineral stoichiometries (from the thermodynamic database), mass densities (thermodynamic database), grain size (estimated) and fracture-matrix surface area (calibrated property set). Recalculation of the feldspar into its 3 endmembers (albite, anorthite, and k-feldspar) was based on compositions from Johnson et al. (1998 [101630], Table 6). The fracture-matrix surface area is part of the calibrated hydrological property set for the mean infiltration and is listed by DTN in Table 2. The calculation of the reactive surface areas and other mineral properties are described in Bodvarsson 2001 [153816], YMP-LBNL-YWT-ELS-1, pp. 37-42.

4.1.2.2 Tptpll THC Model

Mineralogical data for the Tptpll THC Model were derived from the 3-D Mineralogical Model for a stratigraphic column chosen near the center of the potential repository and at the proposed location of the planned Cross Drift Thermal Test (CDTT) (Section 6.6). The calculation of the reactive surface areas and other mineral properties are described in Bodvarsson 2001 [153816], YMP-LBNL-YWT-ELS-1, pp. 34–43. These data are given in Attachments II and IV.

Table 2. Data Tracking Numbers for Sources of Data Input to the DST, Tptpmn, and Tptpll THC Models

DTNs	Description
Hydrological and Thermal Rock Properties:	
LB990861233129.001 [110226]	Calibrated property set † – Mean Infiltration
LB0011DSTFRAC1.001 [153470]	Calibrated property set (Tptpll THC Model)
LB990861233129.002 [109899]	Calibrated property set † – Upper bound
LB990861233129.003 [111479]	Calibrated property set † – Lower bound
LB997141233129.001 [104055]	Fracture porosity (DST and Tptpmn THC models)
LB991091233129.001 [125868]	Infiltration rate – mean
LL000114004242.090 [142884]	Infiltration rates – Average Infiltration Rate (mean, lower bound, and upper bound for present day, monsoon, and glacial transition climates) from the TH drift-scale models.
Mineralogical Data	
LA0009SL831151.001 [153485]	Mineralogic characterization of the ESF SHT Block
LA9912SL831151.001 [146447] LA9912SL831151.002 [146449]	DST and SHT fracture mineralogy data
MO0008THRMODYN.000 [153742]	Thermodynamic Data
LA0008SC12213N.001 [153386]	Zeolite compositions and thermodynamic data
LA9908JC831321.001 [113495]	Model input and output files for Mineralogic Model “MM3.0” Version 3.0.
Water and Gas Chemistry Data	
LB991215123142.001 [128157] *	CO_2 gas analyses (1st, 2nd, 3rd and 7th Qtr.)
LB990630123142.003 [111476] *	4th, 5th, and 6th Qtr. DST CO_2 data
LB000121123142.003 [146451] *	DST CO_2 data (Aug. ’99 – Nov. ‘99)
LB0011CO2DST08.001 [153460] *	DST CO_2 data (Nov. ’99 – Aug. 2000)
CRWMS M&O 2001 [153814] *	DST CO_2 data (Jul. ’98)
MO0005PORWATER.000 [150930]	Analyses of pore waters from the ESF (HD-PERM-2 and HD-PERM-3 samples)
LL990702804244.100 [144922] *	Aqueous chemistry of water sampled from the DST (6/4/98 to 3/30/99)
LL001100931031.008 [153288] *	Aqueous chemistry of water sampled from the DST (collected 10/27/99 to 1/25/00)
LL001200231031.009 [153616] *	Aqueous chemistry of water sampled from the DST (8/9/99 and 8/10/99)
MO0101SEPFDDST.000 [153711] *	Field pH of water sampled from DST on 5/23/00 and 6/29/00
Repository Drift Data	
SN9907T0872799.001 [111485]	Heat load (Tptpmn Backfill THC model) and repository footprint
SDD-EDS-SE-000001 REV 01 [150953]	Heat load (no-backfill THC models)
ITN: PA-SSR-99241.T [124263]	Heat removal by ventilation (70%)
CRWMS M&O 2000 [151014]	Hydrologic and thermal properties of drift design elements
SN9907T0872799.002 [124205]	Effective thermal conductivity (Tptpmn Backfill THC Model)
SN0002T0872799.009 [153364]	Effective thermal conductivity (no-backfill THC models)
ITN: PA-SSR-99218.Tc [149137] (Design Criterion, pg. 23)	Lower invert thermal conductivity (no- backfill THC models)
CRWMS M&O 2000 [142736]	Upper invert thermal conductivity (no- backfill THC models)

Tptpmn and Tptpll THC Model Grid Data	
LB990501233129.004 [111475]	Borehole SD-9 (column i64) in UZ site-scale calibration model grid UZ99_2_3D.mesh (Tptpmn THC models) CDTT proposed location (column j34) (Tptpll THC Model)
LB990701233129.002 [125604]	Top and bottom boundary temperatures, pressure, liquid/gas saturations, and boundary elevations
LB990601233124.001 [105888]	Permeability Measurements in Tptpmn
Plug Flow Reactor Data	
LB0011THCDISSX.001 [153380]	Experimental Data
LB0011THCDISSM.001 [153381]	Model Input Data
DST Model Data	
MO0007SEPDSTPC.001 [153707]	Heater power
MO0012SEPDSTPC.002 [153708]	Power reductions
LB0101DSTTHGRD.001 [153687]	2-D DST mesh

NOTES: Thermodynamic data for minerals, aqueous, and gaseous species are found in Attachments V and VI . Kinetic data for mineral-water reactions are listed in Table 4.

[†] Data taken from the calibrated property sets include calibrated and uncalibrated hydrological and thermal properties. Fracture porosities used in the DST and Tptpmn seepage models were taken from another data set with a separately listed DTN.

* Corroborative use in model validation.

4.1.3 Water and Gas Chemistry

Sources of water and gas chemistry data are provided in Table 2. The pore water compositions chosen for the input to the simulations are summarized in Table 3. As discussed in Section 6, no full characterization of pore waters from the Tptpll is available. The only nearly complete pore water analyses for samples collected from a potential repository unit near the potential repository footprint are analyses of two samples obtained from the Tptpmn geologic unit in Alcove 5 near the DST, and reported in DTN: MO0005PORWATER.000 [150930]. The average of these two analyses is shown in Table 3 for the analyzed species, and indicated in Table 3. Because this set of species is insufficient input for the simulations required by the scope of this AMR, concentrations of all other required species were calculated as indicated in Table 3 and the corresponding footnotes, and are reported in DTN: LB0011DSTTHCR1.001. Iron, aluminum, and total aqueous carbonate concentrations (hereafter listed as HCO_3^-) were not measured in ambient pore waters of the potential repository unit and are calculated as shown in Table 3. Different models made use of different aluminum concentrations, as shown in Table 3, and further discussed in Section 4.1.4.2. All the data in Table 3 are input to the simulations documented in this AMR; however only those data traceable to DTN: MO0005PORWATER.000 [150930] are input to the AMR itself; all other data are output from this AMR, since they are calculated in this AMR, and are reported in DTN: LB0011DSTTHCR1.001.

For all model simulations, the initial water composition was set to be the same in fractures and matrix and the same throughout the model domain (see also Section 6.1.2). For the Tptpmn Backfill THC model, this same composition was also used for infiltrating water at the top model boundary. However, for simulations added in Rev01 (Tptpmn and Tptpll THC models), a modified water composition was used for infiltrating water at the top model boundary, as shown in Table 3. This boundary water is essentially the same as the initial pore water, but re-equilibrated at a lower pH, temperature, and higher CO_2 partial pressure more representative of shallow water compositions (see below) and temperatures. Using this boundary water in seepage models yielded chemically steadier ambient water compositions at the location of the modeled drift (Section 6.4.3).

The initial CO_2 partial pressure in fractures and matrix (F, M in Table 3) was calculated as the partial pressure of CO_2 in chemical equilibrium with the initial water at 25°C, assuming ideal gas behavior (i.e. partial pressure is equal to fugacity). The 25°C temperature is close to the initial temperature at the location of the drift.

Table 3. Initial Water Composition and CO_2 Partial Pressure in Fractures (F), Matrix (M), Infiltration Waters (I), and Drift Air (D)

Parameters	**Units**	**Concentration (1)**	**DST THC Model Rev00 (6.2.7)**	**DST THC Model Rev01 (6.2.8)**	**Tptpmn THC Backfill Model (6.3)**	**Tptpmn THC No-Backfill Model (6.4, 6.5)**	**Tptpll THC Model (6.6)**
pH	pH Units	8.32 (at 25°C) (1) 7.75 (at 17°C) (9)	F, M	F, M	F, M, I	F, M I	F, M I
Na^+	mg/L	61.3 (1)	F, M	F, M	F, M, I	F, M, I	F, M, I
SiO_2(aq)	mg/L	70.5 (1)	F, M	F, M	F, M, I	F, M, I	F, M, I
Ca^{2+}	mg/L	101 (1)	F, M	F, M	F, M, I	F, M, I	F, M, I
K^+	mg/L	8.0 (1)	F, M	F, M	F, M, I	F, M, I	F, M, I
Mg^{2+}	mg/L	17 (1)	F, M	F, M	F, M, I	F, M, I	F, M, I
Al^{3+}	mg/L	$9.92x10^{-7}$ (2) $1.67x10^{-5}$ (6) $2.64x10^{-6}$ (7)	F, M	F, M	F, M, I	F, M I	F, M I
Fe^{3+}	mg/L	$6.46x10^{-8}$ (3) $2.88x10^{-8}$ (8)	F, M	F, M	F, M, I	F, M I	F, M I
HCO_3^-	mg/L	200 (4) 216 (9)	F, M	F, M	F, M, I	F, M I	F, M I
Cl^-	mg/L	117 (1) 118 (9)	F, M	F, M	F, M, I	F, M I	F, M I
SO_4^{2-}	mg/L	116 (1)	F, M	F, M	F, M, I	F, M, I	F, M, I
F^-	mg/L	0.86 (1)	F, M	F, M	F, M, I	F, M, I	F, M, I
CO_2 (gas)	Pa	85.2 (5) 316 (9) 35.4 (10)	F, M D	F, M D	F, M I, D	F, M I D	F, M, D I

DTN: LB0101DSTTHCR1.001 (this Table) and MO0005PORWATER.000 [150930] for water composition

NOTES:

(1) Average of Tptpmn Porewater Analyses ESF-HD-PERM-2 (30.1'-30.5') and ESF HD-PERM-3 (34.8'-35.1'), DTN: MO0005PORWATER.000 [150930]

(2) Calculated by equilibrating with Ca-smectite at 25°C and pH 8.32 (using SOLVEQ V1.0).

(3) Calculated by equilibrating with hematite at 25°C and pH 8.32 (using SOLVEQ V1.0).

(4) Total aqueous carbonate as HCO_3^-, calculated from charge balance computed by speciation at 25°C and pH 8.32 (using SOLVEQ V1.0).

(5) Calculated at equilibrium with the solution at 25°C and pH 8.32 (using SOLVEQ V1.0) (approximately equal to 960 ppmv at the drift ambient pressure near $0.88x10^5$ Pa).

(6) Calculated by equilibrating with illite at 25°C and pH 8.32 (using SOLVEQ V1.0).

(7) Calculated by equilibrating with illite at 17°C and pH 7.75 (using SOLVEQ V1.0).

(8) Calculated by equilibrating with hematite at 17°C and pH 7.75 (using SOLVEQ V1.0).

(9) HCO_3- calculated from equilibrium with $\log(P_{CO_2}) = -2.5$, and pH adjusted until charge balancing with chloride yields a chloride concentration close to its original value (i.e. until charge balance is achieved) at 17°C (infiltration water only) (CO_2 approximately 3700 ppmv at a top boundary pressure near $0.85x10^5$ Pa).

(10) Ambient CO_2 concentration of 400 ppmv at drift pressure near $0.88x10^5$ Pa.

The initial CO_2 partial pressure in the drift (D in Table 3) was set to be consistent with a CO_2 concentration of 400 parts per million by volume (ppmv) in the drift, which is within the range of measured ambient concentrations in the ESF (DTN: LB990630123142.003 [111476]). For some simulations (Table 3), this concentration was also used for the top model boundary concentration in the gas phase. However, for Tptpmn No-Backfill and Tptpll THC Model simulations, the CO_2 concentration at the top model boundary significantly increased to reflect a value more consistent with the range of higher concentrations measured in shallow geologic units in borehole UZ-1 (Table 8 in Yang et al. 1996 [100194]). It should be noted that the infiltrating water injected into the grid-block below the top boundary block is always equilibrated with a CO_2 concentration that is elevated relative to the drift initial CO_2 concentration.

Very few complete pore-water analyses exist from other units of the Topopah Spring Tuff, and none from the lower lithophysal unit (Tptpll). Water compositions from the lower non-lithophysal unit (Tptpln) (DTN: GS950608312272.001 [145617]) exhibit a slightly more sodium-carbonate character (and less of a calcium-chloride character) than the water composition shown in Table 3; however, these waters may have interacted with zeolites which are more prevalent at deeper levels of the Topopah Spring welded unit (TSw) that would shift compositions in this direction.

4.1.4 Thermodynamic Database

All thermodynamic data discussed in this Section are listed with their sources in Attachments V and VI. Data from DTN: MO0008THRMODYN.000 [153742] are qualified. All other sources cited in these Attachments are unqualified; these data are considered as “assumed” data as stated in Assumption A-19 (Section 5).

4.1.4.1 DST Rev00 Simulations and Tptpmn Backfill THC Model

Thermodynamic data can be a major source of uncertainty because they dictate reaction trends (dissolution or precipitation) regardless of input mineral surface areas or rate constants. Dissociation constants (log(K) values) for aqueous species, minerals, and CO_2 gas as a function of temperature were taken from various sources (Attachment V). Most values are from the EQ3/6 V7.2b database (data0.com.R2, STN: LLNL:UCRL-MA-110662 [126891]), which were themselves primarily derived using SUPCRT92 (Johnson et al. 1992 [101632]). Other log(K) values were computed as indicated in Attachment V and further documented in YMP Scientific Notebooks Spycher 1998 [153571], pp. 72-77, 115, and 137; Spycher 2000 [153572], pp. 96 and 104-117; and Bodvarsson 2001 [153816], YMP-LBNL-YWT-JA-1A pp. 28-43 and 48-51.

Other data included in the thermodynamic database include molecular weights, molar volumes, and parameters used for the calculation of activity coefficients for aqueous species. The latter consist of the ionic charge and the parameters a_o used in the Debye-Hückel equation (e.g. Drever 1997 [140067], p. 28). These data were for the most part taken from the EQ3/6 V7.2b database [126891], with exceptions as noted in Attachment V. The molecular diameter of CO_2 (Lasaga 1998 [117091], p. 322) is also included in the database for calculation of the CO_2 diffusion coefficient.

As referenced in Attachment V, the data for all silicate minerals (with the exception of anorthite) were revised for consistency with the most recent quartz solubility data of Rimstidt (1997 [101709]). This revision was done in a way that ensured consistency between the thermodynamic data of aqueous (aq) silica species and silicate minerals as follows. The original log(K) data for quartz (SUPCRT92, Johnson et al. 1992 [101632]) and silicate minerals (Attachment V) were first used to compute log(K) values for the dissociation of these minerals with respect to quartz (no aqueous silica in the reactions). These values were then added to the log(K) values from Rimstidt (1997 [101709]) for the reaction of quartz to aqueous silica. For albite and microcline, the revised log(K) data are essentially the same as values obtained using equations in Arnórsson and Stefánsson (1999 [153329], p. 173) (Bodvarsson 2001 [153816], YMP-LBNL-YWT-NS-1.2, p. 9-10). The original log(K) data for anorthite were not revised for consistency with the quartz solubility data of Rimstidt (1997 [101709]), however appropriate revisions were made to these data in the updated database described in Section 4.1.4.2 (a change by approximately -1.3 log(K) unit at 25°C - Attachments V and VI). In all THC model simulations, anorthite remains undersaturated by several orders of magnitude, and therefore its dissolution rate is not affected by this difference in log(K) values.

The revised EQ3/6 V7.2b [126891] thermodynamic database data0.ymp.R0 (DTN: MO0008THRMODYN.000 [153742]) was not available prior to the start of this study. As mentioned above, most of the aqueous species data used here are close to or identical to those in this revised EQ3/6 database. The few differences for other aqueous species are not expected to affect model results significantly. The data for all non-silicate minerals are also identical to those in the revised EQ3/6 database (except for goethite, for which data are available only at the 25°C in the revised database). Revisions to the silicate minerals described above, and further in Section 4.1.4.2, were necessary to better constrain model results and increase the model accuracy. Simulations using all data from the revised EQ3/6 V7.2b [126891] database (DTN: MO0008THRMODYN.000 [153742]) may not yield results as consistent with field observations as simulations using the data presented here. A full evaluation of the impact of using the revised EQ3/6 V7.2b [126891] database (DTN: MO0008THRMODYN.000 [153742]) is currently underway.

4.1.4.2 DST Rev01 Simulations, Tptpmn THC Model (No-Backfill), Tptpll THC Model

These simulations were performed using a revision of the thermodynamic data listed above in Section 4.1.4.1, as listed in Attachment VI and further documented in YMP Scientific Notebooks Spycher 2000 [153572], pp. 149-156 and Bodvarsson 2001 [153816], YMP-LBNL-YWT-NS-1.2 pp. 9-12, 18-20, 31, 41 and 42.

Revisions made for Rev01 to the thermodynamic data can be viewed as a “calibration” to measured ambient pore-water data (which are limited and have their own uncertainty). These revision were necessary to provide better initial conditions for the THC simulations and thus reduce the model uncertainty. Thermodynamic data for minerals (e.g. ΔG_f°, ΔH_f°) are commonly based on calorimetric measurements (rather than dissolution experiments) or estimation procedures traceable to calorimetric determinations. Such data typically have associated uncertainty ranges of several percent. The small adjustments made in Rev01 for zeolites, smectites, and K-feldspar are well within this uncertainty (less than 0.5%) yet had a large effect on the saturation state of these minerals (several log[Q/K] units). Such changes significantly affect reaction trends and rates for these minerals, and resulted in modeled ambient concentrations closer to measured data under the ambient percolation flux.

As discussed in Sections 6.3.5.2 and 6.4.3, reactive transport simulations of initial waters (under the ambient geothermal gradient) with the thermodynamic data listed in Attachment V yields "unsteady" water composition trends and mineralogic changes. Using these data and pore-water compositions in Table 3, the zeolite minerals (particularly stellerite) are oversaturated relative to feldspars, with measured pore-water compositions falling well within the zeolite stability field. For this reason, the dissociation constants of stellerite were adjusted such that the pore-water composition fell on the equilibrium line between albite and stellerite (by balancing on aluminum). This required an adjustment of the stellerite Gibbs free energy by approximately 0.4%. The free energies of the other zeolites were then adjusted by the same proportion, which is well within errors associated with determining the original Gibbs free energies for zeolites in the database (Spycher 2000 [153572], p. 153).

Although the adjustment of thermodynamic data for zeolites significantly improved ambient simulations, adjustments of log(K) data for smectites were also necessary to achieve relatively steady ambient water compositions. This was done by calculating aluminum concentrations by equilibrating with illite, then adjusting log(K) values for Ca-, Na-, and Mg-smectite to yield saturation as an ideal solid solution at 25°C (not including K-smectite because modeled near steady-state ambient potassium concentrations are closer to the measured values without this mineral). The required changes in the Gibbs free energy are less than 0.5% for these minerals. The illite log(K) values were not changed because these data rely on dissolution experiments (Kulik and Aja 1997 [128132]) which are expected to yield thermodynamic properties that are more accurate than for smectites. By setting the aluminum concentration from equilibration with illite, and using the original microcline log(K) value, the simulated ambient potassium concentrations are somewhat smaller than the observed (microcline much more stable than illite). Microcline was therefore replaced by a K-feldspar phase ('k-spar') with a log(K) calculated to yield saturation at 25°C (thus yielding water compositions falling on the illite-K-feldspar equilibrium line). Doing so yielded a Gibbs free energy for this phase within the range of data reported in the literature (in Table 1 of Arnórsson and Stefánsson 1999 [153329]).

Other changes to the revised thermodynamic data base (Attachment VI) included the addition of a few other aqueous species ($NaSO_4^-$, $Ca(OH)^+$, and $Mg(OH)^+$). However, their addition does not yield significantly different results because these are not dominant species in the simulations presented in this AMR. A silica phase ('opal_proxy') was also added to the database. Upon further review of original data sources (Fournier 1973 [153464]) this phase appears to be a low-temperature silica mineral that may correspond to opal-CT. The solubility of this phase was taken to be the same as that for the mineral called "β-cristobalite" in the SUPCRT92 database (Johnson et al. 1992 [101632]) because the latter is consistent with the measured aqueous silica concentration in the pore water (Table 3). Sepiolite was removed from the list of input minerals (Section 6.1.7) because its simulated precipitation under ambient conditions resulted in unusually low magnesium concentrations compared to the measured pore water concentration (also the initial model concentration). As noted earlier, anorthite log (K) value, were also updated for consistency with the data reported by Arnórsson and Stefánsson (1999 [153329], p. 173) which are consistent with the quartz solubility data of Rimstidt (1997, [101709]) discussed in Section 4.1.4.1.

Parameters used for the calculation of activity coefficients for aqueous species were changed to reflect a change in activity coefficient model between TOUGHREACT V2.2 [153219] and V2.3 [153101] (Section 6.1.3). The effective ionic radii r_{ej} (Helgeson et al. 1981 [106024], Table 3) are input into the revised database instead of the Debye-Hückel a_o parameters. The $NaCl_{(aq)}$ species was also removed from the database, because calculated NaCl activity coefficients at high ionic strength were closer to measured values (Robinson and Stokes, 1965 [108567], p. 492) without it.

4.1.5 Kinetic Data

Kinetic data refer to the reaction rate constants (k_o), activation energies (E_a), and related data required to describe the rates of dissolution and precipitation of minerals at different temperatures and fluid chemistries. These data are taken directly from or are recalculated (or estimated) from published scientific literature. These data and their sources are listed in Table 4; see also assumption A-19.

Table 4. Kinetic Rate Law Data for Mineral-Water Dissolution and Precipitation

Mineral	k_0 (mol m^{-2} s^{-1})	E_a (kJ/mol)$^{(1)}$	m$^{(2)}$	n$^{(2)}$	Comment$^{(3)}$	Reference
α-Cristobalite	3.1623x10^{-13} see reference	69.08 0.0	1 1	1 1	dissolution precipitation	Renders et al. (1995 [107088], p. 81) Log k = -0.707-2598/T(K) from Rimstidt and Barnes (1980 [101708], p. 1683)
Quartz	1.2589x10^{-14}	87.5	1	1	no precip.	Tester et al. (1994 [101732], p.2415)
Tridymite	3.1623x10^{-13}	69.08	1	1	no precip.	Set to α-cristobalite
Amor. Silica	7.9433x10^{-13} 1.0x10^{-10}	62.8 0.0	1 4.4	1 1	dissolution precipitation	Rimstidt and Barnes (1980 [101708], p. 1683) Carroll et al. (1998 [124275], p. 1379)
Opal_proxy	7.9433x10^{-13}	62.8	1	1	no precip.	Set to amorphous silica
Calcite	1.6x10^{-6} (a) 1.6x10^{-9} (b) equilibrium	41.87	1	1	reversible	(a) Svensson and Dreybrodt (1992 [127978], p. 129) (b) Modified (.001 x (1)) average E_a from Inskeep and Bloom (1985 [128129], p. 2178)
Microcline	1.0x10^{-12}	57.78	1	1	reversible	Blum and Stillings (1995 [126590], estimated from Figure 5 and Table 2)
Albite-Low	1.0x10^{-12}	67.83	1	1	reversible	Blum and Stillings (1995 [126590], estimated from Figure 4 and Table 2)
Anorthite	2.5x10^{-19} (a) 1.0x10^{-12} (b)	67.83	1	1	no precip.	(a) Set to albite, then modified for equivalent Q/K (b) Set to albite
Smectite-Ca	1.0x10^{-14}	58.62	1	1	reversible	Set to illite
Smectite-Na	1.0x10^{-14}	58.62	1	1	reversible	Set to illite

Smectite-Mg	1.0x10^{-14}	58.62	1	1	reversible	Set to illite
Smectite-K	1.0x10^{-14}	58.62	1	1	reversible	Set to illite
Illite	1.0x10^{-14}	58.62	1	1	reversible	Assumed equal to muscovite (Knauss and Wolery 1989 [124300], p. 1500)
Kaolinite	1.0x10^{-13}	62.8	1	1	reversible	Johnson et al. (1998 [101630], Table 3)
Sepiolite	1.0x10^{-14}	58.62	1	1	reversible	Set to illite
Stellerite	1.99x10^{-12}	62.8	1	1	reversible	Set to heulandite
Heulandite	1.99x10^{-12}	62.8	1	1	reversible	Ragnarsdottir (1993 [126601] p. 2439, 2447)
Mordenite	1.99x10^{-12}	62.8	1	1	reversible	Set to heulandite
Clinoptilolite	1.99x10^{-12}	62.8	1	1	reversible	Set to heulandite
Glass (vphyr)	7.7233x10^{-15}	91	1	1	no precip.	Recalculated k_o based on diffusion-limited model of Mazer et al. (1992 [124354] pp. 573, 574)
Gypsum	equilibrium	-	-	-		Not applicable
Hematite	7.9433x10^{-13}	62.8	1	1	reversible (1) no. precip (2)	Set to dissolution rate of amorphous silica
Goethite	equilibrium	-	-	-		Not applicable
Fluorite	1.2224x10^{-7}	0	1	2	reversible	Calculated k_o from linear growth rate of Knowles-Van Cappellan et al. (1997 [124306] p. 1873)

NOTES: k_o Rate Constant
E_a Activation Energy
† First line refers to dissolution rate, second line to precipitation rate (unless otherwise stated in "Comment" and/or "Reference" column). "Vphyre" refers to the basal vitrophyre of the TSw unit. This composition of glass was used for all glass-bearing units, including the nonwelded PTn glassy tuffs.
(1) Some values differ slightly from sources because of number of significant figures retained in unit conversions.
(2) Exponents *m* and *n* in Equation 6.
(3) "no precip" means precipitation of this mineral is not allowed. "reversible" indicates that the absolute value of the precipitation rate constant is equal to the dissolution rate constant.

The quantities listed in Table 4 are defined and used in Equations 6 to 9 in Section 6.1.4. Some of the sources cited in Table 4 require pH to calculate k_0; in those cases a near-neutral pH (~7.0) was assumed as justified in Section 5 (Assumption A-8). For minerals where relevant kinetic data could not be found in the literature, rate constants were assumed (Section 5; Assumption A-8) to be equal to those of minerals with similar crystal structure or mineral group (based on comparison of the characteristics of the mineral groups in Klein and Hurlbut 1993 [153700]).

Sensitivities on the rate constants of certain minerals are included in Table 4 as alternate values. Rev00 model simulations used a value of k_0 assigned for calcite of 1.6 x 10^{-9} mol m^{-2} s^{-1}, which is three orders of magnitude smaller than the value reported in Svensson and Dreybrodt (1992 [127978]). Additional model simulations (DST THC Model Rev01) considered calcite using the published value of the rate constant as well as under equilibrium conditions; the latter is equivalent to the overall rate required for instantaneous equilibration. Rev01 Tptpmn and Tptpll

THC models treated calcite as an equilibrium mineral. Rev00 simulations considered an anorthite rate constant approximately six orders of magnitude smaller than the rate constant for albite. Rev01 simulations considered the rate constant to be equal to that for albite, but considered differences of three orders of magnitude in the reactive surface area. Such differences in the rate constants used reflect uncertainties more encompassing than the rate constants themselves. They incorporate uncertainties in the conceptual models for treating the thermodynamics and kinetics of solid solution phases and various processes that tend to inhibit mineral precipitation/dissolution.

Reaction rate laws can take numerous forms, of which a restricted number are used for the model analyses. The form of these rate laws and their significance are described in Section 6.1.

4.1.6 Transport Parameters

Transport parameters considered in the model are diffusion coefficients for aqueous and gaseous species and tortuosities of the fracture, matrix, and engineered system components. Diffusion coefficients for all aqueous species are considered to be identical and equal to the tracer diffusion coefficient of a single aqueous species (Cl) at infinite dilution. The aqueous diffusion coefficient of Cl at infinite dilution is 2.03 x 10^{-9} m^2/s at 25°C (Lasaga 1998 [117091], Table 4.1, p. 315), which in the model input was rounded to 2.0 x 10^{-9} m^2/s. In the gas phase, CO_2 is the only transported reactive species (other than H_2O vapor). For an ideal gas, the tracer diffusion coefficient of a gaseous species can be expressed as a function of temperature and pressure in the following form (Lasaga 1998 [117091], p. 322):

$$D = \frac{RT}{3\sqrt{2}pPN_A d_m^2}\sqrt{\frac{8RT}{pM}} \qquad \text{(Eq. 1)}$$

where

D = diffusion coefficient (m^2/s)
R = gas constant (8.31451 m^2 kg s^{-2} mol^{-1} K^{-1})
$T(K)$ = temperature in Kelvin units
P = pressure (kg m^{-1} s^{-2})
N_A = Avogadro's number (6.0221367 x 10^{23} mol^{-1})
d_m = molecular diameter (m)
M = molecular weight (kg/mol)

For CO_2, the following values were used:

d_m = 2.5 x 10^{-10} m (Lasaga, 1998 [117091], p. 322)
M = .04401 kg/mol (calculated from atomic weights, Klein and Hurlbut 1993 [153700], p. 172)

Tortuosities were set to 0.7 for fractures (DTN: LB990861233129.001 [110226]) based on models of *in-situ* testing. This value corresponds to the highest tortuosity given by de Marsily (1986 [100439], p. 233), with the rationale that fracture tortuosity should be high compared to matrix tortuosity (i.e. less tortuous path in fractures than in the matrix). Fracture tortuosities were further modified for fracture-fracture connections by multiplication of the tortuosity by the fracture porosity of the bulk rock. This operation yields the correct value for the fracture-to-fracture interconnection area (only for calculation of diffusive fluxes; the entire gridblock connection area is used for calculating advective fluxes, because the bulk fracture permeability of the entire gridblock is entered into the model). Matrix tortuosities are unknown, and therefore a value of 0.2 was estimated from values reported by de Marsily (1986 [100439], p. 233). The matrix tortuosity is assumed from the latter reference to be applicable to the tuff matrix at Yucca Mountain (Section 5, Assumption A-11).

4.1.7 Design Data

Design data are potentially subject to change, and are not data in the same sense as results of measurements. Therefore, it is assumed (Section 5; Assumption C-3) that the design information used in this AMR are accurate. Design data are presented in this section because they are used as input.

4.1.7.1 Drift Scale Test

The two-dimensional numerical mesh for the DST include the drift layout (e.g., drift diameter, concrete invert, bulkhead, and insulation) and the location of wing heaters (DTN: LB0101DSTTHGRD.001 [153687]). Other data include the drift and wing-heater power output (DTN: MO0007SEPDSTPC.001 [153707]). Some modifications to the properties of the insulation are given in Bodvarsson 2001 [153816], YMP-LBNL-YWT-ELS-1, p. 35.

4.1.7.2 Design of Potential Waste-Emplacement Drifts - Backfill Case

This design was used for the Tptpmn Backfill THC Model (Section 6.3). Two time periods are considered in the drift design and related data input into the model:

- A 50-year pre-closure period during which 70 percent of the heat released by the waste packages is removed by ventilation.
- A post-closure period immediately following the initial 50-year pre-closure period and extending to 100,000 years (the total simulation time), during which a drip shield and backfill are above the waste packages and no heat is removed by ventilation.

Accordingly, some of the drift-specific model input data are not the same for the pre-closure and post-closure time periods. These design data are for the Total System Performance Assessment-Site Recommendation (TSPA-SR), Rev.01, base case.

The model drift geometry and thermophysical properties of design elements (waste package, backfill) are shown in Table 5 and Figure 1. DTNs for these data are referenced in Table 2. These design data are for the TSPA-SR, Rev.01, base case. The discretization of the drift is consistent with the dimensions shown in Figure 1, within the limits imposed by the resolution of the model mesh.

Table 5. Drift Design Parameters

Model Input	Value
Drift diameter	5.5 meters
Waste package outer diameter	1.67 meters
Location of waste package center above bottom of drift	1.945 meters
Location of waste package center below the springline	0.805 meters
Angle of Repose	26°
Minimum depth of backfill cover (this occurs at an angle equivalent to the angle of repose measured off the vertical drawn from the waste package centerline)	1.495 meters
Drip shield thickness	0.02 meters
Air gap between waste package surface and the inside of drip shield	0.396 meters
Location of backfill spoil peak (this is the location where the top of the backfill intersects the vertical drawn from the drift centerline) above the drift springline	2.25 meters
Backfill/drift wall intersection point	1.0 meter above the springline at the drift wall intersection
Air gap above invert and below waste package surface	0.504 meters
Inside radius of drip shield	1.231 meters
Top of invert as measured from bottom of drift	0.606 meters
Waste package thermal conductivity	14.42 W/m-K
Waste package density	8189.2 kg/m^3
Waste package specific heat	488.86 J/kg-K
Invert intrinsic permeability	6.152x10^{-10} m^2
Invert porosity	0.545
Invert grain density	2530 kg/m^3
Invert residual liquid saturation	0.092
Invert alpha (van Genuchten)	1.2232x10^{-3} Pa^{-1}
Invert n (van Genuchten)	2.7
Invert specific heat	948 J/kg-K
Invert thermal conductivity	0.66 W/m-K
Backfill intrinsic permeability	1.43x10^{-11} m^2
Backfill porosity	0.41
Backfill grain density	2700 kg/m^3
Backfill residual liquid saturation	0.024
Backfill alpha (van Genuchten)	2.7523x10^{-4} Pa^{-1}
Backfill n (van Genuchten)	2.0
Backfill specific heat	795.492 J/kg-K
Backfill thermal conductivity	0.33 W/m-K

Source: CRWMS M&O 2000 [151014]

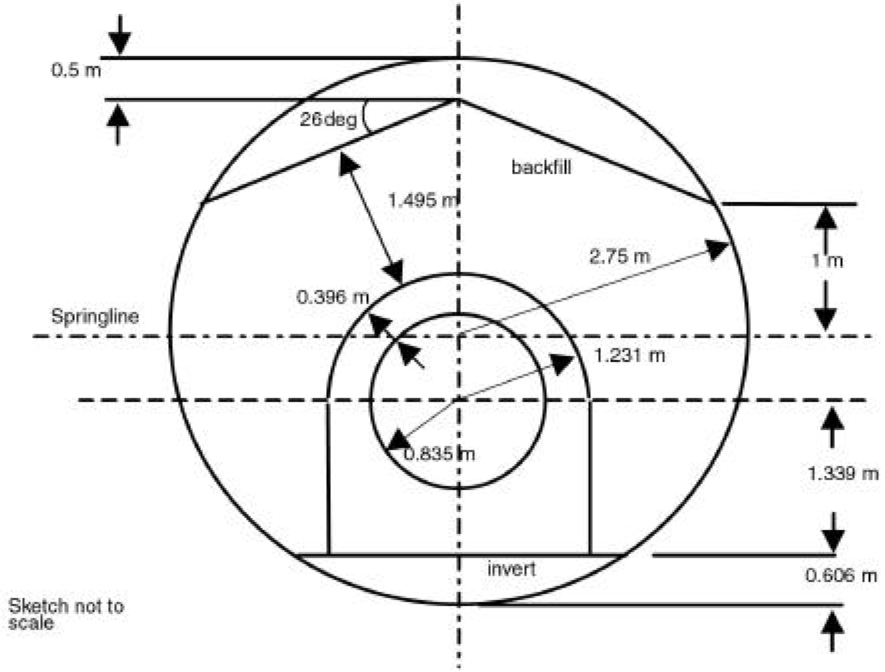

Source: CRWMS M&O 2000 [151014]

Figure 1. Sketch (Not to Scale) Corresponding to In-Drift Data for Drift-Scale Models for TSPA-SR (Rev 01)

To account for the 50-year pre-closure period without backfill, backfill (as shown on Figure 1) was included in the model only for simulation times greater than 50 years. The drip shield was not explicitly modeled, but its thickness and thermal conductivity were considered in the width and thermal properties, respectively, of the open zone between the waste package and backfill during the post-closure period.

The heat load from the waste package was obtained from DTN: SN9907T0872799.001 [111485]. The averaged heat transfer from the waste package, as a function of time, is shown in Attachment VII. The initial heat transfer from the waste package is 1.54 kW/$m_{(drift)}$ which decays after 50 years to 0.187 kW/m and less than 0.003 kW/m after 1,000 years. For the simulated first 50 years, only 30 percent of this heat is input into the model to account for 70 percent heat removal by ventilation during the pre-closure period.

Heat transfer from the waste package to the drift wall is implemented in the model by using time-varying “effective” thermal conductivities (for open spaces within the drift) that were calculated to account for radiative and convective heat-transport components. These time-varying data were input into the model as coefficients (values between 0 and 1) for each open zone within the drift. Each zone was also assigned a constant maximum thermal conductivity (Kth_{max}), which was then multiplied by the corresponding time-varying coefficients to obtain effective conductivities as a function of time (Attachment IX). The sources of these data are listed in Table 2.

The effective thermal conductivities and corresponding open zones of the drift during preclosure are not the same as during post-closure. Only one open space between the waste package and the drift wall is considered for the pre-closure period (no backfill or dripshield, Kth_{max} = 10.443 W/m K). For post-closure, two zones are considered: (1) the open space between the waste package and the dripshield (Inner Zone, dripshield included, Kth_{max} = 3.426 W/m K), and (2) the open space between the backfill and the drift wall (Outer Zone, Kth_{max} = 9.068 W/m K) (Figure 1). Accordingly, model runs were started with the pre-closure thermal conductivity data, then stopped after 50 years and restarted with the corresponding post-closure data.

The implementation of the drift design into the model is further documented in Bodvarsson 2001 [153816], YMP-LBNL-DSM-NS-1, pp. 11-14.

4.1.7.3 Design of Potential Waste-Emplacement Drifts - No-Backfill Case

A design similar to that described above (Section 4.1.7.2) was used for the Tptpmn THC model (no backfill) (Section 6.4) and the Tptpll THC Model (Section 6.6). Pre-closure and post-closure time periods are considered for the no-backfill model as for the backfill model, with the difference that backfill is not placed above the drip shield 50 years after waste emplacement. The same design data and drift properties are used as for the case with backfill, except as noted below to reflect revised thermal properties resulting from the absence of backfill, and a more current drift design (CRWMS M&O 2000 [150953]).

The heat load from the waste package was revised from an initial 1.54 kW/m to 1.45 kW/m. The revised averaged heat transfer from the waste package, as a function of time, is shown in Attachment VIII. Time-varying "effective" thermal conductivity data (for open spaces within the drift) were revised as shown in Attachment X. For pre-closure, Kth_{max} = 10.568 W/m K for the zone between the waste package and the drift wall. For post-closure, Kth_{max} = 2.298 W/m K for the Inner Zone (between the waste package and the dripshield), and Kth_{max} = 14.407 W/m K for the Outer Zone (between the dripshield and the drift wall). The sources of these data are listed in Table 2.

For the Tptpll THC model (Section 6.6), the invert thickness was increased from about 0.6 to 0.8 m to reflect the more current drift design (Figure 1, p. 22 in CRWMS M&O 2000 [150953]). For the Tptpmn THC models (no-backfill) (Section 6.4), the original thickness of 0.6 m was used for consistency (for comparison purpose) with the original Tptpmn seepage model including backfill (Section 6.3). For both no-backfill THC models (Tptpmn and Tptpll), the invert was divided in two zones with different thermal conductivities: 1.52 W/m K for the upper half and 0.15 W/m K for the lower half (Table 2).

4.2 CRITERIA

This AMR complies with the DOE interim guidance (Dyer 1999 [105655]). Subparts of the interim guidance that apply to this analysis or modeling activity are those pertaining to the characterization of the Yucca Mountain site (Subpart B, Section 15), the compilation of information regarding geochemistry and mineral stability of the site in support of the License Application (Subpart B, Section 21(c)(1)(ii)), and the definition of geochemical parameters and conceptual models used in performance assessment (Subpart E, Section 114(a)).

The NRC’s *Issue Resolution Status Report, the Key Technical Issue: Near-Field Environment* (NRC 2000 [153292], Subissues 1 and 4) establishes technical acceptance review criteria that the NRC staff will use in their review of DOE’s submittals describing coupled processes in the near-field environment. Specifically, Subissue 1 of this Key Technical Issue provides review criteria for the effects of THC processes on seepage and flow and Subissue 4 provides review criteria for the effects of coupled THC processes on radionuclide transport through engineered and natural barriers.

The drift spacing of 81 m center-to-center is found in *Subsurface Facility System Description Document* (CRWMS M&O 2000 [151467], Section 1.2.1.5) as a design criterion.

4.3 CODES AND STANDARDS

No specific formally established standards have been identified as applying to this analysis and modeling activity.

INTENTIONALLY LEFT BLANK

5. ASSUMPTIONS

Many assumptions generally underlie numerical modeling of heat and fluid flow in unsaturated porous fractured media. In addition to these assumptions, numerous other assumptions underlie the calculation of mineral-water reactions, the transport of aqueous and gaseous species, and the conceptual models used to describe the chemical and physical systems. Another class of assumptions are those that are inherent to the data that describe potential repository designs and associated parameters on which model simulations rely.

The model assumptions are categorized according to the section to which they apply and are as follows:

A. General THC Process Model Assumptions (used in Sections 6.1 to 6.7)

1. It is assumed that the rock can be described by the dual-permeability model that considers separate but interacting fracture and matrix continua. In the dual-permeability model, the fracture continuum is considered as ~~separate~~ co-located JEH 2/9/01 but interacting with the matrix continuum, in terms of the flow of heat, water, and vapor through advection and conduction. Aqueous and gaseous species are transported via advection and molecular diffusion between fractures and matrix. Each continuum has its own well-defined initial physical and chemical properties. It is assumed that the dual permeability approach, with appropriate material and fracture properties and an appropriate discretization of time and space, is an adequate approximation of the real world. The dual permeability approach for modeling physical processes in fractured-porous media is discussed in detail in Doughty (1999 [135997]). This approach is validated by the comparison of measured geochemical data to results of simulations presented in this AMR (Sections 6.2.7 and 6.2.8). No further justification is necessary.

2. It is assumed that the thermal conductivity and heat capacity of the precipitated mineral assemblage are the same as that of the host rock. This is justified for two reasons. First, the mass of minerals precipitated is much smaller than the mass of mineral originally in place. Also, nearly all of the minerals treated in the model are naturally occurring at Yucca Mountain, and are similar or identical to those in the initial rock. Therefore, this assumption is reasonable and does not need to be validated.

3. For some model simulations, it is assumed that the infiltrating water and that in the fractures have the same chemical composition as the matrix pore water that was collected from Alcove 5, near the DST location, as given in Table 3. This analysis is the average of two samples taken near the DST location; therefore it may be taken as typical. A more detailed discussion of this assumption is given in Section 6.1.2. No further justification is required for this assumption.

4. It is assumed that the physical properties of the gas phase are unaffected by changes in the partial pressure of CO_2 resulting from heating, calcite reactions, and gas-phase transport. This assumption is justified by the results of the model runs (Figures ~~28~~ 39 and ~~29~~ 40), which show that the volume fraction of CO_2 is generally less than 5% and always less than 10%. Although the molecular weight of CO_2 is greater than that of air

JEH 2/9/01

JEH 2/9/01

(approximately 44 g/mol versus 29 g/mol), the density is only increased proportionally to the volume fraction of CO_2 and the ratio of the molecular weights. This would result in a density increase of about 5% for a gas with a CO_2 volume fraction of 10%. These conditions make the effect of evolved CO_2 on the physical properties of the gas phase negligibly small, and justify the use of this assumption without further justification. The presence of steam (molecular weight approximately 18 g/mol) would increase this effect somewhat, although increases in the steam fraction accompanying boiling tend to dilute the CO_2 fraction.

5. It is assumed that changes in water chemistry have no effect on the thermodynamic and physical properties of the water, i.e. density and viscosity. This assumption is valid because aqueous species concentrations are low in waters at most values of the liquid saturation. In cases where concentrations are significantly higher, the liquid saturation is generally much less than 1% and therefore the liquid is nearly immobile because of the very small relative permeability for the liquid phase under such conditions. No further justification or confirmation is necessary.

6. Diffusion coefficients of all aqueous species are assumed to be the same. This is justified because the tracer diffusion coefficients of aqueous species differ by at most about one order of magnitude, with many differing by less than a factor of 2 (Lasaga 1998 [117091], p. 315). This assumption does not need to be confirmed, for the above reason.

7. The dissolution rate of silica-rich glass has been found to follow a dependence of H_2O diffusion through a reaction-product layer (Mazer et al. 1992 [124354]). Because the volcanic glass in the rocks at Yucca Mountain is approximately 10 million years old and has undergone varying degrees of alteration, a constant thickness product layer on the glass surface was assumed for recalculation of the dissolution rate constant at 25°C. It is assumed that the uniform layer is 10 µm thick. The layer cannot be thicker than a typical grain diameter (100 µm). However, if it is too thin, a typical grain would be completely dissolved in less than 10 million years. A thickness of 10 µm results in an inferred grain thickness dissolved of about 30 µm, thus satisfying both the above requirements. Details of the calculations are given in Bodvarsson 2001 [153816], YMP-LBNL-YWT-ELS-1, p. 43. No further justification or confirmation is necessary.

8. Values for kinetic rate constants were assumed for near-neutral pH values (~ 5 to 9). Rate constants for silicate minerals typically vary by less than an order ~~for~~ of magnitude JEH 2/9/01 over this pH range (Langmuir 1997 [100051], Figure 2.11, p. 78). Measured pH from pore waters and those collected from the DST are well within this range, (for DTNs, see Table 2) and model results are also generally in this range, except for some model compositions that are present at very low saturations just prior to dryout. Calcite, which has a rate sensitive to pH, is shown to have a similar effect on water chemistry for equilibrium or kinetic conditions because of its fast rate (Section 6.2) and therefore the pH effect is not important for the THC processes examined in this AMR. Also, given other factors such as the reactive surface area that may change the effective rate by orders of magnitude, this assumption is justified. Minerals for which relevant kinetic data were not available, rate constants were assumed equal to those for

structurally or chemically similar minerals. This assumption is reasonable and requires no further justification or verification.

9. Density changes in the water due to thermal or compositional effects are assumed to be negligible for calculations of the concentrations of aqueous species. This assumption is justified because of the unsaturated conditions characterizing the near-field environment at Yucca Mountain and the lack of significant pressure changes that would modify the water density significantly. Density changes are typically less than 5%, which is small compared to most other uncertainties in chemical equilibrium calculations. No further justification or confirmation is necessary.

10. It is assumed that mineral precipitation and dissolution take place uniformly over the area of smooth plane-parallel fracture walls. The location of mineral precipitation may be nonuniform leading to a different relationship of permeability to porosity changes. This assumption can be justified by the use of bulk permeabilities and porosities that initially take into account the net effect of variability in fracture aperture at a macroscopic scale. Sensitivity studies were performed using a smaller effective aperture (hydraulic aperture) instead of assuming nonuniform precipitation. This did have a greater effect on permeability (Section 6.5), however, changes in flow and chemistry were nonetheless small. Therefore, no further justification or confirmation is necessary.

11. The estimated matrix tortuosity of 0.2 is assumed to be applicable to the tuff matrix at Yucca Mountain (see Section 4.1.6). Since this value is within a range of values that differ by less than one order of magnitude, and is a factor applied along with the porosity to the diffusion coefficient, the effect on reaction-transport processes of a deviation in this number from the true value would be small. Therefore, no further justification or confirmation is necessary.

12. It is assumed that CO_2 gas behaves as a perfect gas (i.e. obeys the ideal gas law and its partial pressure equals its fugacity). This assumption is justified at the low ambient pressures (near atmospheric) under which simulations are performed (Langmuir 1997 [100051], p. 15). Therefore, no further justification or confirmation is necessary.

13. It is assumed that the chemical and physical properties of minerals that form solid solutions can be approximated by their individual endmember compositions and properties. Most mineral thermodynamic properties differ to varying degrees from the properties of the individual endmembers considered separately. An ideal solid solution model (i.e. each endmember's activity equals its mole fraction) is, however, assumed for smectite (Na, Ca, and Mg endmembers) in some of the simulations. Smectite endmembers are calculated to be near equilibrium with pore waters. If smectite is not treated as a solid solution, some of these endmembers are calculated to precipitate while others are predicted to dissolve. By considering a solid solution, individual smectite endmembers either all dissolve or all precipitate, providing a better physical representation of dissolution/precipitation processes. Feldspar solid solutions were not considered because they exhibit strong non-ideality and data for such models have large uncertainties. However, because albite (Na-feldspar) and anorthite (Ca-feldspar) are

generally strongly undersaturated in the simulations, their dissolution rates are governed primarily by the kinetic rate constant rather than the saturation index. In addition, because nearly pure secondary K-feldspar compositions are observed in geothermal systems (Stefánsson and Arnórsson, 2000 [153578], p. 2578), the precipitation of secondary K-feldspar may be approximated fairly well with a pure end-member. The results of the model simulations and these assumptions are further validated by comparison to measured water chemistry in the DST and the plug-flow reactor experiments. Therefore, no further justification or confirmation is necessary.

14. It is assumed that the fracture continuum has an initial porosity less than one (0.99 in the DST THC Rev00 Model and Tptpmn THC models, and 0.5 in the Tptpll THC Model). These values are chosen such that that the fracture medium contains solids that can react with fluids in fractures. The total fracture void space in the fracture continuum is set to be consistent with the fracture porosity (the fraction of the bulk rock occupied by fracture void space). This assumption does not need justification or confirmation.

15. The thermal conductivities of fracture and matrix nodes are calculated assuming a linear interpolation between dry and wet conductivities as a function of liquid saturation. These are the thermal conductivities for the solid + fluid system. For fractures, thermal conductivities are multiplied by the fracture porosity to account for the correct fracture-to-fracture connection area in calculations of heat conduction (i.e. this is needed because full grid block areas are input into the model). Fracture thermal conductivities are also multiplied by 0.1 (an estimated value) to account for the limited spatial continuity and connectivity between fracture grid blocks). The volume of the fracture continuum is, however, only a small fraction of the matrix continuum. Therefore heat conduction occurs primarily through the matrix continuum and, as a result, the model is not sensitive to the amount of heat conduction in fractures. This assumption does not need further justification or confirmation.

16. Vapor-pressure lowering (the Kelvin effect) is assumed to have a secondary effect on the results of the THC simulations and is neglected. If included, the magnitude, spatial extent and duration of rock dryout may be less than predicted. However, the magnitude of mineral precipitation and permeability reduction is likely to be less with vapor pressure lowering. Also, a smaller range of fracture saturations leading a smaller range of water chemistries in the near-field would be expected. Therefore, the assumption of neglecting vapor-pressure lowering is conservative with respect to specific THC processes in the near-field. This assumption does not need further justification or confirmation.

17. Upon boiling or evaporation, it is assumed that the aqueous phase becomes unreactive and is not concentrated further once its ionic strength reaches an input upper limit (2 for the REV 00 DST THC Model and the Tptpmn THC Backfill Model, and 4 for the other models) or if the liquid saturation drops below an input lower limit (10^{-4} for the Rev 00 DST THC Model and the Tptpmn THC Backfill Model, and 10^{-5} for the other models). This ensures that the calculated ionic strength remains within the range of applicability of activity coefficient models (Section 6.1.3). Past these limits, concentrations of

aqueous species are saved (unchanged) during dryout, and become available again for reaction at the time of rewetting when the liquid saturation increases and the ionic strength decreases. This scheme has the effect of assuming that all salts that would precipitate from the point of the lower saturation limit or higher ionic strength limit, up to the point of complete dryout, would instantly redissolve upon rewetting. This assumption is justifiable in light of the observation that, in the simulations presented here, the liquid saturation limit is almost always reached before the ionic strength limit. At liquid saturations as small as 10^{-4} or 10^{-5}, the total amount of dissolved mass present in any given model grid node is exceedingly small so that ignoring chemical reaction for such small mass amounts (and over a limited time period) does not significantly affect the general computed trends of aqueous phase concentrations and precipitated mineral amounts over long periods of time and a wide range of liquid saturations. Therefore, this assumption is justified and does not need confirmation.

18. It is assumed that hydrogeologic rock properties in each hydrogeologic unit of the model are laterally homogeneous, except in the Tptpmn Heterogeneous THC Model where fracture permeability in an area spending 150 m above and 150 m below the modeled emplacement drift is assigned spatial heterogeneity (Section 6.5.1). This assumption is confirmed by the results of the Tptpmn Heterogeneous THC Model (Section 6.5.2), which do not show significantly different water chemistry in space or time compared to the homogeneous model (Section 6.4.5) and the good comparisons between modeled and measured water and gas chemistry for the DST. No further confirmation is required.

19. Thermodynamic data (Section 4.1.4 and Attachments V and VI) and kinetic data (Section 4.1.5 and Table 4) that were obtained from the open literature are assumed to be accurate for the purposes of the analyses presented in this AMR. Because the model results are validated against measurements from the DST (Section 6.2) and a laboratory experiment (Section 6.7) no further justification or confirmation is necessary.

B. Specific Drift Scale Test THC Model Assumptions (used in Section 6.2)

1. Heat transfer from the electrical heaters in the drift to the drift wall is approximated by applying heat directly to the drift wall, instead of calculating radiative heat effects. Because our main objective is the quantification of THC processes in the rock outside the drift, it is only necessary to capture the effective heat flux into the wall of the drift. This assumption does not need to be confirmed because it is solely used as an alternative method for specifying the heat flux into the rock mass.

2. The concrete invert is considered non-reactive and does not affect the chemistry of waters and gases outside the drift. Because the modeled system is in a heating phase, the concrete is drying out over the time-scale investigated and thus no seepage water can interact with it. Therefore, no further justification or confirmation is required.

3. Water and gas chemical analyses listed in Table 2 and described in Section 6 are assumed to be representative of samples around the DST. This is justified by the fact

that their compositions do not deviate markedly over time from a given location and that they are similar to most other samples collected over the past three years. Only a few other water samples (borehole interval 59-4) out of numerous others that have been collected are different in character from the samples described in this AMR, and their early time of collection and unusual chemical characteristics make them suspect. No such samples were used in this AMR. This assumption requires no further justification or confirmation for the data used in this AMR.

C. Specific Model Assumptions for the Tptpmn and Tptpll THC Models (used in Section 6.3)

1. For the Tptpmn and Tptpll THC Model simulations, the drift wall is assumed closed to fluid fluxes except for gaseous CO_2 diffusive fluxes. The latter are limited because the drift is assumed to be closed at each end. Therefore, the drift has a finite volume that is small compared to the near-field rock volume, and assuming that no reactions are occurring in the drift, the effect of exchange of components with the near-field environment would have little effect on near-field THC processes. There are further reasons for assuming the drift closed to most fluid fluxes. First, our objective is to calculate the water and gas compositions that reach the drift wall, and not THC processes in the drift itself. In-drift THC processes are considered in documents that support the Engineered Barrier Systems PMR (CRWMS M&O 2000 [151804]). Because processes in the rock outside the drift govern compositions of aqueous liquids and gases entering the drift this assumption is valid. Second, for a homogeneous fracture system with constant vertical infiltration (from the top model boundary), the wall acts as a capillary barrier. Therefore, the liquid fluxes very close to the drift wall are adequately described by the model as chosen (except where there is backfill and in the invert at the base of the drift). If the drift wall were open to all fluid fluxes, advective fluxes of gas at the wall could differ from those calculated here, because convection across this boundary could occur locally around the drift. However, the simulation of such convection patterns would be questionable because it would involve computing fluid flow through open spaces of the drift using a model designed to calculate flow through porous media. The gas flux toward the drift wall (but not through it) was calculated, and may approximate ~~of~~ the total gas flux into or out of the 2/19/01 drift, assuming that the drift responds only to TH-induced pressure changes in the near-field environment. Thus, given the scope of addressing processes in the near-field and not in the drift itself, the assumption is reasonable. No further justification is required for assumptions regarding gas and liquid fluxes; however, further confirmation of gas fluxes at the drift wall may be required. No further confirmation is necessary for liquid fluxes.

2. The backfill and invert are assumed to be non-reactive. Because only THC processes outside the drift are considered, this assumption does not need to be confirmed.

3. All drift design geometries, properties of in-drift design components, and heat loading values are assumed. These data are specific to a certain analysis and therefore the model simulations are valid for that set of data. Drift design data are discussed in Section 4.1.7, where this assumption is referred to. No further justification or confirmation is required.

4. Effective thermal conductivities (Attachments IX and X) were calculated based on 50% heat removed instead of the 70% heat removal used in the Tptpmn and Tptpll THC Models. This change in the heat removal is thought to have little effect on the calculations, however, the impact will be documented at a later date. This assumption needs no further justification, but will require confirmation.

5. A tortuosity of 1 is assumed for backfill (no tortuosity effect), and a value of 0.7 is assumed for the invert. These values only slightly affect diffusive transport of CO_2 in the drift. The tortuosity of sand is about 0.7 (de Marsily 1986 [100439], p. 233) and because the invert and backfill are coarse granular materials, their tortuosities would be expected to be between 0.7 and 1.0. Because reactions involving CO_2 are not considered in the drift, the diffusivity of CO_2 within in-drift components has a negligible effect on THC processes outside of the drift. Therefore, this assumption needs no further justification or confirmation.

6. Potential sources or sinks of CO_2 within the drift (e.g., microbial activity or atmospheric CO_2) were not considered because their combined effects have not been assessed and are not in the scope of this AMR. This assumption will require confirmation.

INTENTIONALLY LEFT BLANK

6. ANALYSIS/MODEL

This AMR does not directly support any of the principal factors of the postclosure safety case as presented in Repository Safety Strategy (CRWMS M&O 2000 [153225], Volume II, Section 4.1). However, the other factor for site recommendation considerations, “Effects of Heat on the Flow,” (CRWMS M&O 2000 [153225], Volume II, Section 4.2.2) is addressed by this AMR in that the effect of mineral dissolution and precipitation on the permeability of the fracture continuum is simulated.

The conceptual model, the DST THC model, the Tptpmn and Tptpll THC models, and simulation results are presented in this section. Section 6.1 describes the conceptual model for THC processes. Section 6.2 describes the DST THC model and provides validation of the conceptual model by comparison to measured water and gas chemical data. The Tptpmn and Tptpll THC models are presented in Sections 6.3 to 6.6, giving predictions of coupled THC processes for 100,000 years under boundary conditions that are varied to represent the effects of potential climatic change, various drift designs, and two potential repository host units. A modeling analysis of a crushed tuff plug-flow reactor experiment is presented in Section 6.7.

The model development, data, and results are documented in the scientific notebooks (SNs) listed in Table 6 below.

Table 6. Scientific Notebooks

LBNL Scientific Notebook ID	YMP M&O Scientific Notebook ID	Page numbers	Citation
YMP-LBNL-YWT-ELS-1	SN-LBNL-SCI-109-V1	35–70, 87–91	Bodvarsson 2001 [153816]
YMP-LBNL-YWT-NS-1	SN-LBNL-SCI-111-V1	72–77, 115, 137	Spycher 1998 [153571]
YMP-LBNL-YWT-NS-1.1	SN-LBNL-SCI-112-V1	96, 104–156	Spycher 2000 [153572]
YMP-LBNL-YWT-JA-1A	SN-LBNL-SCI-005-V1	28–43, 48–51	Bodvarsson 2001 [153816]
YMP-LBNL-DSM-ELS-1	SN-LBNL-SCI-142-V1	3–20, 27–52	Bodvarsson 2001 [153816]
YMP-LBNL-DSM-NS-1	SN-LBNL-SCI-141-V1	1–143	Bodvarsson 2001 [153816]
YMP-LBNL-YWT-NS-1.2	SN-LBNL-SCI-112-V2	1–47	Bodvarsson 2001 [153816]
YMP-LBNL-DSM-ELS-PD-1	SN-LBNL-SCI-190-V1	7–60	Bodvarsson 2001 [153816]
YMP-LBNL-GSB-1.6.4	SN-LBNL-SCI-085-V2	24–33	Bodvarsson 2001 [153816]

6.1 THE DRIFT SCALE THC CONCEPTUAL MODEL

This section describes the THC process model underlying the numerical simulations of THC processes in the DST and for all other drift-scale THC models in this AMR. There are many considerations involved in the development of a conceptual model that describes processes involving liquid and vapor flow, heat transport, and thermal effects resulting from boiling and condensation, transport of aqueous and gaseous species, mineralogical characteristics and changes, and aqueous and gaseous chemistry. A conceptual model of reaction-transport processes in the fractured welded tuffs of the potential repository host rock must also account for the different rates of transport in very permeable fractures, compared to the much less permeable rock matrix. The following subsections describe the conceptual models for the various physical and chemical processes.

6.1.1 Dual Permeability Model for THC Processes

Transport rates greater than the rate of equilibration via diffusion necessarily leads to disequilibrium between waters in fractures and matrix. This disequilibrium can lead to differences in the stable mineral assemblage and to differences in reaction rates. Because the system is unsaturated and undergoes boiling, the transport of gaseous species is an important consideration. The model must also capture the differences between initial mineralogy in fractures and matrix and their evolution. To handle these separate yet interacting processes in fractures and matrix, we have adopted the dual permeability method. In this method, each gridblock is separated into a matrix and fracture continuum, each of which is characterized by its own pressure, temperature, liquid saturation, water and gas chemistry, and mineralogy. Figure 2 illustrates the dual permeability conceptual model used for THC processes in the DST THC Model and all other drift-scale THC models described in this AMR.

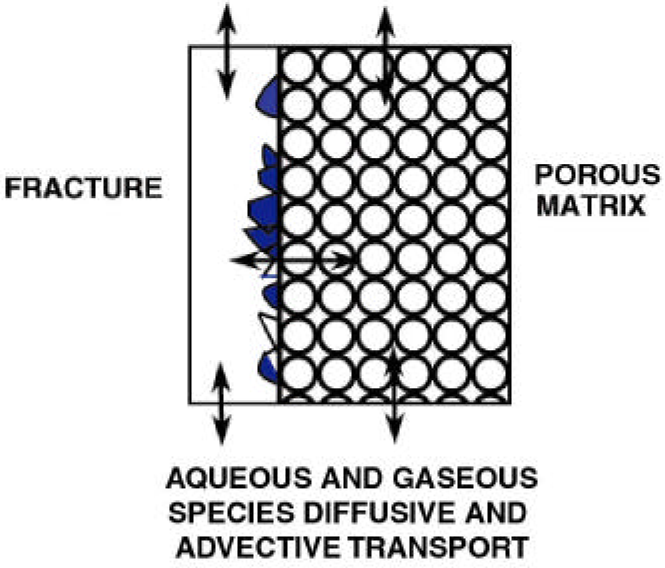

Figure 2. Conceptual Model (Schematic) for Reaction-Transport Processes in Dual Permeability Media. Arrows refer to aqueous and gaseous species transport pathways. Angular objects in fracture are secondary fracture mineralization.

6.1.2 Initial Water Chemistry

The infiltrating water chemistry could be chosen from either the pore water chemistry in the UZ at or above the potential repository horizon, or from a more dilute composition found in the perched water or saturated zone. The perched waters are much more dilute than UZ pore waters and isotopic compositions (^{36}Cl/Cl, ^{18}O/^{16}O, D/H, ^{14}C) and Cl concentrations suggest that they have a large proportion of late Pleistocene/early Holocene water (Levy et al. 1997 [126599], p. 906; Sonnenthal and Bodvarsson 1999 [117127], pp. 107–108). Consequently, we assume that the infiltrating water and the water in the fractures have the same chemical composition as the matrix pore water (Assumption A-3, Section 5).

However, for drift-scale THC processes in the TSw unit, the water entering the top of the unit comes from the base of the Paintbrush Tuff nonwelded unit (PTn) and is not necessarily the same composition as water entering the Tiva Canyon welded unit (TCw) near the land surface. A conceptual model that explains the aqueous chemistry and background ^{36}Cl/Cl isotopic ratios in the Exploratory Studies Facility holds that percolating water must pass mostly through the PTn matrix (because of its high permeability and low fracture density) before reverting to predominantly fracture flow in the TSw. As discussed in Levy et al. (1997 [126599], pp. 907–908), this seems to be true everywhere except near large structural discontinuities in the PTn (i.e., faults). Hence, percolating water in the TSw ultimately had come predominantly through the PTn matrix. Analyses of PTn pore waters (and some at the top of the TSw) and many Cl analyses of TSw pore waters are consistent with this interpretation (Sonnenthal and Bodvarsson 1999 [117127], pp. 140–141). Therefore, as stated in Section 4.1.3, the infiltrating water and the water in the fractures are set to the same chemical composition as the matrix pore water collected from Alcove 5 and listed in Table 3.

6.1.3 Numerical Model for Coupled THC Processes

The geochemical module incorporated in TOUGHREACT V2.2 [153219] and V2.3 [153101] simultaneously solves a set of chemical mass-action, kinetic-rate expressions for mineral dissolution/precipitation, and mass-balance equations. This provides the extent of reaction and mass transfer between a set of given aqueous species, minerals, and gases at each gridblock of the flow model (Xu and Pruess 1998 [117170]; Xu et al. 1998 [101751]). Equations for heat, liquid and gas flow, aqueous and gaseous species transport, chemical reactions, and permeability/porosity changes are solved sequentially (e.g., Steefel and Lasaga 1994 [101480], p. 550).

The setup of mass-action and mass-balance equations in TOUGHREACT V2.2 [153219] and V2.3 [153101] is similar to the formulation implemented in Reed (1982 [117901], pp. 514–516). Additional provisions are made for mineral dissolution and precipitation under kinetic constraints and a volume-dependent formulation for gas equilibrium, as described below. The chemical system is described in terms of primary aqueous species (the independent variables). Minerals, gases, and secondary aqueous species are defined in terms of reactions involving only the primary species. It has been shown that if the diffusivities of all aqueous species are equal, as assumed in Section 5, only the transport of primary species (in terms of total dissolved concentrations) needs to be considered to solve the entire reactive flow/transport problem (Steefel and Lasaga 1994 [101480], p. 546).

The system of nonlinear equations describing chemical mass-balance, mass-action, and kinetic rate expressions is solved by a Newton-Raphson iterative procedure. In TOUGHREACT V2.2 [153219], activity coefficients of aqueous species are computed by an extended Debye-Hückel equation (e.g., Drever 1997 [140067], p. 28, Equation 2-12). In V2.2 [153219], activity coefficients of neutral species are assumed equal to one, and the activity of water is computed using a method described in Garrels and Christ (1965 [105797], pp. 64–66), which essentially equates the water activity to its mole fraction. These methods are generally reliable for ionic strengths up to 2 molal. In TOUGHREACT V2.3 [153101], activity coefficients of charged species and the activity of water are calculated with the method of Helgeson et al. (1981 [106024], Equations 298, 190, 106, and Tables 1, 3, 29, and 30) as further described in Bodvarsson 2001 [153816], YMP-LBNL-YWT-NS-1.2, pp. 21–27. Using this method, activities of water and activity coefficients of electrolytes typical of natural systems (NaCl, $CaCl_2$, Mg_2SO_4, Ca_2SO_4) were fairly well reproduced up to ionic strengths of 6 molal (Bodvarsson 2001 [153816], YMP-LBNL-YWT-NS-1.2, pp. 28–30 and 32). In TOUGHREACT V2.3 [153101], activity coefficients of selected neutral species are calculated using salting-out coefficients as described in Langmuir (1997 [100051], Equation 4.62 and Table 4.5).

Equilibration with mineral phases is computed by adding a mass-action equation, for each saturated mineral, into the system of nonlinear equations as follows:

$$\log(K_i) = \log(Q_i) \qquad \text{(Eq. 2)}$$

where K_i denotes the equilibrium constant and Q_i the product of the ion activities in the reaction that expresses mineral i in terms of the primary aqueous species. A term representing the amount of primary aqueous species consumed or produced by equilibration of minerals is added to the mass-balance equation for each primary species involved in mineral reactions, and this term is solved simultaneously with the concentrations of all primary species. Minerals are thus dissolving if $\log(Q_i/K_i) < 0$ and precipitating if $\log(Q_i/K_i) > 0$. For some minerals (e.g., calcite in this report, see Section 6.4.3) a "supersaturation gap" can be specified, by which the mineral is not allowed to precipitate if $\log(Q_i/K_i)$ is greater than zero but less than a specified "gap" value (positive). This gap can be set to decrease exponentially with temperature, as described in Bodvarsson 2001 [153816], YMP-LBNL-YWT-NS-1.2, p. 33.

Gas species, such as CO_2, are treated as ideal mixtures of gases in equilibrium with the aqueous solution. A mass-action equation is added to the system of simultaneous equations for each saturated gas present-except for H_2O vapor and air, which are handled separately through the flow module in TOUGHREACT V2.2 [153219] and V2.3 [153101]. The gas mass-action equation takes the form:

$$\log(K_i) = \log(Q_i) - \log(P_i) \qquad \text{(Eq. 3)}$$

where P_i is the partial pressure of gaseous species i. P_i is first calculated from the advective-diffusive gas transport equation in TOUGHREACT V2.2 [153219] and V2.3 [153101]. Then P_i is replaced with the ideal gas law,

$$P_i = \frac{n_i RT}{V_g} \qquad \text{(Eq. 4)}$$

where n_i denotes the number of moles of gas species i, R is the gas constant, T is absolute temperature, and V_g is the gas total volume. By expressing V_g in terms of the gas saturation S_g, the porosity of the medium ϕ, and the volume of each gridblock in the flow model V_{block}, Equation 4 is rewritten as:

$$P_i = \frac{n_i RT}{V_{block} f S_g} \qquad \text{(Eq. 5)}$$

The gas saturation is computed in the flow module of TOUGHREACT V2.2 [153219] and V2.3 [153101] (reflecting H_2O and air partial pressures computed in this module). The amount of trace gas species (n_i/V_{block}) is then obtained by substitution of Equation 5 into 3 and solving together with the concentrations of all primary species.

The partial pressures of trace gas species are not fed back to the multiphase flow module of TOUGHREACT V2.2 [153219] and V2.3 [153101] for solving the water and gas flow equations. Therefore, this method should only be applied to gases (excluding H_2O and air) with partial pressures significantly lower than the total gas pressure. No absolute cutoff exists at which this approximation breaks down, and therefore it is validated by comparison to DST measured CO_2 concentrations. For cases where the partial pressures of a trace gas become closer to the total pressure, chemical equilibrium with the aqueous phase is computed correctly, but the gas pressure will be underestimated in the mass-balance equation solved for gas flow. Because CO_2 concentrations encountered in the DST and model simulations are generally less than a few percent, and rarely over 10%, this model for the gas species is a reasonable approximation for this particular system (see Section 5).

6.1.4 Kinetic Rate Laws

Rates of mineral dissolution and precipitation close to equilibrium can be described via a relationship of the rate to the saturation index (*Q/K*), as follows (Steefel and Lasaga 1994 [101480], p. 540):

$$Rate(mol/s) = \operatorname{sgn}\left[\log\left({Q}/{K}\right)\right] k A_m \prod_i a_i^p \left|\left[\left({Q}/{K}\right)^m - 1\right]\right|^n \qquad \text{(Eq. 6)}$$

where a_i is the activity of each inhibiting or catalyzing species, and p is an empirically determined exponent. The rate constant (k) is given as (Steefel and Lasaga 1994 [101480], p. 541):

$$k = k_0 \exp\left[\frac{-E_a}{R}\left(\frac{1}{T} - \frac{1}{298.15}\right)\right] \qquad \text{(Eq. 7)}$$

Following Steefel and Lasaga (1994 [101480], p. 568) by neglecting the effect of pH or other aqueous species activities on reaction rates, we set p=0 for each species so that the product $\prod_i a_i^p = 1$ has been eliminated from Equation 6. The ratio of the species activity product (Q) and the equilibrium constant (*K*) describes the extent to which a mineral is in disequilibrium with a given solution composition. For *Q/K* equal to one, the mineral is at equilibrium and thus the net rate of reaction becomes zero. For *Q/K* greater than one, the mineral is oversaturated and thus the rate becomes positive. The expression "*sgn [log(Q/K)]*" ensures that the correct sign is enforced when the exponents *m* and *n* are not equal to one. The variable A_m is the reactive surface area expressed in units of $\mathrm{m}^2_{\mathrm{mineral}} / \mathrm{kg}_{\mathrm{water}}$. The temperature dependence of reaction rates is given by the activation energy (E_a) in units of kJ/mol. *T* is the temperature in Kelvin units. In the case of ideal solutions, the saturation index of the solid solution is calculated as the sum of the saturation indexes of the individual endmembers, and the reaction rate of the solid solution is calculated as described in Bodvarsson 2001 [153816], YMP-LBNL-YWT -NS-1.2, pp. 37–40.

Carroll et al. (1998 [124275], p. 1379) noted that the calculated rates of amorphous silica precipitation, based on Rimstidt and Barnes (1980 [101708], p. 1683) are about three orders of magnitude lower than those observed in geothermal systems. Carroll et al. (1998 [124275], p. 1379) presented experimental data on amorphous silica precipitation for more complex geothermal fluids at higher degrees of supersaturation, and also for a near-saturation simple fluid chemistry. Under far from equilibrium conditions, the rate law for amorphous silica precipitation has been expressed as (Carroll et al. 1998 [124275], p. 1382):

$$Rate(mol/s) = k_0 A_m \left(Q/K \right)^m \qquad \text{(Eq. 8)}$$

This rate does not tend to zero as Q/K goes to one, and therefore, a modification was made to this law so that it tends to zero as Q/K approaches one (described in Bodvarsson 2001 [153816], YMP-LBNL-YWT-ELS-1, p. 45), as follows:

$$Rate(mol/s) = k_0 A_m \left[\left(Q/K \right)^m - \frac{1}{\left(Q/K \right)^{2m}} \right] \qquad \text{(Eq. 9)}$$

The dissolution rate of silica-rich glass has been found to follow a dependence of H_2O diffusion through a reaction product layer (Mazer et al. 1992 [124354]). Given that the volcanic glass in the rocks at Yucca Mountain is at least 10 million years old and has undergone varying degrees of alteration, there should be a significant development of a reaction product layer. A constant product layer thickness of 10 microns on the glass surface was assumed (Assumption A7 in Section 5) for recalculation of the rate constant at 25°C. Details of the calculation are given in Bodvarsson 2001 [153816], YMP-LBNL-YWT-ELS-1 (p. 43).

The rate constant for dissolution and precipitation of fluorite was recalculated from the linear growth rate of grains (Knowles-Van Cappellan et al. 1997 [124306], p. 1873) by taking the grain to have a cubic morphology. Details of the calculation are given in Bodvarsson 2001 [153816], YMP-LBNL-YWT-ELS-1 (p. 44).

Kinetic data for minerals that were used in the simulation of drift-scale THC processes are given in Table 4, with comments regarding their sources and derivations.

Over a finite time step (Δt), the change in the concentration of each primary species j on account of mineral precipitation or dissolution under kinetic constraints is computed from the sum of the rates, r_i, of all j-containing minerals i as follows:

$$\Delta C_j = -\sum r_i \nu_{ij} \Delta t \qquad \text{(Eq. 10)}$$

where ν_{ij} is the stoichiometric coefficient of component j in mineral i. These concentration changes are incorporated into the mass-balance equation of each primary species involved in mineral reactions, using Equations 6 through 8, and solved simultaneously with the concentrations of all primary species.

6.1.5 Fracture and Matrix Mineral Reactive Surface Areas

6.1.5.1 Fracture Mineral Reactive Surface Areas

In the dual permeability method, the porosity of the fracture medium can be taken as 1.0; however, for modeling of mineral dissolution and precipitation, there would then be no rock to dissolve. Because the dissolution rates of many minerals are quite small at temperatures below 100°C, only a small volume of rock adjoining the open space of the fracture needs to be considered as the starting rock fraction. In the DST THC Rev00 and Tptpmn THC models, the porosity of the fracture medium was set to 0.99, thus making available 1% of the total fracture volume for reaction. In the Tptpll THC Model, the fracture medium porosity was set to 0.5 (Section 5, Assumption A14).

Reactive surface areas of minerals on fracture walls were calculated from the fracture-matrix interface area/volume ratio, the fracture porosity, and the derived mineral volume fractions. The fracture-matrix interface areas and fracture porosities for each unit were taken from the calibrated properties set (DTN: LB990861233129.001 [110226]). These areas were based on the fracture densities, fracture porosities, and mean fracture diameter. The wall of the fracture is treated as a surface covered by mineral grains having the form of uniform hemispheres. The grain diameter and spatial density are not included in this calculation, so that the area is actually only marginally greater than the fracture geometric surface area. An alternative method to approximating the surface area in excess of the geometric area would be to include a roughness factor. The geometric surface area of the fracture wall can be approximated by:

$$A_r = \frac{\pi A_{f\text{-}m}}{2\phi_{f-m}} \qquad \text{(Eq. 11)}$$

where A_r is the reactive surface area ($\mathrm{m}^2 / \mathrm{m}^3_{\text{fracture medium}}$), $A_{f\text{-}m}$ is the fracture-matrix interface area/volume ratio ($\mathrm{m}^2_{\text{fracture}} / \mathrm{m}^3_{\text{fracture+matrix}}$ volume), and $\phi_{f\text{-}m}$ is the fracture porosity of the rock. $A_{f\text{-}m}$ is the surface area used as input to the model simulations (REV00 DST and Tptpmn THC

Backfill Model runs) as an approximation of the reactive surface area. This model for the fracture surface area considers that the areal coverage is approximately equivalent to the mineral volume fraction. A further modification, which was implemented in TOUGHREACT V2.3 [153101], relates the 3-D cross-sectional area to the 2-D surface area in the fracture, which yields a factor of 3/2, i.e. an increase of 50 % in the reactive surface area. This relation was used for all DST THC Model Rev01 sensitivity studies, Tptpmn, and Tptpll THC simulations, discussed in Sections 6.4–6.6.

The reactive surface area of each mineral (in units of $\mathrm{m}^2_{\mathrm{min\,eral}} / \mathrm{kg}_{\mathrm{water}}$) that is used in Equations 6 and 9 is then given by:

$$A_m\,(m^2/\,kg_{water}\,) = \frac{A_r f_m}{r_w f_f} \qquad \text{(Eq. 12)}$$

where f_m is the volume fraction of the mineral in the mineral assemblage, r_w is the density of water (taken as a constant 1000 kg/m^3) and f_f is the porosity of the fracture medium, as opposed to the fracture porosity of the rock. This is the surface area/water mass ratio for a mineral in a liquid-saturated system. Calculated volume fractions of minerals are tabulated in Attachments I and II.

To provide the correct rock/water ratio in an unsaturated system, the form of this surface area can be written as:

$$A_m\,(m^2/\,kg_{water}\,) = \frac{A_r f_m}{r_w f_f S_w} \qquad \text{(Eq. 13)}$$

where S_w is the water saturation. However, as S_w goes to zero, the reactive surface area would tend to infinity. Clearly, at a very low liquid saturation, the surface area of the rock contacted by water is likely much smaller than the total area.

Two methods have been implemented to address this phenomenon. The first method considers that the surface area contacted by water diminishes proportionately to the saturation. This yields the saturated surface area given by Equation 11. The second method employs the active-fracture-model concept (Liu et al. 1998 [105729], pp. 2636–2638) modified to consider water-rock reactions taking place below the residual saturation. The form of the active fracture parameter for reaction is then given by the following set of equations:

$$S_{ar} = (S_w - S_m)/(1 - S_m) \qquad \text{(Eq. 14)}$$

$$a_{fmr} = S_{ar}^{\,(1+g)} \qquad \text{(Eq. 15)}$$

where S_m is the minimum liquid saturation for which water-rock reactions are considered and S_{ar} is the effective saturation for reaction. The active fracture parameter, g, is obtained from the calibrated hydrological property set (DTN: LB990861233129.001 [110226]). The factor that reduces the surface area contacted by the water phase is given by a_{fmr}. In all simulations S_m is set to the very small saturation of 1×10^{-4}, to ensure that reactions take place until virtually no water is left (e.g., during dryout via ventilation or heating). Finally, the reactive surface area, using this modified form of the active fracture model, is given by:

$$A_m(m^2/kg_{water}) = \frac{A_r a_{fmr}}{r_w f_f S_w} \qquad \text{(Eq. 16)}$$

The surface area calculated in this way is applicable only to reactions taking place in the fracture medium, and is used directly in Equations 6 and 9. Note that this area is not the input surface areas that are listed in Attachments III and IV.

6.1.5.2 Matrix Mineral Reactive Surface Areas

Mineral surface areas in the rock matrix were calculated using the geometric area of a cubic array of truncated spheres that make up the framework of the rock (Bodvarsson 2001 [153816], YMP-LBNL-YWT-ELS-1, pp. 37–39, Sonnenthal and Ortoleva 1994 [117914], pp. 405–406). Clay minerals are considered as coatings of plate-like grains. The mineral surface areas of framework grains (truncated spheres) in contact with the open pore space are calculated using an initial grain diameter, followed by successive truncation of the grains in the vertical direction until the porosity of this system is close to the measured porosity of the rock. In the welded tuff, crystals are often tightly intergrown with little or no pore space within the aggregate. Thus, a check is made so that the resultant mean-pore throat size and spacing yields a permeability (calculated from a modified Hagen-Poiseuille relation—Ehrlich et al. 1991 [117799], p. 1582, Eq. 11) that is relatively close to the measured saturated permeability.

The grains forming the framework of this rock are considered to be the primary high-temperature phases of the tuff (i.e., quartz, cristobalite, tridymite, and feldspars). The abundance of secondary phases (i.e., those that formed as alteration products or low-temperature coatings on the primary assemblage), such as clay minerals, are used to reduce the free surface area of the framework grains. The surface areas of the secondary phases are calculated assuming a tabular morphology.

The full details of the geometric calculations are given in Bodvarsson 2001 [153816], YMP-LBNL-DSM-ELS-1, pp. 37–39.

6.1.6 Effects of Mineral Precipitation/Dissolution on Hydrologic Properties

6.1.6.1 Porosity Changes

Changes in porosity and permeability from mineral dissolution and precipitation have the potential for modification of the percolation fluxes and seepage fluxes at the drift wall. In this analysis, porosity changes in matrix and fractures are directly tied to the volume changes as a result of mineral precipitation and dissolution. Since the molar volumes of minerals created by hydrolysis reactions (i.e., anhydrous phases, such as feldspars, reacting with aqueous fluids to form hydrous minerals such as zeolites or clays) are often larger than that of the primary reactant minerals, dissolution-precipitation reactions can often lead to porosity reductions. These changes are taken into account in this analysis. The porosity of the medium (fracture or matrix) is given by

$$f = 1 - \sum_{m=1}^{nm} fr_m - fr_u \qquad \text{(Eq. 17)}$$

where nm is the number of minerals, fr_m is the volume fraction of mineral m in the rock ($V_{mineral}/V_{medium}$, including porosity), and fr_u is the volume fraction of nonreactive rock. As the fr_m of each mineral changes, the porosity is recalculated at each time step. The porosity is not allowed to go below zero.

6.1.6.2 Fracture Permeability Changes

Fracture permeability changes can be approximated using the porosity change and an assumption of plane parallel fractures of uniform aperture (cubic law—Steefel and Lasaga 1994 [101480], p. 556). The modified permeability, k, is then given by

$$k = k_i \left(\frac{f}{f_i} \right)^3 \qquad \text{(Eq. 18)}$$

where k_i and f_i are the initial permeability and porosity, respectively. This law yields a permeability of zero only for a zero fracture porosity.

In many experimental and natural systems, permeability reductions to values near zero occur at porosities significantly greater than zero. This generally is the result of mineral precipitation or fracture closure of the narrower interconnecting apertures. The hydraulic aperture, as calculated from the fracture spacing and permeability (as determined through air-permeability measurements) assuming a cubic law relation, is a closer measure of the smaller apertures in the flow system. The initial hydraulic aperture $b_{0,h}$ (m) is calculated using the following cubic law relation:

$$b_{0,h} = [12 k_0 s]^{1/3} \qquad \text{(Eq. 19)}$$

where k_0 is the initial fracture permeability (m^2) and s is the fracture spacing (m). The permeability (k') resulting from a change in the hydraulic aperture, is given by

$$k' = \frac{(b_{0,h} + \Delta b)^3}{12s} \qquad \text{(Eq. 20)}$$

where Δb is the aperture change resulting from mineral precipitation/dissolution. The aperture change resulting from a calculated volume change can be approximated by assuming precipitation of a uniform layer over the entire geometric surface area of the fracture, assuming also that this area as well as the fracture spacing remains constant. In geologic systems, the actual distribution of mineral alteration is much more heterogeneous and depends on many factors that are active at scales much smaller than the resolution of the model. The combined effect of the initial heterogeneities and localized precipitation processes can only be treated through model sensitivity studies and experiments. The initial aperture available for precipitation (b_g, the geometric, rather than the hydraulic, aperture) can be calculated from the ratio of the initial fracture porosity ($f_{f,0}$) to the fracture surface area (A_f), as follows:

$$b_g = {}^{f_{f,0}}\!\big/_{A_f} \qquad \text{(Eq. 21)}$$

For a dual permeability model, changes in the fracture porosity are calculated based on the porosity of the fracture medium, so that Δb can be approximated by

$$Db = \left(f'_{fm} - f_{fm,0}\right)\, b_g \qquad \text{(Eq. 22)}$$

Equations 19, 20, and 22 were implemented in TOUGHREACT V2.3 [153101] with input parameters of b_g and s. This relation was used for sensitivity studies on the Tptpmn THC Model simulations (heterogeneous and homogeneous permeability fields for the no-backfill case), DST THC Rev01 Model simulations, and Tptpll THC Model simulations.

6.1.6.3 Matrix Permeability Changes

Matrix permeability changes are calculated from changes in porosity using ratios of permeabilities calculated from the Carmen-Kozeny relation (Bear 1988 [101379], p. 166, Eq. 5.10.18, symbolically replacing n by f), and ignoring changes in grain size, tortuosity and specific surface area as follows:

$$k = k_i \frac{(1-f_i)^2}{(1-f)^2}\left(\frac{f}{f_i}\right)^3 \qquad \text{(Eq. 23)}$$

6.1.6.4 Effects of Permeability and Porosity Changes on Capillary Pressures

Changing permeability and porosity also implies changes in the unsaturated flow properties of the rock. This effect is treated by modifying the calculated capillary pressure (Pc) using the Leverett scaling relation (Slider 1976 [128146], p. 280) to obtain a scaled Pc' as follows:

$$Pc' = Pc\sqrt{\frac{k_i f}{k f_i}} \qquad \text{(Eq. 24)}$$

6.1.7 Geochemical Systems

Two primary sets of chemical components and mineral assemblages were used for the simulations for the DST THC, the Tptpmn and Tptpll THC models. The systems are denoted as base case and extended case and differ somewhat from one model to another (Tables 7 and 8). The extended case includes the major solid phases (minerals and glass) encountered in geologic units at Yucca Mountain, together with a range of possible reaction product minerals, CO_2 gas, and the aqueous species necessary to include these solid phases and the pore-water composition within the THC model. The base case is a subset of the extended case excluding aluminum silicate minerals, which form or dissolve much less easily than minerals such as calcite or gypsum, and for which thermodynamic and kinetic data are not as well established as for the other minerals. THC simulations with thermodynamic data described in Section 4.1.4.1 (and used in Sections 6.2.7.2 and 6.3.5.2), more closely capture pH and gas-phase CO_2 concentration trends (compared to measured values from the DST and ambient porewater compositions) with the base-case system than with the extended case shown in Table 7, because these simulations may overestimate the reaction rates of aluminum silicate minerals. However, after adjusting some of the thermodynamic data, as discussed in Section 4.1.4.2 and modifying slightly the extended-case mineral assemblage (Table 8), both geochemical systems yield results that are more consistent with each other and measured data (Sections 6.2.8, 6.4.5.2 and 6.6.5.2).

Table 7. Base-Case (*italics*) and Extended-Case Mineral Assemblage, Aqueous and Gaseous Species Used in Rev00 DST THC Simulations (Section 6.2) and in the Tptpmn THC Backfill Model (Section 6.6).

Species	**Minerals**
Aqueous:	
H_2O	*Calcite*
H^+	*Tridymite*
Na^+	*a - Cristobalite*
K^+	*Quartz*
Ca^{+2}	*Amorphous Silica*
Mg^{+2}	Hematite
SiO_2	Fluorite
AlO_2^-	*Gypsum*
$HFeO_2^{-2}$	Goethite
HCO_3^-	Albite
Cl^-	Microcline
SO_4^{-2}	Anorthite
F^-	Ca-Smectite
	Mg-Smectite
Gas:	Na-Smectite
CO_2	K-Smectite
H_2O	Illite
Air	Kaolinite
	Sepiolite
	Stellerite
	Heulandite
	Mordenite
	Clinoptilolite
	Glass (1)

Note: (1) For the base case, glass has the same properties as amorphous silica but is not allowed to precipitate

Table 8. Base-Case (*italics*) and Extended-Case Mineral Assemblage, Aqueous and Gaseous Species Used in the Rev01 DST THC Model Simulations (Section 6.2.8) and in the Tptpmn THC (no-backfill) (Sections 6.4 and 6.5) and Tptpll (Section 6.6) THC Models.

Species	**Minerals**
Aqueous:	
H_2O	*Calcite*
H^+	*Tridymite*
Na^+	*α-Cristobalite*
K^+	*Quartz*
Ca^{+2}	*Amorphous Silica*
Mg^{+2}	Hematite
SiO_2	*Fluorite*
AlO_2^-	*Gypsum*
$HFeO_2^{-2}$	Goethite
HCO_3^-	Albite
Cl^-	K-spar
SO_4^{-2}	Anorthite
F^-	Ca-Smectite
	Mg-Smectite
Gas:	Na-Smectite
CO_2	*Opal_proxy* (2)
H_2O	Illite
Air	Kaolinite
	Glass (1)
	Stellerite
	Heulandite
	Mordenite
	Clinoptilolite

Note: (1) For the base case, glass has the same thermodynamic properties as amorphous silica but is not allowed to precipitate.
(2) Not included in the DST THC Rev01 and Tptpmn THC models (no-backfill).

6.2 THE DRIFT SCALE TEST THC MODEL

The DST is the second underground thermal test that is being carried out in the ESF at Yucca Mountain, Nevada. The purpose of the test is to evaluate the coupled thermal, hydrological, chemical and mechanical processes that take place in unsaturated fractured tuff over a range of temperatures from approximately 25°C to 200°C. The DST THC Model provides an important validation test for the extension of the THC conceptual model to the THC Seepage models. It should be noted that the geochemical-model input parameters have not been calibrated to the data collected from the DST. Modifications to a few rate-law parameters have been made, because of some of the simplifications made in the mineralogy (endmembers instead of solid solutions) and the general effects of inhibition of precipitation or dissolution (e.g., quartz and calcite). However, these input data were not tailored to match any field data, but were modified to correct for processes not considered in the model. More important than matching any particular data, is a better understanding of coupled processes, so that the models can be applied to long-term predictions of near-field THC processes.

Section 6.2.7 and its subsections discuss DST THC REV 00 simulations and document model validation by comparing simulation results to gas-phase CO_2 concentrations measured during the first 21 months of the DST. In Section 6.2.8, a similar comparison is made, between results of the DST THC REV 01 models and 32 months of data. The differences between the REV 00 and REV 01 models are summarized in Section 6.2.8.

Following this first analysis (Rev00), another series of simulations was performed (reported in Section 6.2.8). This set of simulations provided updated results and sensitivity studies for Rev01 of this AMR. Detailed description of these simulations and the results are given in Section 6.2.8.

6.2.1 Background Information

The DST heaters were activated on December 3, 1997, with a planned four-year period of heating, followed by four years of cooling. Our objectives were to make predictions of the coupled thermal, hydrological, and chemical (THC) processes, followed by model refinement and comparison to measured data. It was expected that some water (formed by condensation of steam in fractures) would be collected. From June 1998 to August 2000, samples of water and gas were collected from boreholes, allowing for comparison of analytical data on water and gas chemistry to DST THC model results.

6.2.2 Drift Scale Test 2-D Numerical Grid

Because THC simulations are computationally intensive, and the model area is fairly large, 2-D simulations (rather than 3-D) were conducted, so that the number of model gridblocks, and thus computation time, could be kept to workable dimensions without losing too much resolution.

The two-dimensional dual-permeability numerical grid for the DST consists of 4,485 gridblocks, including fracture and matrix (DTN: LB0101DSTTHGRD.001 [153687]). It represents a vertical cross section through the drift at a distance approximately 30 meters from the bulkhead (Figure 3). Between the grid elements within the drift interior and one representing the heater test alcove are elements designed to act as bulkhead and insulating material. Within the drift, heat is applied directly to the drift wall as an approximation to explicitly represent the electric heaters and calculate the heat transfer across the air mass inside the drift. The test includes a plane of linear wing heaters on each side of the drift that are given small grid elements in the model. Small grid elements are employed adjacent to the wing heaters and drift wall to capture the strong gradients in temperature and liquid saturation in these regions. For the simulations, some mesh elements in the drift interior were removed, and near the drift base they were replaced by nodes representing the concrete invert.

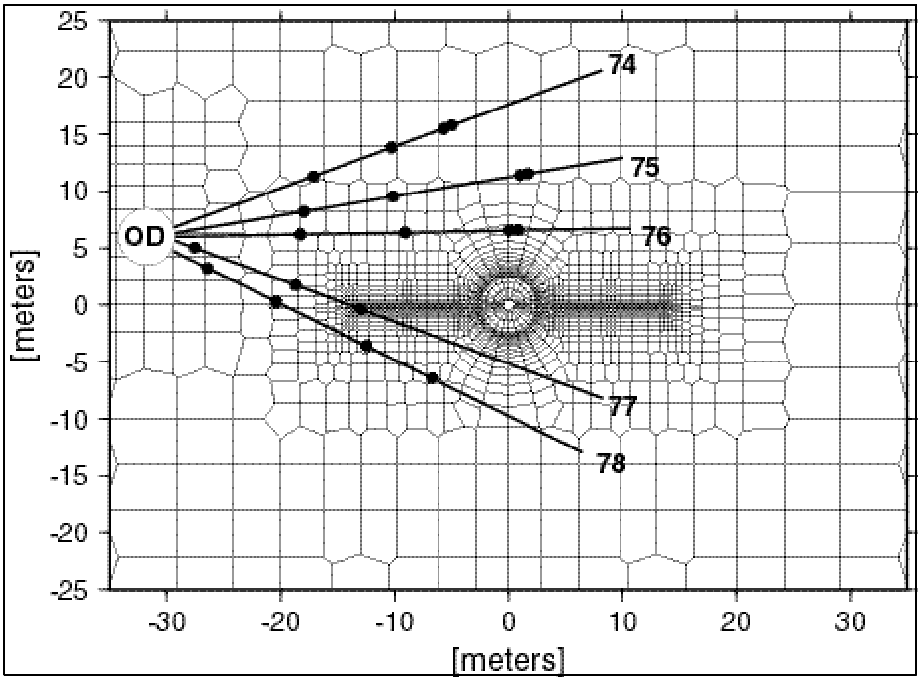

DTN: LB991200DSTTHC.002

NOTE: OD = Observation Drift. Locations of hydrology boreholes and sensor locations are shown for a vertical plane approximately 30 m inward from the bulkhead.

Figure 3. Close-Up of Numerical Mesh Used for DST THC Model Simulations.

6.2.3 Heater Power

Recent calibrated heater power measurements are used in the model (DTN: MO0007SEPDSTPC.001 [153707]). The wing heaters are split into inner and outer zones, with the outer zone producing a greater power output to approximate the presence of an adjacent parallel drift. The DST THC Model employs a 9-month period of preheat ventilation at ambient temperature corresponding approximately to the time that was required to set up the test. The heating schedule imposed on the model is then set in accordance with an interim plan for the test: 21 months of heating at full power (bringing the model simulation to early September 1999), followed by 10% power reduction for each of the next four months. Then, heating continues at 60% of full power until 4 years after initiation of heating, and finally 4 more years of cooling. The 10% power reduction after September 1999 has not been implemented in the simulations, and therefore only model data up to September 1999 will reflect closely the temperature history of the test. For the purpose of validating the THC conceptual model, only results prior to this time for which chemical data on water and gases were collected will be discussed in Section 6.2.7 of this AMR.

The second series of simulations, described in Section 6.2.8, was started with a 10% lower baseline power output to account for approximate differences between a 2-D model and heat losses in a 3-D experiment. Three 5% reductions in power during the year 2000 were implemented in the simulations based on estimated power drops (DTN: MO0012SEPDSTPC.002 [153708]). These simulations included nine months of ambient pre-heating followed by three years of heating.

6.2.4 Hydrological and Thermal Boundary and Initial Conditions

The top boundary is approximately 99 m above the drift center, with the bottom boundary at approximately 157 m below the center. The top and bottom boundaries were set to constant temperature, pressure, and liquid saturation, based on steady-state values obtained from simulations of a 1-D column extending from the land surface to the water table. These values were obtained using the calibrated drift-scale hydrological parameter set for the present climate (mean infiltration) at an infiltration rate of approximately 1.05 mm/year (DTN: LB991091233129.001 [125868]). The side boundaries of the domain are located outside of the test influence area (81.5 m away from the drift center on each side) and can be considered as no-flux boundaries. The air pressure and temperature in the observation drift are set to constant values and therefore do not reflect temporal fluctuations in barometric pressure or tunnel air temperatures. The Heater Drift wall is open to advection and conduction of heat and mass as well as vapor diffusion.

6.2.5 Geochemical Boundary and Initial Conditions

Geochemical data used in the simulations are given in Tables 3 and 4 in Section 4 (sources in Table 2) and Attachments I, III, and V. The top and bottom boundaries were set so that no mineral reactions take place, but they were open to aqueous and gaseous species transport. Their volumes were set to extremely large values so that they act essentially as constant concentration boundaries. All aqueous and gaseous species concentrations in the rock were set initially to uniform value (Section 4.1.3). The heater drift, alcove, and observation drift CO_2 concentrations were set to approximately that of the atmosphere. The alcove and observation drift CO_2 concentrations were kept essentially constant, but the heater drift was allowed to exchange CO_2 between the rock and the observation drift. The side boundaries were treated as no-flux to advection and diffusion. Simulations were run using the extended-case and base-case geochemical systems shown in Table 7.

6.2.6 Measured Geochemical Data Used for Comparison to Simulation Results

Two main sources of data are used in this AMR for comparison to simulation results. Aqueous species concentrations and pH were available for water samples collected from hydrology boreholes (DTNs listed in Table 2). Gas-phase CO_2 concentrations and stable isotopic ratios ($\delta^{13}C$, $\delta^{18}O$, δD, and ^{14}C) were measured from gases pumped from hydrology boreholes (DTNs listed in Table 2). For the gas-phase compositions, direct comparisons of model results will be made only to CO_2 concentrations; however, isotopic data also has provided important insight into THC processes.

6.2.7 Simulation Results and Model Validation by Comparison to Measured Data

Validation of the DST models is done in accordance with AP-3.10Q, section 5.3.c.5, corroboration with experimental data. Data from the DST used for comparison consist of analyses of water and gas samples from borehole intervals between packers (Figure 9). Intervals were selected for comparison based upon the availability of a long continuous sample record, and absence of confounding factors such as the sampling interval being too long to compare with a particular node or pair of nodes, or boreholes being near either end of the DST and affected by third-dimension transport (see below). As stated in Section 1, the DST THC Model is an idealization and therefore differences between the Model and the DST must be considered when comparing the data to the simulations. The DST model is a continuum model, with average properties or realizations of idealized permeability fields, and therefore is meant to represent overall changes in space and time, but cannot be expected to match data exactly at any one point in time. The model represents a two-dimensional slice taken approximately at mid-length of the DST, and therefore does not simulate transport in the third dimension (the mid-length boreholes are least affected by third-dimension transport). Other factors noted in 6.2.7.1 and 6.2.7.2 (including deviations from planned operation and imperfect correspondence between model nodes and sampling locations) also limit the comparability of simulations. With these limitation in mind, the criteria for model validation are either of the following:

1. Where the borehole interval from which samples are taken lies between two nodes, the measured values for the samples fall between the simulated values for the two nodes.

2. The simulated trend of CO2 or aqueous species concentrations over time in the sampling interval is clearly followed, and is clearly distinct from trends in other sampling intervals.

For both these criteria, discrepancies between simulations and data are accepted if they can be accounted for by known major deviations between actual and simulated heater operation, or extensive water loss by condensation from gas samples prior to measurement.

This section will review data and predictions to demonstrate that these criteria have been met for the DST models. There are no experimental data by which the THC seepage models can be validated; because they are essentially identical to the DST THC models, validation of the DST models effectively validates them as well. AP-3.10Q, section 5.3.c.3 also permits model validation on the basis of review of model calibration parameters for reasonableness and consistency in explanation of all relevant data. This condition has also been met, but is considered a less rigorous validation test than the criteria used here. Additional validation of the THC model is presented in Section 6.7, where results of a laboratory plug-flow experiment are compared to simulations.

6.2.7.1 Thermal and Hydrological Evolution

The main driving force for changes in the hydrological and chemical behavior of the system is, of course, the strong thermal load applied to the system. The resulting changes in temperature, liquid saturation, and gas-phase composition lead to changes in the chemistry of water, gas, and minerals. Key aspects of the thermohydrological behavior of the DST that drive the chemical evolution of the system are treated in this section. (A detailed analysis of the thermohydrology of the DST is presented in another AMR.)

The modeled distributions of temperature and liquid saturation are shown in Figures 4a–d, corresponding to twelve and twenty months during the heating phase of the DST. The zone of dryout increases over time, and a wider contour interval in temperature between the 90°C and 100°C isotherms, indicates the presence of an isothermal boiling/condensation zone, especially above the wing heaters. A large drainage zone is apparent in the fractures below the heaters, and in the matrix as well, after 20 months. The buildup of water above the heaters is fairly localized, but moves up into the region of the upper hydrology boreholes after 20 months of heating.

Temperatures predicted by the two-dimensional model tend to be somewhat higher than for a three-dimensional model or the real system because no heat loss occur in the third dimension. Therefore, this model is most applicable to areas near the center of the test—away from both the bulkhead and the opposite end of the Heater Drift.

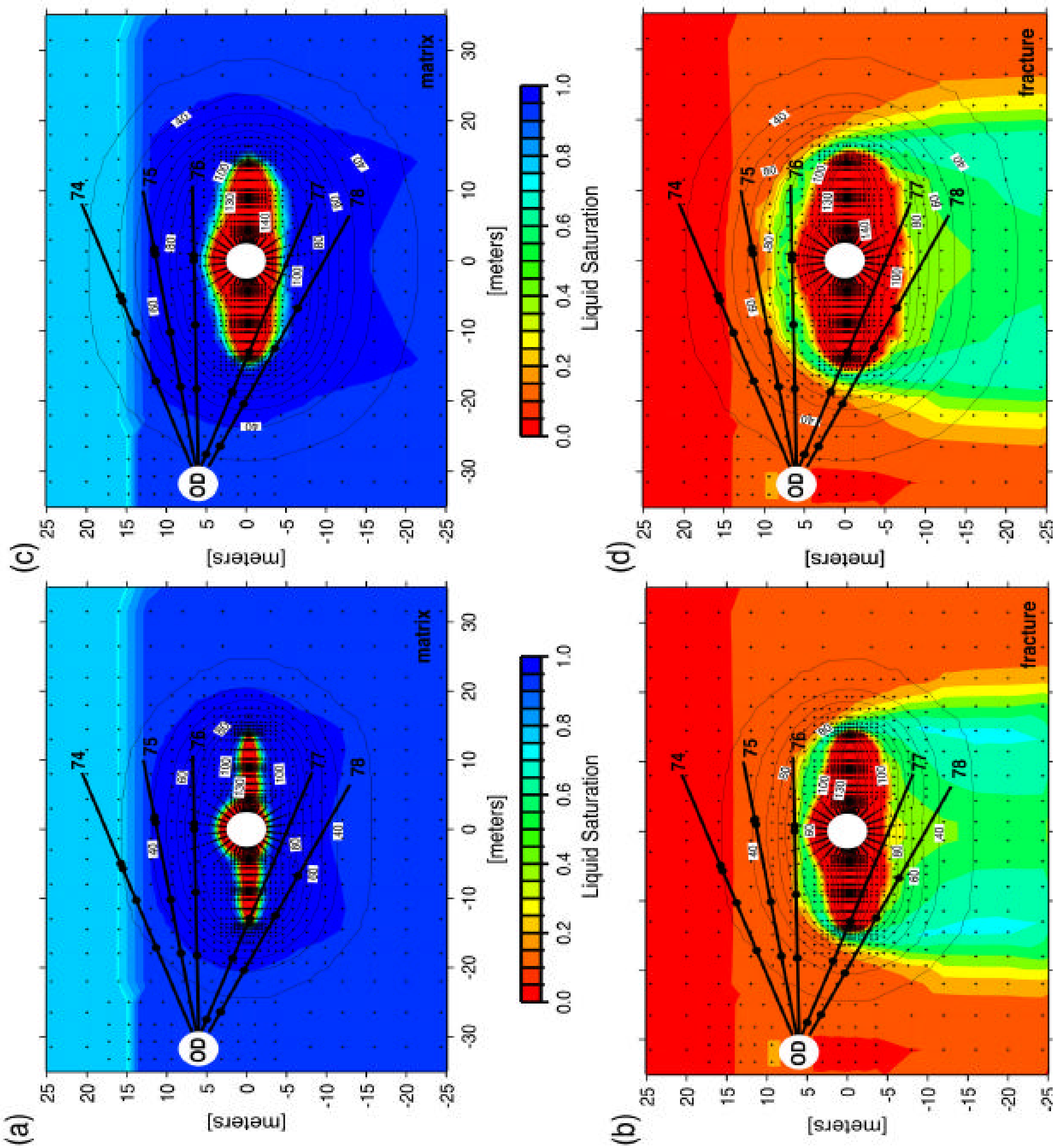

DTN: LB991200DSTTHC.002

Figure 4. Liquid Saturation (Colors) and Temperature (Contour Lines) around the DST (Base Case) at 12 Months (Matrix – 4a, Fracture – 4b) and at 20 Months (Matrix – 4c, Fracture – 4d).

6.2.7.2 Gas Phase CO_2 Evolution

The concentration of CO_2 in the gas phase can change markedly, owing to changes in temperature, aqueous-phase chemical changes and mineral-water reactions, and advective and diffusive transport. Because CO_2 partial pressure has a strong effect on water pH, it is important to validate the CO_2 behavior in our simulations. Numerous measurements of CO_2 concentrations in gases from the DST have been made as a function of space and time, so that a more detailed comparison of the model results to these data can be made than to measured water chemistry. Model results are presented for the two geochemical systems described in Table 7 (extended case and base case).

In this section, we present CO_2 concentrations measured in gas samples taken from boreholes during the DST and compare them to simulation results using the DST THC Model Rev00. Sampling locations are not identical to the mesh node coordinates and are from borehole intervals that are several meters long. Thus, they may encompass a wide range of temperatures as a result of their orientation relative to the heaters. The actual heater operation was also not exactly as planned or as modeled. In addition, the model predicts both fracture and matrix CO_2 concentrations, whereas the measured data may consist of some mixture of gas derived from fractures and that from the matrix, especially if the matrix pore water was actively undergoing boiling. Another complication arises from the gas samples having had much of the water vapor removed (before analysis), whereas the model results give a “humid” gas (air + CO_2 + H_2O) compositions.

Modeled distributions of CO_2 concentrations (log volume fractions) and temperature in fractures and matrix are shown after six and twelve months of heating (which are also times for which CO_2 measurements are available) in Figure 5 for the base-case chemical system. At both times, and in both fractures and matrix, a halo of increased CO_2 concentrations appears, centered approximately at the 60°C isotherm. Over the six-month period, the halo considerably increases in extent and magnitude. Maximum CO_2 concentrations are located above and below the wing heaters and below the Heater Drift. Between approximately the 90°C and 100°C isotherms lies a region where fracture CO_2 concentrations have decreased to approximately 1,000 ppmv, but concentrations in the matrix are still elevated. This area encompasses an isothermal boiling region, as evidenced from the wider spacing of the 90–100°C isotherms compared to adjacent lower and higher temperature contours. More rapid boiling in the matrix leads to higher partial pressures of CO_2 relative to the dry or nearly dry fractures. Within the dryout zone close to the drift and wing heaters, CO_2 concentrations decrease markedly in both fractures and matrix.

Figure 6 shows modeled CO_2 concentrations at 15 and 20 months from the same simulation. The patterns remain similar and continue to grow outward from the heat source, with the area of the maximum concentrations decreasing slightly at 20 months relative to that at 12 months. This decrease is a result of a widening of the zone of high concentrations as it moves away from the heat source, with the peak concentrations diminishing slightly as the isotherms widen. The highest concentration regions are situated above and below the wing heaters and, over time, pass progressively through the radial hydrology boreholes. Once the region around the borehole has dried out, a sharp decrease to low CO_2 concentrations occurs in the gas phase.

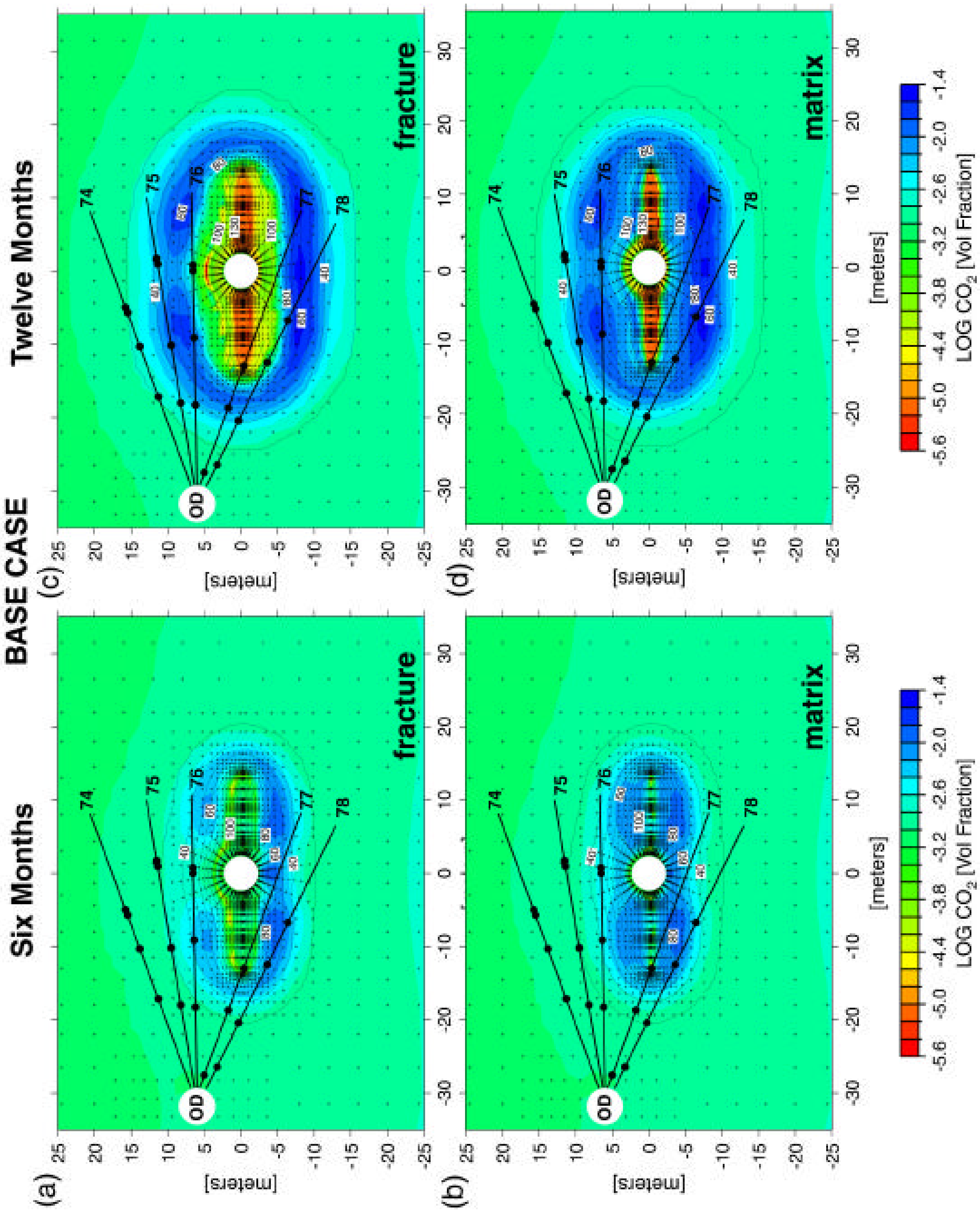

DTN: LB991200DSTTHC.002

Figure 5. CO$_2$ Concentration (Log Volume Fraction) in Gas Phase (Base Case) around the DST at 6 Months (Fracture - 5a, Matrix - 5b) and at 12 Months (Fracture - 5c, Matrix - 5d). Temperature contours are overlain.

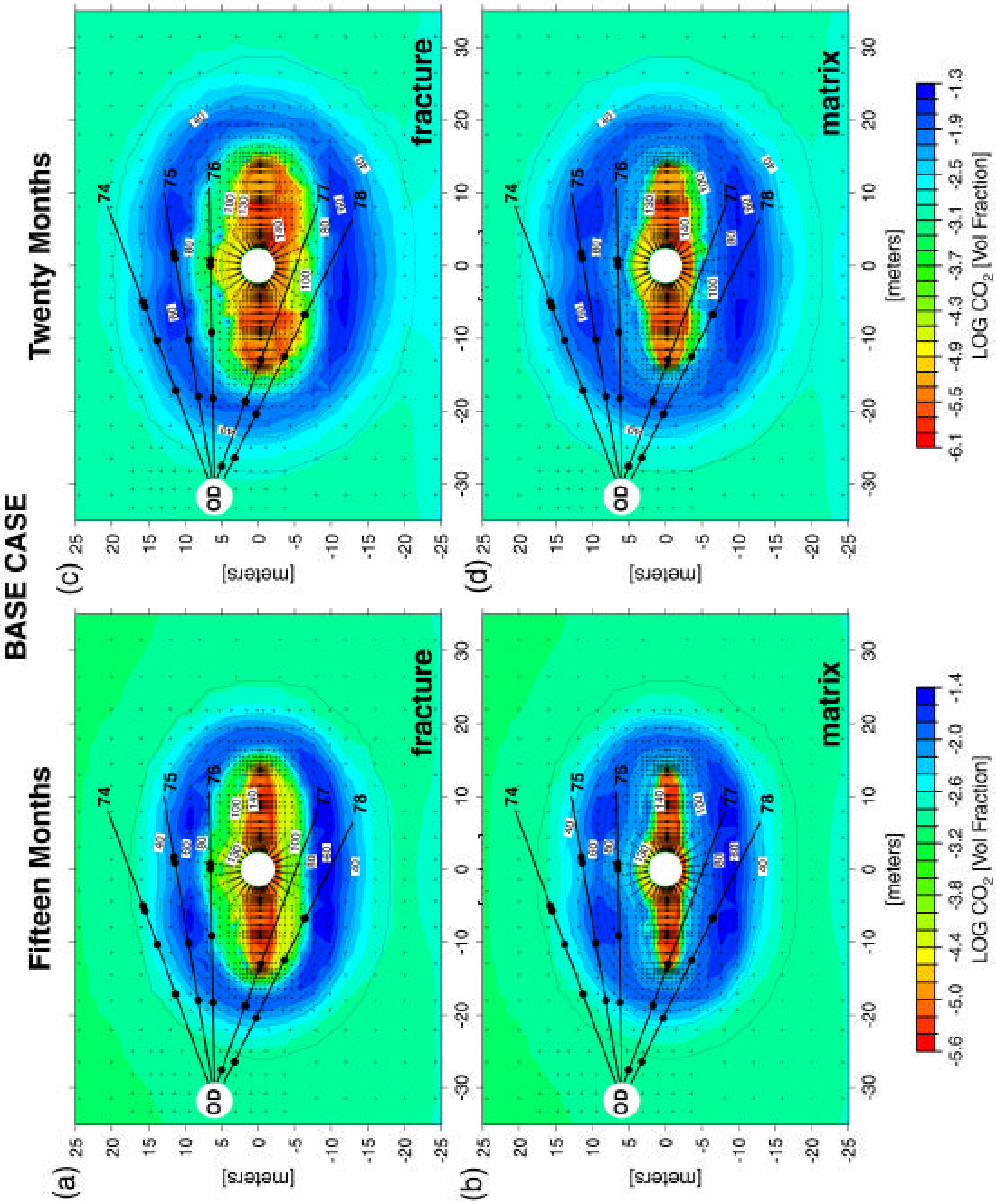

DTN: LB991200DSTTHC.002

Figure 6. CO$_2$ Concentration (Log Volume Fraction) in Gas Phase (Base Case) around the DST at 15 Months (Fracture - 6a, Matrix - 6b) and at 20 Months (Fracture - 6c, Matrix - 6d). Temperature contours are overlain.

For comparison, CO_2 concentrations for a simulation using the extended geochemical system (extended case) are shown in Figure 7. The pattern of concentrations is similar to the previous results; however, the maximum concentrations are significantly lower. Changes in gas chemistry are also taking place in the ambient temperature region.

The reason for the difference in the calculated CO_2 concentrations in the extended geochemical system (compared to the base case) is a result of dissolution and precipitation of various Ca-bearing minerals, such as stellerite, heulandite, calcite, anorthite, and Ca-smectite. Feldspar and calcite dissolve to form zeolites. This increases the pH, which in turn decreases the CO_2 partial pressures through aqueous-species reactions involving carbonate species (CO_2 is more soluble at elevated pH). Large differences in the relative rates of mineral-water reactions drive these reactions, even though the absolute rates are exceedingly small. The other controlling factor is the flux of aqueous species through percolation and of CO_2 through gas-phase diffusion, relative to the rates of mineral reactions. Because the model starting conditions use measured water and gas compositions that reflect a set of mostly unknown conditions (infiltration, mixing, climate changes), it is very difficult to reproduce a steady-state condition that matches the original data (this was achieved for the simulations presented in Section 6.2.8, which show smaller differences between the base-case and extended-case geochemical systems). The percolation flux has little effect over a few years, so that for comparison of the model results, we are left with the relative rates of reaction as the reason for the difference between base-case and extended-case CO_2 concentrations.

Shifts in the ambient system CO_2 concentrations over a relatively short time (away from the areas of thermal effects) indicate that either the relative mineral-water reaction rates are somehow dissimilar to the real system, or that calculated starting water bicarbonate concentration (via charge balance) was off, or the measured pH was altered through the sample collection procedure. Because the starting water was supersaturated in calcite, the latter scenario is a distinct possibility. In addition, the uncertainties in thermodynamic data for the aluminosilicates (e.g., zeolites and clays), the unknown reaction rates for many of the minerals, and the assumption of endmember mineral thermodynamic models (instead of solid-solution models) must play a role in the evaluation of the results. Therefore, comparison to measured data must play an important role in the evaluation of the results.

The distributions of measured CO_2 concentrations (DTNs listed in Table 2) after one year and after 15 months of heating are shown in Figure 8. In general the locations of high concentrations are similar to the modeled concentrations with very high values above and below the wing heaters, with slightly elevated values in borehole 74 well above the wing heaters. Comparison of the 15 month to the one-year data shows that in nearly all of the boreholes, the CO_2 concentrations are higher. The range of measured values compares closely with the span of modeled concentrations.

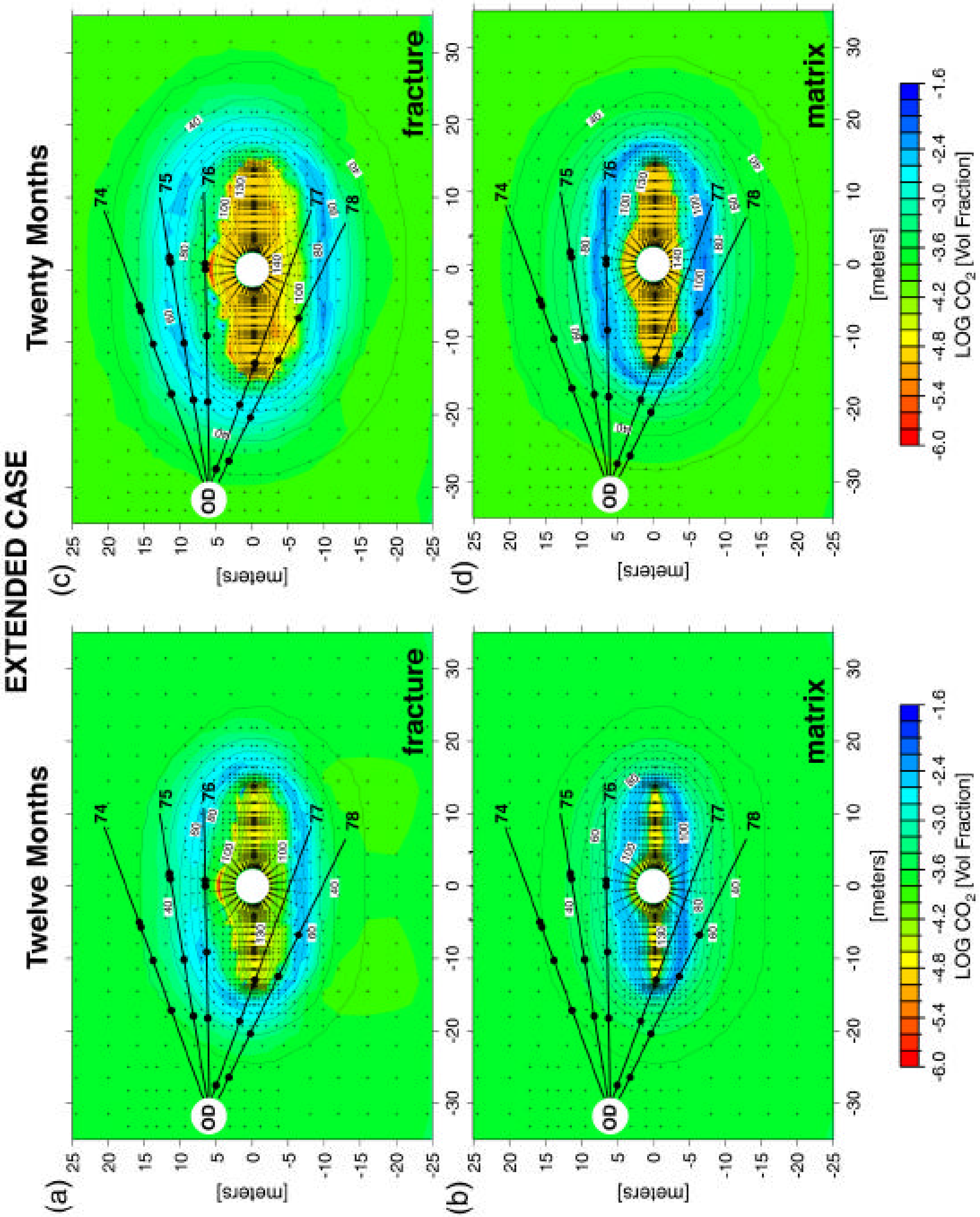

DTN: LB991200DSTTHC.002

Figure 7. CO_2 Concentration (Log Volume Fraction) in Gas Phase (Extended Case) around the DST at 12 Months (Fracture – 7a, Matrix – 7b) and at 20 Months (Fracture – 7c, Matrix – 7d). Temperature contours are overlain.

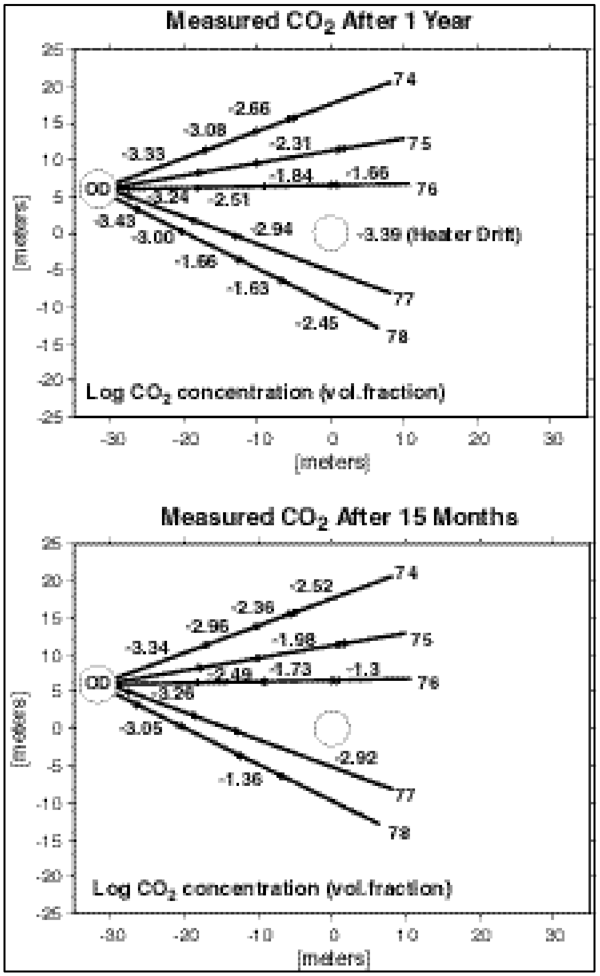

DTN: LB990630123142.003 [111476]

NOTE: Concentrations refer to intervals between pairs of points.

Figure 8. Measured Concentrations of CO_2 (Log Volume Fraction) in Gas Phase around the DST at 1 Year and at 15 Months

To evaluate how the model predicts the time evolution of CO_2 concentration, which is dependent on numerous thermal, hydrological, transport, and geochemical processes, measured CO_2 concentrations from intervals that were repeatedly sampled from February 1998 to August 1999 (DTNs listed in Table 2) were compared to model results at the same times. The locations of these nodes relative to the borehole intervals from which the gas samples were taken are illustrated in Figure 9. Because the measured concentrations come from borehole intervals that are several meters long and not from a specific location, model data are chosen from the gridblock closest to the center of the interval. If a gridblock is not centered on the borehole, a node closest to the center is chosen on the outer (cooler) side of the borehole. Nodes on the cooler side are more comparable to the measured data because the 2-D model, having no heat loss in the rock perpendicular to the drift, gives temperatures that are somewhat higher than the measured temperatures at a given time. Therefore, it is more appropriate to pick a node on the cooler rather than the hotter side. Some additional nodes around the intervals are included in some of the plots, so that the gradations in the CO_2 concentrations around or over the interval can be analyzed.

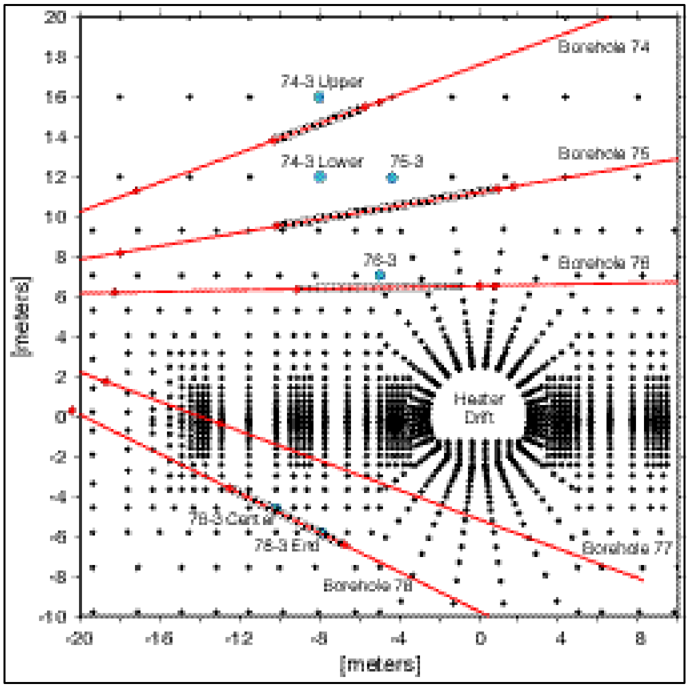

DTN: LB991200DSTTHC.002

Figure 9. Close-Up of DST Grid, Showing Nodes Used to Extract Model Data for Comparison to Concentrations Measured in Gas Samples. Borehole intervals from which gas samples were taken are shown in the hachured regions.

Figures 10a–d show the time evolution of CO_2 concentrations in borehole intervals 74-3, 75-3, 76-3, and 78-3. Measured CO_2 concentrations in interval 74-3 were observed to be only slightly elevated (1434 ppmv) over the ambient rock gas CO_2 concentration when the first sample was collected six months after the start of the test. Temperatures at the borehole sensor were still at the ambient value of 23.7°C. Concentrations rose gradually until about one year after the test, at which time they rose somewhat more rapidly to approximately 7000 ppmv at 18 months. The next sample, collected at just over 20 months into the test, had a composition close to the previous sample. The closest grid node to the center of borehole interval 74-3 lies just about 1.5 meters above the borehole. The calculated concentrations follow a similar early history as the measured concentrations until about 12 months, at which time the measured concentrations rise faster and to greater concentrations than the observed data. However, where the measured concentrations level out at 20 months, the modeled values are still rising and are close to the final value. For comparison, concentrations from a grid node about 2 meters below the interval also rise slowly over the first 10 to 12 months of the test and then increase more dramatically to much higher concentrations. These two nodes bracket the measured concentrations quite well. It is clear that there are very strong gradients in CO_2 concentrations over distances of only a few meters, so that it would be expected that the collected gases would reflect some averaging over a region. Differences in fracture and matrix CO_2 concentrations increase nearer the heat source, which could affect the sampling as the matrix liquid saturations decrease and more of the collected gas comes from the matrix compared to the open fractures.

In Figure 10b, the measured concentrations in borehole interval 75-3, which is closer to the Heater Drift, are also at slightly elevated values after 6 months. They rise smoothly but faster than in 74-3 until about 18 months, at which time the concentrations again reach a plateau. The modeled concentrations match very closely the measured values until 20 months, when measured concentrations stop rising.

The lack of a continuous rise in CO_2 concentrations measured in borehole intervals 74-3 and 75-3 at 20 months does not seem to follow either the model results or the large increases in CO_2 concentrations that occurred in the other intervals as temperatures rose in those regions. A 6-day period of heater power loss took place in July 1999, approximately a month previous to the time the last gas samples were collected. This power loss may explain the low concentrations in these intervals at 20 months. Future sampling has verified a return to increasing CO_2 concentrations (Section 6.2.8).

Carbon dioxide concentrations in borehole interval 76-3 show a much more rapid rise to about 16,000 ppmv after only 10 months of heating. The concentrations appear to reach a plateau, but then continue to rise strongly until 20 months when they drop off somewhat. Modeled concentrations also rise rapidly to a peak in the fractures at 10 months, at which time they drop off sharply. The modeled concentrations in the matrix by contrast, continue to rise slowly and then drop off very gradually until 20 months. The samples collected at 18 and 20 months have considerably higher concentrations than the model predictions, even though the early samples compare closely to the calculated data.

A similar behavior can be seen in borehole interval 78-3 (Figure 10d), which shows an even more rapid rise in measured CO_2 concentrations to about 25,000 ppmv after only 8 months, and then with nearly constant values to 12 months. This is followed by a large increase to 45,000 ppmv at 15 months, dropping off to much lower values at 18 and 20 months. Modeled data taken at the center of the interval and at the end of the interval (deeper part) follow the very steep rise to over 10,000 ppmv after 6 months of heating. From 8 to 12 months, the model data from the end of the interval matches closely the measured levels (matrix only at 12 months). Except for the sharp peak at 15 months, the model data also reproduces quite closely the low values at 18 and 20 months.

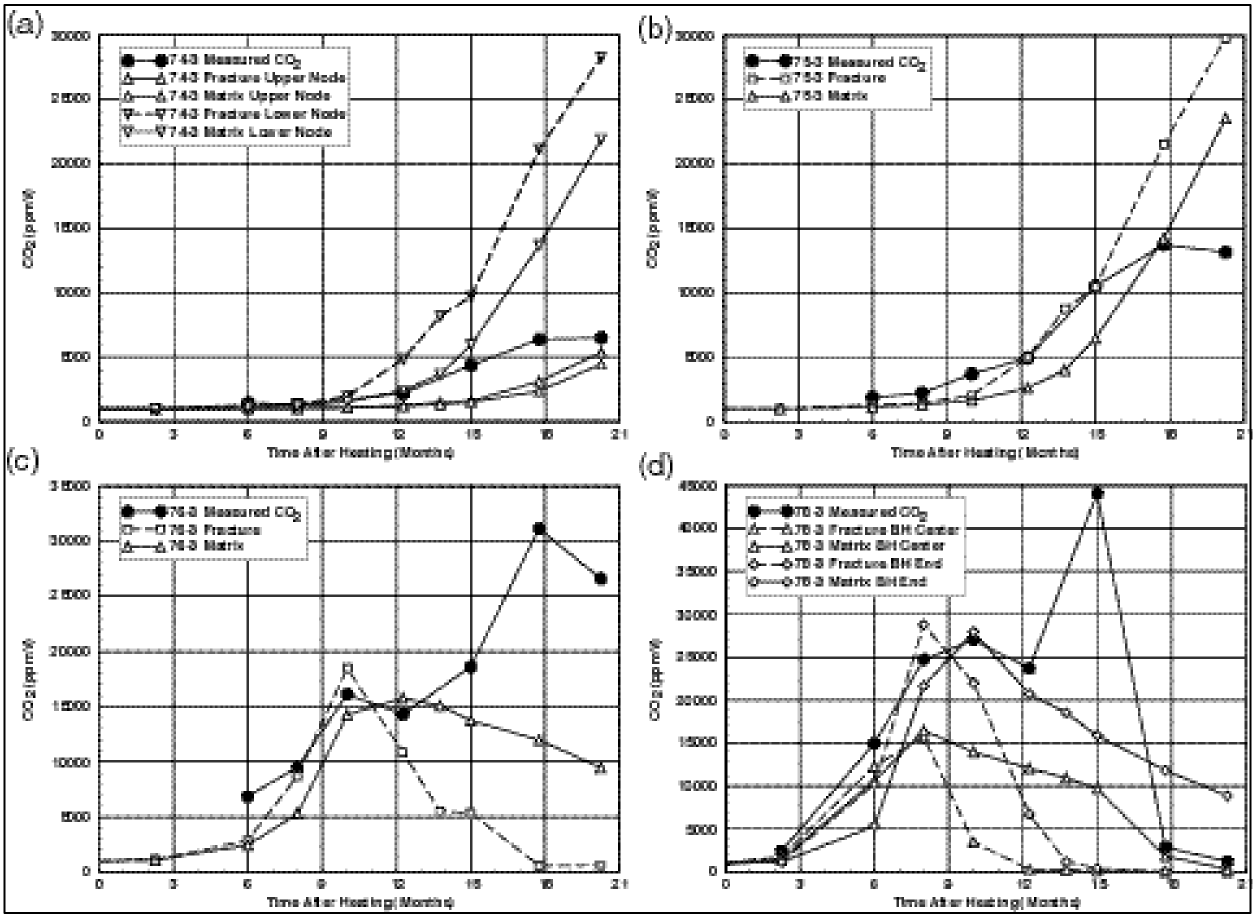

DTN: LB991200DSTTHC.002 (modeled)
LB991215123142.001 [128157] (meas.)
LB990630123142.003 [111476] (meas.)
LB000121123142.003 [146451] (meas.)
CRWMS M&O 2001 [153814] (meas.)

Figure 10. Comparison of Modeled CO_2 Concentrations (Base Case) in Fractures and Matrix to Measured CO_2 Concentrations in Boreholes. (a) Borehole interval 74-3 at nodes above and below; (b) borehole interval 75-3; (c) borehole interval 76-3; (d) borehole interval 78-3 at nodes near center and end.

The strong observed CO_2 concentration increase in 76-3 and 78-3 to values significantly higher than the predicted concentrations, after an apparent earlier maximum, occurs at different times in the two intervals, which cannot be explained simply by some change in the heater power output. Comparison of the measured CO_2 concentrations to the model results at close to boiling temperatures could be significantly affected by the amount of water vapor in the gas phase when the sample was collected. Because the air mass fraction in the gas phase drops considerably because of the production of steam, and the samples are “dried” by condensing much of the water out at a low temperature (~ 4°C), the measured concentrations reflect the CO_2 in the air after water has been condensed out. The model results include the water vapor component and therefore may be very different from the measured value once the air mass fraction drops to a low value and the CO_2/air ratio increases through the condensation of the water vapor.

Although no samples were collected that could be used to measure the water content of the gas directly, the model results can be used to assess the change in air mass fraction as the temperature in a borehole interval increases. Figure 11a shows the variation in air mass fraction in the gas phase over time in the center part of borehole interval 78-3. The drop off to near zero air mass fraction at 12 months indicates that the system trends to relatively pure steam. Also, samples collected after this time could not be compared directly to model results without some correction for the effect of condensing out the water vapor during the sampling. A rough way to evaluate this effect qualitatively from the model results is to calculate the ratio of the CO_2 concentration in the gas phase to the air mass fraction. When the air mass fraction drops to very low values, the CO_2 concentration in the “dry” gas can be very different from that in the water-rich gas. Comparing the trend of the CO_2 to mass fraction air ratio to the measured CO_2 values in borehole interval 78-3 shows clearly that the CO_2 in the dry gas will spike to a level much greater than the initial CO_2 peak in the air-rich gas, and at a later time. After this initial spike, the system loses much more CO_2, compared to air, and the ratio drops off sharply again. While this shows qualitatively the effect of comparing CO_2 concentrations in dry and wet gas samples, a quantitative assessment of the difference in CO_2 concentrations between the samples is more difficult. This difficulty arises because (in the condensation of water during the gas sampling), there will be some drive to equilibrium that would lower the CO_2 concentrations in the gas relative to what the ratio plotted in Figure 11b would predict.

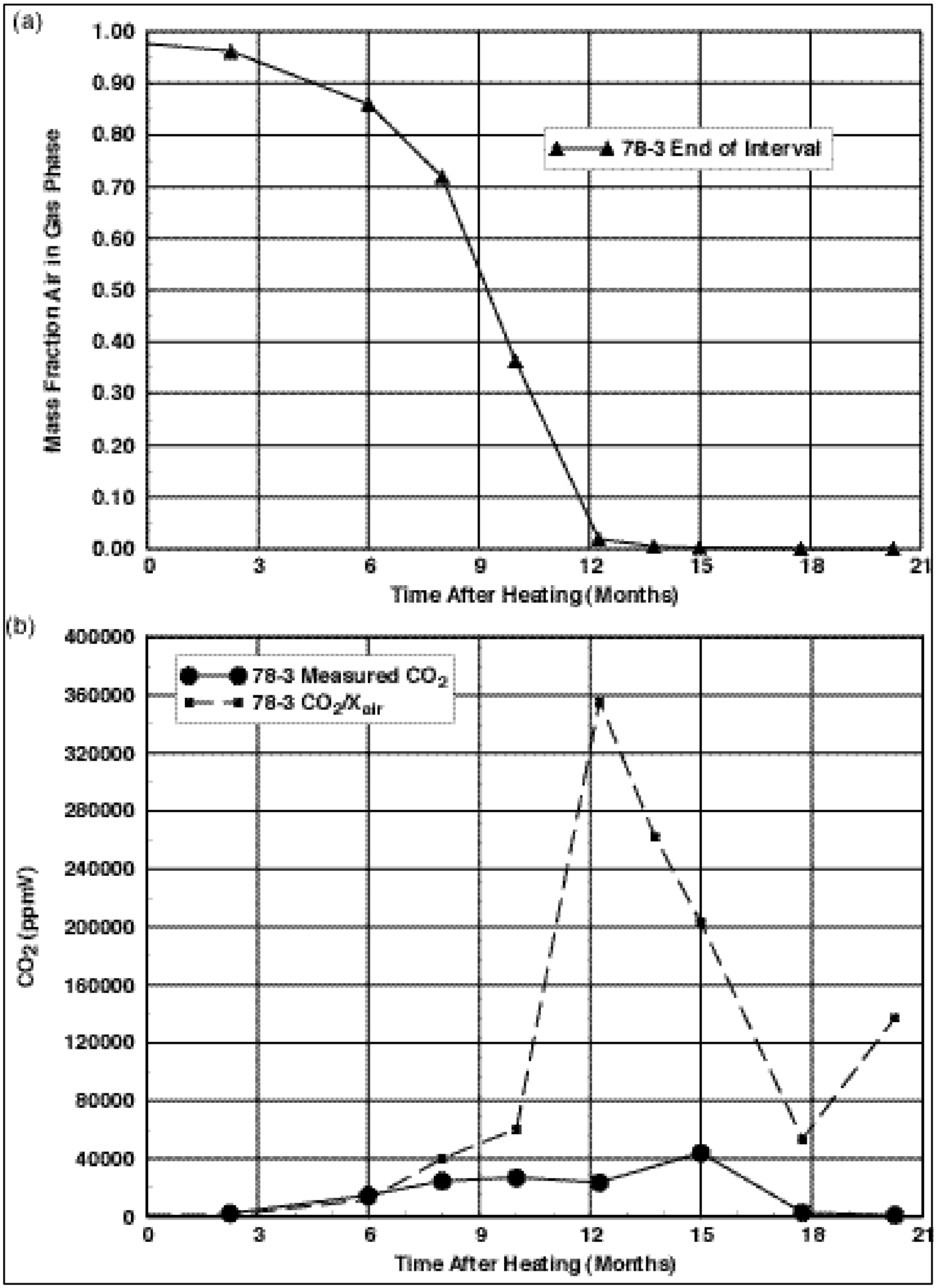

DTN: LB991200DSTTHC.002 (modeled)
LB991215123142.001 [128157] (meas.)
LB990630123142.003 [111476] (meas.)
LB000121123142.003 [146451] (meas.)
CRWMS M&O 2001 [153814] (meas.)

Figure 11. (a) Modeled Air Mass Fraction in Gas Phase at Center of Borehole Interval 78-3 (Fracture): (b) Ratio of Modeled CO_2 Concentration to Air Mass Fraction at Same Location as 11a (Base Case), with Comparison to Measured CO_2 Concentrations.

The last topic on gas-phase CO_2 is the composition of the Heater Drift gas compared to the model results. Because the bulkhead separating the Heater Drift from the Observation Drift is not completely sealed, the model considers some exchange of air between them. This was done originally to correct for heat loss, but it can also be used to assess the balance between the changes in CO_2 concentrations in the rock gas and those in the drift, which is open to advection and diffusion through the bulkhead. The trend of CO_2 concentration in the Heater Drift is shown in Figure 12 for a period 9 months before heating was initiated to about 20 months into the test. Three samples of Heater Drift air are shown, as well as samples taken from the Observation Drift, the latter having essentially the composition of tunnel air. All of the samples and the model results stay at essentially 400 ppmv, with measured fluctuations in the Observation Drift greater than in the Heater Drift. Because CO_2 concentrations in the rock around the test vary over several orders of magnitude, and the variations in the Heater Drift are only about 10% of the initial value, the model captures the necessary exchange of CO_2 between the Heater Drift and the outside air (which is set to a constant value during the simulation in the Observation Drift).

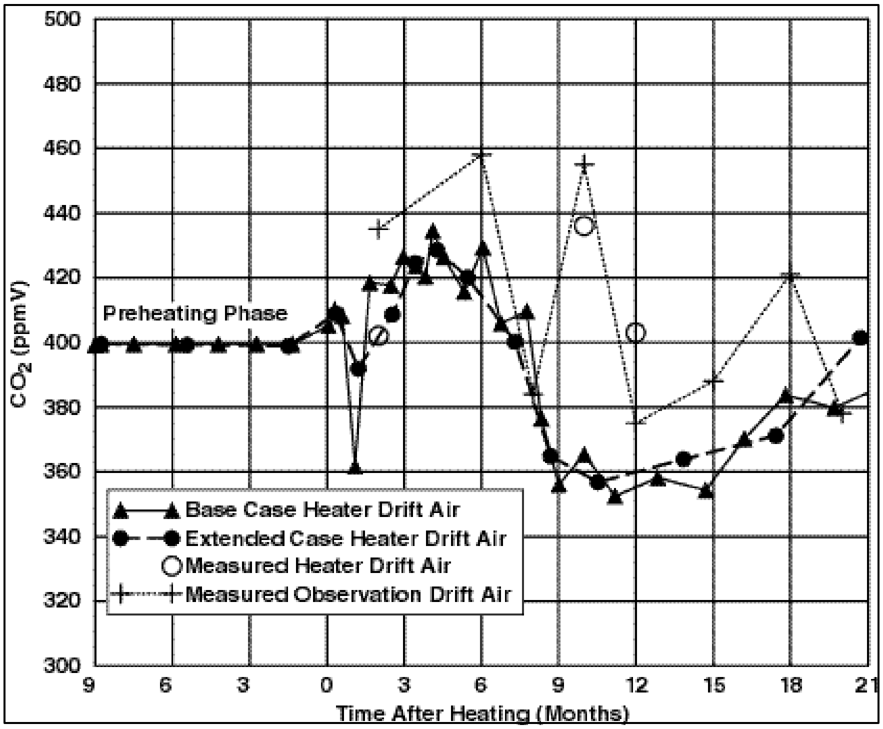

DTN: LB991200DSTTHC.002 (modeled)
LB991215123142.001 [128157] (meas.)
LB990630123142.003 [111476] (meas.)
LB000121123142.003 [146451] (meas.)
CRWMS M&O 2001 [153814] (meas.)

Figure 12. Modeled CO_2 Concentrations in Heater Drift Air, Compared to Measured Concentrations. Also shown are concentrations measured in air from the Observation Drift.

6.2.7.3 Aqueous Species Evolution

6.2.7.3.1 Chemistry of Waters Sampled During the Drift Scale Test

The chemical compositions of four waters collected from hydrology boreholes 60 and 186 on November 12, 1998, and January 26, 1999 (DTN: LL990702804244.100 [144922]), are shown in Table 9. The ambient pore-water composition (Table 3) is repeated here for direct comparison. The water samples collected during the test were obtained from zones that were hotter than the temperatures given for the samples, because water temperatures were measured after collection and had cooled substantially. Both intervals are located in the zone below the wing heaters. Relative to the drift axis, borehole interval 186-3 is lower and probably cooler than 60-3. Borehole 60 is located approximately in the same location as borehole 77, and borehole 186 corresponds to approximately the position of borehole 78.

Waters that were collected from the hydrology boreholes at elevated temperatures are generally more dilute (lower Cl and SO_4) and lower in pH than the initial pore water. Aqueous silica concentrations are similar to or much higher than in the pore water, indicating that these waters are not simple mixtures of pore water and pure condensate water. Some clear trends in water chemistry of the condensate waters in both intervals over time are increases in pH and SiO_2 (aq) concentration, and a drop in Ca. A similar trend for pH and SiO_2 (aq) exists between the boreholes, where the hotter interval (60-3) has a higher pH and SiO_2 (aq) concentration than the 186-3 interval at each time. The concentration of HCO_3 is also lower in 60-3 relative to 186-3, as expected from the higher temperature of 60-3. Some of the processes that could explain the water chemistry of samples collected in the hydrology boreholes include mixing of pure condensate water with fracture pore waters, equilibration of condensate waters with matrix pore waters via molecular diffusion, reaction of condensate waters with fracture-lining minerals, and mineral precipitation resulting from reaction, boiling, temperature changes, or pH changes. The higher silica concentration in the waters collected in January compared to those collected in November, relative to chloride and the initial pore-water silica concentration, is consistent with dissolution of a silicate phase, rather than increased concentration by boiling. However, concentrations of K, Mg, and Na are higher than what would be expected by dilution of original pore water (as evidenced by the low chloride concentrations). Therefore, the silicate phases that dissolved must have been some combination of cristobalite, opal, feldspar, clays or zeolites, rather than just a SiO_2 phase. The drop in Ca over time is consistent with calcite precipitation, which would be expected as the condensate waters were heated further and underwent CO_2 degassing, resulting in an increase in pH. Further discussion of these trends is given in Section 6.2.8.

Table 9. Measured Concentrations in TSw Pore Water from Alcove 5 and Chemistry of Water Samples from Hydrology Boreholes

Parameter	**Units**	**Pore Water**$^{(1)}$	**60-3**$^{(2)}$ **(11/12/98)**	**60-3**$^{(2)}$ **(1/26/99)**	**186-3**$^{(2)}$ **(11/12/98)**	**186-3**$^{(2)}$ **(1/26/99)**
Temperature	°C	25	26.5-49.6	51.7	34.3-34.8	Unknown
pH		8.32	6.92	7.4	6.83	7.2
Na^+	mg/L	61.3	20.3	19.1	17	25.9
SiO_2 (aq)	mg/L	70.5	115.5	139	58.2	105.5
Ca^{2+}	mg/L	101	13.9	5.9	20.2	2.92
K^+	mg/L	8.0	7.8	4.1	3.9	5.9
Mg^{2+}	mg/L	17	3	1.2	5.7	6.3
Al^{3+}	mg/L	9.92×10^{-7} $^{(3)}$	n.d. (< 0.06)	n.d. (< 0.06)	n.d. (< 0.06)	n.d. (< 0.06)
HCO_3^- $^{(4)}$	mg/L	200	n.a.	41	n.a.	116
Cl^-	mg/L	117	20	10	19	23.3
SO_4^{2-}	mg/L	116	30.8	13.5	26.2	21

NOTES:
(1) Average of porewater analyses ESF-HD-PERM-2 (30.1'-30.5') and ESF-HD-PERM-3 (34.8'-35.1'). DTN: MO0005PORWATER.000 [150930]
(2) DTN: LL990702804244.100 [144922].
(3) Calculated by equilibrating with Ca-smectite at 25°C.
(4) Total aqueous carbonate as HCO_3^-, calculated from charge balance.
n.a. = not analyzed,
n.d. = not detected

6.2.7.3.2 Aqueous Species Simulation Results

The model simulates numerous aqueous species, and only a limited discussion will be presented here. Data for all of the species are included in the output files (submitted under DTN: LB991200DSTTHC.002). The modeled variation in pH during the DST is shown in Figure 13 for the base-case geochemical system. The most obvious effect on pH is a reduction to values predominantly around 6.5 in the condensate region, corresponding directly to the increases in CO_2 concentrations shown in Figure 6. As for the CO_2 concentrations, the low pH zone increases in size and moves outward with time. Within the dryout zone, the pH of the last residual water is also plotted, which reaches a maximum of nearly 9.5. However, the liquid saturation associated with these values is usually well below the residual liquid saturation. The modeled pH of condensate waters in fractures compares favorably with those collected from the hydrology boreholes (Table 9). As in the measured data collected at two times before the borehole intervals dried out, the model results show the effect of increasing pH with time and with increasing temperature in areas having greater than 60°C modeled temperatures. Therefore, in a given zone, the pH in the fractures first starts to drop because of steam condensation. Then, once the temperatures increase, so that the rate of evaporation and mineral-water reactions (and loss of CO_2) are greater than the rate of addition of water (and CO_2) via condensation, the pH rises. These trends are documented further in Section 6.2.8.

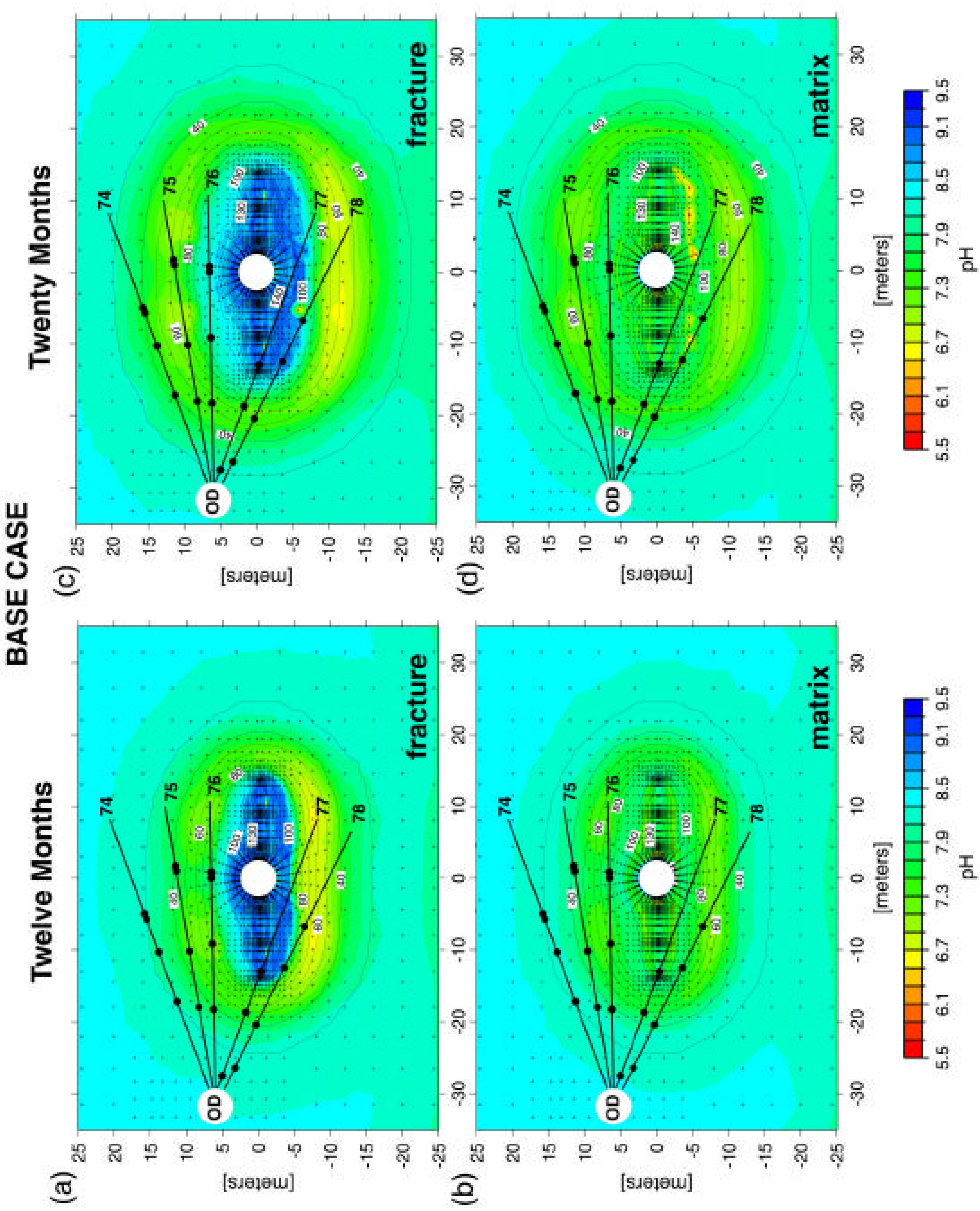

DTN: LB991200DSTTHC.002

Figure 13. Distribution of pH and Temperature at 12 Months (Fracture – 13a, Matrix – 13b) and at 20 Months (Fracture – 13c, Matrix – 13d). Results are for the base-case geochemical system.

The distribution of pH in fractures and matrix over time for the extended geochemical system are plotted in Figure 14. The general trends are similar, but the pH is shifted up to one unit higher in the condensate regions. The maximum pH in the water remaining just prior to dryout is still at about the same value as in the base-case simulations (below 9.5). Because the fractures dry out before the matrix, and the CO_2 concentrations are higher in the matrix, the pH in the matrix pore water remains lower than in the fractures.

Validation criteria for the simulation of water chemistry are more difficult to establish because of the great concentration variation possible in many species. An order-of-magnitude change in the H^+ concentration results in a single pH unit shift. Modeled pH values of fracture waters in the drainage zones of around 6.5–7.5 in extended-case simulations are within a pH unit of measured waters in boreholes. This is much less of a difference than the possible changes that could trend to acidic (pH < 5) or basic values (pH > 9), and which would have stronger implications for PA. It is just as important to capture the trends in the values because they reflect the dynamic coupled process effects. For these changes, the direction is the validation criterion, and this has been met by the model results for the small amount of data examined.

The effects of dilution through condensation of pure water vapor, of increases in concentration due to boiling, and the effects of fracture-matrix interaction can be assessed by the variation in a conservative species such as Cl. The variations in Cl concentration are plotted in Figure 15, at times of 12 and 20 months, and show marked decreases in the condensation zone. An interesting difference between the 12- and 20-month simulation times results from the slow imbibition of dilute condensate water into the matrix. At 12 months, a relatively large region of dilution of Cl appears in fractures due to condensation and drainage well below the wing heaters and Heater Drift. In the matrix, however, there is little change, except in the dryout zone where the residual waters reached high concentrations at very low liquid saturations. At 20 months, the matrix is starting to show signs of decreased Cl concentration owning to imbibition of fracture waters in the drainage zone, and significant dilution effects in the surrounding condensation zone. Further discussion of these trends is given in Section 6.2.8.

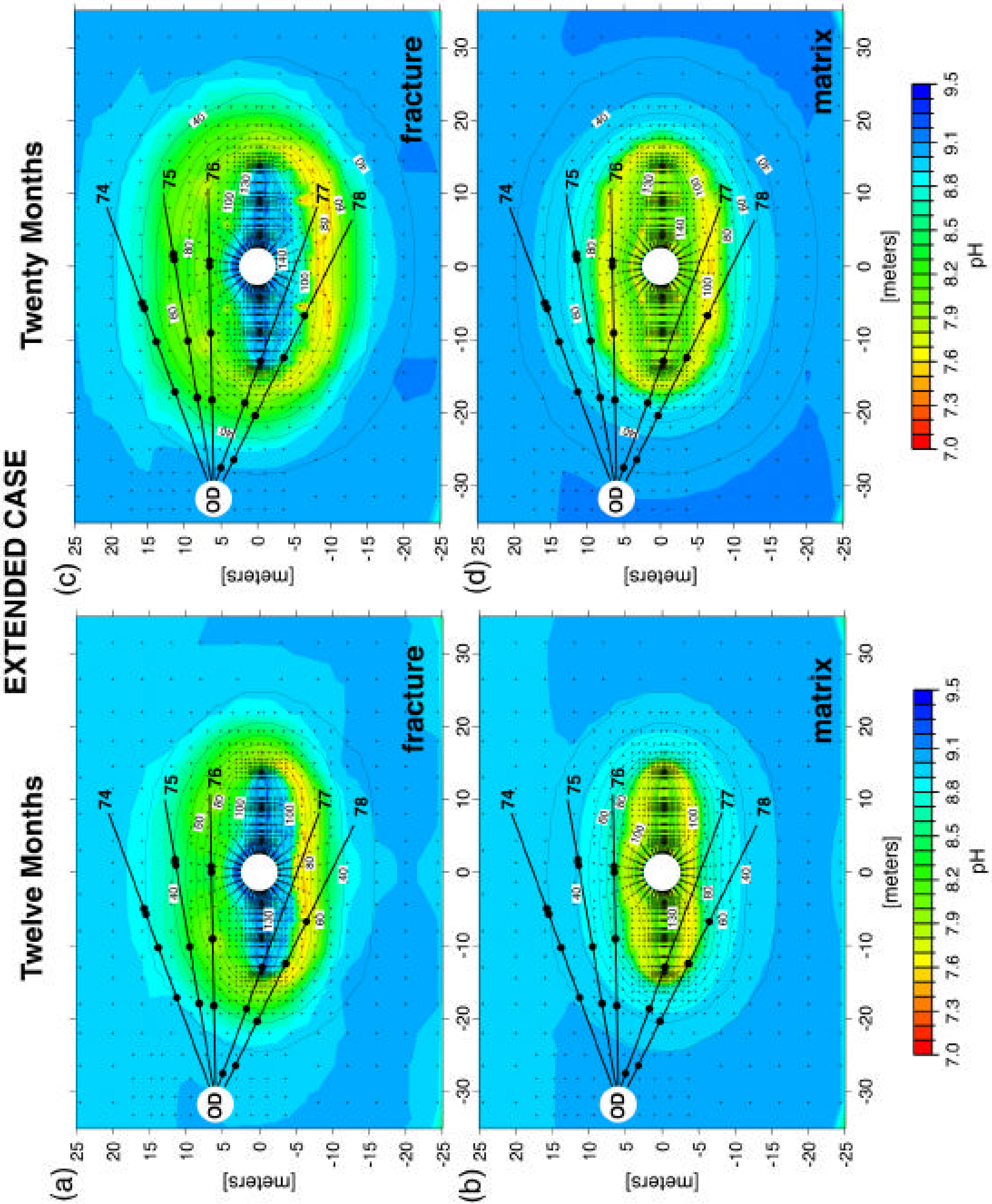

DTN: LB991200DSTTHC.002

Figure 14. Distribution of pH and Temperature at 12 Months (Fracture – 14a, Matrix – 14b) and at 20 Months (Fracture – 14c, Matrix – 14d). Results are for the extended geochemical system.

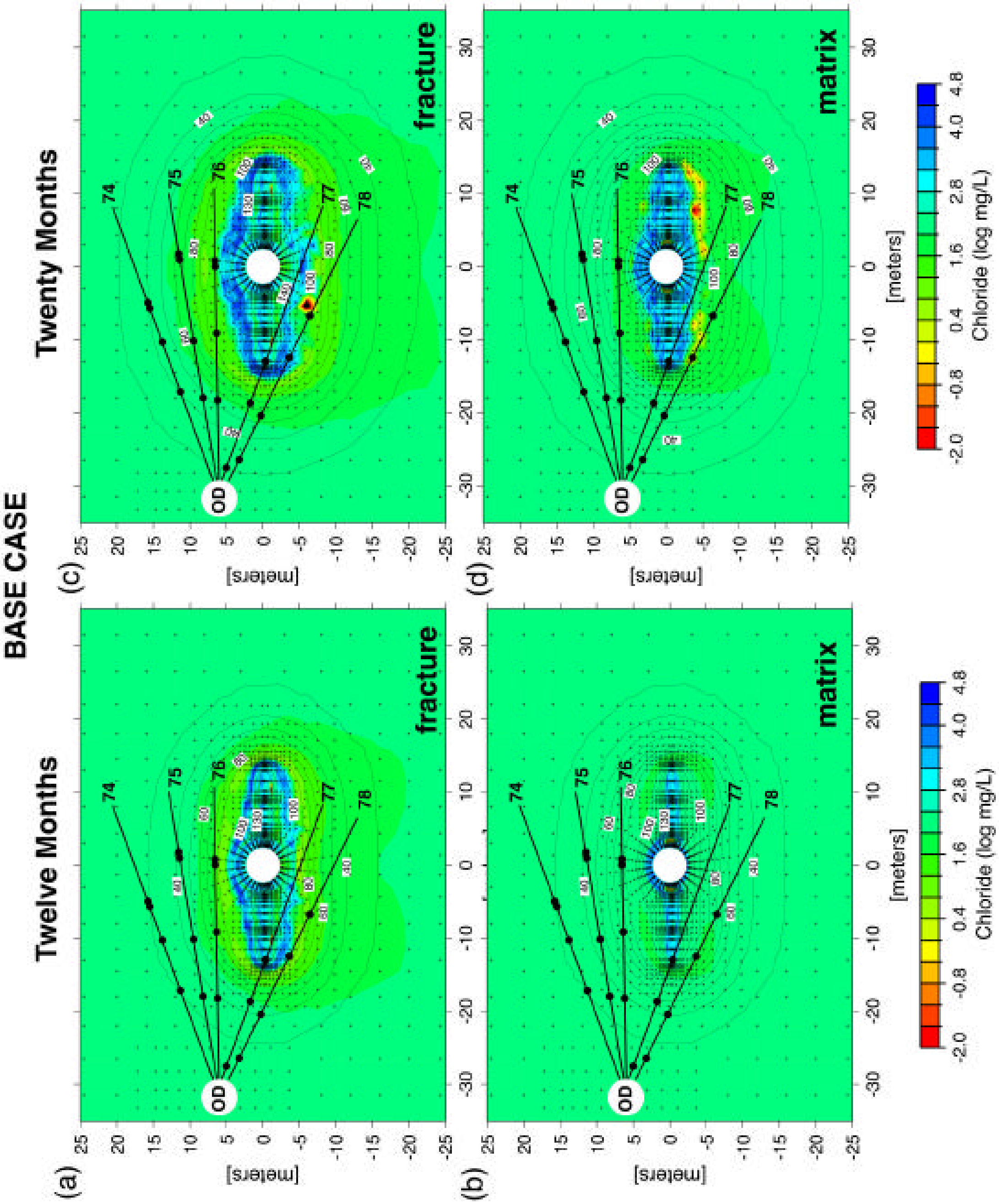

DTN: LB991200DSTTHC.002

Figure 15. Chloride Concentration (log mg/L) and Temperature at 12 Months (Fracture – 15a, Matrix – 15b) and at 20 Months (Fracture – 15c, Matrix – 15d) for the Base-Case Geochemical System.

Main Menu

EXIT

6.2.7.4 Mineralogical Changes

Over the course of the DST, marked changes occur in the water and gas chemistry that are strongly influenced by mineral-water reactions. The total amount of minerals precipitated or dissolved, though, is exceedingly small compared to the available fracture or matrix porosity. In terms of its effect on the chemistry of the system and its abundance in the precipitated mineral assemblage, calcite is the most important mineral over the short duration of the test.

Predicted changes in calcite volume percent after 20 months of heating for both geochemical systems in fractures and matrix are shown in Figure 16. The base-case geochemical system shows a well-defined region of precipitation in the fractures above and to the margins of the Heater Drift and wing heaters. Some dissolution is occurring below the wing heaters, but, it is smaller in magnitude than the precipitation and does not show up on the plots. Within the matrix there is a fairly uniform region of calcite precipitation in the dryout zone. Precipitation in the matrix is driven mainly by increasing temperature and pH, whereas in the fractures there is continuous boiling of condensate waters that are draining back to the heat source from cooler regions above. These waters pick up Ca through interaction with calcite and from mixing of ambient fracture pore water. The continuous process of condensate formation and drainage leads to a well-defined zone of calcite precipitation in the fractures. The results are consistent with the decrease in Ca seen in the condensate waters over time (Table 9, see also Section 6.2.8).

The extended geochemical system shows a similar maximum amount of calcite precipitation, although the band of calcite above the drift is much narrower and more poorly defined. The matrix shows a much broader region of fairly uniform calcite precipitation extending down temperature to about the 80°C isotherm. As in the base-case simulation, calcite is precipitating due to increasing temperature because of its reverse solubility. No dissolution of calcite takes place in the simulations using the extended geochemical system. One obvious difference between the two systems is that in the extended case, calcite is predicted to precipitate in fractures in a zone extending well below the Heater Drift.

Predicted distributions of other minerals are not shown here on account of the very small abundances of these phases. After this short period of time, amorphous silica has only formed in the regions of dryout and in much smaller abundance than calcite. Note that updated simulation results are shown in Figures 27 and 28 (Section 6.2.8).

6.2.7.5 Porosity and Permeability Changes

The predicted change in fracture porosity for the base-case geochemical system after 20 months of heating is shown in Figure 17. Although the simulations were carried out with a feedback between mineral dissolution/precipitation and porosity, permeability, and capillary pressure changes, the effect on the latter parameters and on fluid flow was negligible. Total changes in either fracture or matrix porosity were less than 0.1%. The greatest change takes the form of a few meter wide zone of decreased porosity a few meters above the Heater Drift and wing heaters. Much of this change is a result of calcite precipitation. Likewise, permeability and capillary pressures were virtually unaffected. Even though the changes are very small, it is likely that the actual system would show localized precipitation and therefore greater heterogeneity than the model predictions.

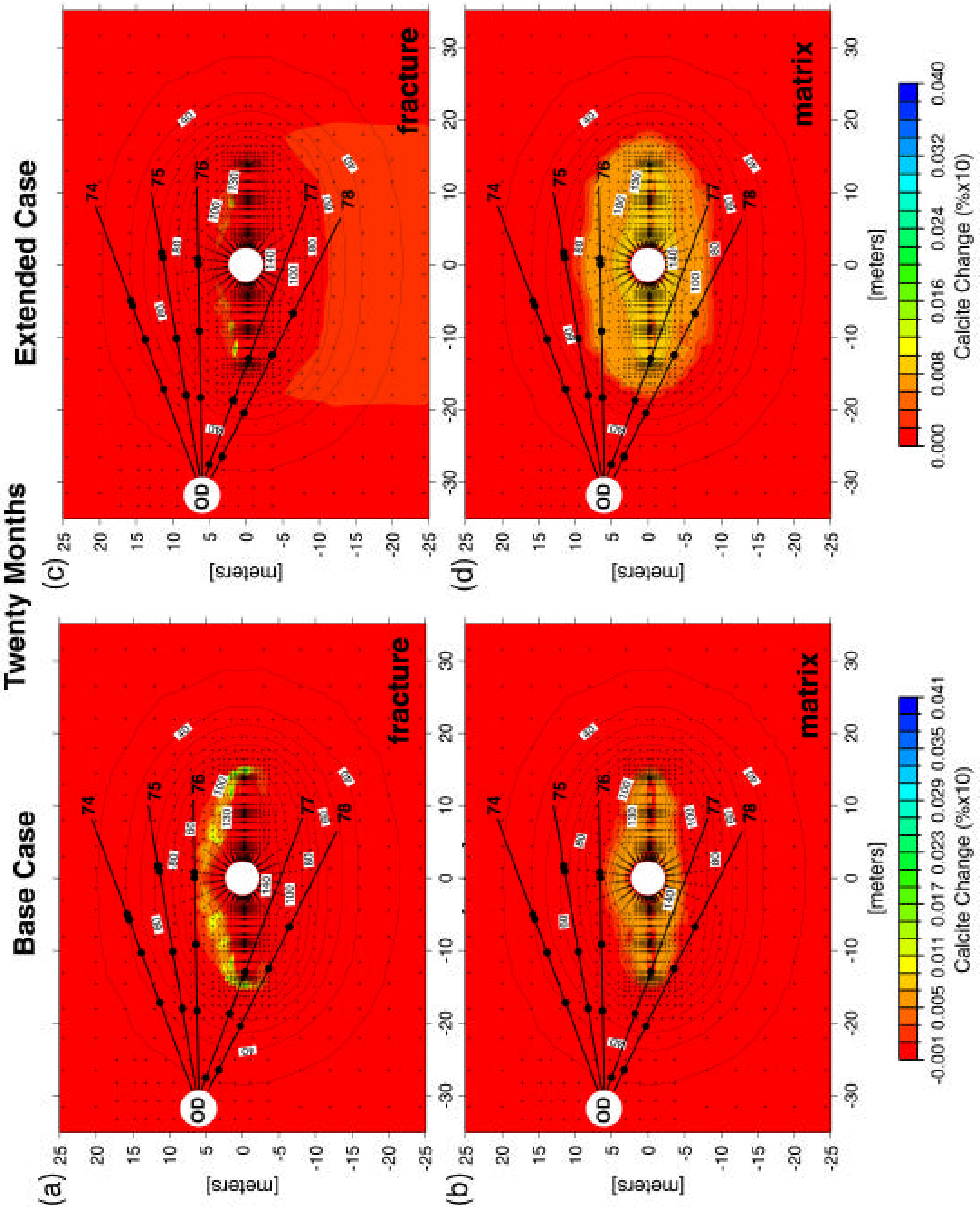

DTN: LB991200DSTTHC.002

Figure 16. Distribution of Calcite Precipitation (+) or Dissolution (-) as a Change in the Volume of the Total Medium (% x 10) at 20 Months. Results are for the base-case geochemical system (fracture – 16a, matrix – 16b) and the extended-case geochemical system (fracture – 16c, matrix – 16d).

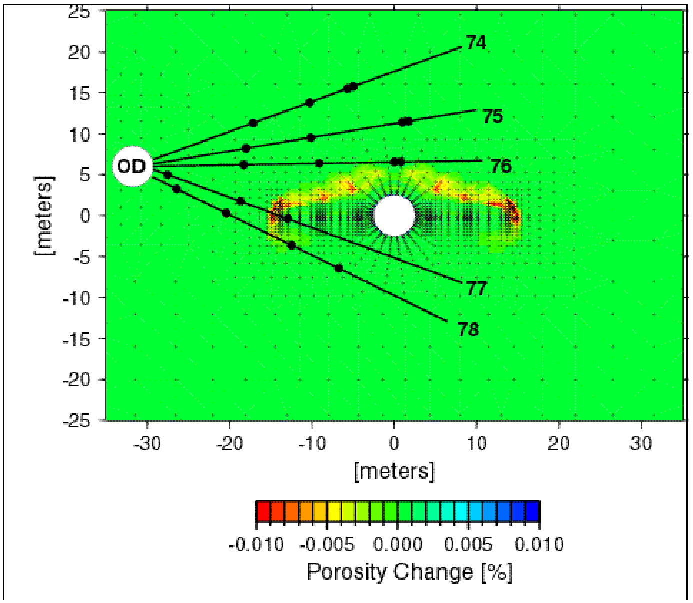

DTN: LB991200DSTTHC.002

Figure 17. Change in Fracture Porosity after 20 Months (Base Case). Negative values indicate a net porosity reduction resulting from mineral precipitation and positive values indicate a net porosity increase resulting from mineral dissolution.

6.2.8 Sensitivity Studies for DST THC Model

Several updates and revisions were made in the DST THC Model simulations for Rev01 of this AMR. These include the following:

1. Incorporated power reductions implemented in 2000 to maintain a near-constant drift-wall temperature of about 200°C. Reduced baseline heater power by 10% to make the 2-D temperature field more closely reflect heat losses in 3-D and the measured temperatures.

2. Used the revised thermodynamic database (Section 4.1.4.2 and Attachment VI).

3. Made some changes in the mineral assemblage (removed sepiolite and K-smectite) and introduced a small initial amount of amorphous silica to account for the presence of opal. Fluorite was added to the base case mineral assemblage and fluoride to the base-case aqueous species (compare Tables 7 and 8).

4. Treated calcite as an equilibrium mineral and as a kinetic mineral using the published rate constant (three orders of magnitude greater than in the first series of simulations). Also employed a supersaturation gap that diminishes with increasing temperature to account for a large degree of supersaturation in the pore water at 25°C (based on pore water analyses—see Section 6.4.3).

5. In the course of software qualification of the interim version of TOUGHREACT V2.2 [153219], it was discovered that the diffusion coefficient of CO_2 was underestimated by a factor of approximately 30. However, this has only a minor effect on these model

simulations, where diffusive transport is accompanied by advective transport and gas-water equilibration. The diffusion coefficient has been corrected in TOUGHREACT V2.2 [153219] and is correct in V2.3 [153101].

6. Changed the kinetic rate constant for dissolution of anorthite to be equivalent to albite, based on their mutual occurrence in plagioclase as a solid solution. Sensitivity studies considered the full reactive surface area and the reduced value (1000 times less) that was also used for Tptpmn THC No-Backfill and Tptpll THC Model simulations.

7. Increased reactive surface in fractures by 50% to account for conversion of 2-D areal coverage from 3-D volume fractions, in addition to another increase of approximately 5% (on top of the 50%) from addition of water-density dependence of areas to TOUGHREACT V2.3 [153101].

8. Introduced a saturation factor for conductive heat transfer between fractures and matrix for the water phase in fractures (new feature of TOUGHREACT V2.3 [153101]). This allows for slightly greater liquid penetration into heated zone.

9. Modified permeability based on a change from the initial hydraulic aperture, as calculated from fracture permeability and fracture spacing.

Six THC simulations of the DST were performed to investigate various aspects of the DST THC model thermodynamic and kinetic data and conceptual models for mineral reactions. All simulations were performed using TOUGHREACT V2.3 [153101]. All were run for 9 months of ambient open-drift conditions followed by 3 years of heating. The maximum time step was one day, using the sequential noniterative approach. Coupling of permeability to fracture aperture changes was employed; however, the changes to flow are very minor over the short time of the DST. Based on differences in the geochemical system and treatment of important mineral reaction rates, the simulations are designated in the figures as follows:

1. Base case CC Kin: Base case, including fluorite (Table 8). Calcite is treated as a kinetic mineral with the published value of the kinetic rate constant.

2. Extended CC Kin: Extended case (Table 8, includes aluminosilicates and iron oxides). Calcite is treated as a kinetic mineral with the published value of the kinetic rate constant.

3. Base case CC Eq: Base case, including fluorite. Calcite is treated as an equilibrium mineral.

4. Extended CC Eq: Extended case. Calcite is treated as an equilibrium mineral.

5. Extended An Full: Extended case. The full reactive surface area is used for anorthite (1000 times larger than in (2) and (4) above). Calcite is treated as a kinetic mineral with the published value of the kinetic rate constant.

6. Base case No CC: Base case, including fluorite. Calcite was removed from this simulation to address observations of lower pH waters that may have condensed in or near the walls of boreholes where water was collected without interacting with calcite.

Tptpmn THC Model simulations for the no-backfill homogeneous and heterogeneous permeability simulations (Sections 6.4 and 6.5) and for the Tptpll THC Model simulations (Section 6.6) used scenarios (3) and (4) above.

6.2.8.1 Gas Phase CO_2 Concentrations

This section compares gas-phase CO_2 concentrations from model simulations to measured concentrations from the same boreholes compared in Section 6.2.7.2. Locations of nodes close to borehole intervals are shown in Figure 9. Note that these simulations and data update those shown in Section 6.2.7.2. Measured concentrations for the current analysis include the most recent collected on August 21–22, 2000, an additional year of data beyond that shown in Section 6.2.7.2. As will be shown in the next section, differences in water chemistry (i.e., pH and Ca) by treating calcite under kinetic or equilibrium conditions are very small and decrease with time as gradients in water and gas composition decrease and the extent of calcite disequilibrium decreases. Therefore, Figures 18a-d show the change in CO_2 concentrations over time for the base-case and extended-case simulations with calcite treated as a kinetic mineral.

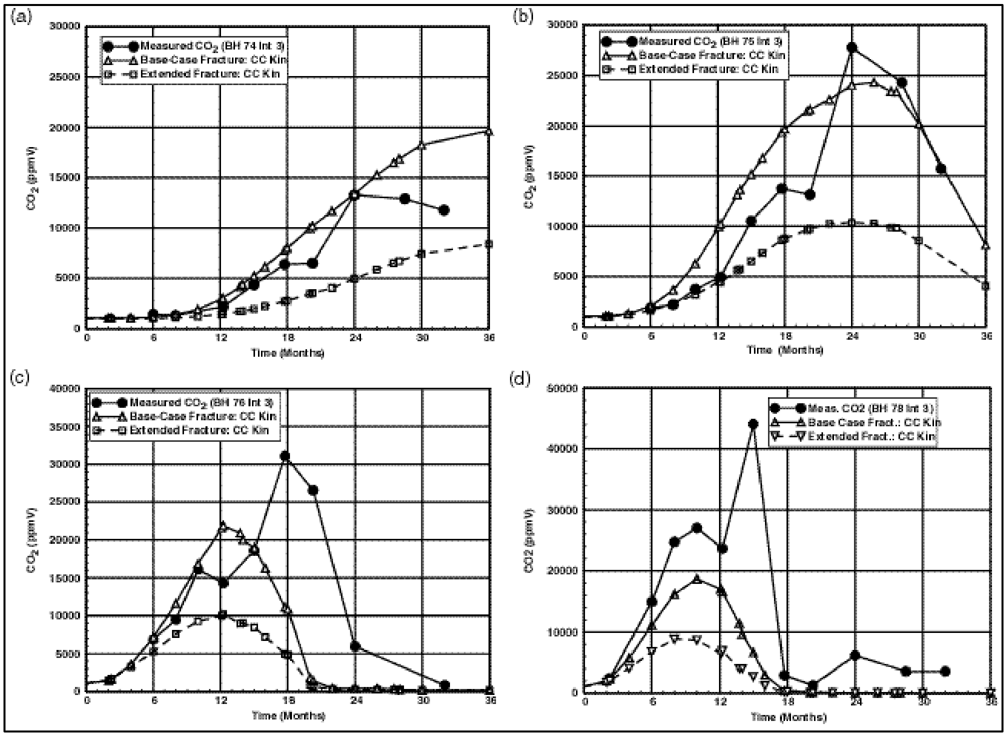

DTN: LB0011DSTTHCR1.002 (simulated), LB991215123142.001 [128157] (meas.), LB990630123142.003 [111476] (meas.), LB000121123142.003 [146451] (meas.), LB0011CO2DST08.001 [153460] (meas.), CRWMS M&O 2001 [153814] (meas.)

Figure 18. Comparison of Modeled CO_2 Concentrations (Base Case CC Kin and Extended Case CC Kin) in Fractures to Measured Concentrations in Boreholes: (a) Borehole Interval 74-3 at Node Above Interval; (b) Borehole Interval 75-3; (c) Borehole Interval 76-3; (d) Borehole Interval 78-3 at Node Near End of Interval.

Measured CO_2 concentrations in borehole 74 interval 3 (hereafter, referred to as "borehole-interval" or 74-3) shown in Figure 18a (the uppermost, lowest-temperature interval) are well-bracketed by the two geochemical systems. The base-case simulations have given the highest concentrations of CO_2 due to differences in water chemistry (e.g., generally lower pH) and their effect on the equilibrium partial pressure of CO_2. The measured concentrations show a sharp increase at 24 months. This increase was predicted (Section 6.2.7.2) because the relatively low value around 21 months seemed to have been affected by an earlier temporary power loss. After 24 months, the measured concentrations declined moderately, whereas the modeled concentrations continue to rise, albeit more slowly. This decrease in measured CO_2 concentrations may reflect the power reductions that were implemented during 2000. The trend in modeled CO_2 concentrations for 75-3 also follow the trend in measured compositions, with a sharp dropoff after 24 months (Figure 18b). The upper interval closest to the heaters is 76-3, and the new measured data (Figure 18c) shows a large decline after 21 months, which came earlier in the simulations. This difference may result from the fact that the grid node is closer to the interval in 76-3 than in 74-3 and 75-3, and therefore slightly hotter at a given time. In borehole interval 78-3 (Figure 18d) the model trends in the early and late time periods are similar to the measured values, but the maximum measured values are higher. Because of the steep angle of the borehole relative to the temperature isotherms, gas mixing likely occurs across the interval. As discussed previously, modeled and measured compositions become less directly comparable at higher temperatures, so that the second peak may be explained by the rapid decline in the air-mass fraction during boiling.

The base-case geochemical system appears to compare more closely than the extended system for CO_2 concentrations, still the increasing water-vapor fraction in the gas phase over time means that the actual CO_2 concentrations in the vapor phase become increasingly lower than the measured values. This fact may be used to infer that the extended system CO_2 values may be closer to the actual values, if they were corrected for the vapor that was removed during sample collection. Evidence that the base-case geochemical system yields CO_2 concentrations closer to the measured values comes from the better match to pH values measured in waters collected from boreholes. Even though the maximum CO_2 concentrations differ for the two geochemical cases, the trends are also similar. Thus, they provide a range of possible values similar to the range expected if there were also differences in initial dissolved inorganic carbon in the pore water. Further work in sample collection and analysis is aimed at resolving differences between the measured values and the actual values that are for the steam-air mixture. In this AMR, we can only qualitatively evaluate the effect of steam in the air on the concentrations.

6.2.8.2 Water Chemistry

Figures 19 through 26 show the evolution of water chemistry in borehole interval 60-3, which is below the heaters, and borehole interval 59-2, which is above the heaters. For reference, borehole interval 60-3 is approximately equivalent to the middle of borehole interval 77-4, below the intersection of the wing heaters and the heater drift (see Figure 9). The location of borehole interval 59-2 is equivalent to that of borehole interval 76-2 (see Figure 9). These intervals are the most valuable because they have the most complete sampling record (approximately one year). Therefore, trends in the composition of the waters resulting from various processes can be evaluated, such as the rates of condensate formation, water–rock reaction, mixing with ambient waters in fractures and fracture-matrix interaction, changes in gas-phase CO_2 concentrations, and changes in temperature. It should be noted that variable amounts of vapor condensation formed in the sampling tube mixed with water derived from the borehole, and the lack of an explicit representation of the borehole interval probably makes definite conclusions from any individual sample unjustified. Water samples described in this section are assumed to be representative of fracture waters in the region around the DST that are produced by THC processes (Section 5, Assumption B-3). Nearly all of the water samples described in DTNs listed in Table 2 from the DST have compositions consistent with those in 60-3, 59-2, and 186-3. Those few that are inconsistent have other reported characteristics (color, time of collection, etc.) that render them suspect.

Figures 19a and b show the evolution of pH in the sampled waters compared to the modeled base-case and extended systems. In general, both geochemical systems capture the trend in pH changes of fracture waters in this region. However, the base-case system captures the drop in pH more closely than the extended system. The system without calcite also shows a reasonable match to the measured pH values compared to the other simulations. The early trend to lower pH is related to the addition of condensate to this area and to increases in CO_2 in the gas phase (due to boiling closer to the heaters and diffusive and advective gas transport outwards). Later increases in pH are related to boiling of the water in this area, leading to a reduction in CO_2 concentrations as the temperature reaches boiling and the zone finally dries out. The model results for interval 60-3 showing complete dryout at approximately 18 months are consistent with the observation that water was absent from this interval shortly after the last sample was collected at 16 months of heating.

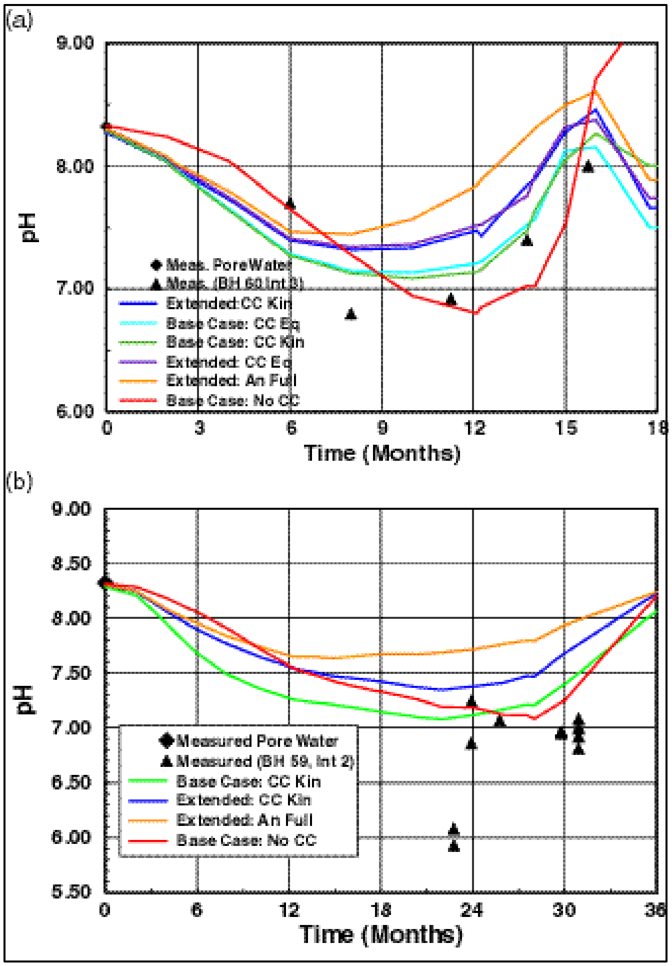

DTN: LB0011DSTTHCR1.002 (simulated)
LL990702804244.100 [144922] (meas.)
LL001200231031.009 [153616] (meas.)
MO0101SEPFDDST.000 [153711] (meas.)
MO0005PORWATER.000 [150930] (meas.)

Figure 19. Changes in pH in Water Samples Collected from Borehole Intervals 60-3 (a) and 59-2 (b), Compared to Modeled Fracture Water pH at Nearby Model Grid Nodes. The ambient pore-water pH is approximately 8.3.

The extent of mixing of condensate with ambient fracture water or matrix pore water can be evaluated by analysis of species such as chloride (Cl; Figure 20a, b) and sulfate (SO_4; Figure 21a, b) because they are not expected to be affected by water-rock interaction. Only at the final dryout (rapid rise in concentration at later time) may minerals such as halite and gypsum precipitate, of which only gypsum is considered in the model systems. Anhydrite may actually be a more stable sulfate phase, but gypsum serves as a useful proxy for a sulfate mineral and was observed in overcores of the Single Heater Test (LA0009SL831151.001 [153485]). The model results capture the overall extent of dilution or fracture-matrix interaction in the system (compared to the initial matrix pore water) for both chloride and sulfate. The largest discrepancy in interval 60-3 is at the earliest time when the first waters collected are more dilute than the modeled fracture waters. In borehole interval 59-2 the early samples are more closely matched than the later collected samples, although the overall trend is still captured reasonably well.

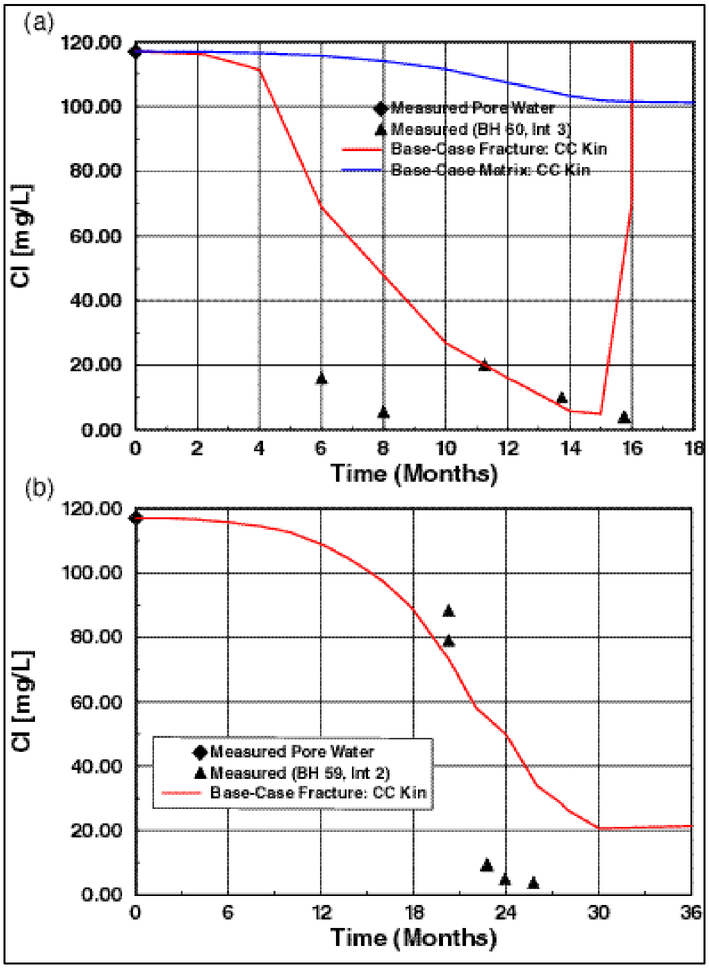

DTN: LB0011DSTTHCR1.002 (simulated)
LL990702804244.100 [144922] (meas.)
LL001200231031.009 [153616] (meas.)
MO0005PORWATER.000 [150930] (meas.)

Figure 20. Changes in Cl (mg/L) in Water Samples Collected from Borehole Intervals 60-3 (a) and 59-2 (b), Compared to Modeled Fracture Water Cl at Nearby Model Grid Nodes.

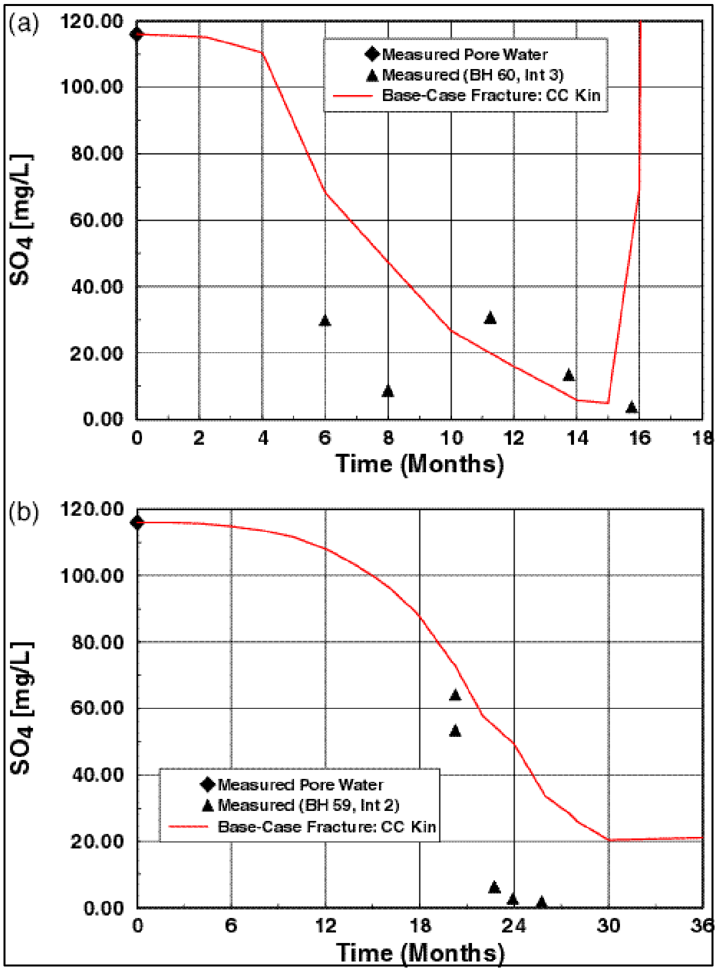

DTN: LB0011DSTTHCR1.002 (simulated)
LL990702804244.100 [144922] (meas.)
LL001200231031.009 [153616] (meas.)
MO0005PORWATER.000 [150930] (meas.)

Figure 21. Changes in SO_4 (mg/L) in Water Samples Collected from Borehole Intervals 60-3 (a) and 59-2 (b), Compared to Modeled Fracture Water SO_4 at Nearby Model Grid Nodes.

Measured sodium concentrations (Na; Figure 22a, b) are also much lower than in the initial pore water and close to the model predictions. However, the extent of dilution in interval 60-3 is only from 3 to 6 times, whereas for Cl it was from 6 to about 20 times. This difference indicates some contribution of water-rock interaction to the Na concentrations, which is shown in the extended-case model results as a shift to higher Na concentrations from the base-case results. The origin of the sodium in the DST waters could be alkali feldspar and/or reaction or exchange with clays. In the model simulations, the main source of Na is from alkali feldspar dissolution. As in the Cl and SO_4 variations over time, the sharp rise to higher concentrations at later times is due to rapid dryout.

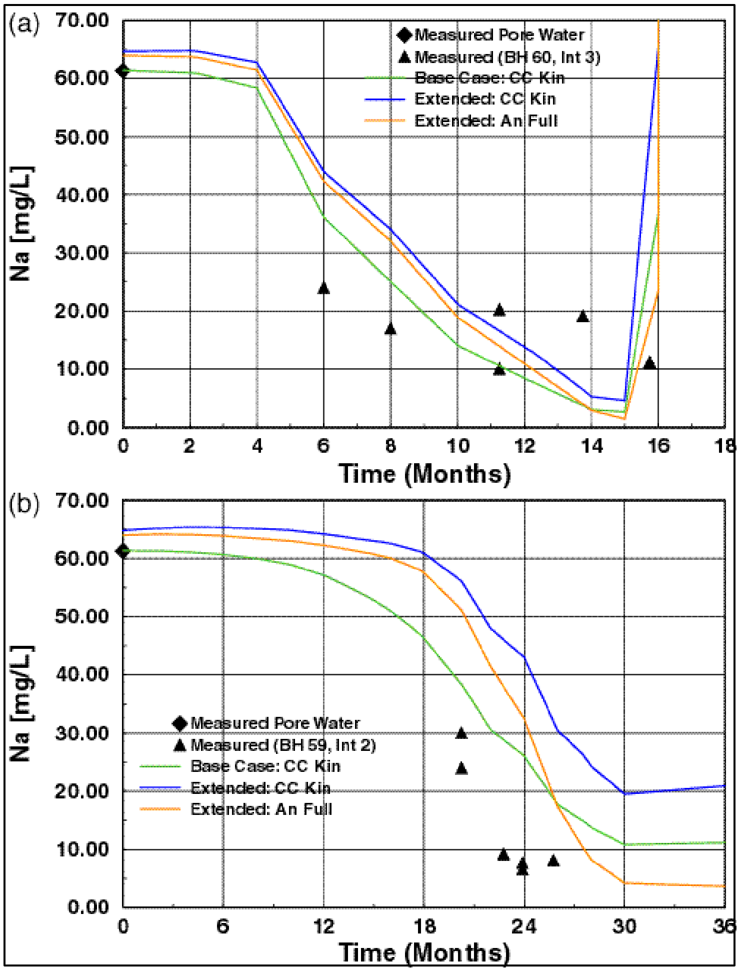

DTN: LB0011DSTTHCR1.002 (simulated)
LL990702804244.100 [144922] (meas.)
LL001200231031.009 [153616] (meas.)
MO0005PORWATER.000 [150930] (meas.)

Figure 22. Changes in Na (mg/L) in Water Samples Collected from Borehole Intervals 60-3 (a) and 59-2 (b), Compared to Modeled Fracture Water Na at Nearby Model Grid Nodes.

Calcium is more sensitive to water-rock interaction than some other species because of the fast reaction rate of calcite and its common occurrence in fractures. Other potential sources of Ca in the rock include Ca-rich zeolites, such as stellerite (which is abundant in the fractures), as well as Ca from plagioclase feldspar. Waters collected from intervals 60-3 and 59-2 show a large drop from the pore-water concentration (about 100 mg/L) to below 10 mg/L with a consistent decrease over time in 60-3 (Figure 23a, b). The continued drop in Ca in 60-3 and the very low concentrations in 59-2 may be caused by calcite precipitation, because of its reverse solubility with increasing temperature. The model results shown also in Figures 23a and b show a similar drop, albeit not to as low concentrations.

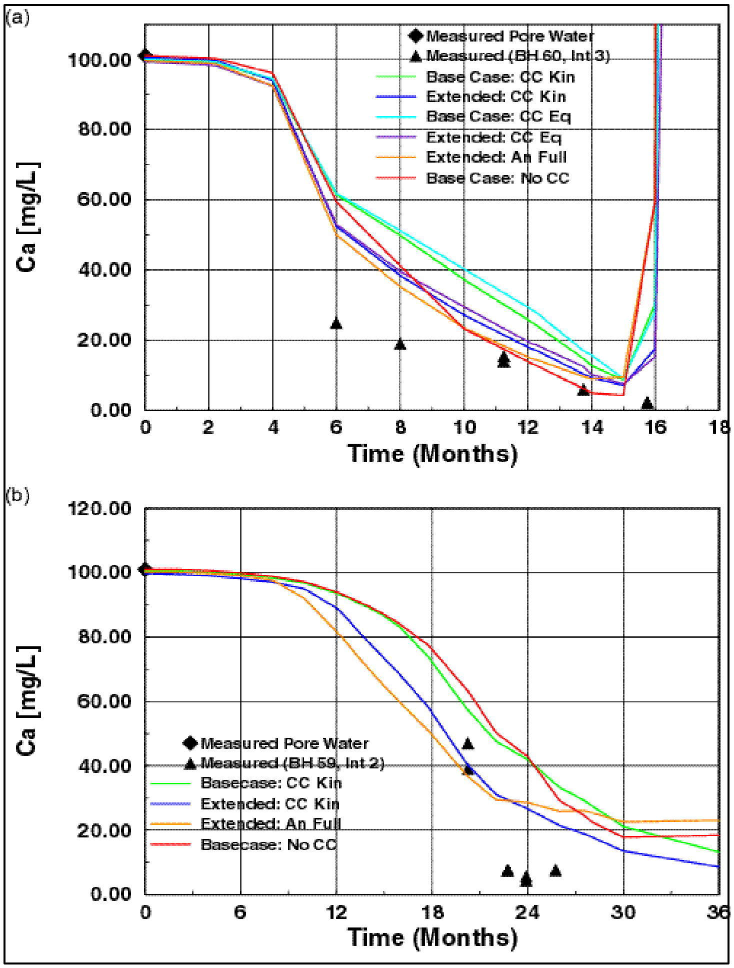

DTN: LB0011DSTTHCR1.002 (simulated)
LL990702804244.100 [144922] (meas.)
LL001200231031.009 [153616] (meas.)
MO0005PORWATER.000 [150930] (meas.)

Figure 23. Changes in Ca (mg/L) in Water Samples Collected from Borehole Intervals 60-3 (a) and 59-2 (b), Compared to Modeled Ca in Fracture Water at Nearby Model Grid Nodes.

Measured silica concentrations (Figure 24a, b) show an increase to significantly higher concentrations in the borehole waters compared to the initial pore-water concentration. Model results in borehole interval 60-3 decrease to lower concentrations, although the extent of dilution is moderated by water-rock reaction. In 59-2, the extended-case results match the concentrations of waters collected at later times, although the earliest samples collected had much higher concentrations. For comparison, modeled matrix silica concentrations for these same locations are also shown that seem to capture these larger concentrations, especially in interval 60-3. Because concentrations of conservative species, such as chloride and sulfate, are captured by the model quite well, and are in fact generally higher in the model results at later times, the possibility of greater fracture-matrix interaction can be ruled out. Also, modeled Na and K concentrations do not deviate substantially from measured values, suggesting that the additional silica is not likely to have been derived from increased dissolution of feldspars. Thus, the higher measured silica concentrations are likely to be a result of a higher effective reaction rate for a silica phase in the fractures (possibly opal-CT) or reaction of "fresh" mineral surfaces or clays (smectite) in the boreholes.

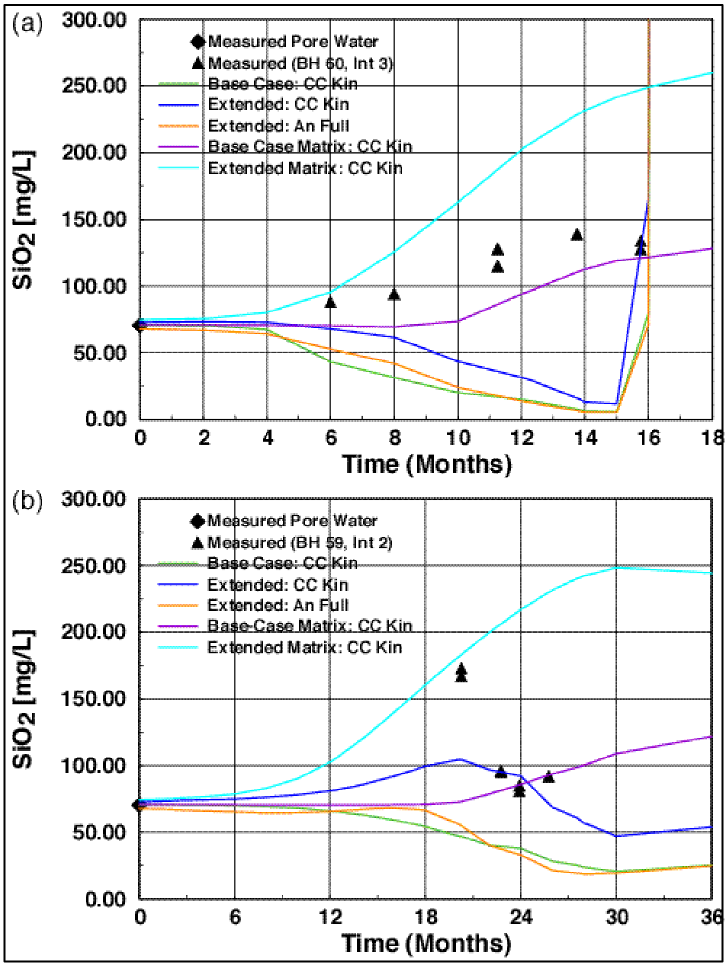

DTN: LB0011DSTTHCR1.002 (simulated)
LL990702804244.100 [144922] (meas.)
LL001200231031.009 [153616] (meas.)
MO0005PORWATER.000 [150930] (meas.)

Figure 24. Changes in SiO_2 (mg/L) in Water Samples Collected from Borehole Intervals 60-3 (a) and 59-2 (b), Compared to Modeled Fracture Water SiO_2 at Nearby Model Grid Nodes.

Modeled and measured potassium (K) concentrations are shown in Figures 25a and b. A deviation occurs in K at time zero, because of some disequilibrium in the initial pore water. Measured concentrations from the boreholes are significantly higher than would be expected from simple dilution of ambient fracture of matrix pore water, indicating that reactions with K-feldspar have likely occurred. Modeled concentrations, although initially lower, quickly rise during heating and are similar to the measured values.

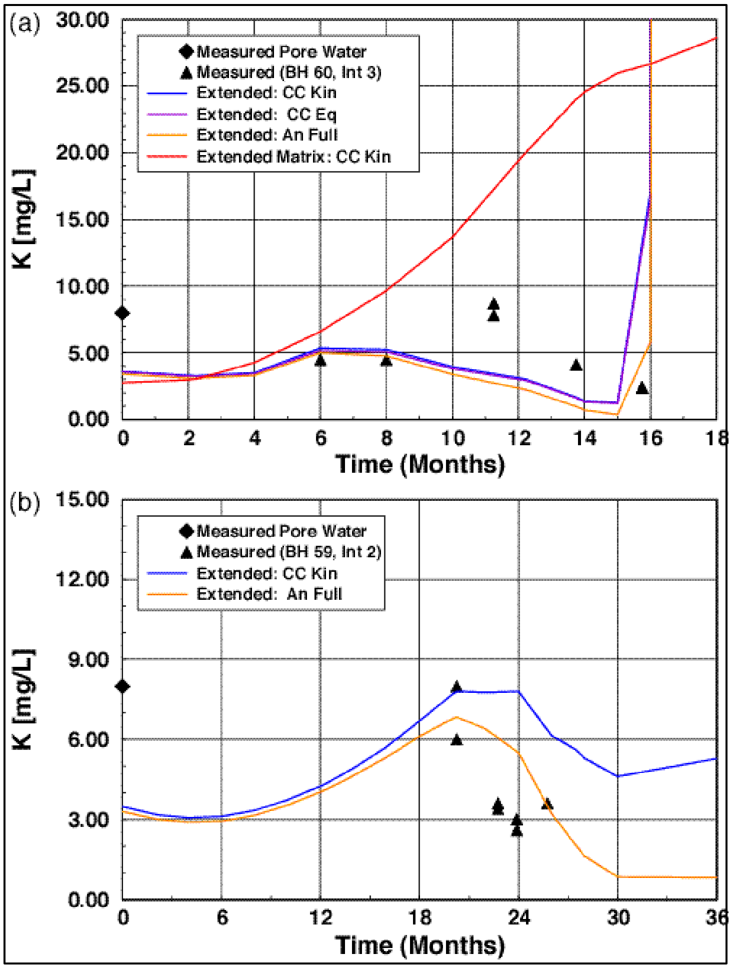

DTN: LB0011DSTTHCR1.002 (simulated)
LL990702804244.100 [144922] (meas.)
LL001200231031.009 [153616] (meas.)
MO0005PORWATER.000 [150930] (meas.)

Figure 25. Changes in K (mg/L) in Water Samples Collected from Borehole Intervals 60-3 (a) and 59-2 (b), Compared to Modeled Fracture Water K at Nearby Model Grid Nodes.

Fewer bicarbonate (HCO_3) concentrations were measured, but those available are plotted in Figures 26a and b compared to the model results. Measured bicarbonate concentrations are much lower than the initial pore-water concentration, a pattern which is captured well by the model through the combined effects of dilution and loss of CO_2 at higher temperatures to the vapor phase. Given the limited quantity of measured data, it is not possible to distinguish which geochemical system better predicts the bicarbonate concentration.

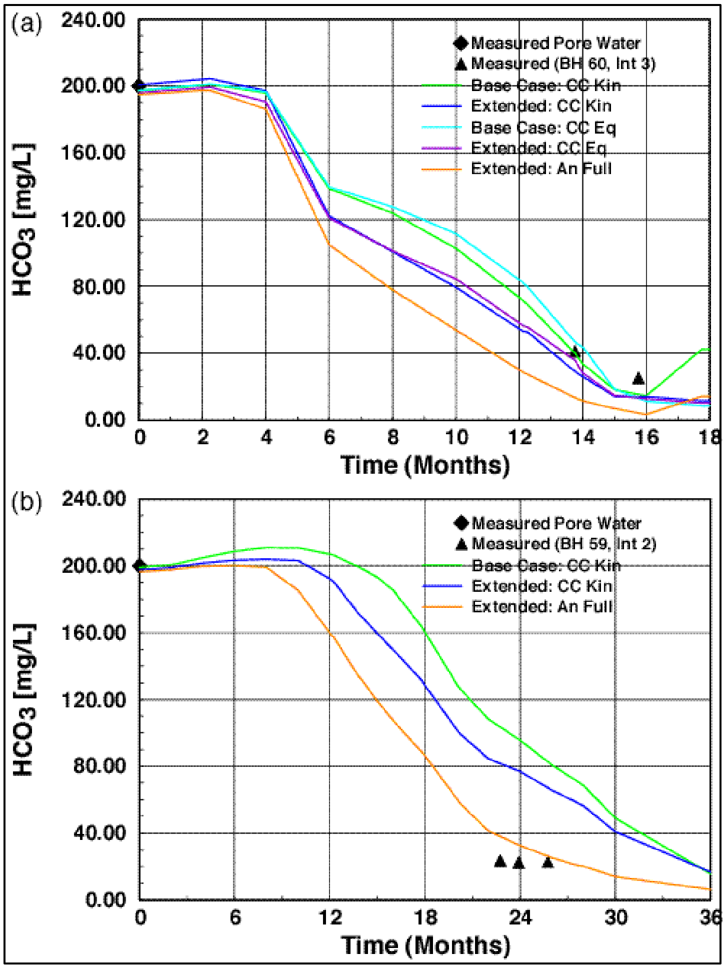

DTN: LB0011DSTTHCR1.002 (simulated)
LL990702804244.100 [144922] (meas.)
LL001200231031.009 [153616] (meas.)
MO0005PORWATER.000 [150930] (meas.)

Figure 26. Changes in HCO_3^- (mg/L) in Water Samples Collected from Borehole Intervals 60-3 (a) and 59-2 (b), Compared to Modeled Fracture Water HCO_3 at Nearby Model Grid Nodes.

6.2.8.3 Mineralogical Changes

Modeled changes in the volume percent of calcite and amorphous silica in fractures are shown in Figures 27 and 28. Calcite shows dissolution in the condensate regions and most strongly in the drainage zones below the wing heaters. Calcite precipitation occurs in the highest temperature boiling regions just prior to dryout, but is not as widespread as dissolution because of the smaller region of dryout compared to the widespread condensation and drainage zones.

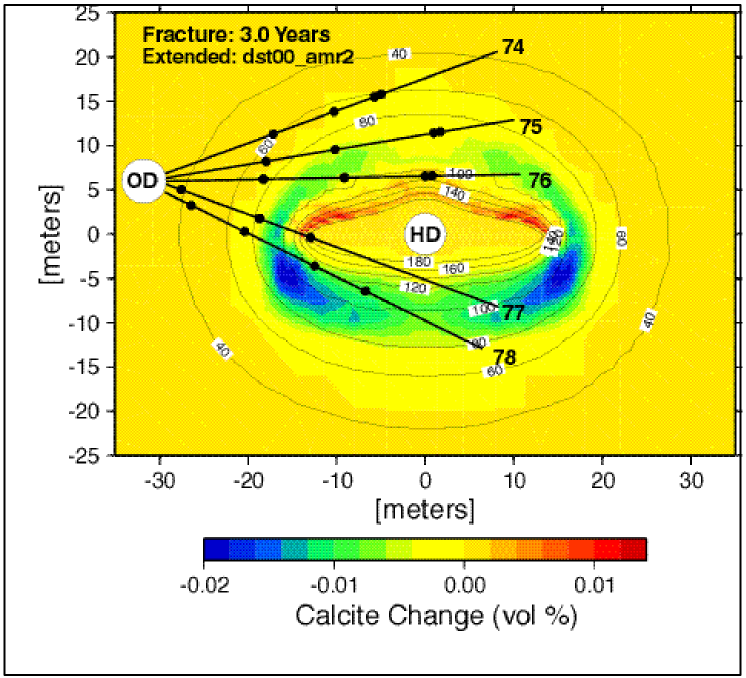

DTN: LB0011DSTTHCR1.002

Figure 27. Modeled Changes in Calcite in Fractures after 3 Years of Heating. Modeled temperature contours are overlain, as well as boreholes and approximate locations of temperature sensors.

Areas of modeled amorphous silica precipitation are shown in Figure 28 for the extended system (cc kin), because silica concentrations are closest to measured values (Figure 24) for this system. Only areas of greater than 1 x 10^{-6} volume percent are shown so that the precipitation areas can be readily discerned. Silica precipitation is concentrated in the reflux zones above the heaters. Although the volume percents are very small, the greatest amount of precipitation occurs at the outer edge of the wing heaters (where flow is focused into boiling regions).

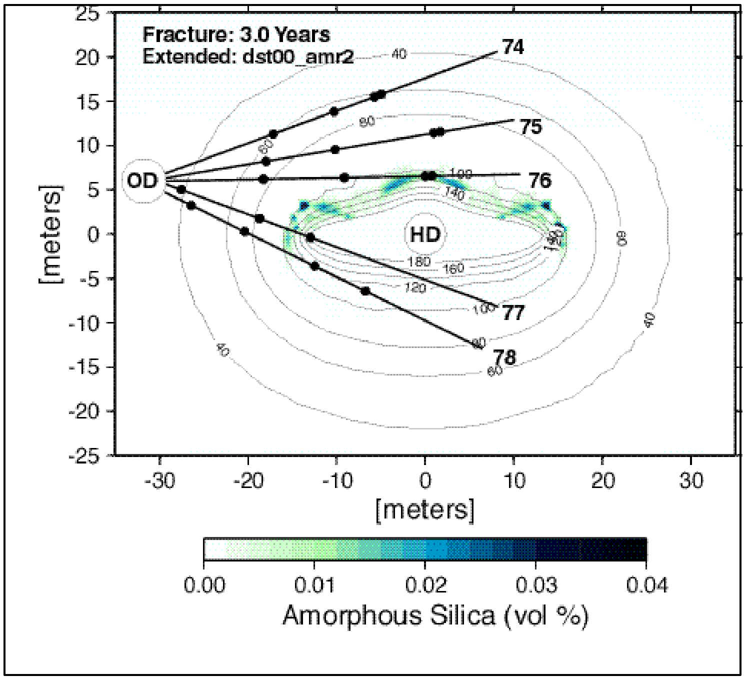

DTN: LB0011DSTTHCR1.002

Figure 28. Modeled Changes in Amorphous Silica in Fractures after 3 Years of Heating. Modeled temperature contours are overlain, as well as boreholes and approximate locations of temperature sensors.

6.3 Tptpmn THC BACKFILL MODEL

The purpose of the DST THC Model (Section 6.2) was to compare simulation results against actual measurements during the first 32 months of the DST. The THC Seepage models presented in Sections 6.3 to 6.6 apply the same methods as in the DST THC Model for simulating coupled THC processes. These models predict drift-scale coupled processes in the NFE around the potential repository over 100,000 years. The general setup of this numerical model is described below. Simulations were performed in two dimensions along a laterally continuous, vertical geologic section with stratigraphy similar to that in borehole USW SD-9 (at Nevada State Plane coordinates E171234, N234074; DTN: LB990501233129.004 [111475]). The simulations consider a drift located in the Topopah Spring Tuff middle non-lithophysal geologic unit (Tptpmn unit, corresponding to model layer name tsw34, DTN: LB990501233129.004 [111475]). Only part of the potential repository is planned to be located in the Tptpmn, and therefore the model may not be representative of the entire potential repository. However, most hydrogeologic data available for the potential repository horizon are from the Tptpmn unit, including data from the Single Heater Test (SHT), DST, and many other data collected in the ESF. Another model, presented in Section 6.6, considers a drift in the geologic unit where most of the potential repository is planned to be located (in the Topopah Spring Tuff lower lithophysal geologic unit, or Tptpll).

The model presented in this section was developed for a drift design with backfill during the post-closure period. Simulations using the current drift design without backfill are presented in Sections 6.4 and 6.5. The main differences between the model described in this section and the simulations in Sections 6.4 and 6.5 are as follows:

- Backfill is added after 50 years (Figures 1 and 30)
- Slightly higher heat load (1.54 kW/m compared to 1.45 kW/m)
- Slightly different in-drift thermal conductivities (Attachment IX compared to X)
- A lesser dependence of fracture permeability on fracture porosity changes
- Thermodynamic data for clays and zeolites (no-backfill models use revised data leading to steadier ambient concentrations under steady-state flow conditions)
- A slower initial precipitation rate of secondary minerals

The simulations presented in this section may be viewed as superseded by those in later sections, because they consider an earlier drift design and make use of an earlier version of the TOUGHREACT code (V2.2 [153219]) together with an ambient geochemical system that is not as steady for the infiltration rates used in the AMR. However, they remain useful to illustrate the effects of backfill in the drift design and the effect of thermodynamic and kinetic data revisions for comparisons with the work presented in Sections 6.4 and 6.5. Simulations in this section also document a range of infiltration rates that are not considered in simulations presented in Sections 6.4 through 6.6.

6.3.1 Numerical Mesh

Simulations were performed on a vertical 2-D mesh, using a drift spacing of 81 m (center to center, *Subsurface Facility System Description Document* (CRWMS M&O 2000 [151467], Section 1.2.1.5) and a drift radius of 2.75 m (CRWMS M&O 2000 [151014]). With rock properties laterally homogeneous between drifts (Section 5, Assumption A-18), this setup can be viewed as a series of symmetrical, identical half-drift models with vertical no-flow boundaries between them. Accordingly, the numerical mesh was reduced to a half-drift model with a width of 40.5 m, corresponding to the midpoint between drifts (Figure 29). Geologic data from borehole USW SD-9, as implemented in UZ model grid UZ99_2_3D.mesh (DTN: LB990501233129.004 [111475]), were used as a basis to map geologic contacts into the 2-D mesh. The mesh coordinate system was set with reference to the center of the drift (Table 10). The gridblock size was kept fine sufficient to provide enough resolution at key model locations (such as at the vicinity of drift and geologic contacts), but as coarse as possible to provide the computing efficiency needed for reasonable simulation times. The area extending approximately 50 meters above the drift is more finely gridded than other areas to capture THC effects potentially affecting seepage into the drift. Outside the drift, the smallest grid spacing was specified at the drift wall (20 cm), and increasing outward. Because of its minor relevance to this modeling effort, the geology below the tsw38 model layer was simplified compared to the original USW SD-9 data, which allowed for coarser gridding in this area. The mesh has a total of 2,510 gridblocks, including those representing matrix, fracture, and in-drift design elements.

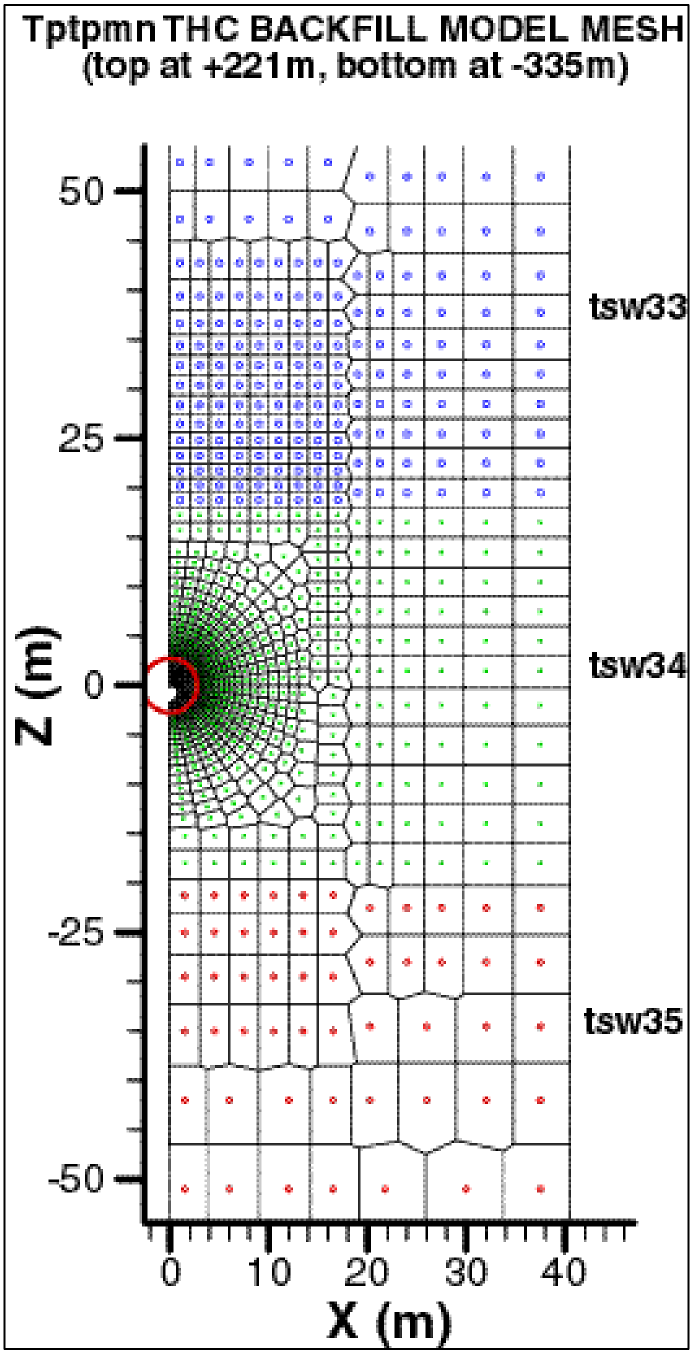

DTN: LB991200DSTTHC.002

NOTE: Grid detail around (0, 0) is shown in Figure 30.

Figure 29. Tptpmn THC Backfill Model Mesh with Hydrogeologic Units Shown in the Vicinity of the Drift: Topopah Spring Tuff Upper Lithophysal (tsw33 - circles), Middle Non-Lithophysal (tsw34 - dots), and Lower Lithophysal (tsw35 - diamonds) Units.

Table 10. Vertical Mesh Dimensions and Geologic Contacts in the Tptpmn THC Backfill Model

Model Layer	USW SD-9 Top of Layer Elevation (masl)	Mesh Top of Layer Z Coordinate (m)
Top	1286.00	220.7
tcw13	1285.44	220.1
ptn21	1279.57	214.2
ptn22	1275.00	209.7
ptn23	1269.09	203.7
ptn24	1264.51	199.2
ptn25	1255.45	190.1
ptn26	1233.79	168.4
tsw31	1221.01	155.7
tsw32	1219.01	153.7
tsw33	1165.71	100.4
tsw34	1080.37	18.0*
Drift center	1065.34	0.0
tsw35	1045.14	-20.2
tsw36	942.62	-122.7
tsw37	906.92	-158.4
tsw38	889.08	-176.3
ch2z	868.38	-197.0
Bottom	730.00	-335.3

DTN: LB990501233129.004 [111475]

NOTE: * Contact raised, compared to USW SD-9 data, to provide for better lateral continuity between the fine mesh above the drift and coarser mesh laterally away from the drift (See Figure 29)

The drift was discretized to include the design elements and dimensions shown on Figure 1 (338 gridblocks total). The dripshield is not explicitly modeled (Section 4.1.7.2). The gridblock size inside the drift was chosen small enough to provide a realistic drift model (compare Figure 30 to Figure 1). As mentioned in Section 4.1.7.2, two drift configurations are considered in this model that includes backfill:

- Pre-closure configuration: waste package, invert, and one open space between the waste package and the drift wall during the first 50 years (pre-closure)
- Post-closure configuration: waste package, invert, dripshield, backfill, and two open zones: the inner zone, between the waste package and the dripshield; and the outer zone, between the backfill and drift wall.

The discretization of the drift (Figure 30) was kept the same for the two configurations. As such, the pre-closure period was simulated by assigning identical open-space properties to gridblocks representing the inner zone, backfill, and outer zone.

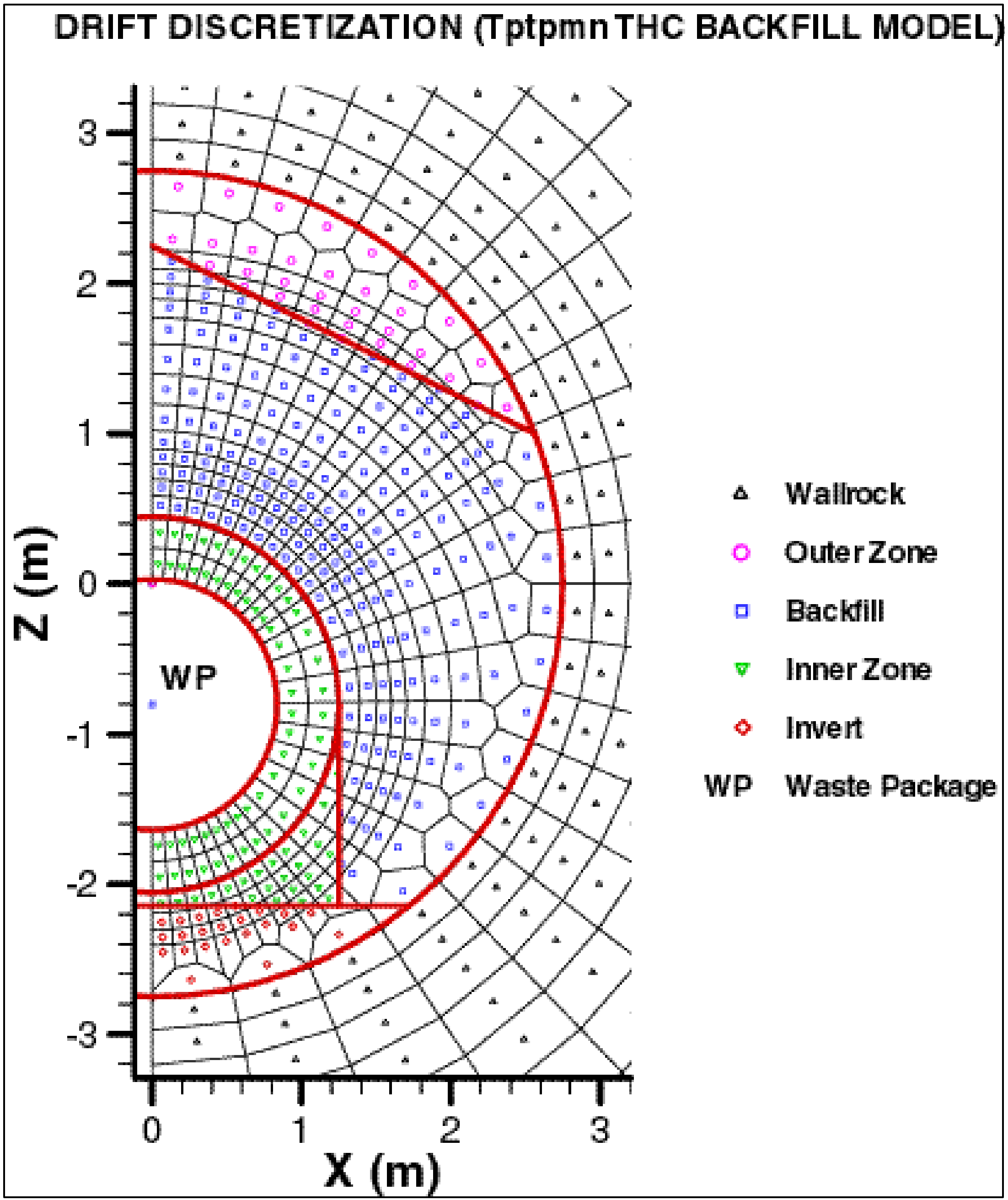

DTN: LB991200DSTTHC.002

Figure 30. Discretization of the Repository Drift in the Tptpmn THC Backfill Model

6.3.2 Boundary Conditions

The following boundary conditions were imposed on the Tptpmn THC Backfill Model (Table 11):

- Top boundary: stepwise changing infiltration rate (Table 12), temperature, pressure, and gas saturation (representing open atmosphere); constant CO_2 partial pressure and composition of infiltrating water
- Bottom boundary: constant temperature, pressure, and liquid saturation (representing the water table). Constant water composition and CO_2 partial pressure at equilibrium
- Side boundaries: no heat, fluid, and chemical fluxes
- Waste package: variable heat load with time, including effect of 70% heat removal by ventilation for first 50 years (pre-closure).

Three different infiltration regimes were modeled (mean, upper bound, and lower bound), each simulating a range of future climate conditions including present day, monsoon, and glacial transition periods (Table 12). These were developed to support TSPA-SR.

Table 11. Tptpmn THC Backfill Model Boundary Conditions

Boundary	Boundary Condition	Reference
Top	T = 17.68°C S_g = 0.99 P = 86339 Pa Time-varying infiltration rate Constant composition of infiltration and CO_2 partial pressure	Table 2 Table 2 Table 2 Table 12 Section 4.1.3
Bottom	T = 31.68°C S_L = 0.99999 P = 92000 Pa Constant water composition and CO_2 partial pressure	Table 2 Table 2 Table 2 Section 4.1.3
Sides	No flux for water, gas, heat, and chemical species	Not Applicable
Drift Wall	No-flux for water, gas and chemical species (except diffusive CO_2 flux); conduction only for heat	Not Applicable
Waste Package	Initial full heat load of 1.54 kW/m decreasing with time (due to radioactive decay), and reduced by 70% during the first 50 years (due to heat removal by ventilation)	Attachment VII and Table 2

NOTES: T = Temperature, S_g = Gas saturation, S_L = Liquid saturation, P = Pressure

Table 12. Tptpmn THC Backfill Model Infiltration Rates and Corresponding Rock Properties Sets

Case	Infiltration Rate (mm/yr)	Time Period (years)	Calibrated Properties Set	Reference
Ambient Mean Infiltration at USW SD-9 (no thermal load)	1.05	0 to 100,000	Present Day Mean	Table 2
Mean Infiltration	6 16 25	0 to 600 (present day) 600 to 2000 (monsoon) 2000 to 100,000 (glacial transition)	Present Day Mean	Table 2
Upper Bound Infiltration	15 26 47	0 to 600 600 to 2000 2000 to 100,000	Present Day Upper Bound	Table 2
Lower Bound Infiltration	0.6 6 3	0 to 600 600 to 2000 2000 to 100,000	Present Day Lower Bound	Table 2

6.3.3 Input Data and Modeling Procedure

This model was run using TOUGHREACT V2.2 [153219], the thermodynamic data shown in Attachment V, and the kinetic data in Table 4 (all those for Rev00). Input water and gas compositions are shown in Table 3. Initial mineral volume fractions and mineral surface areas are given in Attachments I and III, respectively. Heat load and drift thermal properties are given in Attachments VII and IX, respectively. This model was run using the base-case and extended-case sets of chemical components and mineral assemblages described in Table 7. The base case represents a set with a limited number of components and minerals while the extended case includes added components and minerals. The limits of minimum liquid saturation and maximum ionic strength at which chemical speciation in the water is no longer computed by the model were set at 10^{-4} and 2 molal, respectively (Section 5, Assumption A-17).

Different calibrated rock-properties sets were used to run the various infiltration cases (Table 12). For each infiltration case, a simulation was performed without reactive transport, heat load, or a drift (i.e., with rock at the location of the drift) until steady-state thermal and hydrologic conditions were achieved. A steady state was considered to have been met under at least one of the following conditions:

1. Liquid saturations, temperatures, and pressures remained constant within the model over a time span of at least 100,000 years.
2. The total liquid and gas inflow at the top of the model matched the total liquid and gas outflow at the base of the model within 0.01 percent.

THC simulations were then run with the drift in place and heat transfer from the waste package, using the steady-state temperatures, pressures, and liquid saturations as starting conditions. Open spaces within the drift were set to zero liquid saturation. “Ambient” reactive transport simulations with the drift in place but without heating (i.e., no heat release from the waste package) were also performed for comparison of chemical trends to simulations under thermal loading. These ambient simulations were run with the constant ambient mean infiltration rate at the location of borehole USW SD-9 (Table 12).

As discussed in Section 4.1.7.2, THC simulations were run for an initial period of 50 years, using the pre-closure drift configuration and thermal properties. The simulations were then restarted using the post-closure drift configuration and properties from 50 years to a total simulation time of 100,000 years. At times corresponding to changes in infiltration rates (at 600 and 2000 years, Table 12), the simulations were stopped and then restarted with the new infiltration rate (thus resulting in a stepwise change in infiltration).

Maximum time steps of 6 months for pre-closure simulations, 10 years for simulation times between 50 and 20,000 years, and a maximum of 50 years for simulation times between 20,000 and 100,000 years were used.

6.3.4 Tptpmn THC Backfill Model Runs

A total of nine simulations were completed, as summarized in Table 13. For each of the base-case and extended-case geochemical systems, THC simulations with thermal loading were carried out using three variable infiltration rates involving future climate changes. In addition, simulations under ambient conditions, without heating, were performed for the base case and extended case using a constant infiltration rate (approximately 1.05 mm/year). The latter represents the base-case present-day infiltration rate at the location of borehole USW SD-9, which was used to define the geology of the model. These ambient simulations were run to assess the extent to which the base-case and extended-case geochemical systems approached a geochemical steady state. These runs also provide a baseline to which the results of thermal loading simulations can be compared.

Table 13. Tptpmn THC Backfill Model Runs

Infiltration-Property Set (Table 12)	Geochemical System (Table 7)	Simulation Type	Run ID (used in DTN: LB991200DSTTHC.002; Attachment XI)
Mean Infiltration	None	TH	th6_16_25_3
Ambient Mean (no thermal load)	Base Case	THC	thc1mm_amb1
	Extended Case	THC	thc1mm_amb2
Mean Infiltration	Base Case	THC	thc6_16_25_3
	Extended Case	THC	thc6_16_25_4
Upper Bound Infiltration	Base Case	THC	thc15_26_47u_3
	Extended Case	THC	thc15_26_47_4
Lower Bound Infiltration	Base Case	THC	thc0.6_6_3l_3
	Extended Case	THC	thc0.6_6_3_4

6.3.5 Simulation Results

Model results are presented below in Figures 31 through 53, and focus on areas in the vicinity of the drift. THC effects in other geologic horizons, even if considered in the model, are not discussed in this AMR because they are not directly relevant to the primary purpose of evaluating THC effects in the NFE. Much of the data (temperatures, liquid saturations, water compositions, CO_2 concentrations, and liquid/gas fluxes) are examined as a function of time at three locations around the modeled drift. These are the crown, the side (approximately 20 cm above the springline) and the base (model nodes F257, F 92, and F272, respectively), at points located 10 cm to the outside (i.e., in the rock) of the drift wall. These data are in DTN: LB991200DSTTHC.002 and are further discussed below.

6.3.5.1 Thermohydrology Simulation Results

For comparison to the THC simulations, simulations were performed considering only thermal and hydrological processes (thermal-hydrological or TH). This simulation was run using the mean infiltration rates and corresponding rock property set (Table 12) and serves as a basis for interpreting the effects of water-gas-rock chemical interaction on the thermal and hydrological behavior of the system. Calculated temperatures, liquid saturation, and air mass fractions around the drift are shown in Figures 31 through 33.

Post-closure temperatures quickly climb above the boiling point (near 97°C at Yucca Mountain), and are higher at the base of the drift where the waste package is closest to the drift wall (Figure 31). The return to ambient temperatures after heating takes 50,000 to 100,000 years. The highest modeled temperature in the waste package (near 270°C) is attained shortly after closure at a time of 55 years.

Around the drift, the matrix is predicted to rewet after 1,000 to 2,000 years (Figure 31). Rewetting of fractures occurs within the same time frame, except at the drift base where fractures do not rewet until approximately 3,000 years (Figure 31). A contour plot of temperatures and matrix saturations in the vicinity of the drift at a simulated time of 600 years (near maximum dryout) shows the dryout zone (represented by zero matrix saturations) extending approximately 10 meters above the drift, 17 meters to the side of it, and 22 meters below it (Figure 32). Air mass fractions in the gas phase at the drift wall (the complement of the steam mass fraction; Figure 33) drop to near-zero values during dryout (i.e., the gas phase is almost entirely water vapor) and are essentially identical in matrix and fractures.

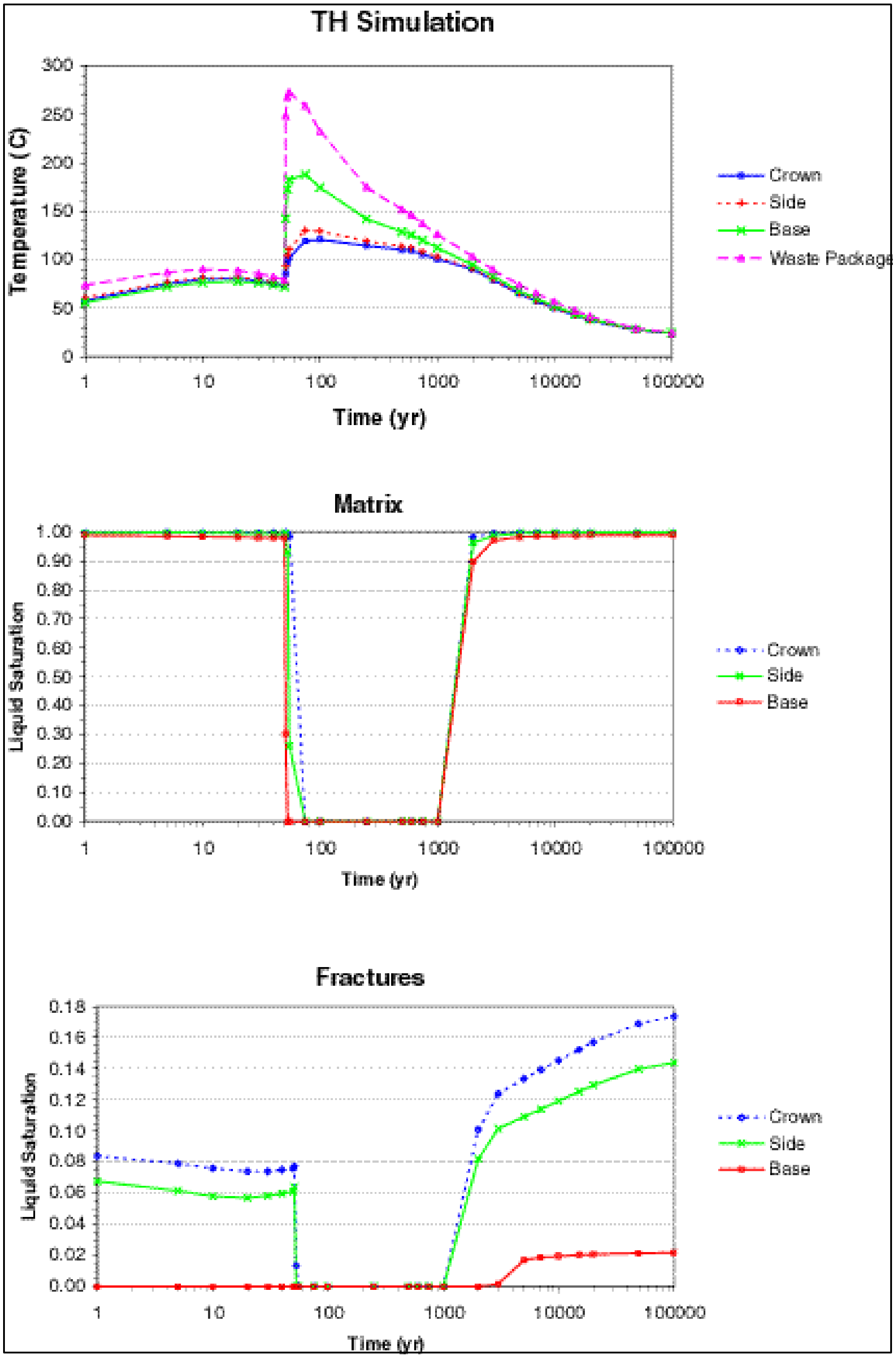

DTN: LB991200DSTTHC.002

Figure 31. TH Simulation (Tptpmn - Backfill). Time Profiles of Modeled Temperatures and Liquid Saturations in Fractures and Matrix at Three Drift-Wall Locations.

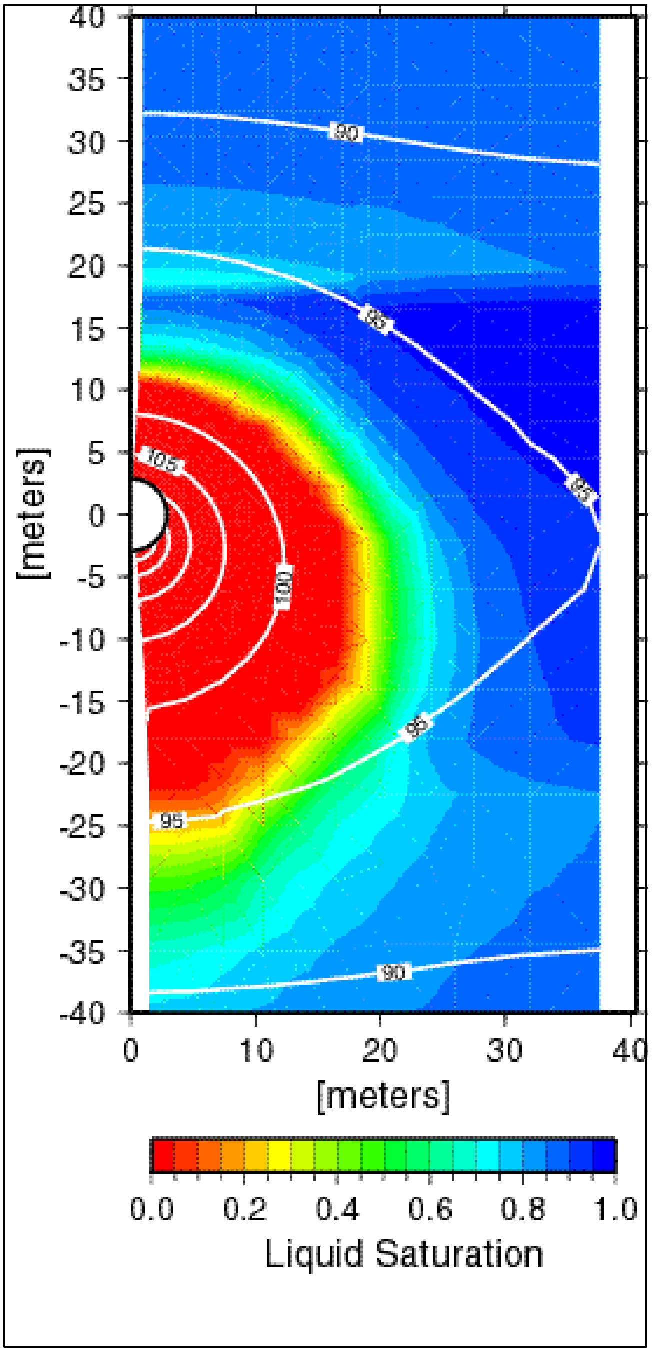

DTN: LB991200DSTTHC.002

Figure 32. TH Simulation (Tptpmn - Backfill). Contour Plot of Modeled Temperatures and Liquid Saturations in the Matrix at 600 Years (Near Maximum Extent of Dryout).

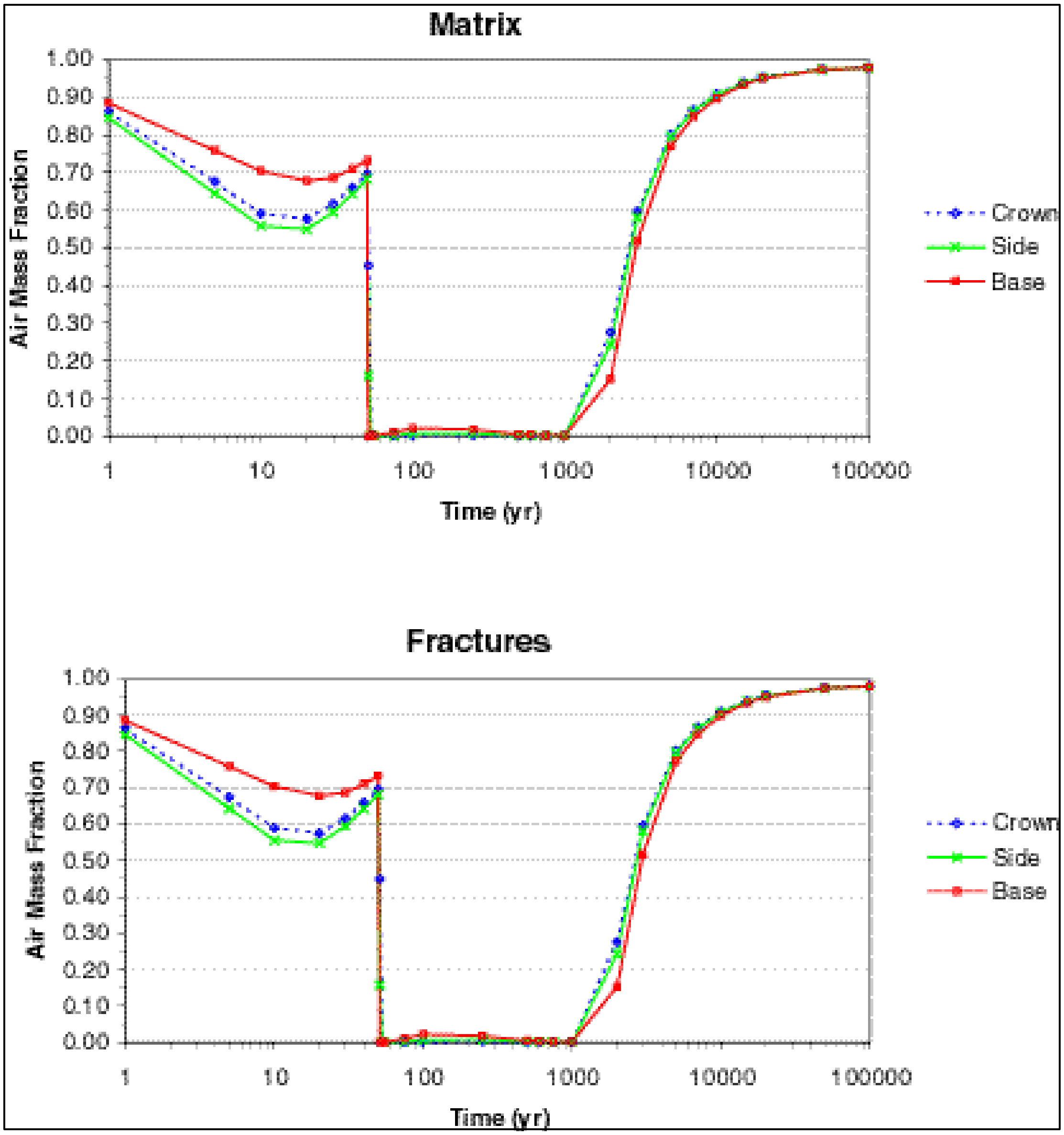

DTN: LB991200DSTTHC.002

Figure 33. TH Simulation (Tptpmn - Backfill). Time Profiles of Modeled Air Mass Fractions in the Gas Phase in Fractures and Matrix at Three Drift-Wall Locations.

6.3.5.2 THC Simulation Results for the Tptpmn THC Backfill Model

Calculated temperatures, liquid saturations, and air mass fractions in fractures around the drift are shown in Figures 34 through 38. These thermohydrologic data are essentially identical for the base-case and the extended-case geochemical systems, so results are presented only for the extended case. The data are shown for the four infiltration scenarios shown in Table 12. Temperatures, liquid saturation, and air mass fractions calculated for the mean infiltration case (6/16/25 mm/year) are directly comparable to those obtained from the TH simulation (Figures 31 through 33) because the latter was carried out using the same infiltration rates. The results of the

TH and THC simulations are essentially identical. As discussed later, the thermal and hydrologic behavior of the system is not significantly affected by mineral precipitation or dissolution. Consequently, temperatures, liquid saturations, and air mass fractions calculated with THC (base and extended cases) and TH simulations are nearly the same. The Tptpmn THC Backfill Model makes use of a simple porosity-permeability coupling model (Equation 18) that may underestimate changes in fracture permeability due to mineral precipitation or dissolution. A more conservative model (i.e. predicting a greater fracture permeability change for a given porosity change) is used for simulations presented in Sections 6.4, 6.5, and 6.6.

The temperature-time profiles for the different infiltration cases (Figure 34) remain within approximately 15°C of each other. The plots also show that the return to ambient temperatures takes about 100,000 years for all infiltration cases. At the drift crown, rewetting of fractures is predicted to occur around the same time period (1,000 to 2,000 years) for all infiltration cases (Figure 35). Matrix rewetting at the drift crown occurs around the same time period as fractures, except for the high infiltration case where the matrix rewets approximately 200 years earlier (Figure 36). The size of the dryout zone (represented by zero matrix saturations) decreases at the highest infiltration rate (Figure 37c), to approximately 6, 12, and 16 meters above, to the side, and below the drift, respectively. The smaller dryout zone in the lowest infiltration case (Figure 37a) compared to the mean infiltration case is apparently the result of the differing rock property sets rather than the infiltration rate. Air mass fractions (Figure 38) are little affected by the different infiltration rates.

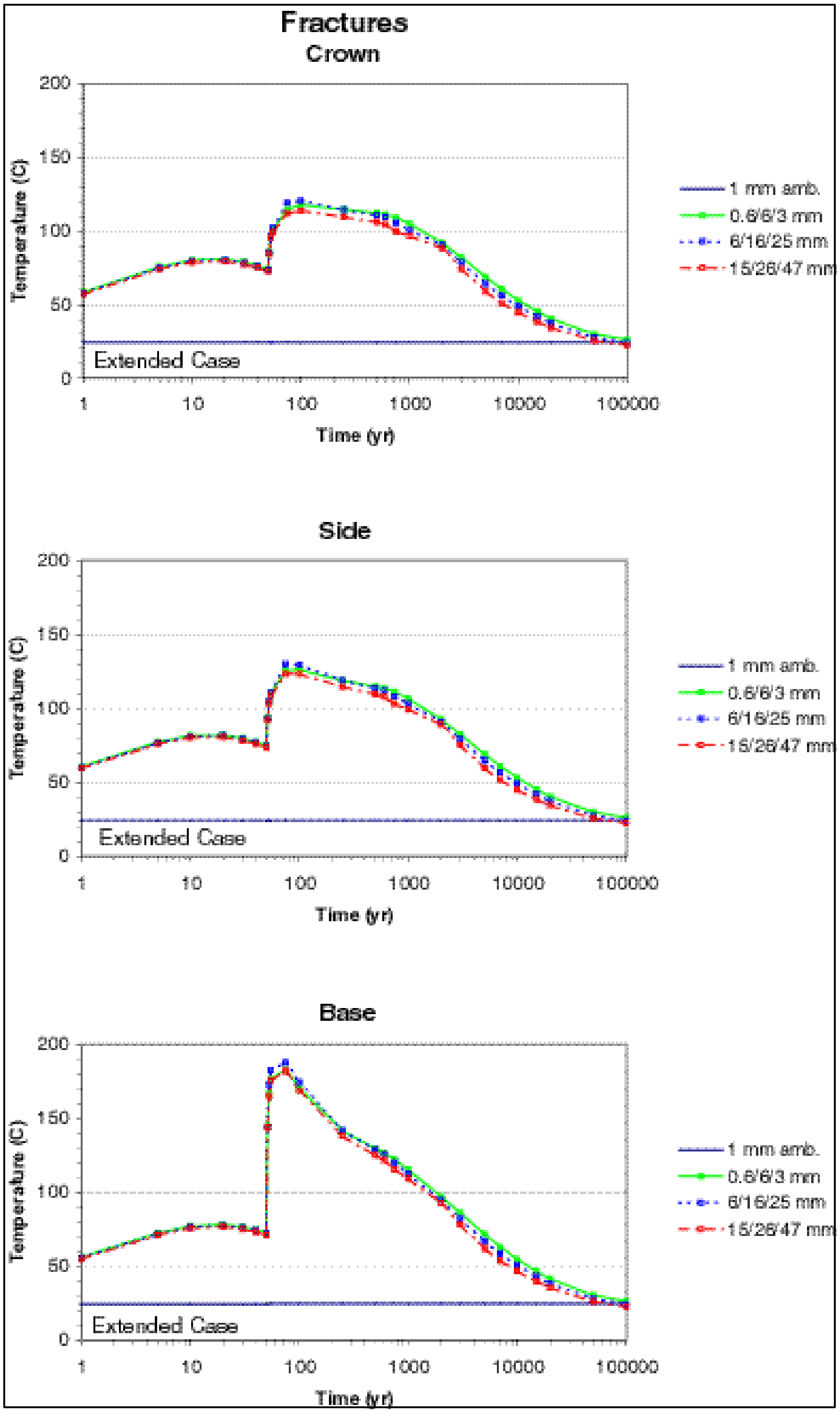

DTN: LB991200DSTTHC.002

Figure 34. THC Simulation (Tptpmn - Backfill). Time Profiles of Modeled Temperatures in Fractures at Three Drift-Wall Locations for Different Climate Scenarios, Extended Case.

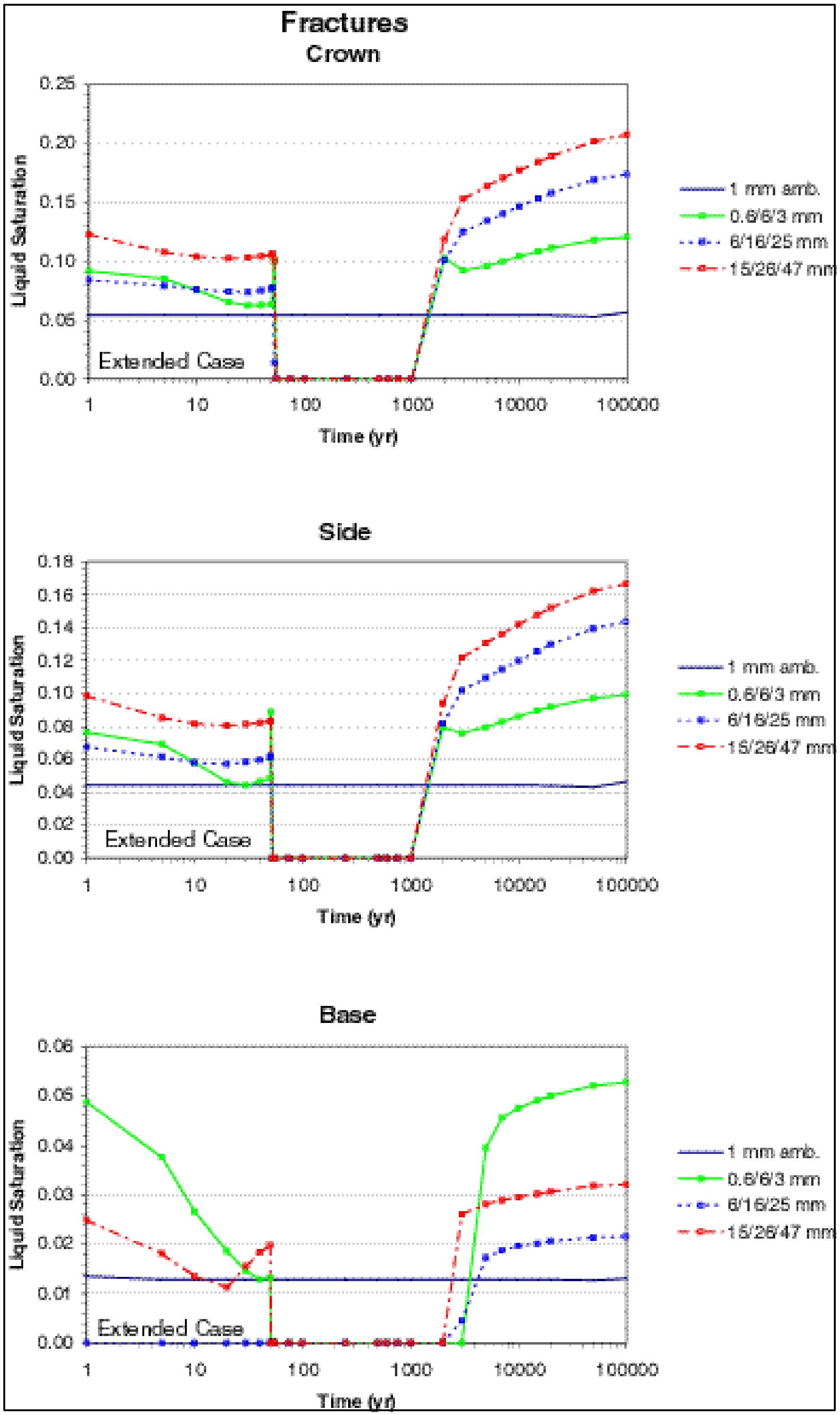

DTN: LB991200DSTTHC.002

Figure 35. THC Simulation (Tptpmn - Backfill). Time Profiles of Modeled Liquid Saturations in Fractures at Three Drift-Wall Locations for Different Climate Scenarios, Extended Case.

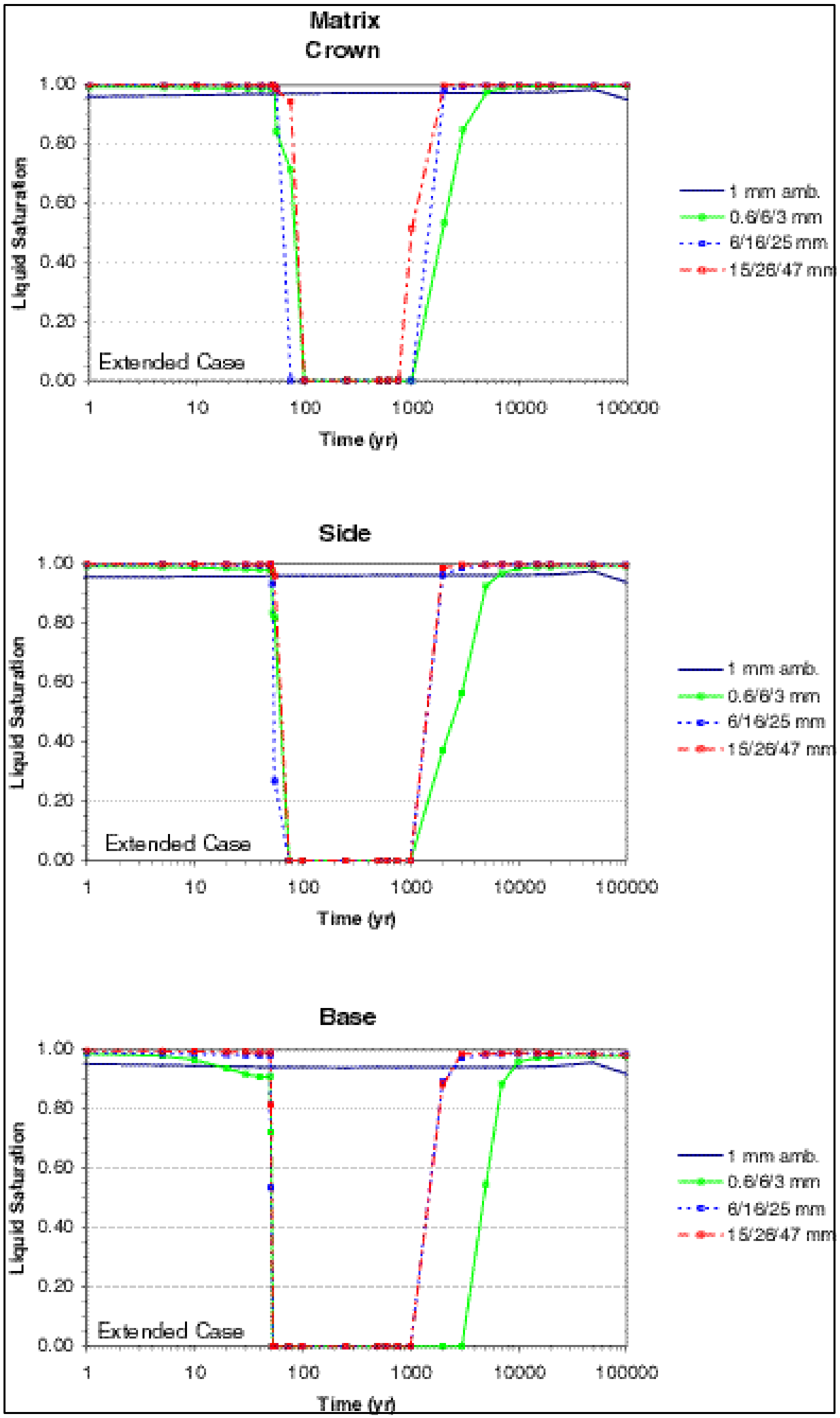

DTN: LB991200DSTTHC.002

Figure 36. THC Simulation (Tptpmn - Backfill). Time Profiles of Modeled Liquid Saturations in the Matrix at Three Drift-Wall Locations for Different Climate Scenarios, Extended Case.

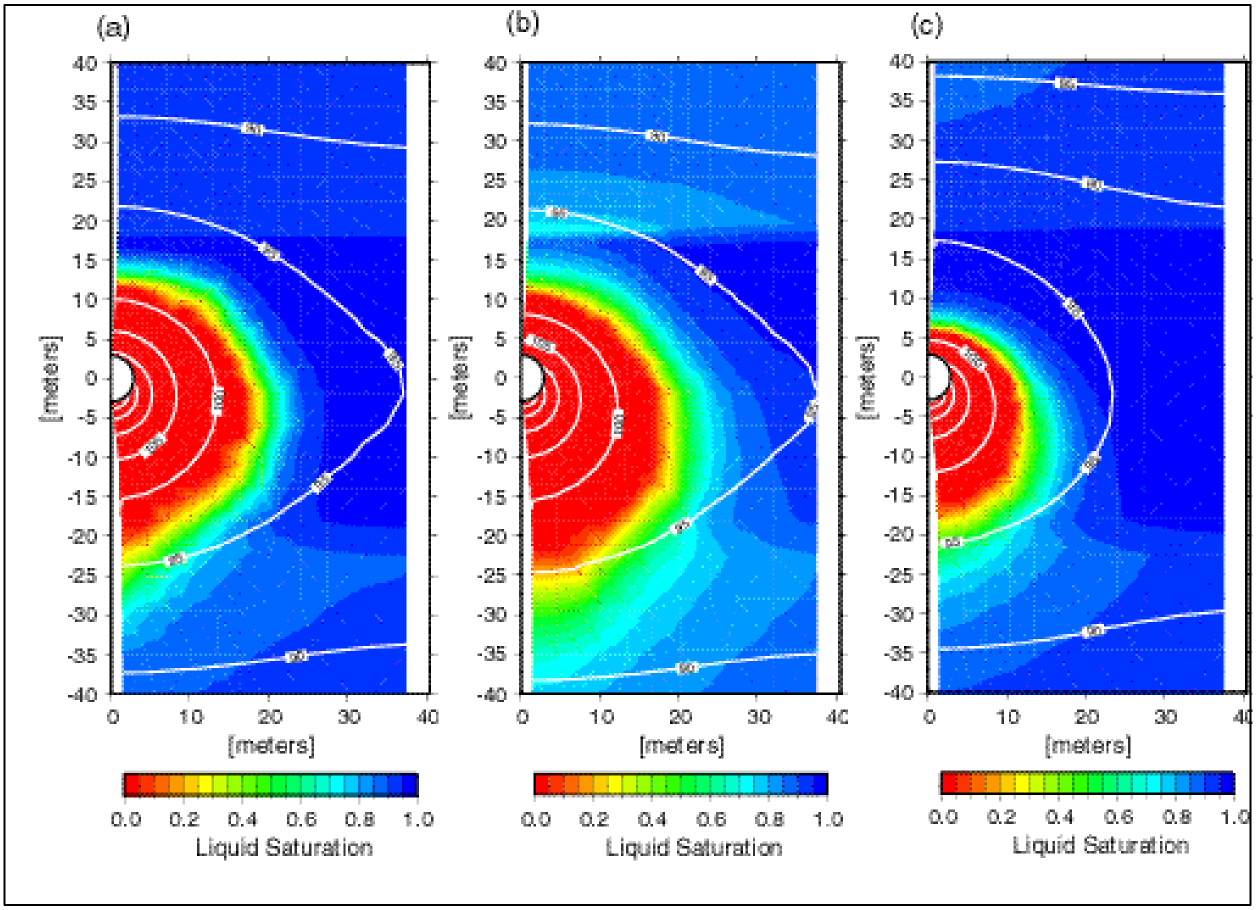

DTN: LB991200DSTTHC.002

Figure 37. THC Simulation (Tptpmn - Backfill). Contour Plot of Modeled Temperatures and Liquid Saturations in the Matrix at 600 Years (Near Maximum Dryout) for Three Climate Scenarios: (a) Lower Bound, (b) Mean, and (c) Upper Bound, Extended Case.

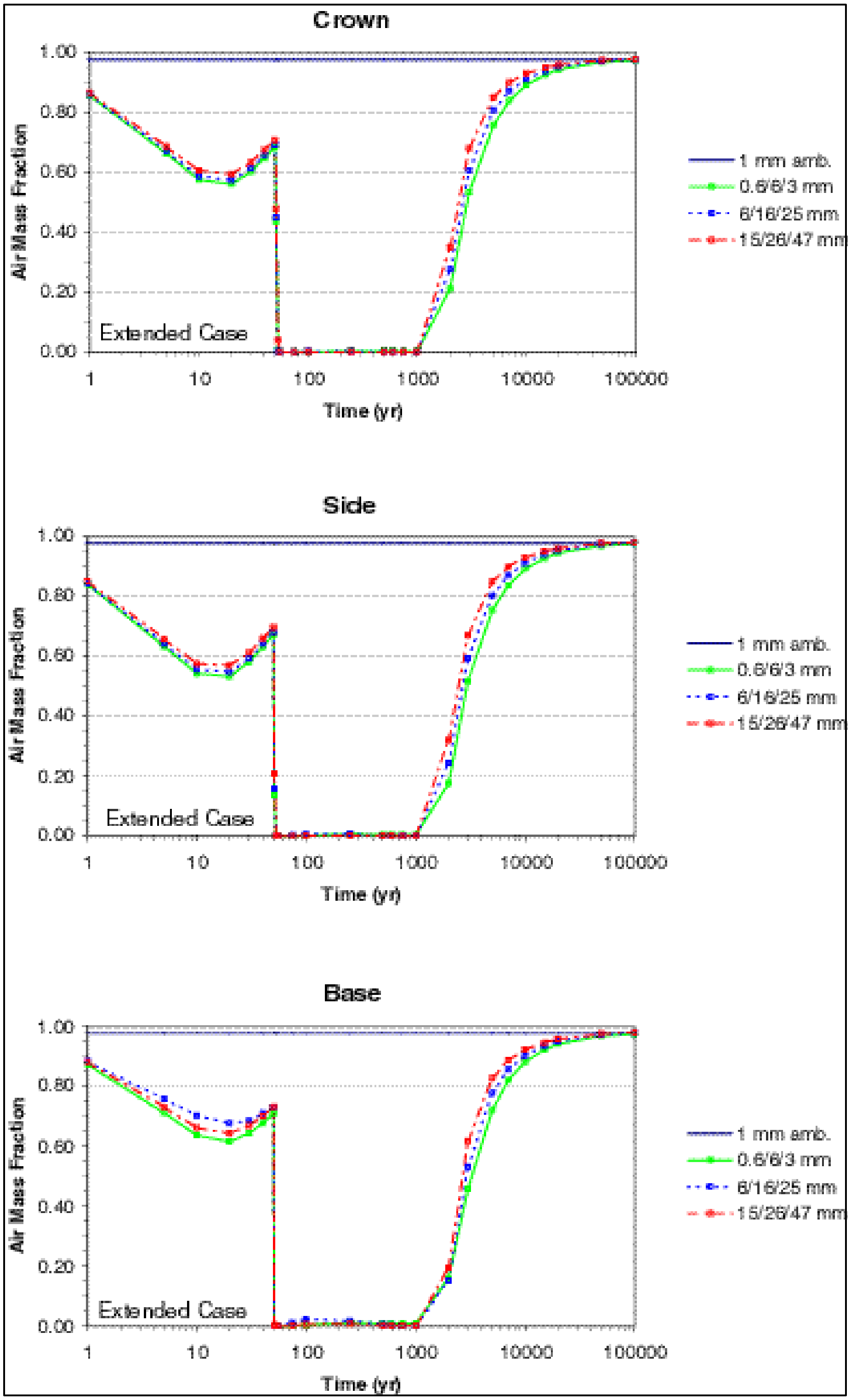

DTN: LB991200DSTTHC.002

Figure 38. THC Simulation (Tptpmn - Backfill). Time Profiles of Modeled Air Mass Fractions in the Gas Phase in Fractures at Three Drift-Wall Locations for Different Climate Scenarios, Extended Case.

Predicted CO_2 concentrations in the gas phase in fractures at equilibrium with the fracture pore water around the drift are shown in Figures 39 and 40 for the base-case and extended-case geochemical systems, respectively. CO_2 concentrations in fractures drop significantly during dryout and increase again during rewetting. In the extended case, the most significant CO_2 concentration increase after rewetting (to approximately 33,000 ppmv) occurs in the low infiltration case. In contrast, with the base case, the largest CO_2 concentration after rewetting (near 12,000 ppmv) occurs for the high infiltration case.

Predicted pH and total aqueous carbonate concentrations (as HCO_3^-) in fracture pore water are shown in Figures 41 through 44. The calculated pH is generally higher for the extended case (approximate range 8.5 to 10) than for the base case (approximate range 7 to 8.5). Total aqueous carbonate concentrations are larger in the extended case (maximum, after rewetting, near 10,000 mg/L for the low infiltration case) than in the base case (near ambient values of 200 mg/L after rewetting). Note that the mean infiltration case (6/16/25 mm) dries out before one year, so that no results are shown until rewetting.

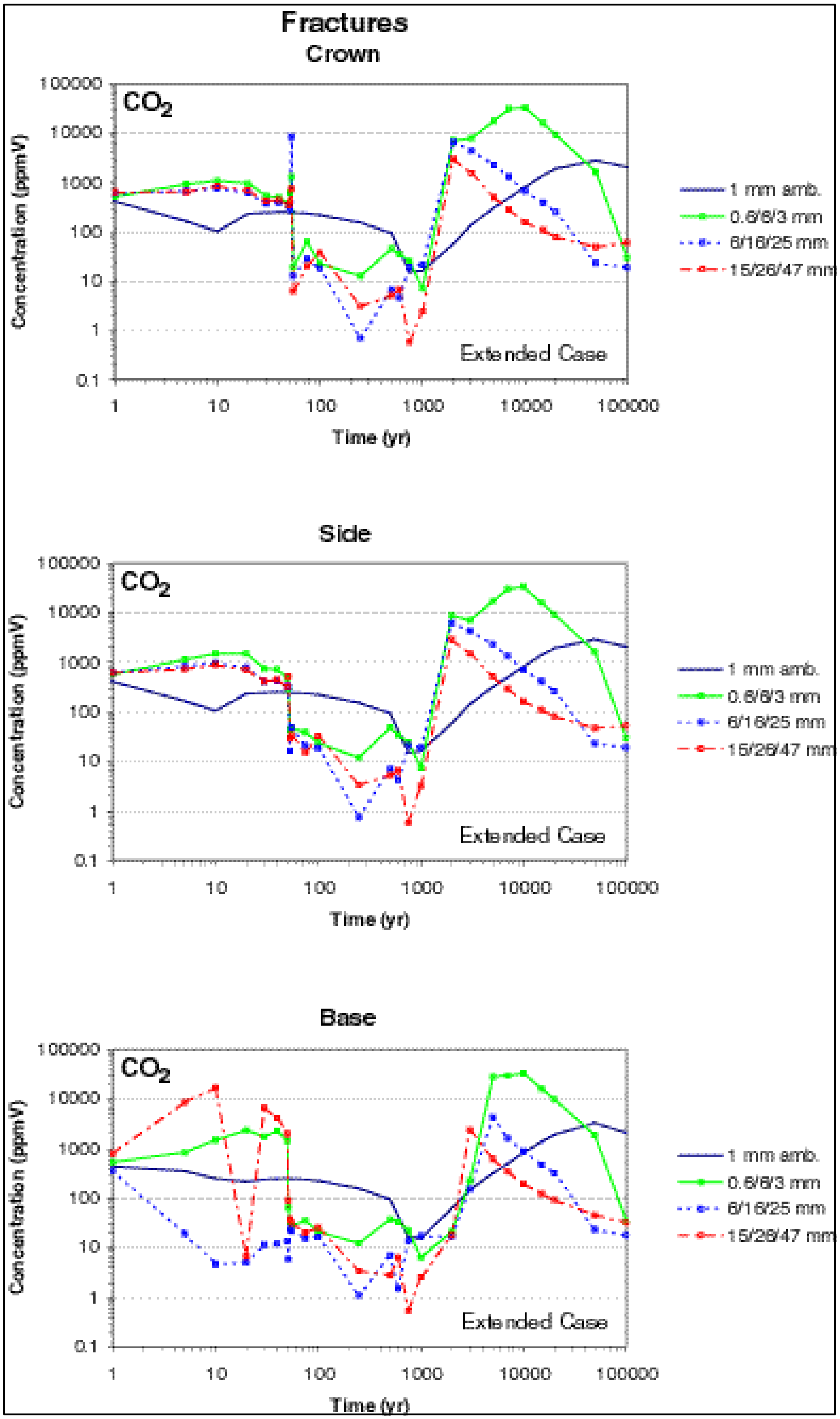

DTN: LB991200DSTTHC.002

Figure 39. THC Simulation (Tptpmn - Backfill). Time Profiles of Modeled CO_2 Concentrations in the Gas Phase in Fractures at Three Drift-Wall Locations for Different Climate Scenarios, Extended Case.

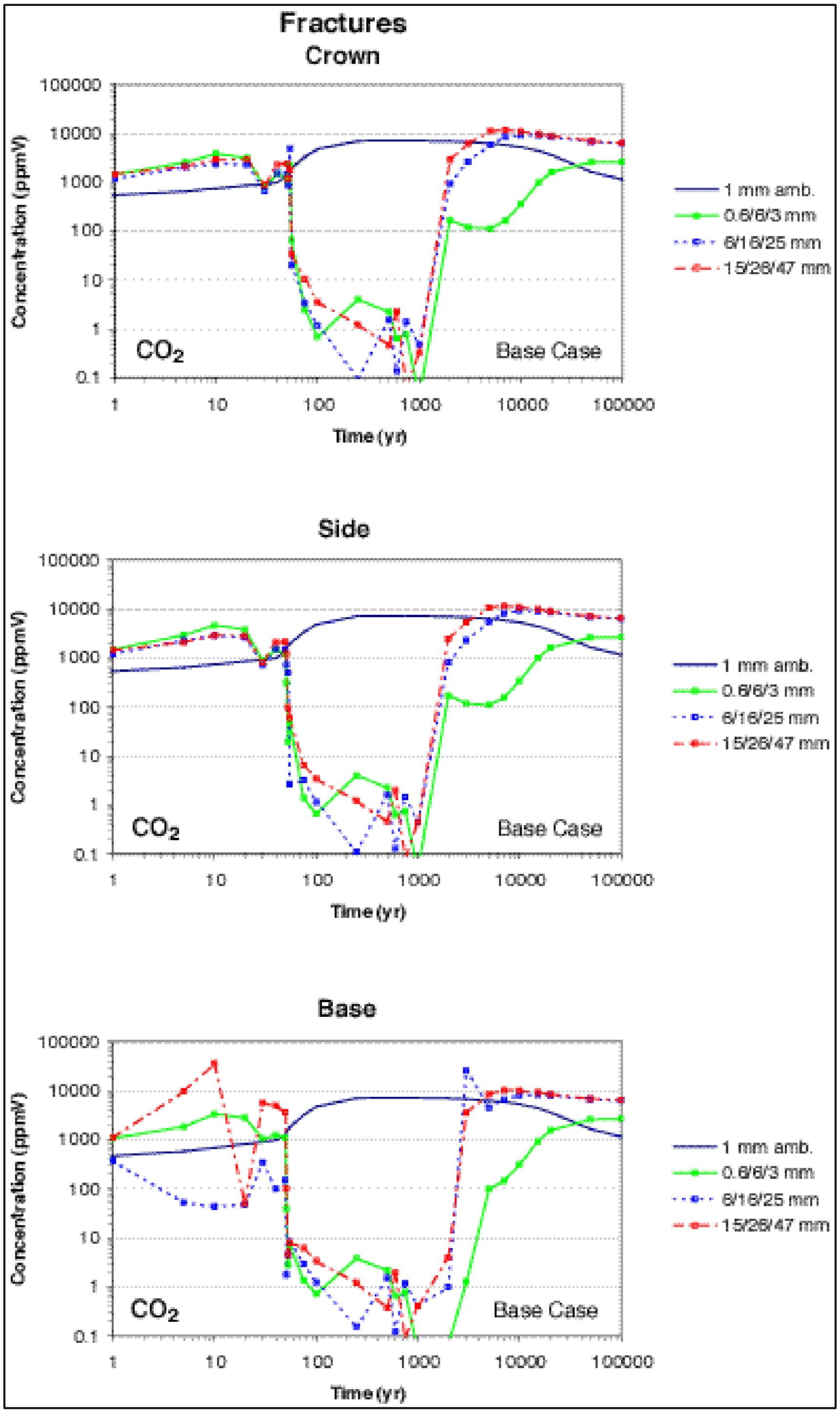

DTN: LB991200DSTTHC.002

Figure 40. THC Simulation (Tptpmn - Backfill). Time Profiles of Modeled CO_2 Concentrations in the Gas Phase in Fractures at Three Drift-Wall Locations for Different Climate Scenarios, Base Case.

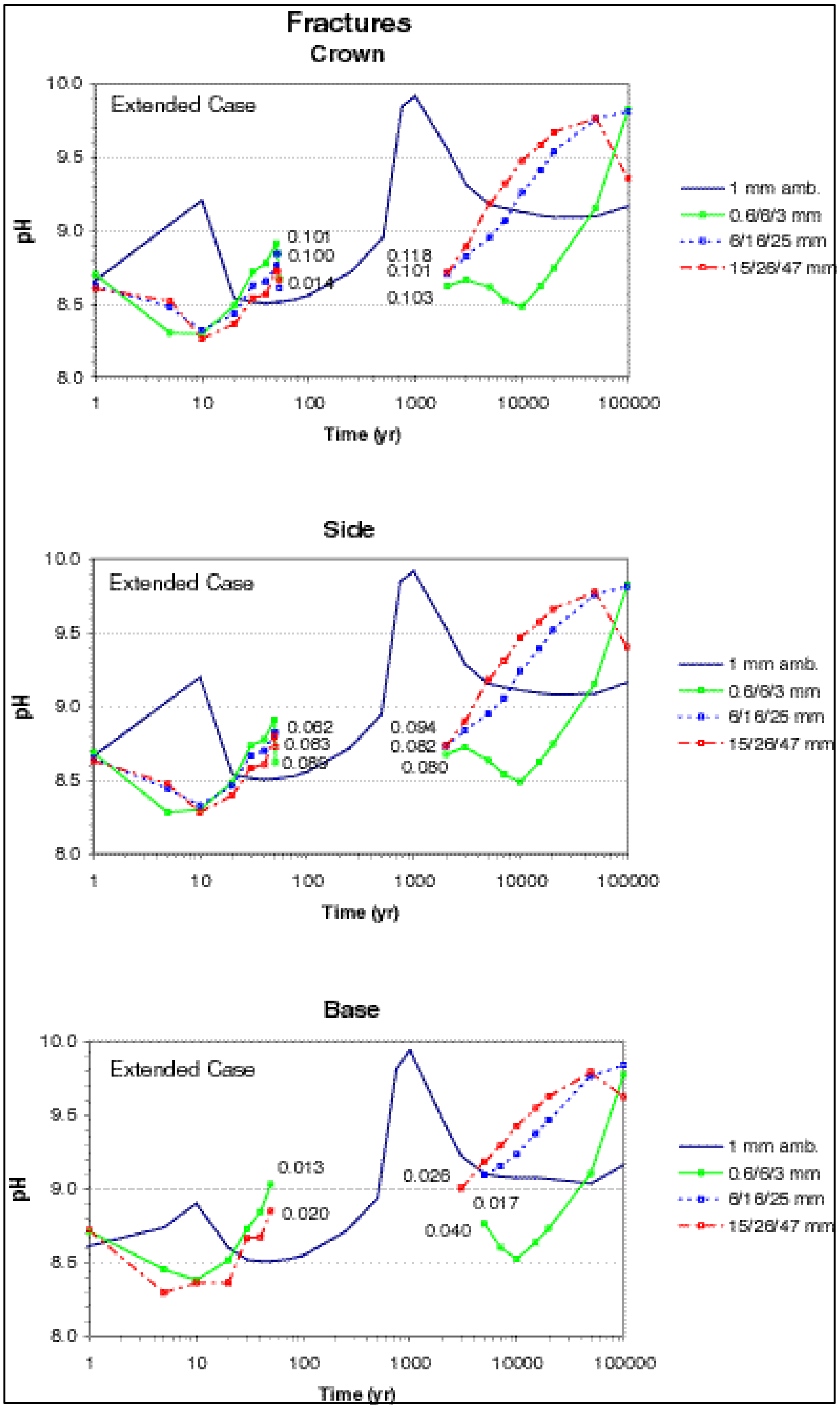

DTN: LB991200DSTTHC.002

Figure 41. THC Simulation (Tptpmn - Backfill). Time Profiles of the Modeled pH of Fracture Water at Three Drift-Wall Locations for Different Climate Scenarios (Extended Case). The dryout period is left blank. Numbers by each curve indicate the last output liquid saturation before dryout and the first output liquid saturation during rewetting.

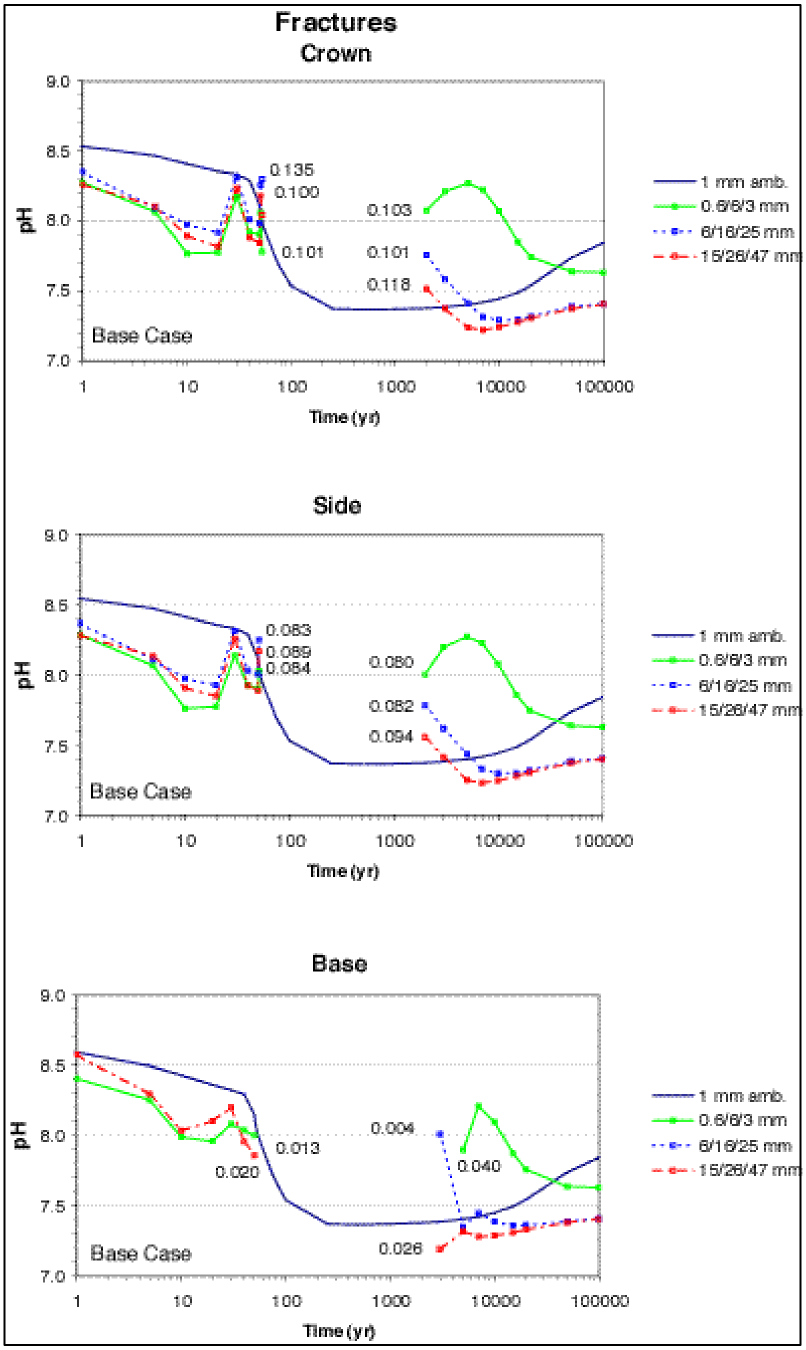

DTN: LB991200DSTTHC.002

Figure 42. THC Simulation (Tptpmn - Backfill). Time Profiles of the Modeled pH of Fracture Water at Three Drift-Wall Locations for Different Climate Scenarios (Base Case). Designations denoted in Figure 41.

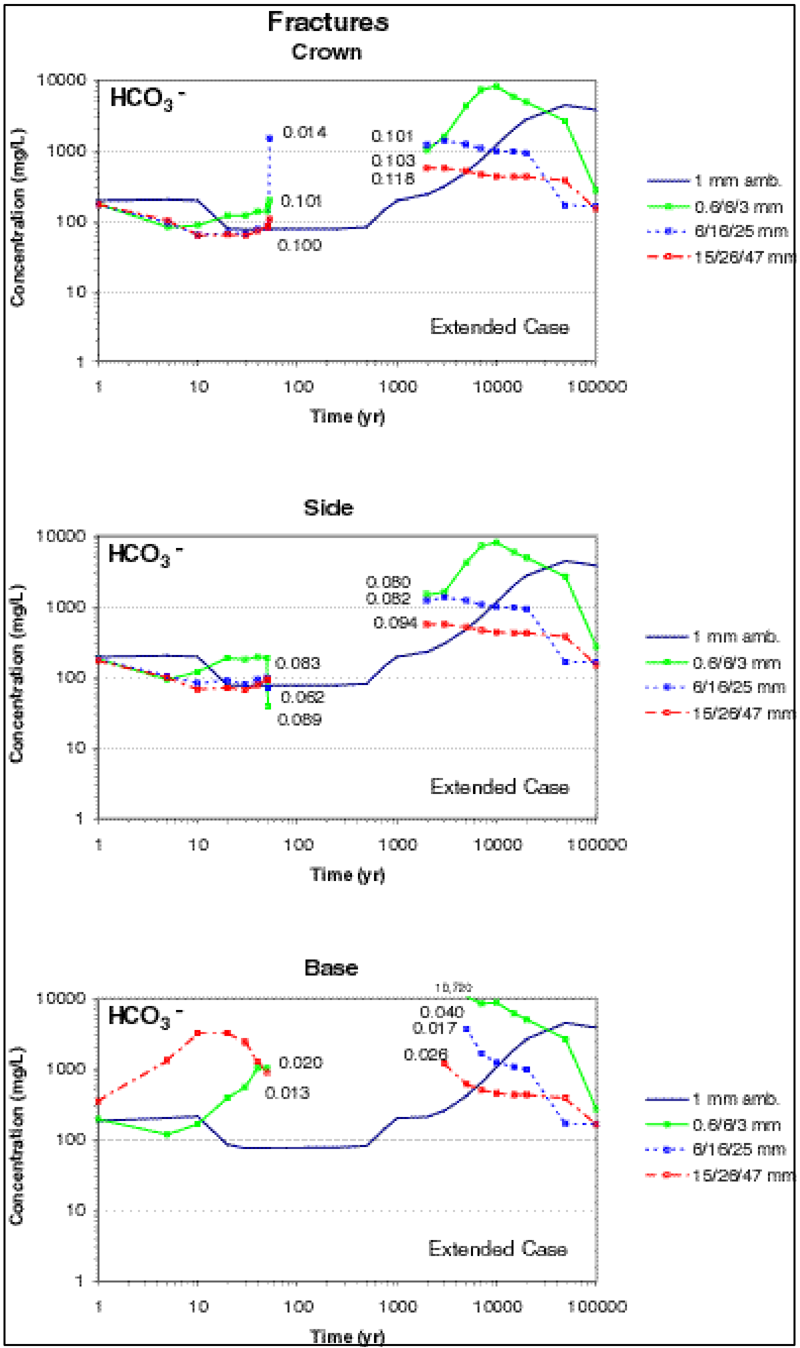

DTN: LB991200DSTTHC.002

Figure 43. THC Simulation (Tptpmn - Backfill). Time Profiles of Modeled Total Aqueous Carbonate Concentrations (as HCO_3^-) in Fracture Water at Three Drift-Wall Locations for Different Climate Scenarios (Extended Case). Designations denoted in Figure 41.

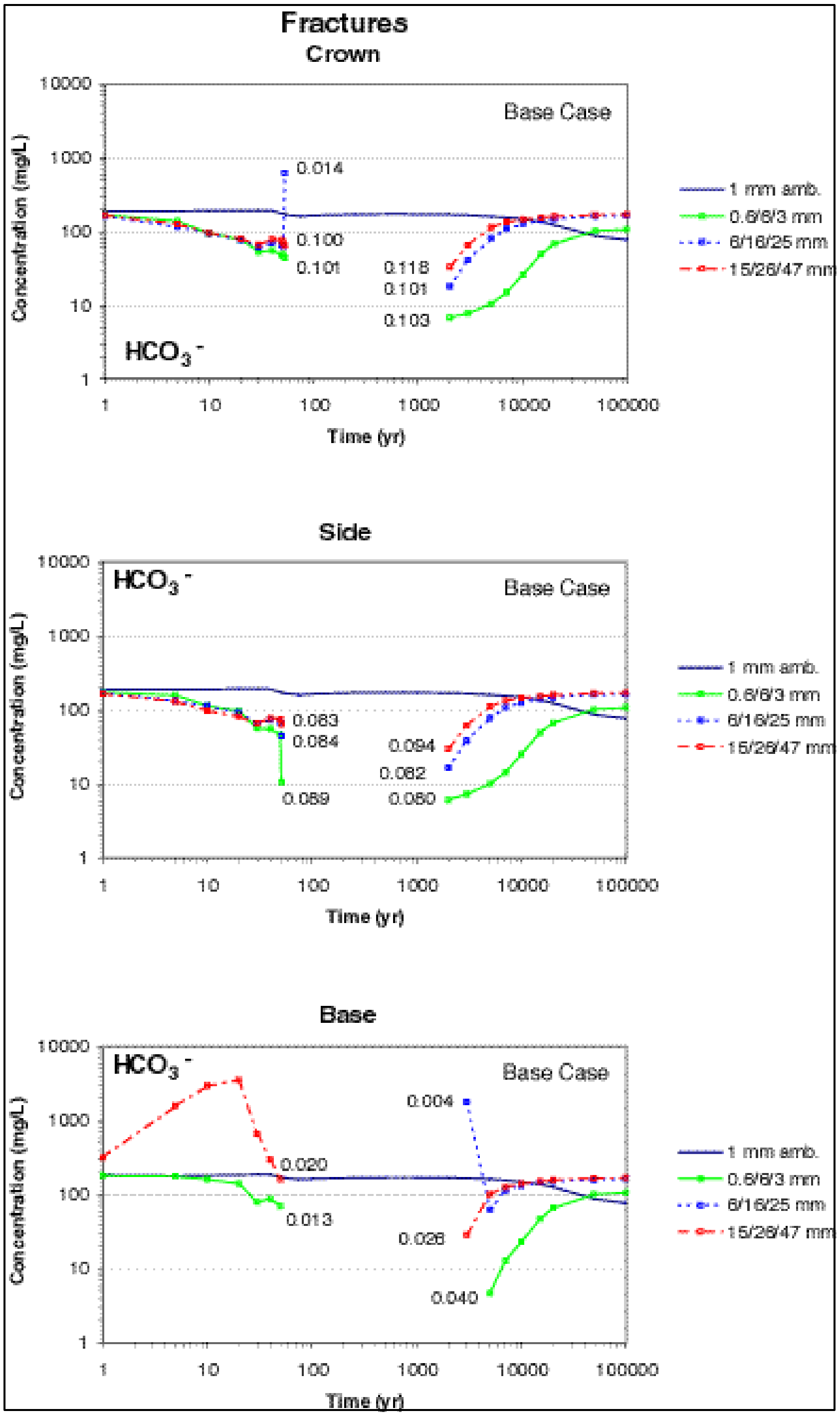

DTN: LB991200DSTTHC.002

Figure 44. THC Simulation (Tptpmn - Backfill). Time Profiles of Modeled Total Aqueous Carbonate Concentrations (as HCO_3^-) in Fracture Water at Three Drift-Wall Locations for Different Climate Scenarios (Base Case). Designations denoted in Figure 41.

The pH-carbonate-CO_2 data show very different trends depending upon whether the base-case or extended-case mineral assemblage is considered. This results from competing effects, depending on the relative rates of infiltration, calcite dissolution/precipitation, feldspar dissolution, and calcium-zeolite and clay precipitation. Extended-case simulations are quite sensitive to the effective reaction rates of aluminum silicate minerals and particularly calcium zeolites. The dissolution of feldspars to form zeolites and clays directly affects the pH. For example, the dissolution of albite (a sodium feldspar) to form sodium smectite (a clay) results in an increase in pH (decrease in H^+ activity), as follows:

$$2.33NaAlSi_3O_8 \text{ (albite)} + 2H^+ ==>$$

$$Na_{0.33}Al_{2.33}Si_{3.67}O_{10}(OH)_2 \text{ (smectite)} + 3.32SiO_2 + 2Na^+$$

The dissolution of albite and calcite to form stellerite (a calcium zeolite) affects pH directly through consumption of H^+ (from calcite dissolution at intermediate pH) and indirectly by depleting calcium from solution. The latter effect inhibits calcite precipitation as a means of controlling increasing pH and total aqueous carbonate concentrations, as in the following reaction:

$$2NaAlSi_3O_8 \text{ (albite)} + SiO_2 + CaCO_3 \text{ (calcite)} + H^+ + 7H_2O ==>$$

$$CaAl_2Si_7O_{18} \bullet 7H_2O \text{ (stellerite)} + 2Na^+ + HCO_3^-.$$

As a result, simulations with the extended geochemical system generally yield higher pH and total aqueous carbonate concentrations, and generally lower CO_2 partial pressures than with the base-case system. Calcium depletion and increased sodium concentrations (Figure 45 and 47) are further indicators of feldspar (albite) dissolution and calcium zeolite precipitation with the extended system. These trends are not observed with the base-case system (Figures 46 and 48).

In the extended-case simulations for the Tptpmn THC Backfill Model, calcium depletion, increasing sodium concentrations, and large CO_2, pH and carbonate concentration variations calculated under ambient conditions provide evidence that feldspar dissolution rates and precipitation rates for zeolites and clay may be overestimated. Variations in CO_2, pH, and carbonate under ambient flow conditions are more pronounced with the extended geochemical system than with the base-case system, and these variations reflect an initially “unsteady” hydrochemical system. Therefore, concentration variations in these figures cannot be attributed to repository effects alone, and must be carefully evaluated. Obtaining an initial “steady-state” hydrochemical system yielding aqueous-species concentrations consistent with measured data (available only for a few points) is difficult because the steadiness of the system depends on reaction rates (as well as infiltration rates and rock properties). The difficulty in reaching a chemical steady state increases with the number of reactive minerals included in the system because each additional mineral adds its own uncertainty in reaction rate to the total model uncertainty (thus explaining why calculated concentration trends under ambient flow conditions are more variable for the extended case than for the base-case geochemical system). A “steadier” ambient hydrochemical system than the one presented here was achieved (by revising some of the thermodynamic data and input water/gas compositions) in more recent simulations presented in Sections 6.4 through 6.6.

Given this model uncertainty with respect to reaction rates and the difficulty in reproducing an initially balanced hydrogeochemical system, a more limited set of minerals with better-constrained reaction rates such as for the base-case system may tend to predict pH, bicarbonate, and Ca better than a more complex system. This is shown with simulations of the DST (Section 6.2.7), which indicate that the base-case geochemical system provides better estimates of pH and possibly CO_2 concentrations than the extended case, compared to waters and gases collected in the first 32 months of heating. The more recent simulations (with a better constrained extended system) presented in Section 6.4 show CO_2 concentrations, pH, and total aqueous carbonate concentrations having smaller maximum values (during the cooling phase), than shown in Figures 39, 41, and 43. These simulations do not result in the large sodium concentration increase and calcium depletion shown in Figures 45 and 47.

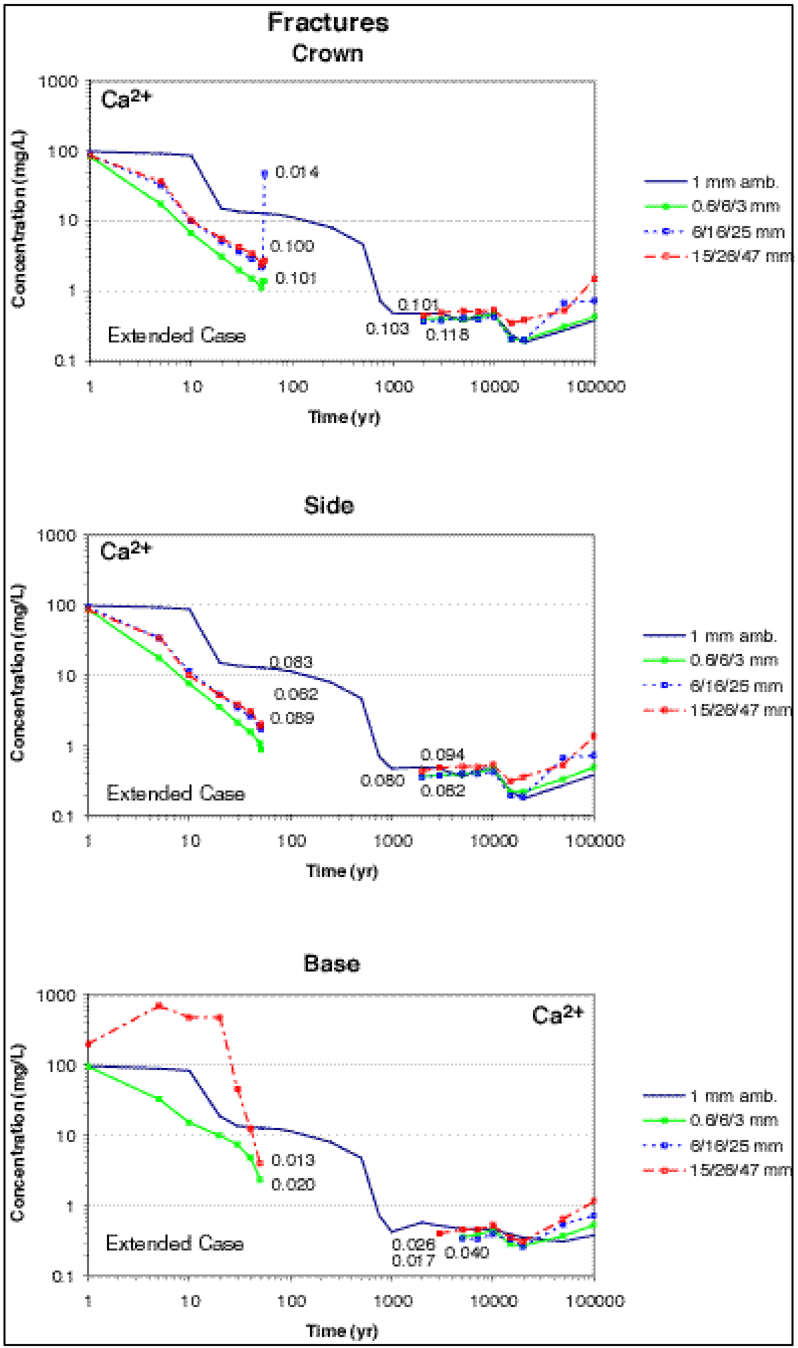

DTN: LB991200DSTTHC.002

Figure 45. THC Simulation (Tptpmn - Backfill). Time Profiles of Modeled Total Aqueous Calcium Concentrations in Fracture Water at Three Drift-Wall Locations for Different Climate Scenarios (Extended Case). Designations denoted in Figure 41.

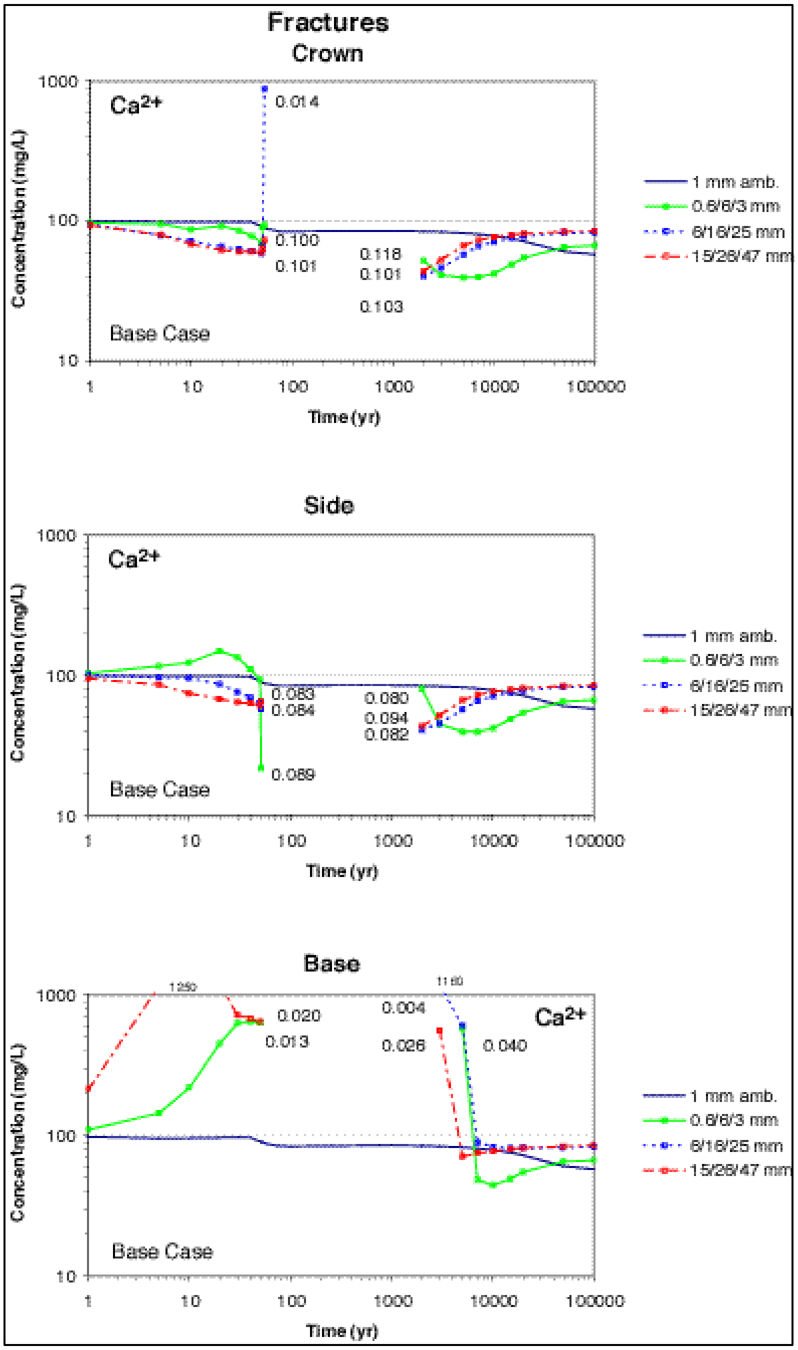

DTN: LB991200DSTTHC.002

Figure 46. THC Simulation (Tptpmn - Backfill). Time Profiles of Modeled Total Aqueous Calcium Concentrations in Fracture Water at Three Drift-Wall Locations for Different Climate Scenarios (Base Case). Designations denoted in Figure 41.

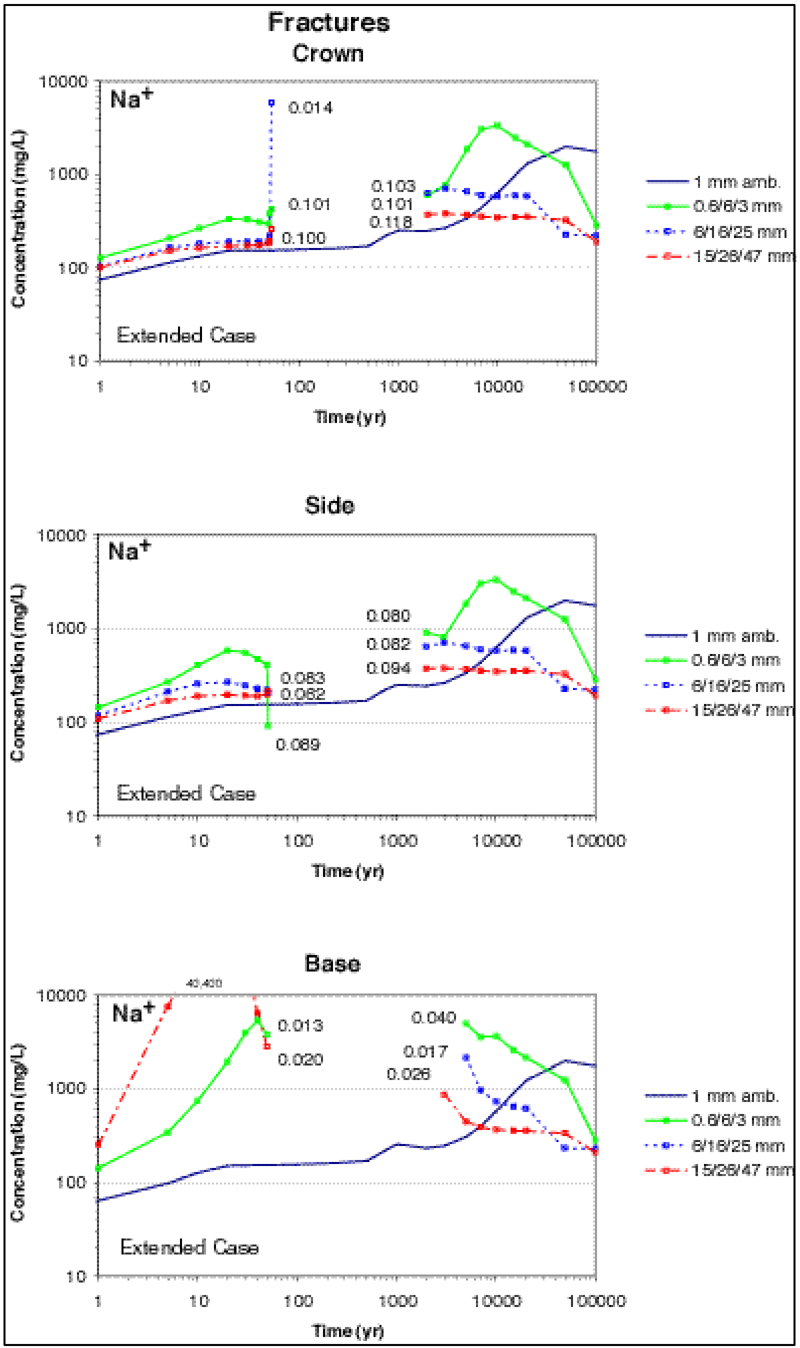

DTN: LB991200DSTTHC.002

Figure 47. THC Simulation (Tptpmn - Backfill). Time Profiles of Modeled Total Aqueous Sodium Concentrations in Fracture Water at Three Drift-Wall Locations for Different Climate Scenarios (Extended Case). Designations denoted in Figure 41.

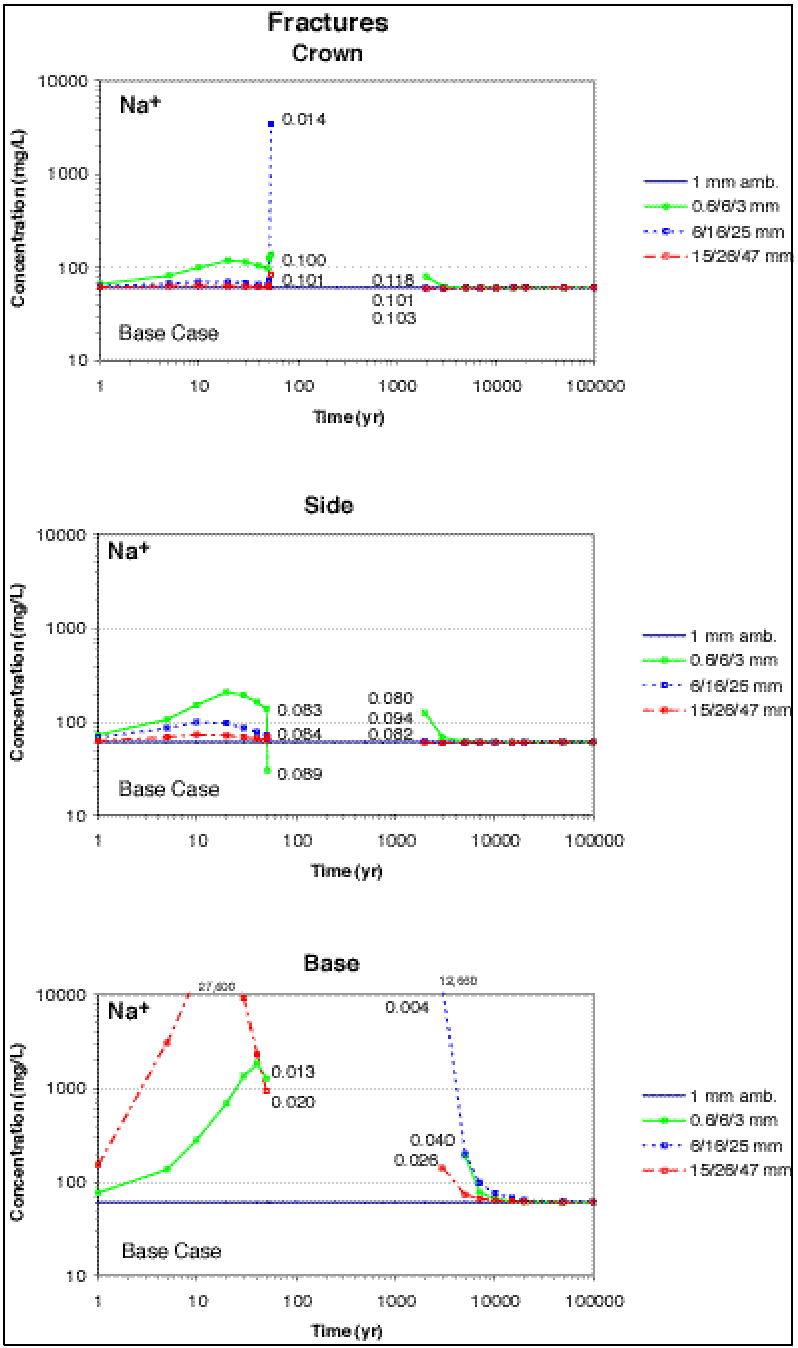

DTN: LB991200DSTTHC.002

Figure 48. THC Simulation (Tptpmn - Backfill). Time Profiles of Modeled Total Aqueous Sodium Concentrations in Fracture Water at Three Drift-Wall Locations for Different Climate Scenarios (Base Case). Designations denoted in Figure 41.

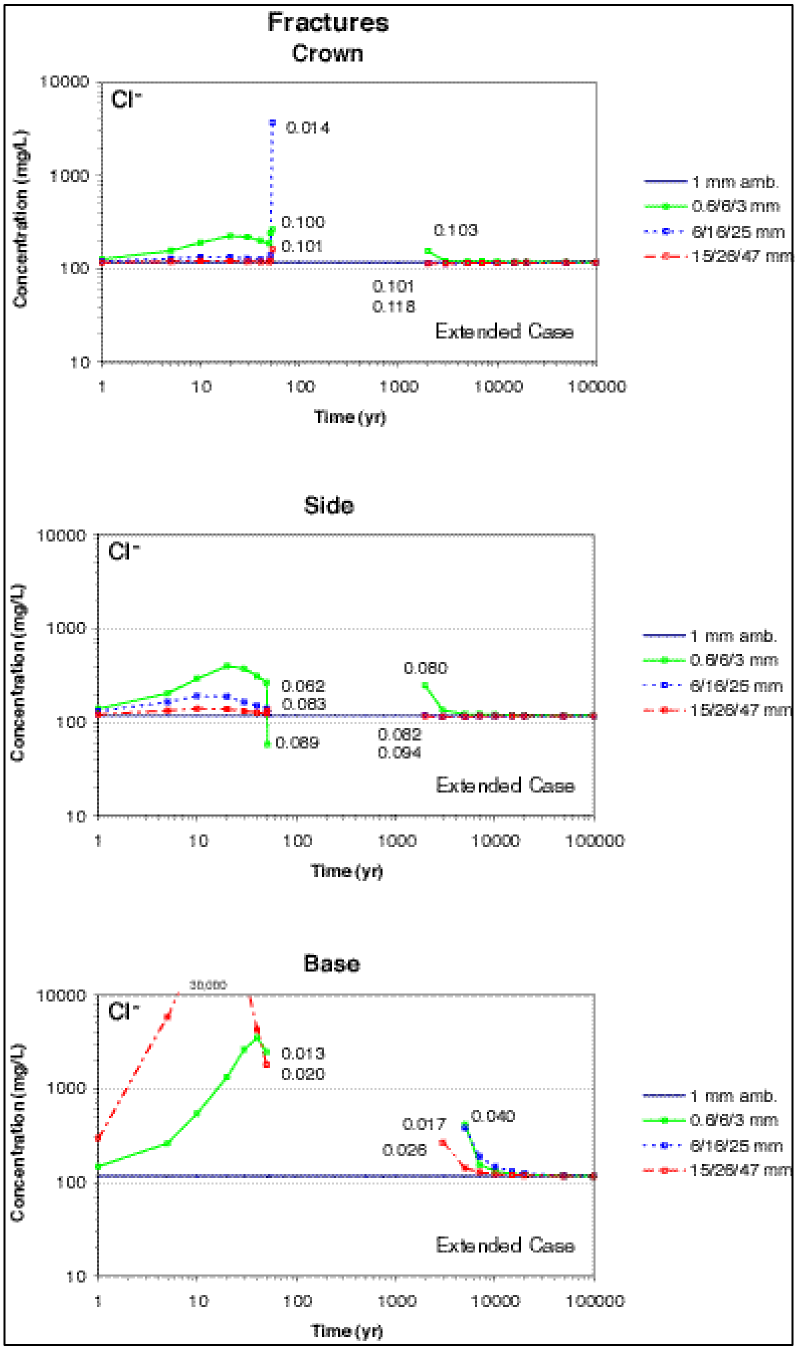

DTN: LB991200DSTTHC.002

Figure 49. THC Simulation (Tptpmn - Backfill). Time Profiles of Modeled Total Aqueous Chloride Concentrations in Fracture Water at Three Drift-Wall Locations for Different Climate Scenarios (Extended Case). Designations denoted in Figure 41.

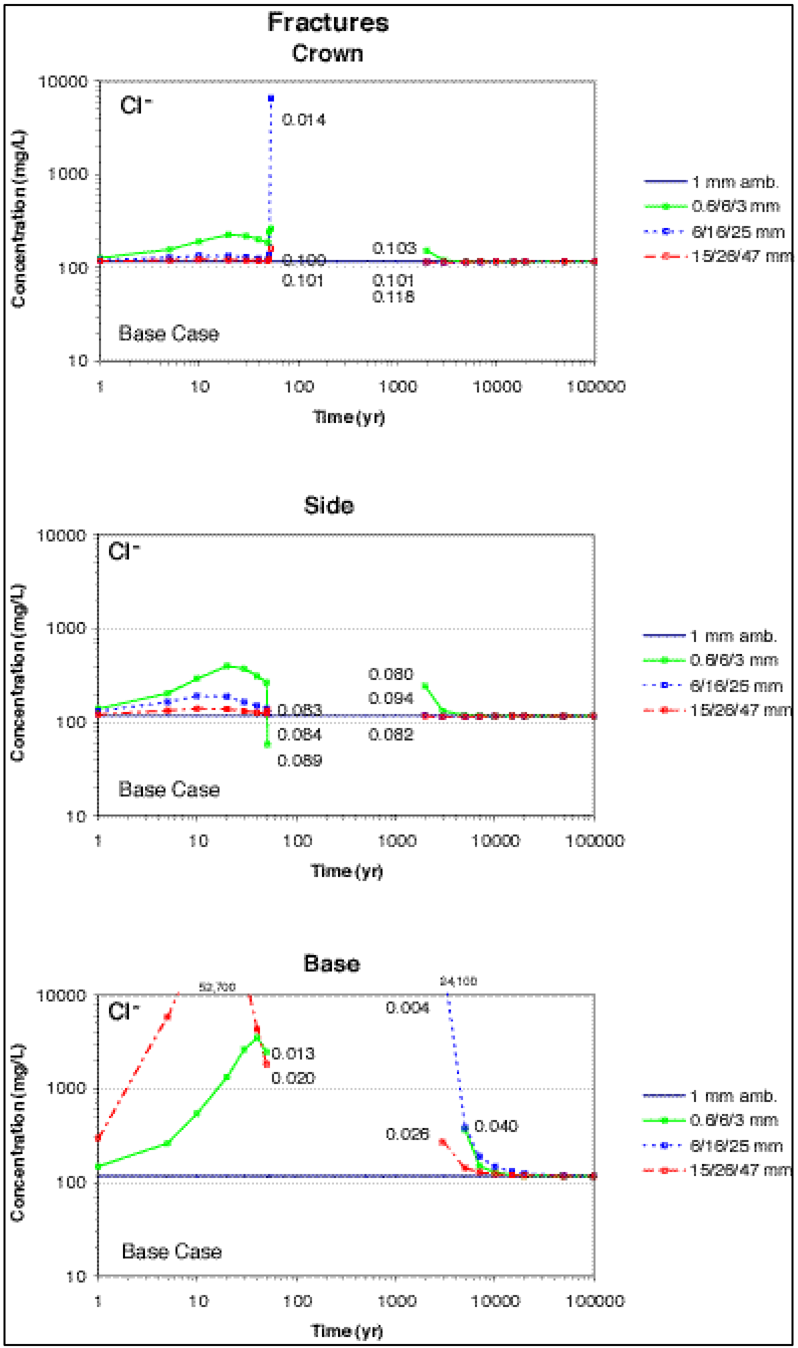

DTN: LB991200DSTTHC.002

Figure 50. THC Simulation (Tptpmn - Backfill). Time Profiles of Modeled Total Aqueous Chloride Concentrations in Fracture Water at Three Drift-Wall Locations for Different Climate Scenarios (Base Case). Designations denoted in Figure 41.

Chloride concentrations computed for the base case and the extended case in fracture water are essentially identical because of the conservative behavior of this aqueous species (i.e. it is not affected by pH or the reaction rates of other minerals in the simulation) (Figures 49 and 50). Differences in the concentration peaks at the drift base between the base case and the extended-case result from a slight difference in the times when the geochemical calculation cutoff point was reached. In this model, the cutoff point is reached at either a minimum liquid saturation of 0.0001 or a maximum ionic strength of 2 molal (Section 5, Assumption A-17), at which point geochemical speciation calculations are suspended in that grid node. Upon rewetting, chloride concentrations drop relatively quickly below 400 mg/L, towards ambient values near 110 mg/L.

In this model, fluoride was included only in the extended-case simulations. Upon rewetting, fluoride concentrations in fracture water (Figure 51) quickly drop below 2 mg/L towards ambient values of less than 1 mg/L. In this chemical system, at intermediate to high pH, fluoride concentrations are not affected significantly by pH. Therefore, the differences between base-case and extended-case simulations should not affect fluoride concentrations, at least at values below the solubility of fluorite (CaF_2). However, at elevated fluoride concentrations, extended-case simulations (for this model) may overestimate fluoride concentrations because they may underestimate the amount of calcium in solution. Hence, this limits the precipitation of fluorite and removal of fluoride from solution. In simulations presented in Section 6.4.5.2, fluoride is included in both a base case and better-constrained extended geochemical system, and displays nearly identical behavior in both systems. It should be remembered that no fluorite is present as a primary mineral here. In the Tptpll simulations presented in Section 6.6.5.2, fluorite is included as a mineral in the repository host rock, causing larger fluoride concentrations to be predicted during the cooling phase than here.

The calculated change in fracture porosity in the vicinity of the drift was contoured for the extended case (Figure 52a-c) and the base case (Figure 53a-c) for the three infiltration scenarios considered, at a simulated time of 10,000 years. The maximum porosity reduction (negative in the plots) occurs for the high infiltration case and is predominantly above the drift, adjacent to the tsw33 and tsw34 hydrogeologic unit contact. In all cases, the porosity change is small (less than 0.5 percent of the initial fracture porosity of 0.01) and mostly negative. The porosity decrease results primarily from zeolite precipitation in the extended case and calcite precipitation in the base case. Because the porosity changes are small, and thus permeability changes are also minor, thermohydrological processes are not significantly affected by mineral precipitation or dissolution. As noted earlier, this model is likely to underestimate both the amount of secondary mineral precipitation (such as amorphous silica) and the change in permeability due to mineral precipitation and dissolution. In the following sections, simulations yielding more mineral precipitation and incorporating a stronger coupling of porosity to permeability are presented. However, even in these cases, the resulting effect of mineral precipitation on fluid flow remains essentially negligible. Note that small fluctuations in porosity at individual grid nodes in Figures 52 and 53 are due to grid orientation effects but do not change the overall pattern.

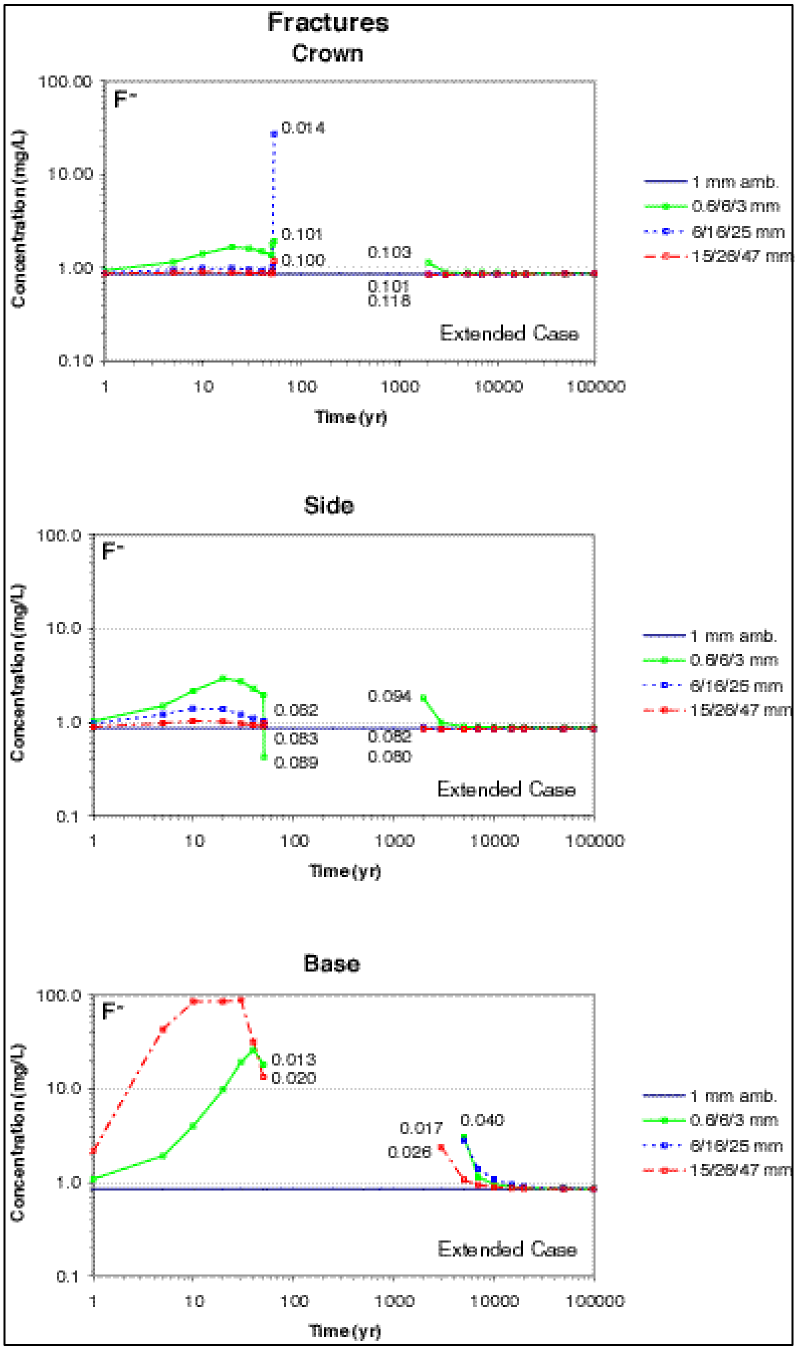

DTN: LB991200DSTTHC.002

Figure 51. THC Simulation (Tptpmn - Backfill). Time Profiles of Modeled Total Aqueous Fluoride Concentrations in Fracture Water at Three Drift-Wall Locations for Different Climate Scenarios (Extended Case). Designations denoted in Figure 41.

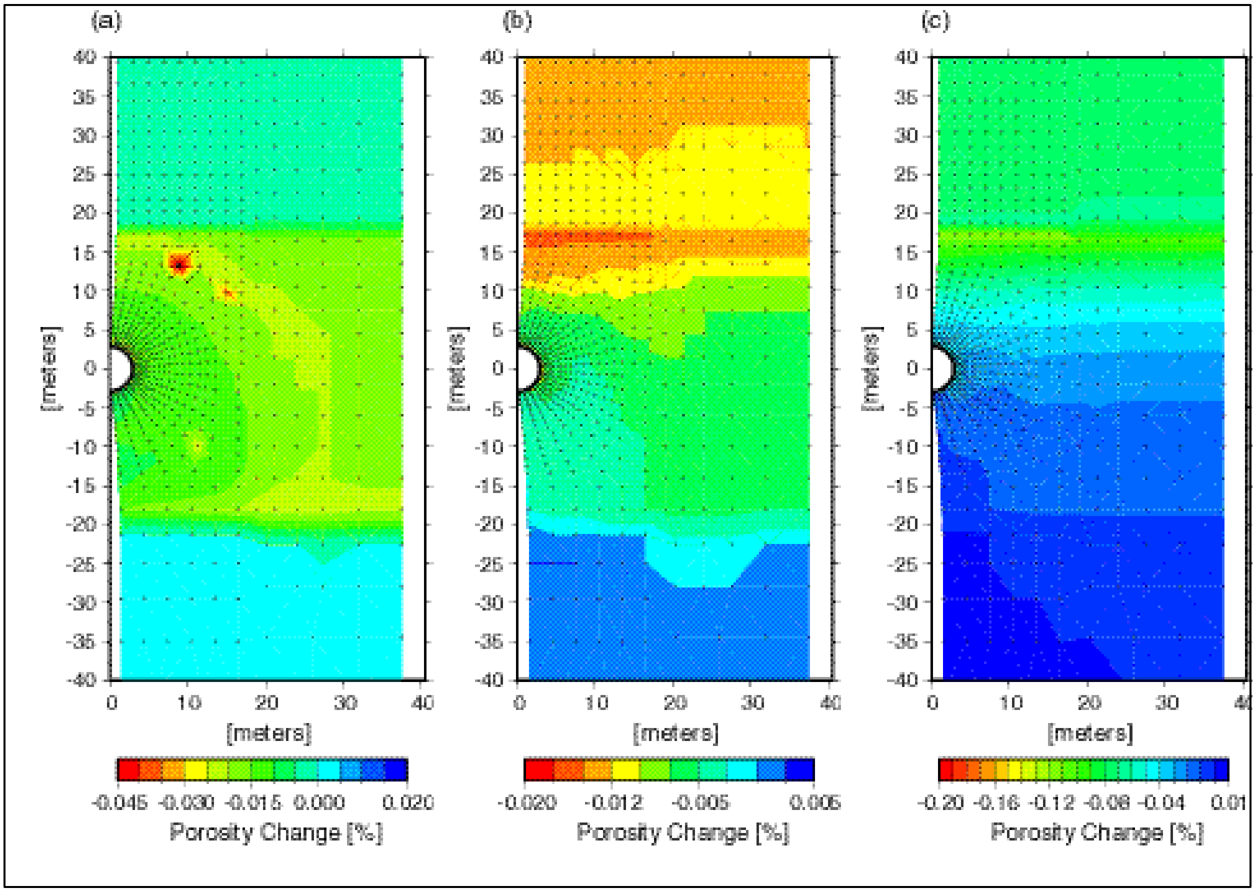

DTN: LB991200DSTTHC.002

Figure 52. THC Simulation (Tptpmn - Backfill). Contour Plot of Modeled Fracture Porosity Change at 10,000 Years for Three Climate Scenarios: (a) Lower Bound, (b) Mean, and (c) Upper Bound. Red areas indicate maximum decrease in porosity due to mineral precipitation (extended case).

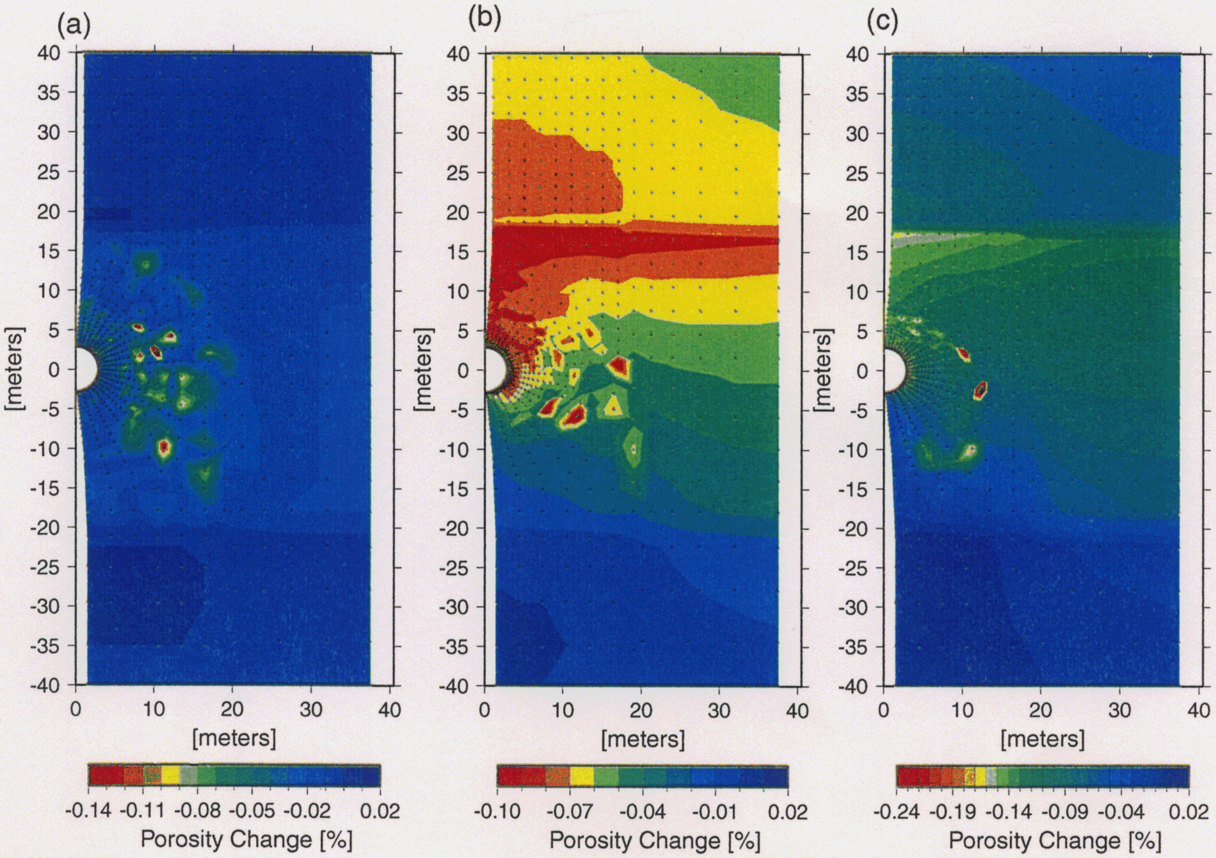

JEH 2/9/01 DTN: LB991200DSTTHC.002

Figure 53. THC Simulation (Tptpmn - Backfill). Contour Plot of Modeled ~~Total~~ Fracture Porosity Change at 10,000 Years for Three Climate Scenarios: (a) Lower Bound, (b) Mean, and (c) Upper Bound. Red areas indicate maximum decrease in porosity due to mineral precipitation (base case).

6.4 Tptpmn THC MODEL (NO BACKFILL)

The Tptpmn THC Model is essentially the same as the Tptpmn THC Backfill Model presented in Section 6.3, with the following significant differences:

- No backfill is placed in the drift
- Slightly lower heat load (1.45 kW/m) (Attachment VIII)
- Revised drift thermal conductivities (invert, inner, and outer zones) (Attachment X)
- Stronger coupling of permeability to porosity changes (Section 6.1.6.2)
- A revised activity-coefficient model for aqueous species (Section 6.1.3), revised thermodynamic and kinetic data (Sections 4.1.4.2 and 4.1.5), and treatment of clay

minerals (smectites) as an ideal solid solution phase rather than individual phases (Section 5, Assumption A-13)

- Calcite at equilibrium with an allowed "supersaturation gap" (Section 6.1.3)
- Increased effective fracture mineral reactive surface areas (over 50% higher; Section 6.1.5.1)
- Increased initial precipitation rate of secondary minerals under kinetic constraints
- Increased CO_2 diffusion coefficient (by a factor of approximately 30)

Changes in the geochemical parameters listed above are related to additions to the TOUGHREACT code from V2.2 [153219] to V2.3 [153101].

6.4.1 Numerical Mesh

For this no-backfill model, the numerical mesh is identical to the mesh described in Section 6.3.1 for simulations with backfill. The drift discretization was unchanged, except that zones previously designated as backfill were assigned thermal properties of the outer zone. Also, the grid nodes corresponding to the invert were reassigned into 'upper invert' and 'lower invert' zones for assignment of different thermal conductivity values (Section 4.1.7.3). The pre-closure and post-closure configurations considered in this seepage model are otherwise similar to previous simulations:

- Pre-closure configuration: waste package, upper invert, lower invert, and one open space between the waste package and the drift wall during the first 50 years.
- Post-closure configuration: waste package, upper invert, lower invert, dripshield, and two open zones: the inner zone, between the waste package and the dripshield; and the outer zone, between the dripshield and drift wall.

The discretization of the drift was kept the same for the two configurations. As such, the pre-closure period was simulated by assigning identical open-space properties to gridblocks representing the inner zone and outer zone.

6.4.2 Boundary Conditions

The boundary conditions imposed on this seepage model (Table 14) were similar to those described in Section 6.3.2, with the exception that the top boundary CO_2 concentration is higher and top boundary water pH lower (and slightly different concentrations of Al, Ca, and carbonate) (Table 3, Section 4.1.3). In addition, the initial full heat load was decreased from 1.54 to 1.45 kW/m to reflect a more recent repository design (CRWMS M&O 2000 [150953], p.20). Only the mean infiltration climate change scenario (Table 12) was considered.

Table 14. Tptpmn THC Model Boundary Conditions (No-Backfill)

Boundary	Boundary Condition	Reference
Top	T = 17.68°C S_g = 0.99 P = 86339 Pa Time-varying infiltration rate (mean infiltration regime only) Constant composition of infiltration and PCO_2	Table 2 Table 2 Table 2 Table 12 Section 4.1.3
Bottom	T = 31.68°C S_L = 0.99999 P = 92000 Pa Constant water composition and PCO_2	Table 2 Table 2 Table 2 Section 4.1.3
Sides	No flux for water, gas, heat, and chemical species	Not Applicable
Drift Wall	No-flux for water, gas and chemical species (except for CO_2 diffusive flux); conduction only for heat	Not Applicable
Waste Package	Initial full heat load of 1.45 kW/m decreasing with time (due to radioactive decay), and reduced by 70% during the first 50 years (due to heat removal by ventilation)	Attachment VIII and Table 2

NOTES: T = Temperature
S_g = Gas saturation
S_L = Liquid saturation
P = Pressure

6.4.3 Input Data and Modeling Procedure

Simulations for the Tptpmn THC Model (No Backfill) model were run using TOUGHREACT V2.3 [153101], the thermodynamic data shown in Attachment VI, and kinetic data in Table 4. Input water and gas compositions are shown in Table 3. Initial mineralogy and mineral surface areas are given in Attachments I and III, respectively. This model was run using the base-case and extended-case sets of chemical components and mineral assemblages described in Table 8, without the opal phase. These are slightly different sets than those previously considered (Table 7), with addition of fluoride in the base case and removal of sepiolite and k-smectite in the extended case. A revised activity coefficient model (Section 6.1.3) allowed for lowering the limit of minimum liquid saturation (from 10^{-4} to 10^{-5}) and increasing the limit of maximum ionic strength (from 2 to 4), at which chemical speciation in the water is no longer computed by the model (see Section 5, Assumption A-17).

In this model, calcite was set to react at equilibrium, to better approximate the fast reaction rates reported in the literature (three orders of magnitude faster than assumed in the simulations with backfill reported in Section 6.3.5.2) (Table 4). Assuming local equilibrium for calcite, rather than a kinetically controlled reaction rate, produced very similar results in simulations of the DST (Section 6.2.8) and has the advantage of allowing simulations with larger time steps than would be required with the fast calcite reaction rate.

Using pH and calcium concentrations measured in pore-water samples (Table 3), together with independently measured CO_2 partial pressures in ambient pore-gas samples (Table 2), calcite is calculated to supersaturate in pore waters by approximately 1 log(Q/K) unit at 25°C. The reason for this supersaturation has not been determined and could be the result of various factors, including (but not limited to) analytical errors, kinetic inhibition due to organic or other compounds in solution, or effects due to high capillary pressure or pressures developed during the ultra-centrifuge water-extraction process. To reconcile measured pH, calcium, and CO_2 concentrations, calcite was allowed to remain supersaturated by approximately 1 log(Q/K) unit at 25°C. This "precipitation gap" was set to decrease exponentially with temperature and become negligible around an arbitrarily selected temperature of 200°C.

A fairly steady hydrochemical system was achieved after revising thermodynamic data primarily for smectites and zeolites and calculating dissolved aluminum concentrations from equilibration with illite (Section 4.1.4.2). The steadiness of water and gas concentrations calculated for ambient conditions over long periods of time was also improved by allowing calcite to remain supersaturated as described above. This configuration included a boundary water with a lower pH (7.75 vs. 8.32) and higher CO_2 partial pressure (approximately 3700 ppmv) than considered in the Tptpmn THC Backfill Model (Table 3).

The calibrated rock-properties set for the mean infiltration rate (Table 2) and mean infiltration regime (Table 12) were used, and steady-state thermal and hydrologic conditions were achieved as described in Section 6.3.3. Similarly, THC simulations were run as described in Section 6.3.3, with the exception that ambient reactive transport simulations (no heat loading) were run using the same mean infiltration regime as the simulations of thermal loading, rather than a constant mean infiltration rate as done previously. This allowed for a clearer distinction between ambient and thermal effects on modeled water and gas compositions than possible in the Tptpmn THC Backfill Model simulations.

Compared to previous simulations in Section 6.3, maximum allowable time step lengths were decreased from 10 years to 1, 2, and 5 years for the time periods spanning 50–600, 600–2000, and 2000–20,000 years, respectively.

6.4.4 Model Runs

A total of six simulations were completed, as summarized in Table 15.

Table 15. Tptpmn THC Model Runs (No-Backfill)

Infiltration-Property Set (Table 12)	**Geochemical System (Table 8)**	**Simulation Type**	**Run ID (used in DTN: LB0011DSTTHCR1.001 Attachment XI)**
Mean Infiltration	None	TH	th6_16_25_7
	None	TH	th6_3_r (backfill, rerun with TOUGHREACT V2.3 [153101])
Mean Infiltration	Base Case	THC	thc6_16_25_9
	Base Case	THC - Ambient	thc6_16_25_9_amb
	Extended Case	THC	thc6_16_25_10
	Extended Case	THC - Ambient	thc6_16_25_10_amb

6.4.5 Simulation Results

Model results are presented below in Figures 54 through 71, and focus on the same three areas around the drift as for previous simulations discussed in Section 6.3.5 (crown, at model nodes F 257 and M 257; side, at nodes F 92 and M 92; and base, at nodes F 272 and M 272). These data were tabulated and submitted to the technical database under DTN: LB0011DSTTHCR1.001 and are discussed further below.

6.4.5.1 Thermohydrology Simulation Results (Backfill Versus No Backfill)

The results of TH simulations for the Tptpmn THC Model (no-backfill) are shown in Figures 54 to 60. Results of simulations of the Tptpmn THC Backfill Model (Section 6.3.5.1) are also included on most of these figures for comparison.

Without backfill, during post-closure, higher temperatures are reached at the drift crown (maximum increase approximately 15°C) and lower temperatures at the drift base (maximum decrease approximately 63°C) compared to the backfill case (Figures 54 to 56). This is mostly a result of removing the insulating effect of backfill over the heat source. Consequently, the extent of the dryout zone below the drift (Figure 55) decreases significantly compared to the backfill case (Figure 32). In addition, the lower modeled heat load for the no-backfill case (1.45 vs. 1.54 kW/m) results in an overall smaller dryout zone around the drift (maximum size extending to approximately 8 m above the drift, 10 m to the side, and 13 m below). However, the time when maximum dryout is reached (nearly 600 years) remains the same in both cases.

Saturation profiles for fractures and matrix (Figures 57 and 58) show little difference at the drift crown between the backfill and no-backfill cases. However, because of significantly lower temperatures at the base of the drift without backfill, this location rewets 400 years sooner than the case with backfill. At the crown, the rewetting time is between 1,200 and 1,400 years without backfill, and between 1,400 and 1,600 years with backfill (in these time profiles, results are presented for more points in the 1,000–2,000-year interval than in simulations shown in Section 6.3 (every 200 years) and thus allow the time of rewetting to be tracked more closely). It should be noted that increasing liquid saturation after 2,000 years is a result of a stepwise increase in infiltration rate from 16 to 25 mm/yr at 2,000 years. Air mass fractions in the gas phase are slightly higher without backfill (Figure 59), reflecting the slightly lower heat load in the no-backfill case.

The calculated rate of vertical water influx in fractures at the drift crown (Figure 60) is generally similar for the backfill and no-backfill cases. Simulations with backfill predict a short-lived large flux increase prior to the start of the post-closure period (when ventilation ends) that may be related to the small cooldown that occurs due to a constant heat removal. Both models show an influx peak at the time of rewetting. However, the intensity of these peaks may only reflect the time intervals at which data are output from the model. The flux increase after 2,000 years reflects the increase in infiltration rate at that time. For the ambient simulation, the flux increase at 600 years also reflects the infiltration rate increase at that time.

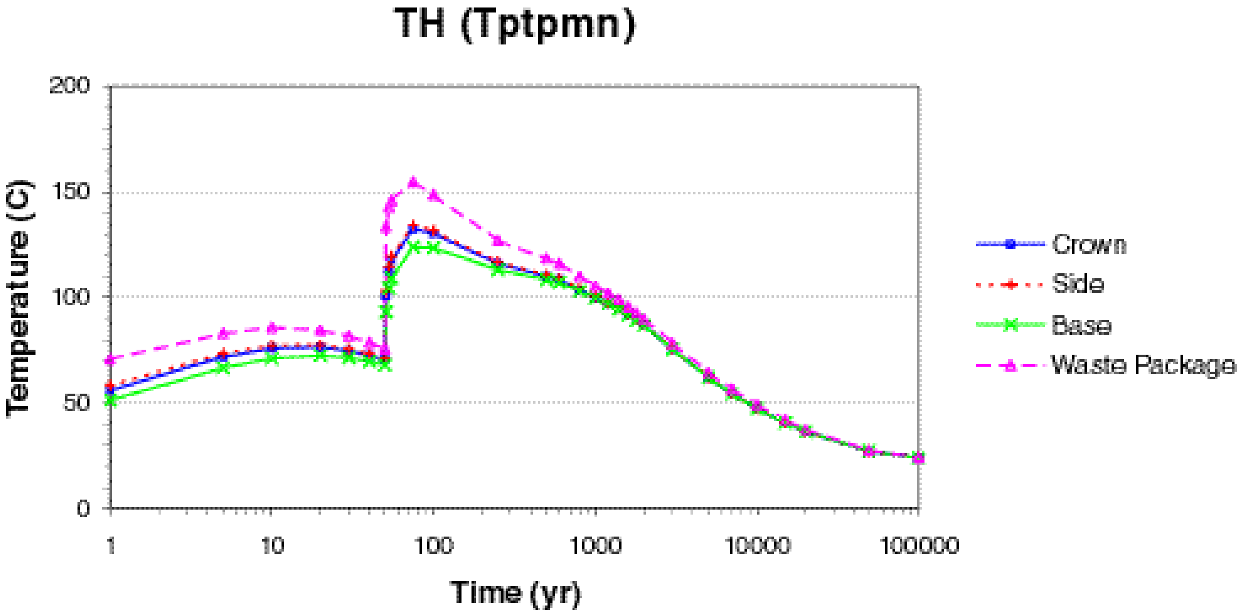

DTN: LB0011DSTTHCR1.001

Figure 54. TH Simulation (Tptpmn - No Backfill). Time Profiles of Modeled Temperatures in Fractures at Three Drift-Wall Locations and in the Waste Package.

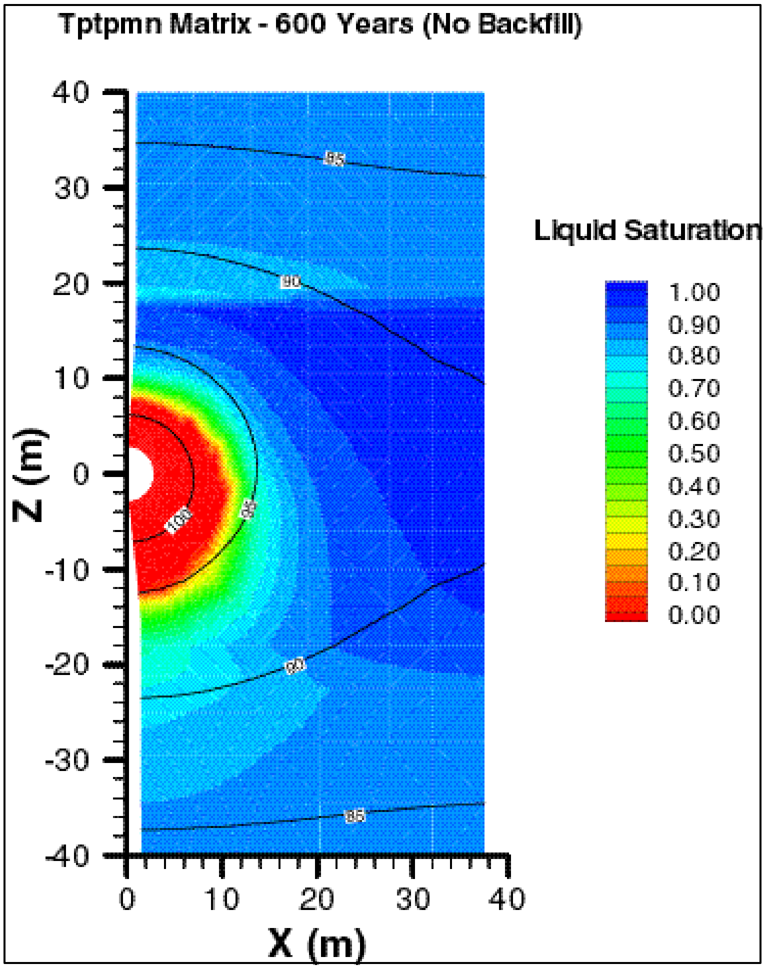

DTN: LB0011DSTTHCR1.002

Figure 55. TH Simulation (Tptpmn - No Backfill). Contour Plot of Modeled Temperatures and Liquid Saturations in the Matrix at 600 Years (Near Maximum Dryout - Mean Infiltration).

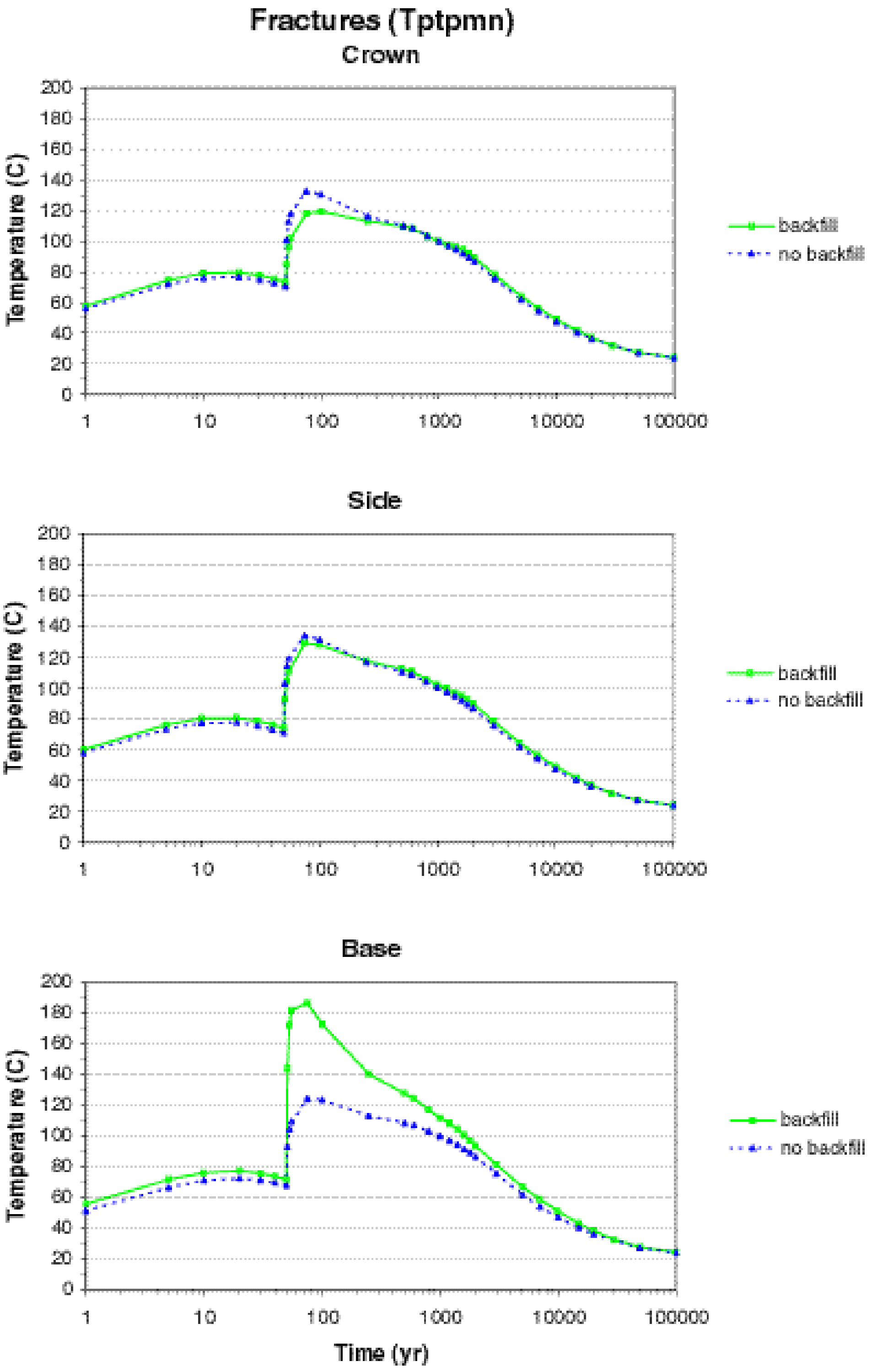

DTN: LB0011DSTTHCR1.001

Figure 56. TH Simulation (Tptpmn - Backfill versus No Backfill). Time Profiles of Modeled Temperatures in Fractures at Three Drift-Wall Locations.

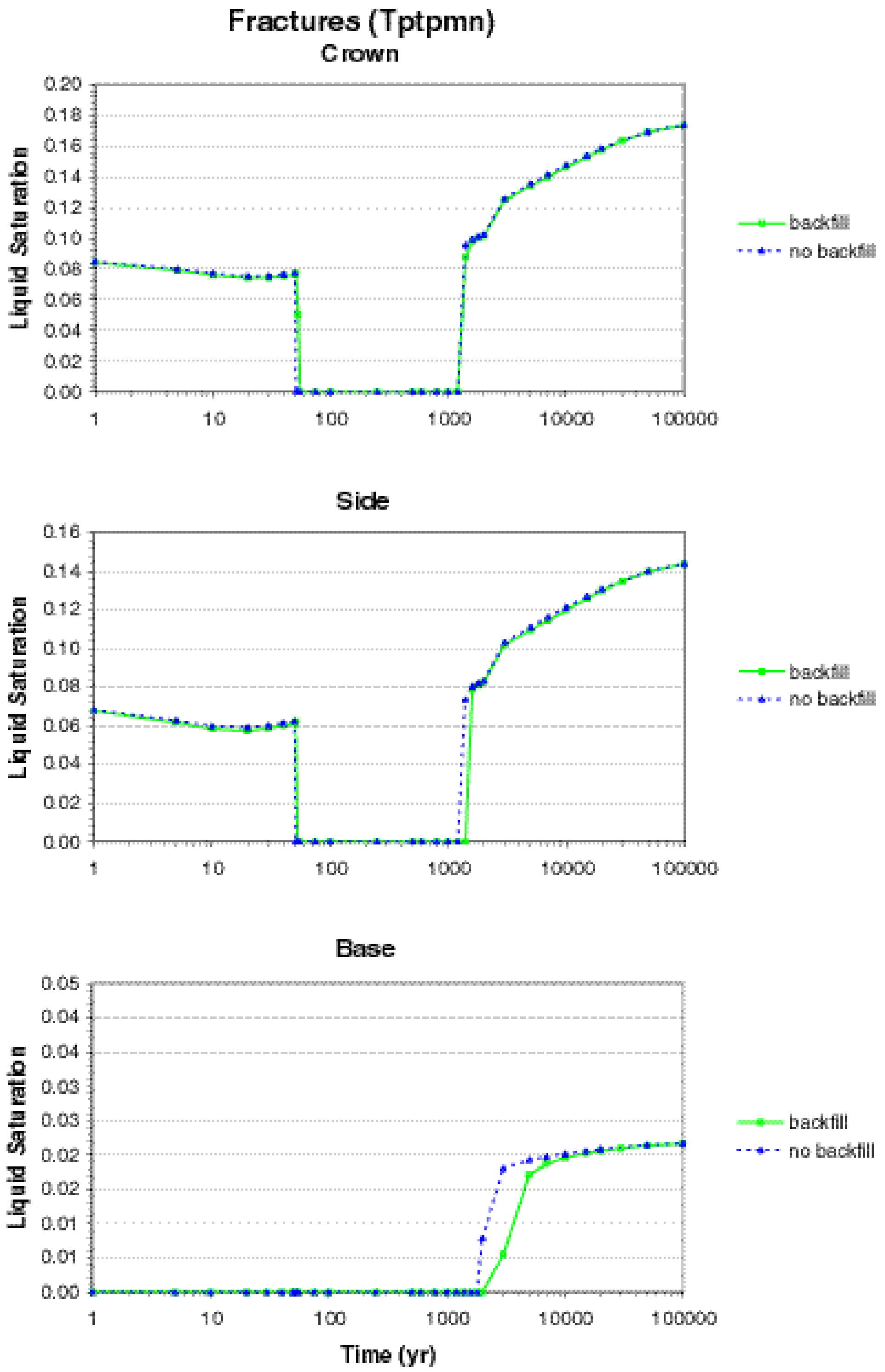

DTN: LB0011DSTTHCR1.001

Figure 57. TH Simulation (Tptpmn - Backfill versus No Backfill). Time Profiles of Modeled Liquid Saturations in Fractures at Three Drift-Wall Locations.

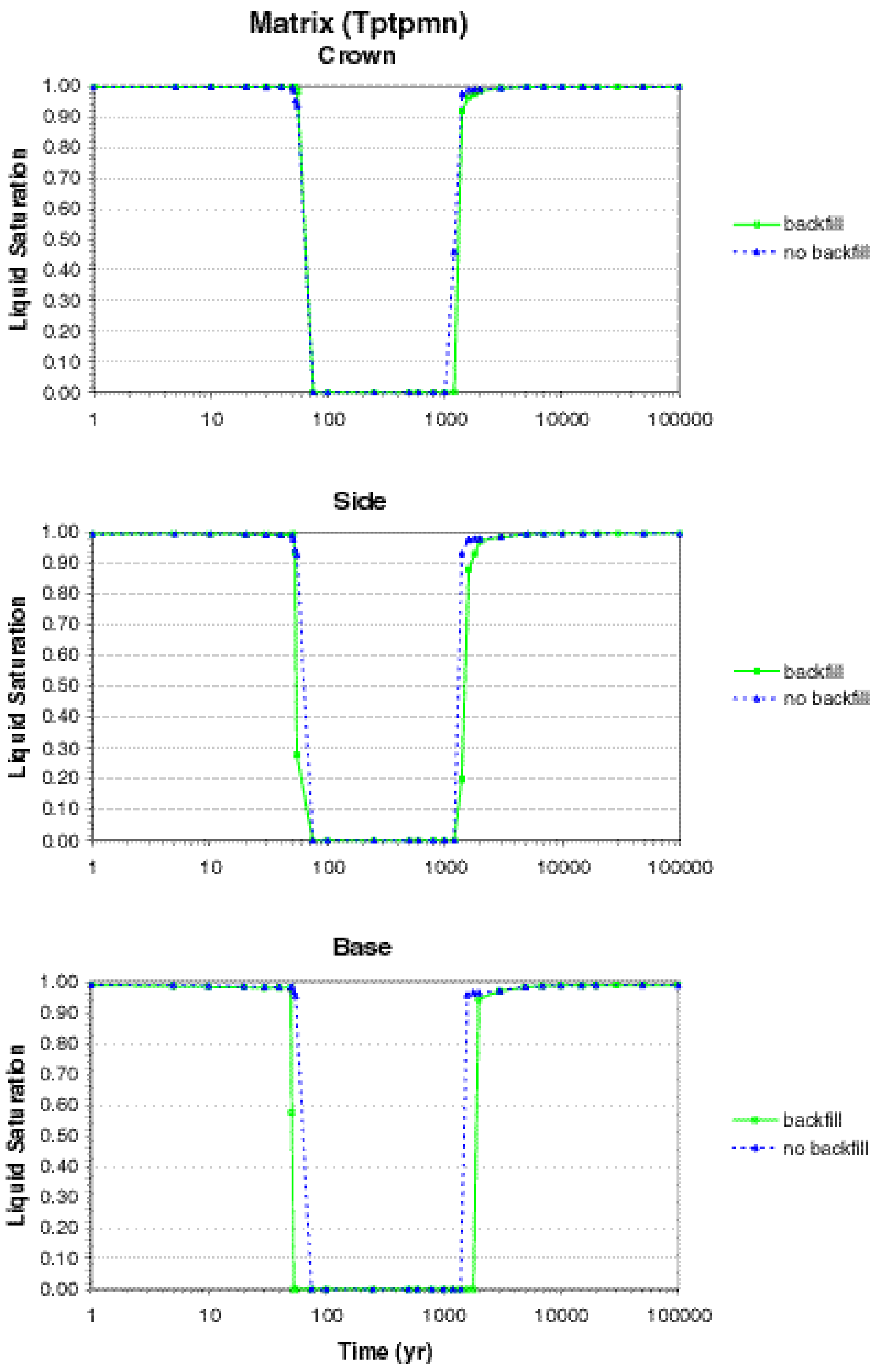

DTN: LB0011DSTTHCR1.001

Figure 58. TH Simulation (Tptpmn - Backfill versus No Backfill). Time Profiles of Modeled Liquid Saturations in Matrix at Three Drift-Wall Locations.

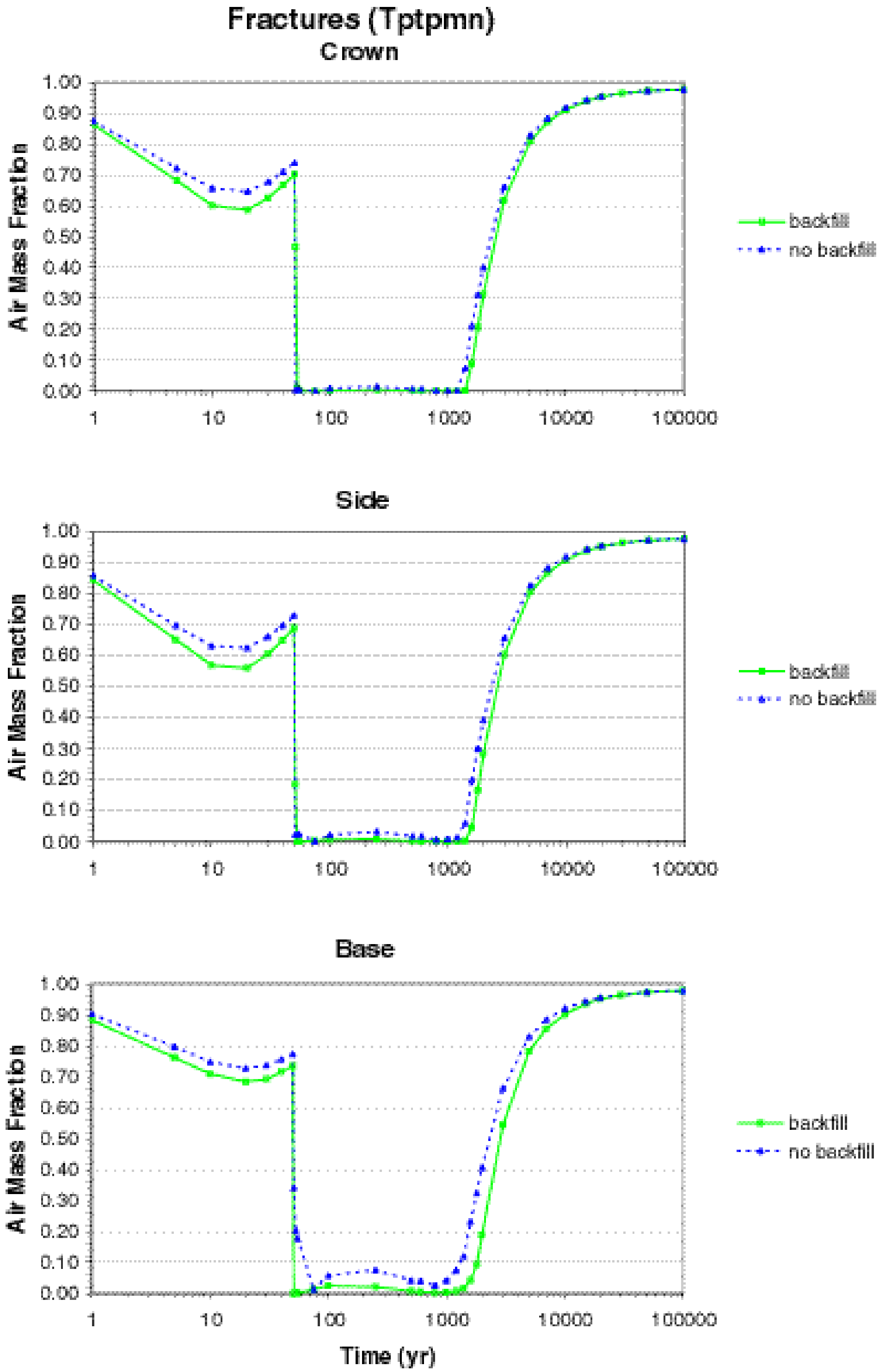

DTN: LB0011DSTTHCR1.001

Figure 59. TH Simulation (Tptpmn - Backfill versus No Backfill). Time Profiles of Modeled Air Mass Fractions in the Gas Phase in Fractures at Three Drift-Wall Locations.

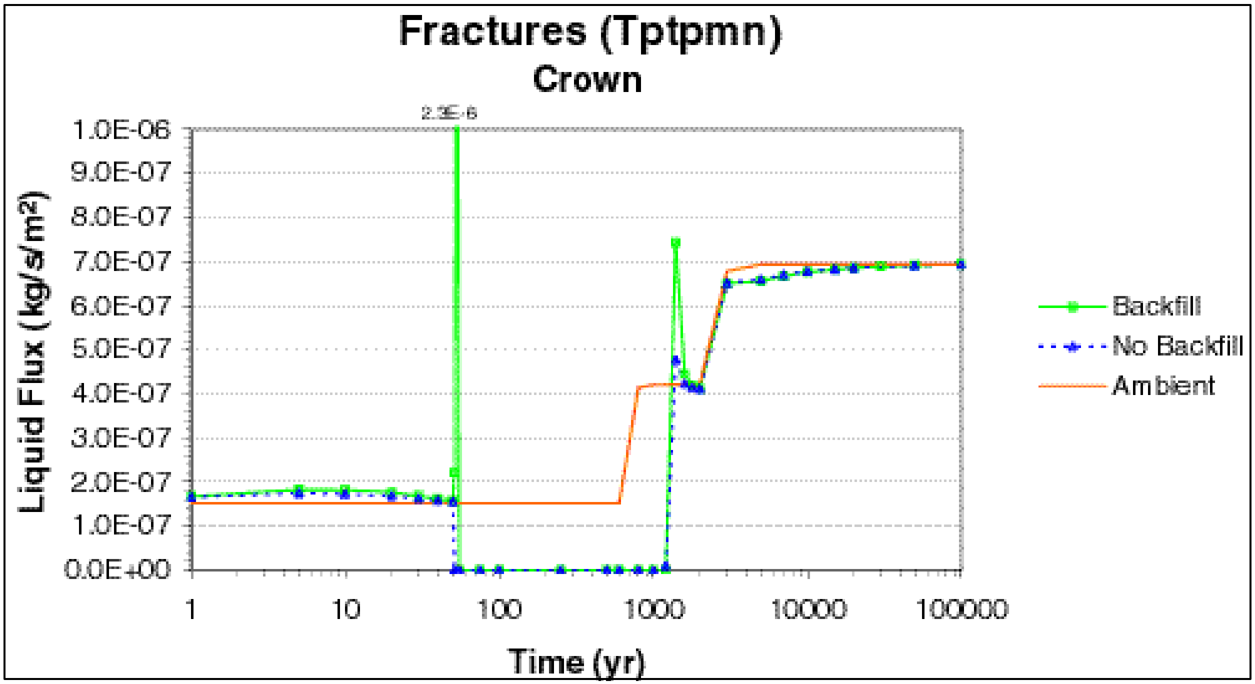

DTN: LB0011DSTTHCR1.001

Figure 60. TH Simulation (Tptpmn - Backfill versus No Backfill). Time Profiles of Modeled Water Flux at the Drift Crown (positive downward).

6.4.5.2 THC Simulation Results (Backfill Versus No Backfill)

Time profiles of predicted CO_2 and various aqueous species concentrations in fractures are shown in Figures 61 to 68. These figures combine the results of ambient and heat-load calculations for both the base-case and extended-case geochemical systems. A "steady" ambient hydrochemical state was achieved for calculations for the current no-backfill design compared to simulations of the prior design with backfill discussed in Section 6.3.5.2. Those simulations entailed reducing the stability of smectites and zeolites (Section 4.1.4.2) such that reactions like those discussed in Section 6.3.5.2 would not proceed to a large extent under ambient conditions. It also entailed allowing some degree of calcite supersaturation (Section 6.4.3) and revising pH and CO_2 concentrations at the top model boundary (Section 4.1.3). As a result, concentration trends predicted here for the base-case and extended-case geochemical systems are better constrained, and more consistent with one another, than for the Tptpmn THC Backfill Model simulations.

Most differences in computed water and gas chemistries between the present no-backfill model and the backfill model in Section 6.5.3.2 are not related to differences in drift design and properties or differences in computer code versions (i.e. TOUGHREACT V2.2 [153219] vs. V2.3 [153101]) used for the simulations. These differences, unless specifically noted otherwise, are primarily attributed to the above-described changes required to achieve fairly steady ambient hydrochemical conditions, thus reducing the model uncertainty.

The general predicted trend of CO_2 concentrations with time in fracture gas (Figure 61) is similar to that previously modeled (Figure 40), with a large decrease during dryout followed by a steep increase during the initial cooling and rewetting stage. This increase is not predicted to reach maximum values as high as previously modeled (values remain below 10,000 ppmv for both the base case and the extended case), and concentrations are predicted to return to ambient values after 20,000 to 50,000 years. During the dryout phase, modeled CO_2 concentrations are depressed significantly relative to ambient values, but remain mostly higher than predicted in the backfill case. One reason for this difference is the lower heat load and lower overall temperatures, which drive off CO_2 less strongly than in the no-backfill case. However, another cause for this difference is a correction to the CO_2 gas diffusion coefficient, resulting in an increase by a factor of approximately 30 compared to values used in simulations with backfill.

Modeled trends in pH (Figure 62) and total aqueous carbonate concentrations (expressed as HCO_3^-) (Figure 63) are better constrained than in the Tptpmn THC Backfill Model simulations (Figures 41 to 44), ranging between pH 7.1 and 8.6, and carbonate concentrations no greater than 250 mg/L over the 100,000-year simulated time interval. During pre-closure, pH and carbonate concentrations drop quickly to values near pH 7.8 and 80 mg/L, respectively, because of calcite precipitation upon increasing temperatures. This drop occurred more slowly in previous simulations because calcite was reacting under kinetic constraints (instead of equilibrium in the current case) with a smaller rate constant than the published value. However, over longer simulation times and less transient conditions during post-closure, this difference in reaction rate has little effect on calculated pH and carbonate concentrations.

Calcium and sodium concentrations for the extended case (Figures 64 and 65) do not show as high and low values, respectively, as indicated in the Rev00 simulations (Figures 45 and 47). Although better constrained than in those simulations, ambient sodium concentrations approximately double over the 100,000-year simulated time period, which could reflect somewhat higher feldspar and/or glass dissolution rates relative to the precipitation rate of clay minerals.

Upon heating, aqueous silica concentrations (Figure 66) rise significantly above ambient values due to the dissolution of silica phases at higher temperatures. Simulations with the extended geochemical system yield higher aqueous silica concentrations because of the dissolution of aluminosilicate minerals (feldspars and zeolites) not included in the base-case system (mostly cristobalite dissolves with the latter). Upon boiling to dryness, aqueous silica concentrations may significantly exceed the solubility of amorphous silica (near 370 mg/L at 100°C) because the precipitation rate of this mineral, even though quite fast, may not keep up with boiling rates. During the initial cooling stage, primarily the 600- to 2000-year time interval, aqueous silica around the drift precipitates as amorphous silica and, as will be discussed later, accounts for most of the reduction in porosity around the drift during this time. With the base-case geochemical system, ambient aqueous silica concentrations remain fairly constant and well below the solubility of amorphous silica (approximately 120 mg/L at 25°C), increasing slightly with increases in infiltration rates, thus reflecting a kinetic control on the dissolution of silica phases. With the extended case, modeled ambient aqueous silica concentrations increase to values at or near amorphous silica solubility (higher than measured pore water concentrations), which seems to further indicate that the dissolution rate of feldspar and or glass may be somewhat overestimated relative to the precipitation rate of clays.

Chloride and fluoride concentrations (Figures 67 and 68) show trends similar to those previously modeled for similar infiltration rates (Figures 50 and 51). As in simulations with backfill, fluorite was not considered an initial constituent in the rock around the drift (Tptpmn unit), and fluoride concentrations in the aqueous phase quickly return to smaller near-ambient values during the rewetting stage. The Tptpll THC model presented in Section 6.6 includes fluorite in the mineral assemblage around the drift and predicts larger fluoride concentrations than calculated here.

Overall, in a qualitative sense, water compositions predicted in this model do not differ significantly from previous model results, except that large variations in pH, CO_2, and aqueous carbonate concentrations during the cooling stage are no longer predicted when the extended geochemical system is considered. In this respect, the predicted water composition in fractures around the drift fall within a narrower range than for the Tptpmn THC Backfill Model simulations. As noted earlier, this is largely a result of a steadier ambient hydrochemical system, achieved primarily through the revision of thermodynamic data for clays and zeolites. As such, comparison between results here and those in Section 6.3.5 provide some qualitative analysis of the model sensitivity to the thermodynamic data for these minerals. Because ambient simulations with revised thermodynamic data predict water compositions more consistent with observed data than those in the ambient simulations presented in Section 6.3.5.2, it is expected that the uncertainty of this model has been reduced compared to the earlier model.

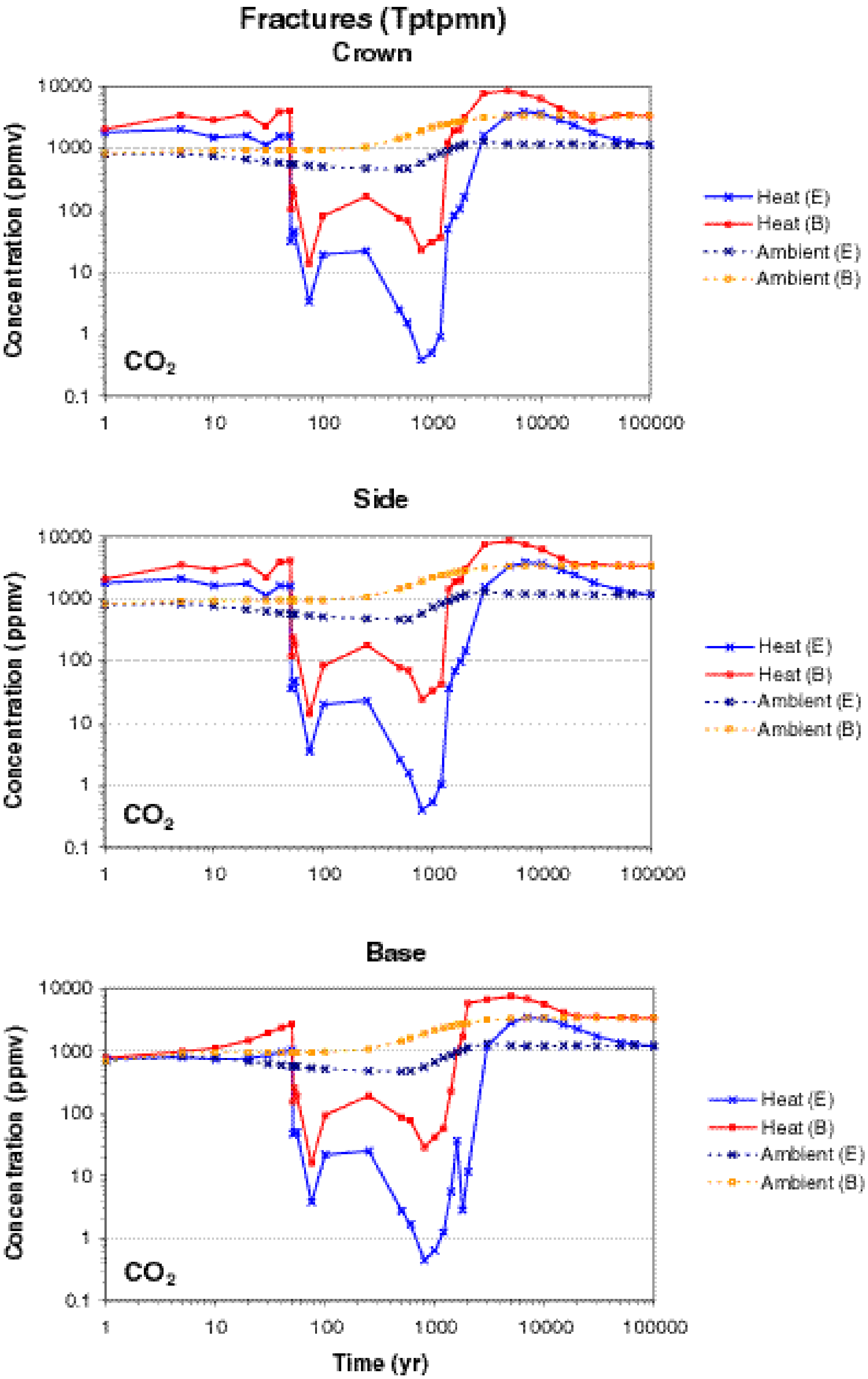

DTN: LB0011DSTTHCR1.001

Figure 61. THC Simulation (Tptpmn - No Backfill). Time Profiles of Modeled CO_2 Concentrations in the Gas Phase in Fractures at Three Drift-Wall Locations under Heat Load (Heat) and No Heat Load (Ambient) Conditions for the Extended (E) and Base-Case (B) Geochemical Systems.

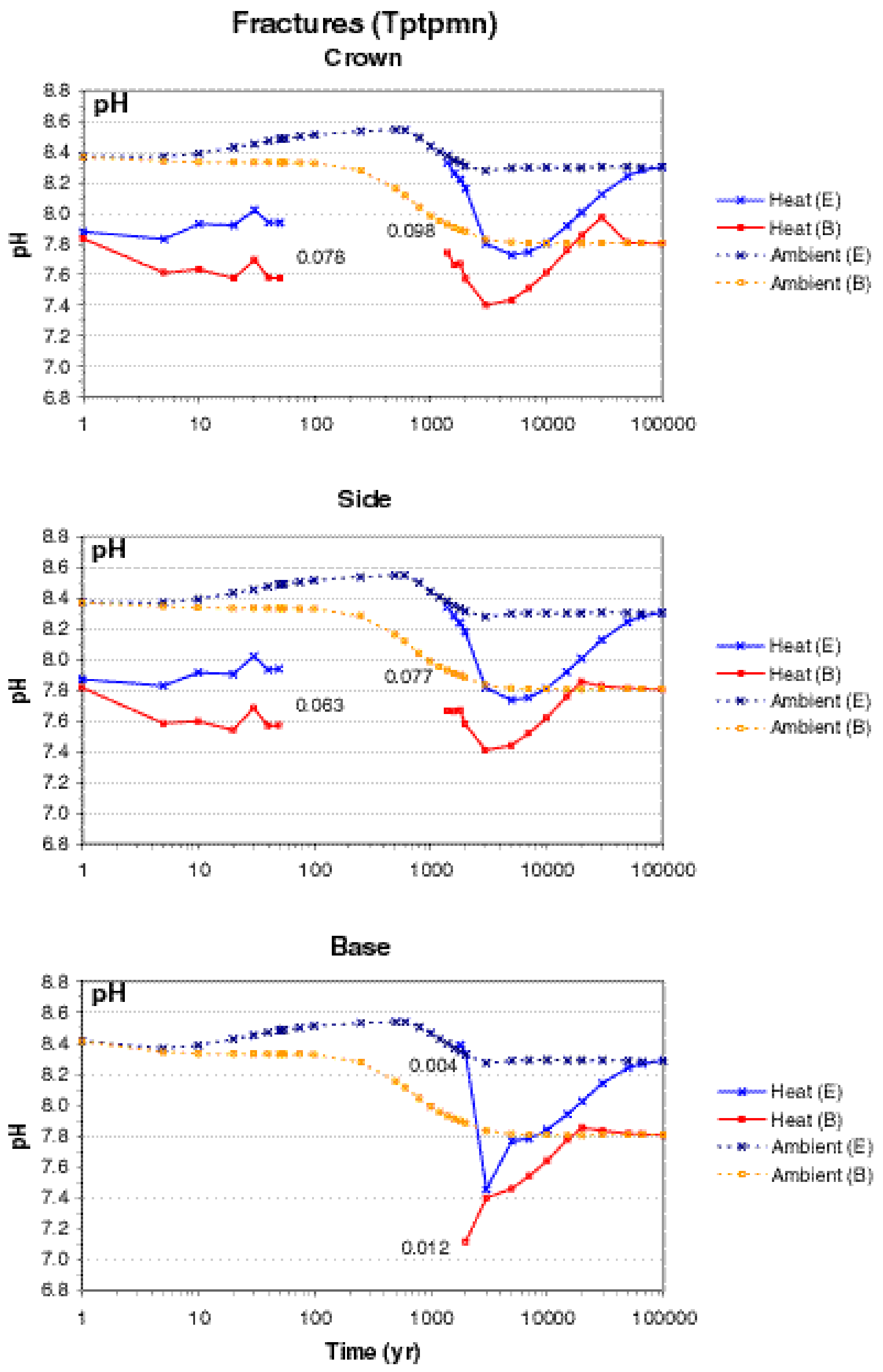

DTN: LB0011DSTTHCR1.001

Figure 62. THC Simulation (Tptpmn - No Backfill). Time Profiles of the Modeled pH of Fracture Water at Three Drift-Wall Locations under Heat Load (Heat) and No Heat Load (Ambient) Conditions for the Extended (E) and Base-Case (B) Geochemical Systems. The dryout period is left blank. Numbers by each curve indicate the last output liquid saturation before dryout and the first output liquid saturation during rewetting.

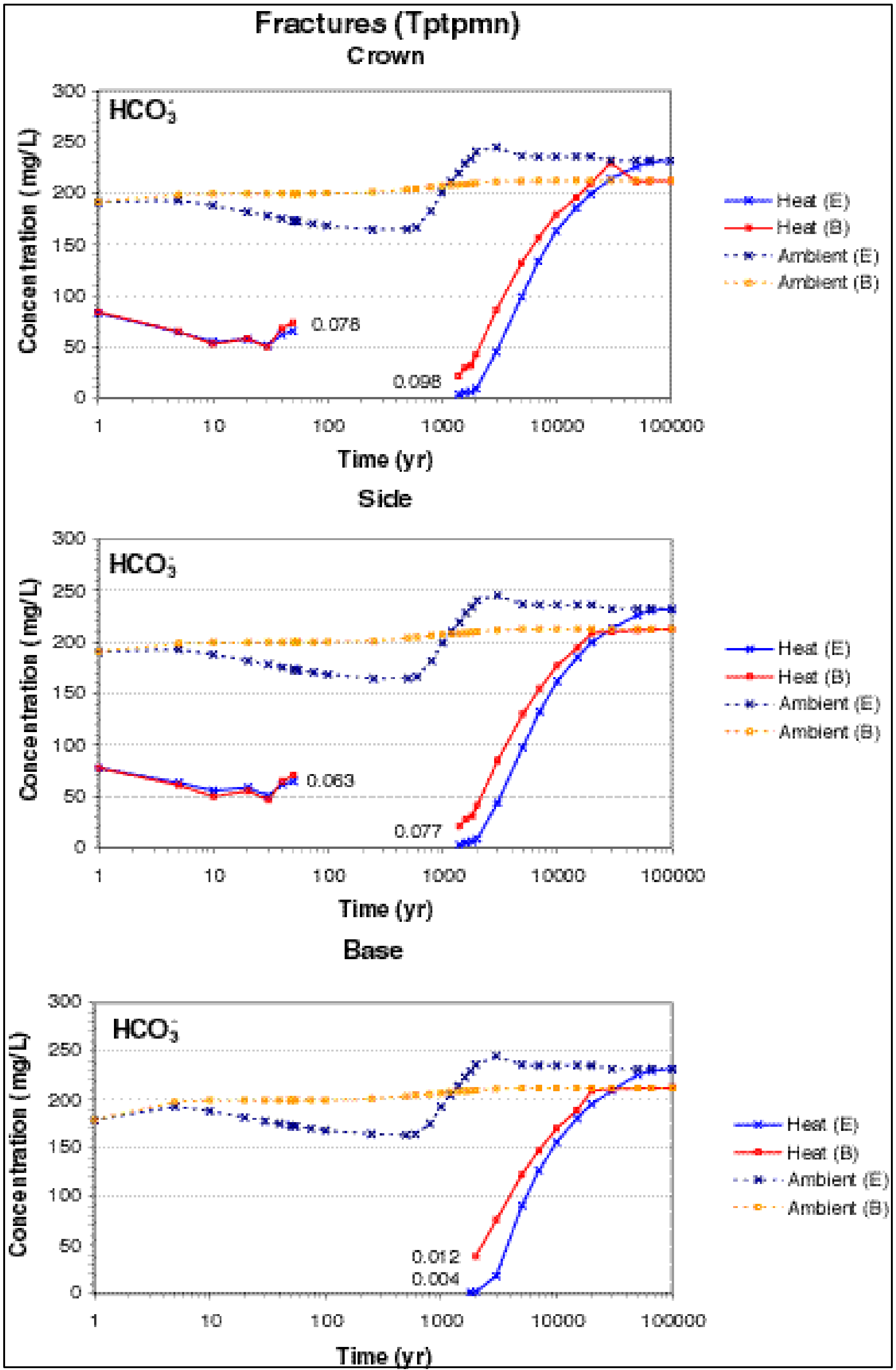

DTN: LB0011DSTTHCR1.001

Figure 63. THC Simulation (Tptpmn - No Backfill). Time Profiles of Modeled Total Aqueous Carbonate Concentrations (as HCO_3^-) in Fracture Water at Three Drift-Wall Locations (designations denoted in Figure 62).

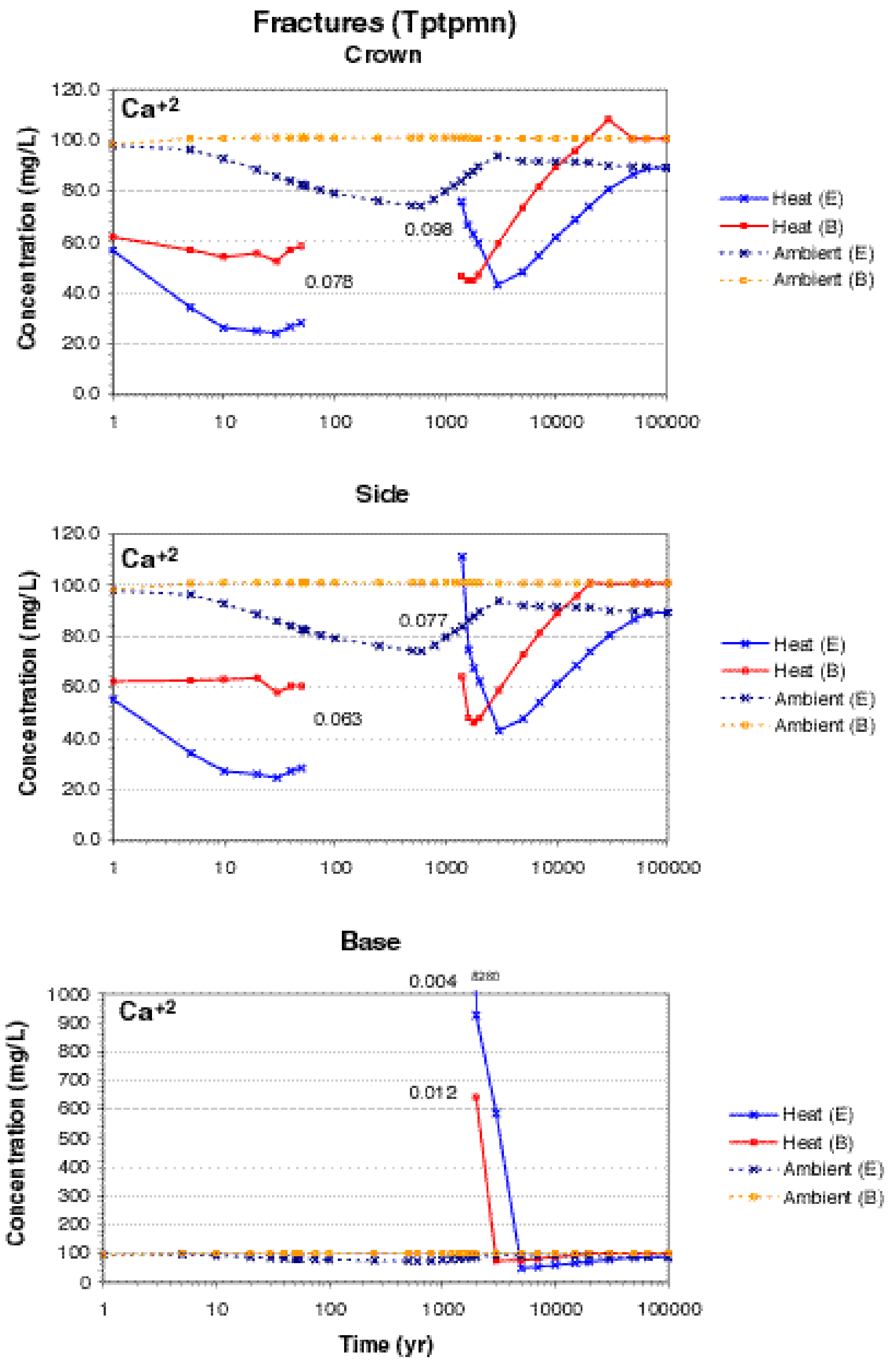

DTN: LB0011DSTTHCR1.001

Figure 64. THC Simulation (Tptpmn – No-Backfill). Time Profiles of Modeled Total Aqueous Calcium Concentrations in Fracture Water at Three Drift-Wall Locations (designations denoted in Figure 62).

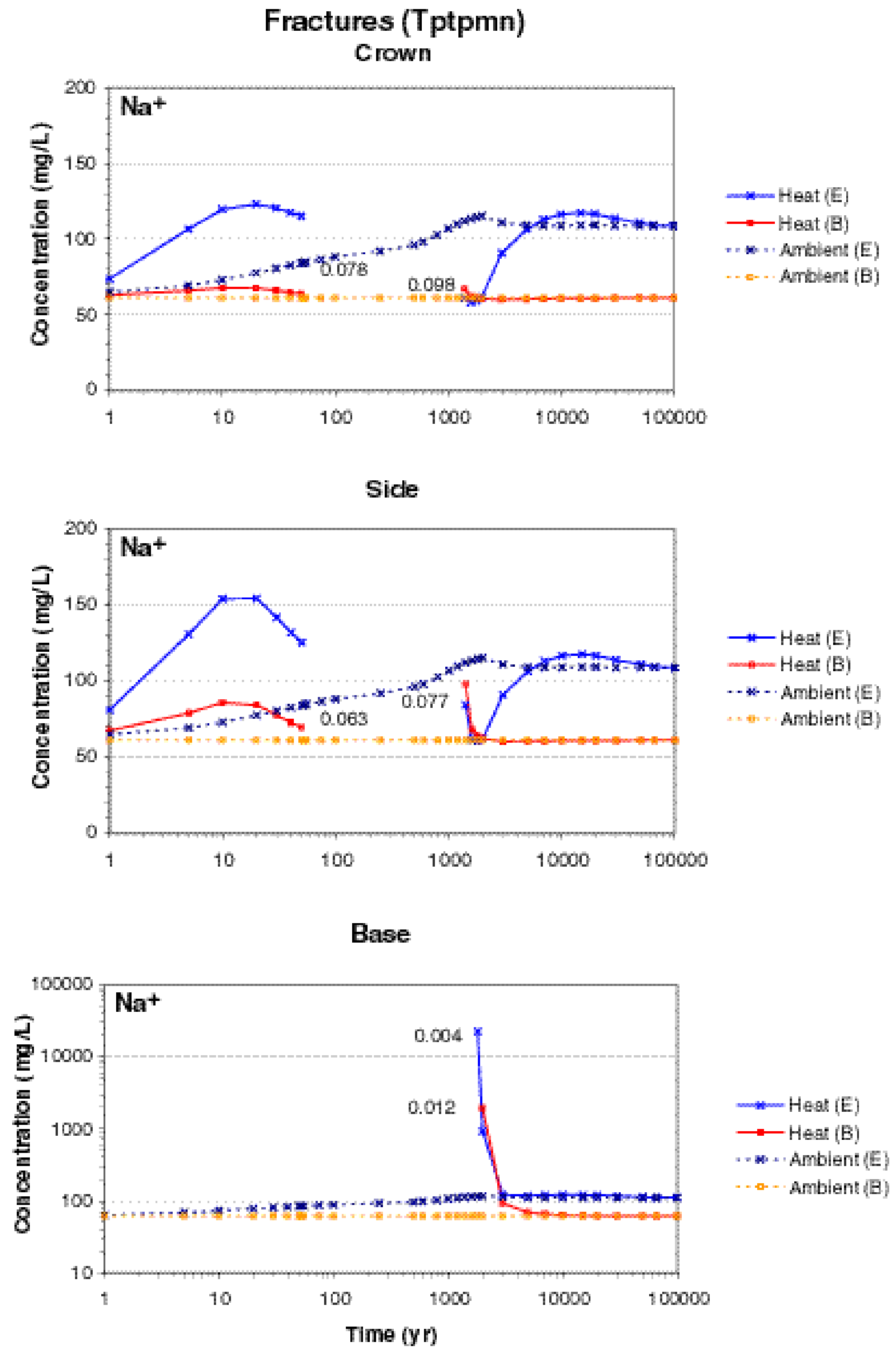

DTN: LB0011DSTTHCR1.001

Figure 65. THC Simulation (Tptpmn - No Backfill). Time Profiles of Modeled Total Aqueous Sodium Concentrations in Fracture Water at Three Drift-Wall (designations denoted in Figure 62).

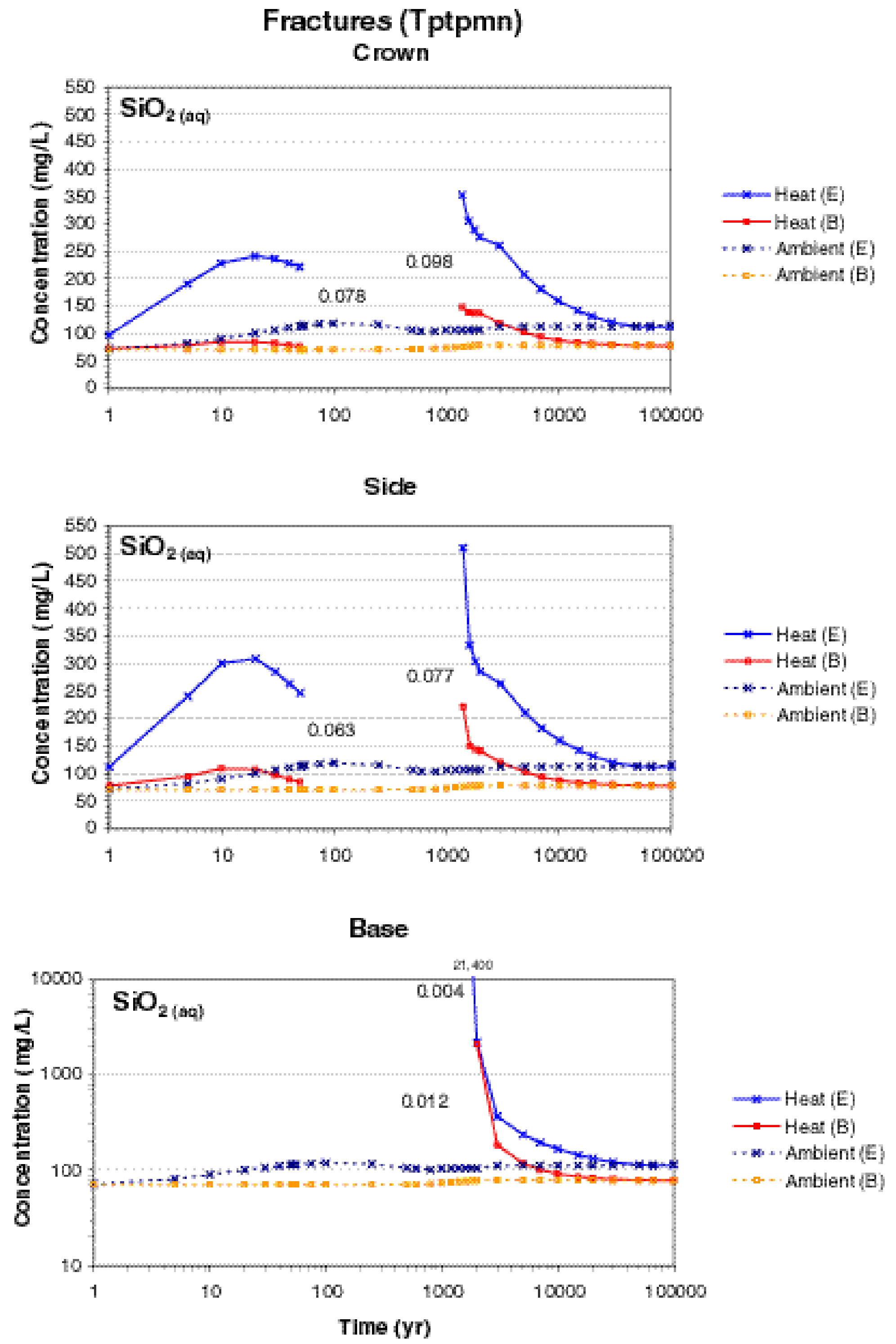

DTN: LB0011DSTTHCR1.001

Figure 66. THC Simulation (Tptpmn - No Backfill). Time Profiles of Modeled Total Aqueous Silica Concentrations in Fracture Water at Three Drift-Wall Locations (designations denoted in Figure 62).

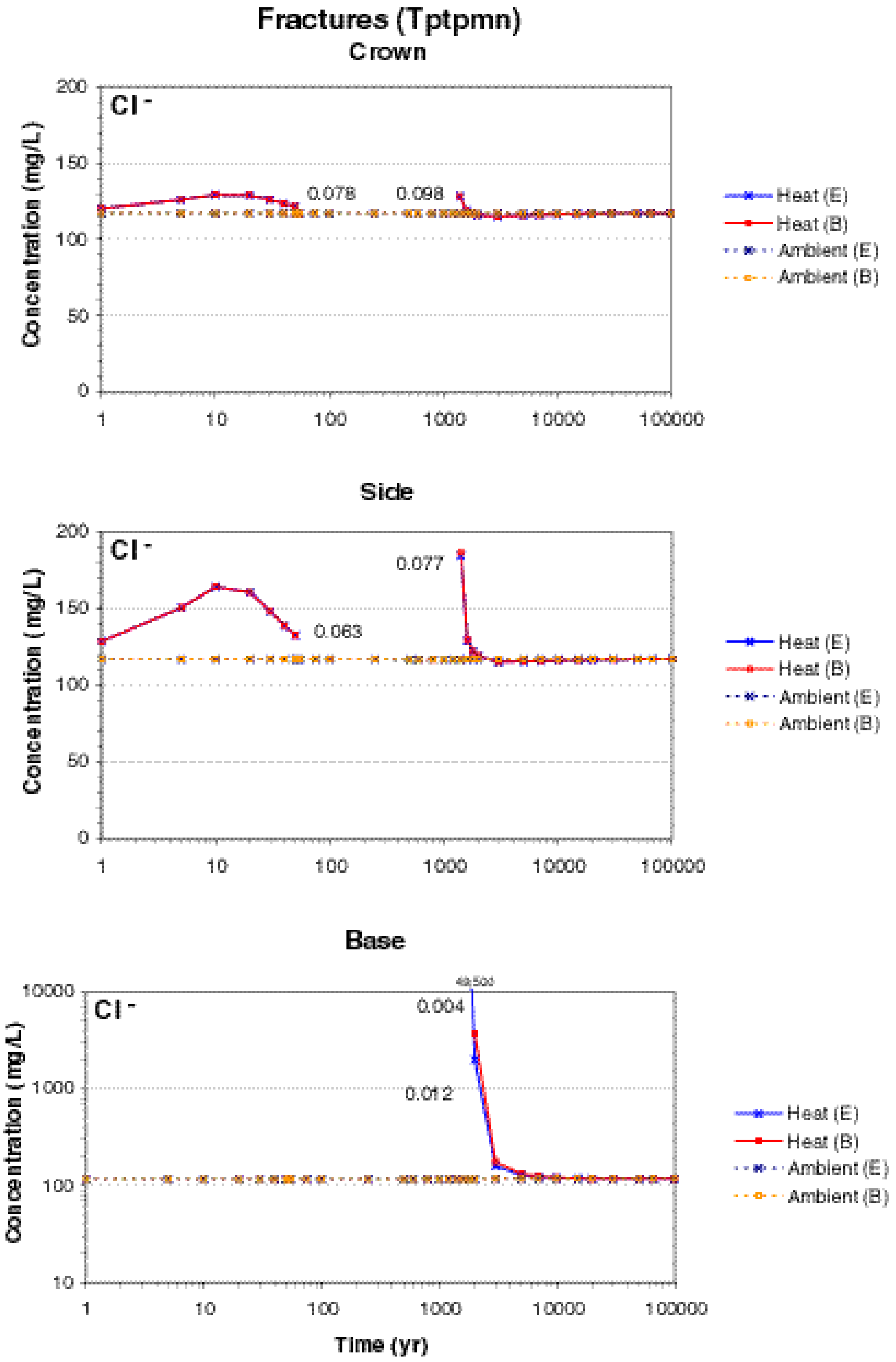

DTN: LB0011DSTTHCR1.001

Figure 67. THC Simulation (Tptpmn - No Backfill). Time Profiles of Modeled Total Aqueous Chloride Concentrations in Fracture Water at Three Drift-Wall Locations (designations denoted in Figure 62).

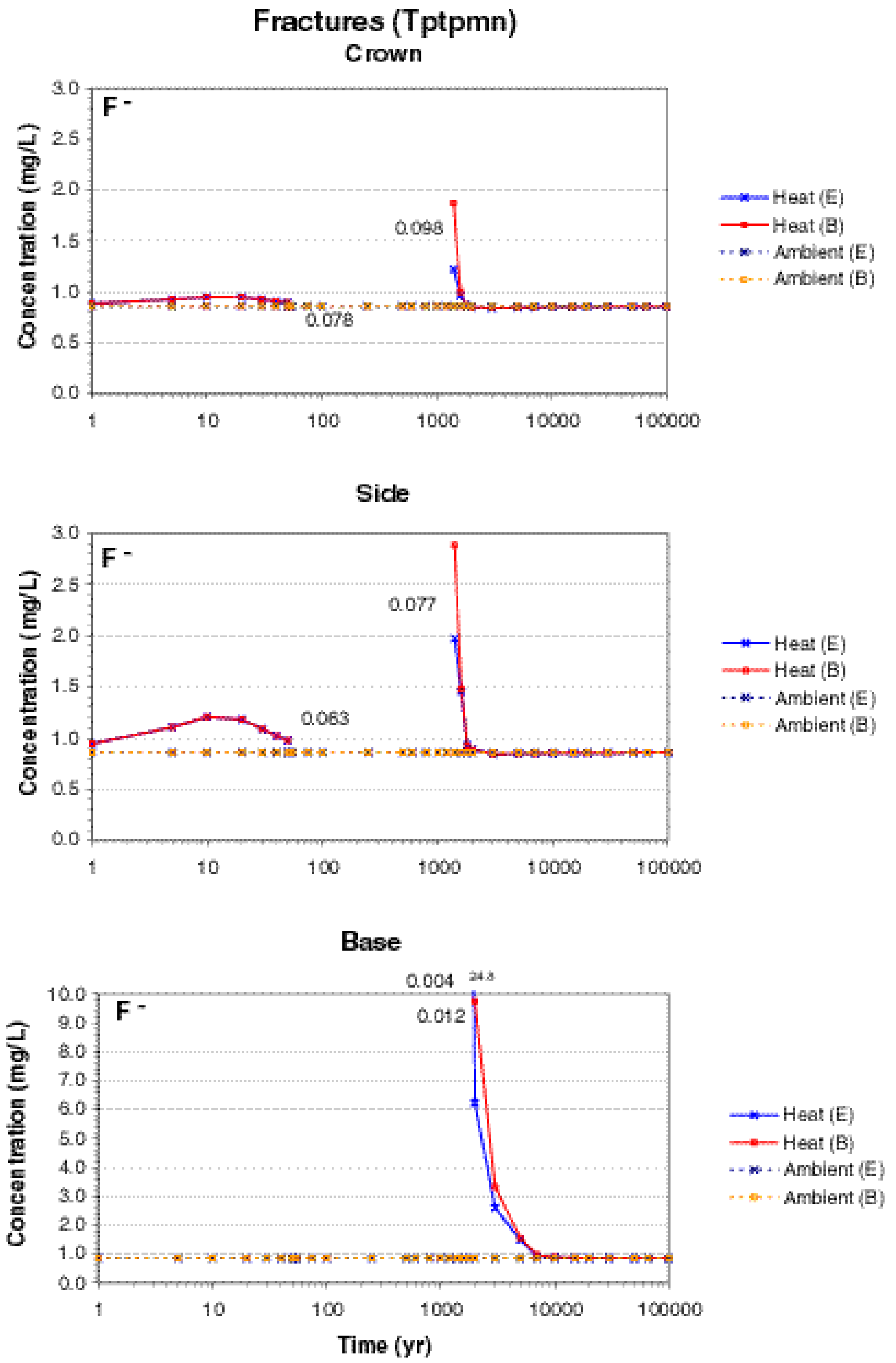

DTN: LB0011DSTTHCR1.001

Figure 68. THC Simulation (Tptpmn - No Backfill). Time Profiles of Modeled Total Fluoride Concentrations in Fracture Water at Three Drift-Wall Locations (designations denoted in Figure 62).

The calculated fracture porosity change around the drift is negative. A maximum decrease occurs approximately 8 to 9 m above drift center, in a pattern approximately delineating the maximum extent of the dryout zone (Figure 69). At this location, the porosity decreases by approximately 1% after 20,000 years and 3% after 100,000 years. This decrease is due primarily to the precipitation of amorphous silica and calcite. Amorphous silica precipitates mostly from 600 to 2000 years, accounting for approximately a 0.5 percent porosity decrease. Amorphous silica precipitation is followed at later times by calcite precipitation as infiltration waters, replenished in aqueous carbonate and calcium, are heated up as they percolate back towards the drift where temperatures remain above ambient values for several tens of thousands of years. Lesser amounts of gypsum (to a maximum near 0.3% volume at 600 years) and very small amounts of fluorite also precipitate in the same zone but dissolved rapidly upon rewetting. The magnitude of porosity changes predicted for the base-case and extended-case systems is similar (Figures 69a and b). The maximum porosity reduction is predicted with the extended case, but the overall extent of the decrease is slightly larger for the base case because of somewhat more widespread calcite precipitation than with the extended case. The predicted porosity change, here, is larger than modeled with previous simulations (Figures 52 and 53) because the current model allows for higher initial precipitation rates of secondary minerals, such as amorphous silica. The larger amount of calcite precipitation is in part due to the higher calcium and carbonate concentrations in the infiltrating water. Also, the calcite supersaturation gap (Section 6.4.3) allows more calcium to remain in solution, in shallow infiltrating waters, until those waters percolate to warmer areas and deposit calcite.

It should be noted that in this model, zeolites in fractures around the drift (mostly stellerite primarily dissolve, rather than precipitate as in the Tptpmn THC Backfill Model simulations in Section 6.3. Small amounts of stellerite (less than 0.02% volume) precipitate in the rock matrix mostly below the drift during the initial cooling stage, but redissolve entirely after approximately 5,000 years. Clay minerals are predicted to precipitate around the drift, but only in minute quantities (less than 10^{-4}% by volume). Figures showing predicted patterns for some of these minerals around the drift are shown in Section 6.5, where the effect of heterogeneous permeability fields are investigated. Predicted mineral patterns of illite and stellerite are similar to those shown in Section 6.6.5.2 for the Tptpll THC model.

THC simulations reported in this section incorporate a more sensitive coupling of fracture permeability to fracture porosity implemented in TOUGHREACT V2.3 [153101] (Section 6.1.6.2) than was used in THC simulations for the backfill design using TOUGHREACT V2.2 [153219] (Section 6.3.5.2). Consequently, the larger porosity reduction, due to mineral precipitation caused more noticeable differences in liquid saturation and water fluxes between TH and THC simulations.

Slightly higher liquid saturations in fractures during the cooling phase are calculated when THC processes are considered (Figure 70), the direct result of increased capillarity due to permeability reduction. However, the permeability reduction is not large enough to significantly affect modeled fluxes at the drift crown (Figure 71) or the general thermohydrology around the drift. A slight flux increase above ambient values after 20,000 years is predicted in THC simulations when the extended geochemical system is considered. However, the small flux increase at that boundary node is caused by minor flow focusing, stemming from uneven precipitation of calcite enhanced by numerical discretization effects. In this case, an average of a few grid nodes would give a closer approximation to the flux at the drift crown. Changes in permeability due to THC effects around the drift are further investigated in Section 6.5 for heterogeneous fracture permeability fields. It should also be noticed that steps in the curves displayed for ambient simulations on Figures 70 and 71 reflect change in infiltration rates input into the model (Section 6.4.2).

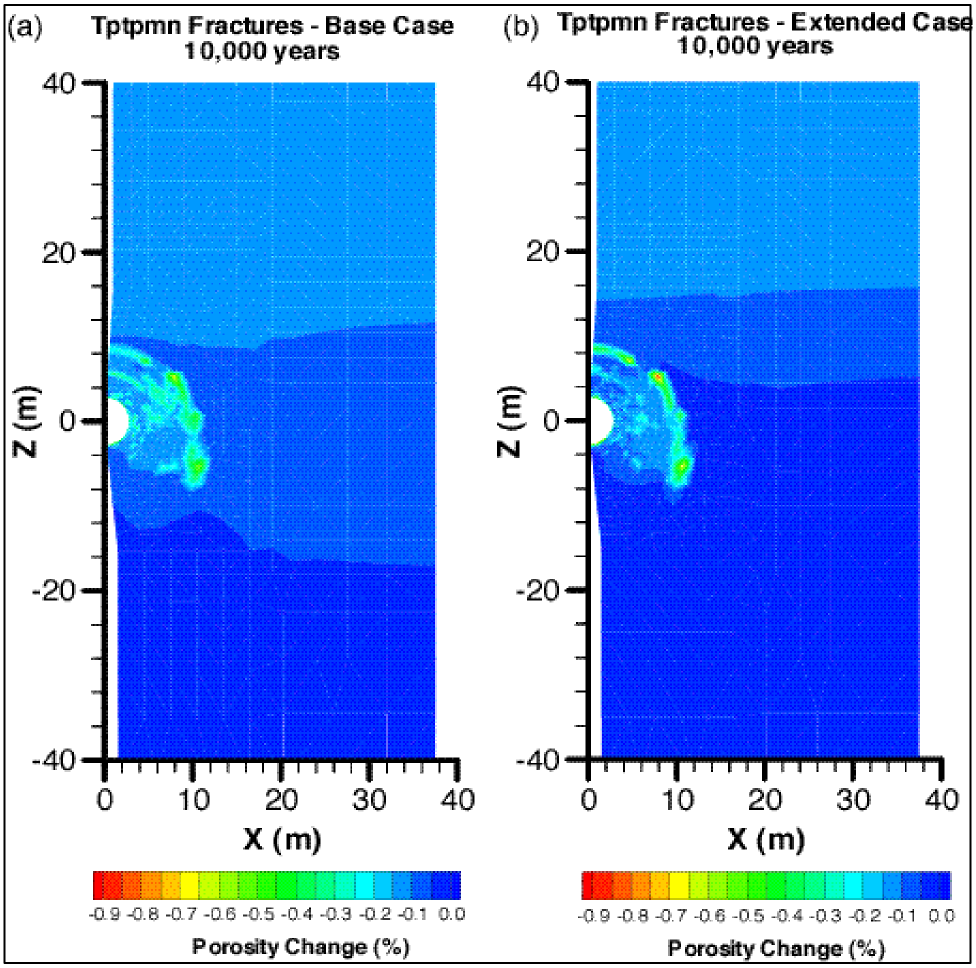

DTN: LB0011DSTTHCR1.002

Figure 69. THC Simulation (Tptpmn - No Backfill). Contour Plot of Modeled Fracture Porosity Change at 10,000 Years. (a) Base-case geochemical system. (b) Extended case. Red areas indicate maximum decrease in porosity, primarily due to precipitation of calcite and amorphous silica.

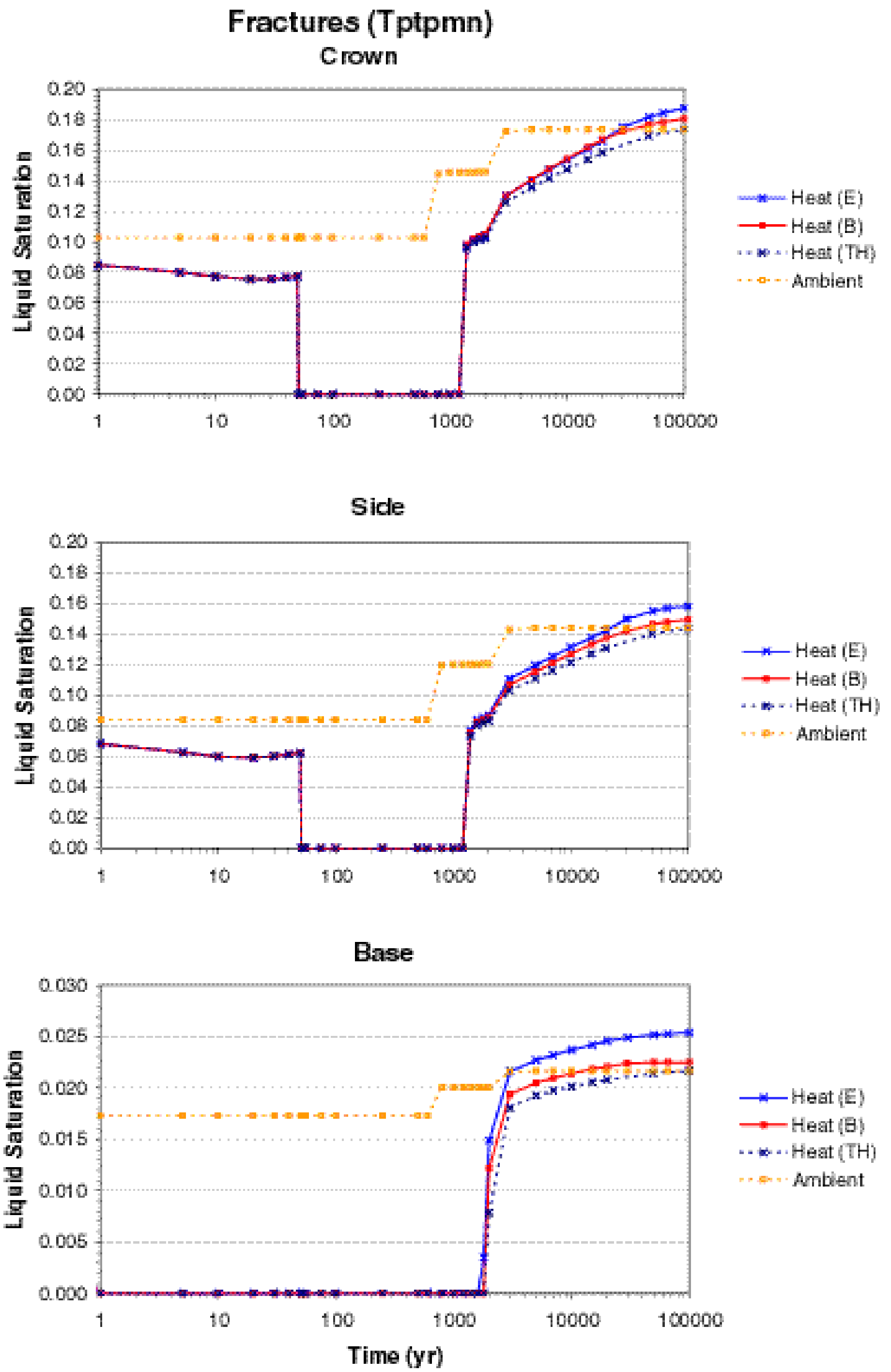

DTN: LB0011DSTTHCR1.001

Figure 70. TH and THC Simulations (Tptpmn - No Backfill). Comparison of Modeled Liquid Saturations in Fractures at Three Drift-Wall Locations under Heat Load (Heat) and No Heat Load (Ambient) Conditions for the Extended (E) and Base-Case (B) Geochemical Systems, and for the TH Simulation.

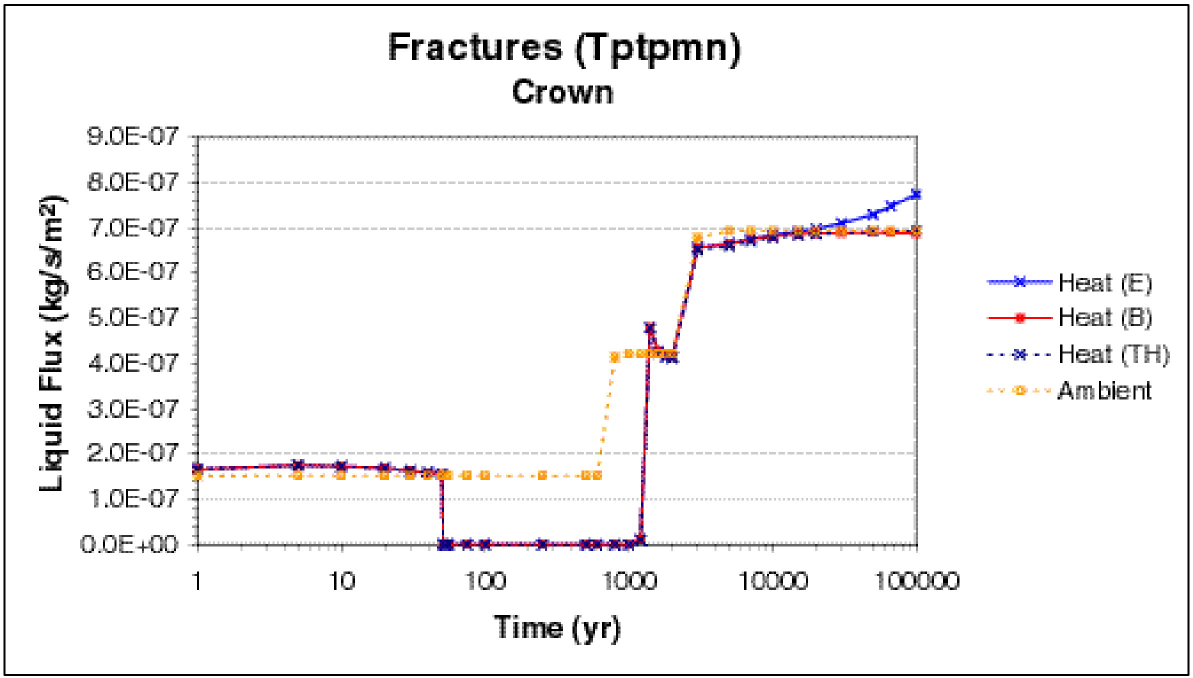

DTN: LB0011DSTTHCR1.001

Figure 71. TH and THC Simulations (Tptpmn - No Backfill). Comparison of Modeled Liquid Flux at the Drift Crown in Fractures under Heat Load (Heat) and No Heat Load (Ambient) Conditions for the Extended (E) and Base-Case (B) Geochemical Systems, and for the TH Simulation. The small flux increase above ambient values after 20,000 years is in part due to numerical discretization effects (see text).

6.5 Tptpmn THC HETEROGENEOUS MODEL

Fracture permeabilities differ over several orders of magnitude in the Tptpmn unit (DTN: LB990601233124.001 [105888]). In the Tptpmn, the effect of initial spatial heterogeneity in fracture permeability on coupled THC processes was not treated prior to this study. The purpose of this work is to address the effects of fracture permeability heterogeneity at the drift scale on water and gas chemistry, hydrologic properties and UZ flow, and the potential for enhanced or reduced seepage owing to THC processes. Several realizations were performed, because the location of higher and lower permeabilities will differ in relation to the drift crown and therefore the areas of maximum mineral precipitation will differ as a result of THC effects.

6.5.1 Model Set-Up

The numerical mesh, boundary conditions, and modeling procedure are the same as those described in Sections 6.4.1 to 6.4.3 for the Tptpmn THC Model (no backfill). Additional model set-up information described in this section relates to the heterogeneous permeability realizations used in the simulations.

6.5.1.1 Heterogeneous Fracture Permeability Realizations

Three 2-D heterogeneous fracture permeability fields were generated using the GSLIB V1.0 module SISIM V1.204 [153100], based on a cumulative distribution function obtained through analysis of air-permeability testing (Bodvarsson 2001 [153816], YMP-LBNL-GSB-1.6.4, pp. 24-28). The range in fracture permeability is four orders of magnitude (DTN: LB990601233124.001 [105888]), with the mean given by the drift-scale calibrated property set (DTN: LB990861233129.001 [110226]). These heterogeneous permeability fields were generated for a region 150 meters above and below the drift center at a spatial resolution of 0.2 m, based on the scale of air permeability measurements. Because the Tptpmn THC Model grid has gridblocks varying from about 0.2 m across near the drift wall to several meters across in areas away from the drift, the fine resolution field had to be mapped onto the numerical mesh using an appropriate averaging scheme. A circular area was defined around the nodal point within each gridblock corresponding to the average distance of the nodal point to the gridblock edges. Geometric means of the permeability multipliers within this area were calculated and used to modify the mean permeability assigned to the numerical mesh nodes. The net result of this averaging is that the permeabilities near the drift wall have the same or similar spatial variability, whereas areas away from the drift reflect a smoother averaged field appropriate to the resolution of the mesh in these areas. Plots of the three realizations of averaged permeability fields used in the Tptpmn THC simulations are shown in Figures 72a–c.

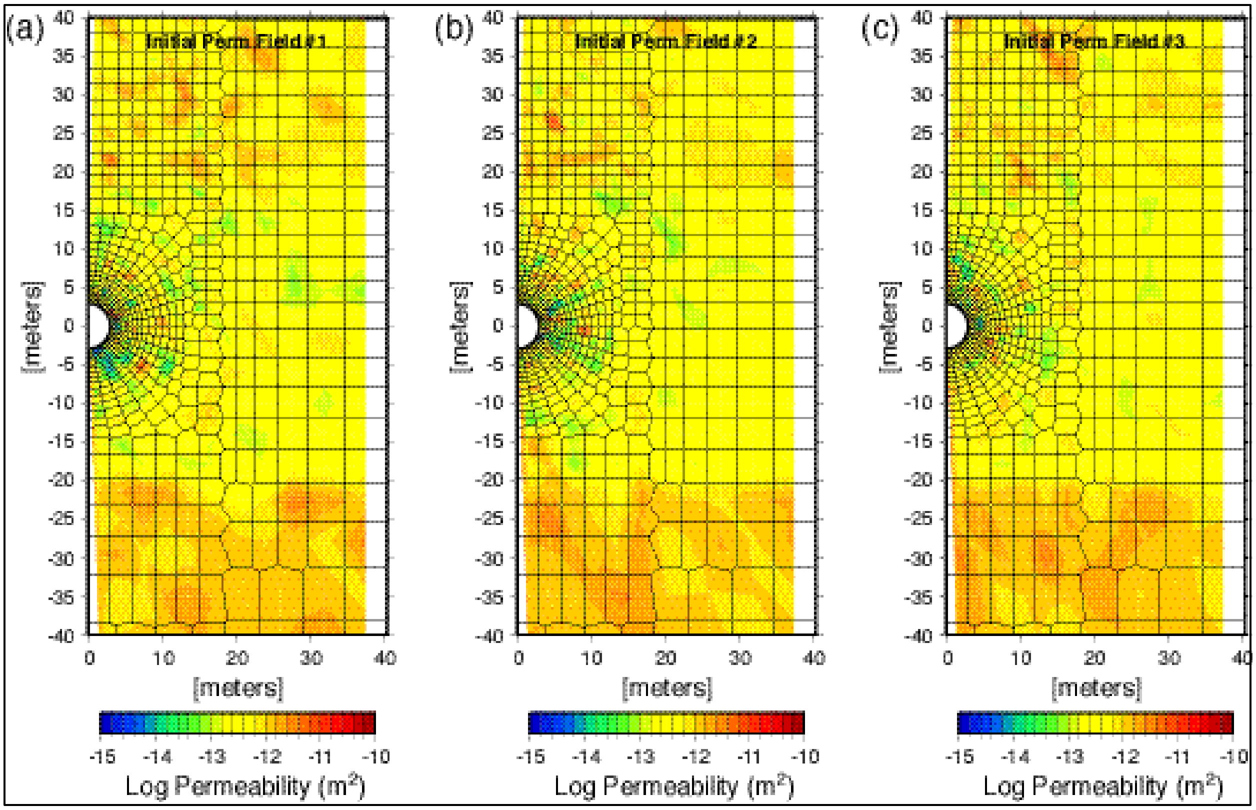

DTN: LB0011DSTTHCR1.002

Figure 72. Fracture Permeability Realizations #1 (a), #2 (b), and #3 (c).

6.5.1.2 Model Runs

Heterogeneous fracture permeability Tptpmn THC Model simulations were performed using the same two sets of chemical components and mineral assemblages as those used for the no-backfill Tptpmn THC Model simulations presented in Section 6.4 (extended case, and base case,

(Table 8). All simulations were performed using the mean infiltration rate climate change scenario (Table 12). TOUGHREACT V2.3 [153101] was used for all simulations.

Table 16. Tptpmn THC Heterogeneous Model Runs

Infiltration-Property Set (Table 12)	**Permeability Realization**	**Geochemical System (Table 8)**	**Simulation Type**	**Run ID (used in DTN:LB0011DSTTHCR1.001; Attachment XI)**
Mean Infiltration	#1	None	Steady-State	ds00ss_het1
		None	TH	ds00th_het1
		Extended Case	Ambient	ds00amb1_het1
		Base Case	Ambient	ds00amb2_het1
		Extended Case	THC	ds00thc1_het1
		Base Case	THC	ds00thc2_het1
Mean Infiltration	#2	None	Steady-State	ds00ss_het2
		None	TH	ds00th_het2
		Extended Case	THC	ds00thc1_het2
		Base Case	THC	ds00thc2_het2
Mean Infiltration	#3	None	Steady-State	ds00ss_het3
		None	TH	ds00th_het3
		Extended Case	THC	ds00thc1_het3
		Base Case	THC	ds00thc2_het3

6.5.2 Simulation Results

6.5.2.1 Hydrological Effects of Fracture Permeability Heterogeneity

Steady-state liquid saturations obtained for the three heterogeneous permeability fields with an infiltration rate of 6 mm/yr show a range of fracture saturations from approximately 2% to 90% (Figures 73a–c). This large range results from the roughly four order-of-magnitude variation in fracture permeability and its effect on capillary pressure through the Leverett scaling relation (Equation 24). For comparison, the steady-state fracture liquid saturation for the Tptpmn in the Tptpmn THC model simulations (homogeneous permeability) was about 4.7%. The greatest differences in fracture saturation are within about 3 meters of the drift wall, where there was little or no averaging of the stochastically-generated fine-scale permeabilities. Because some of the mesh volumes have high fracture liquid saturations, there exists an initial condition more conducive to seepage, although these regions also have much smaller absolute permeabilities. Further from the drift, differences in fracture saturation between grid nodes are much less, owing to the much smoother averaged permeabilities.

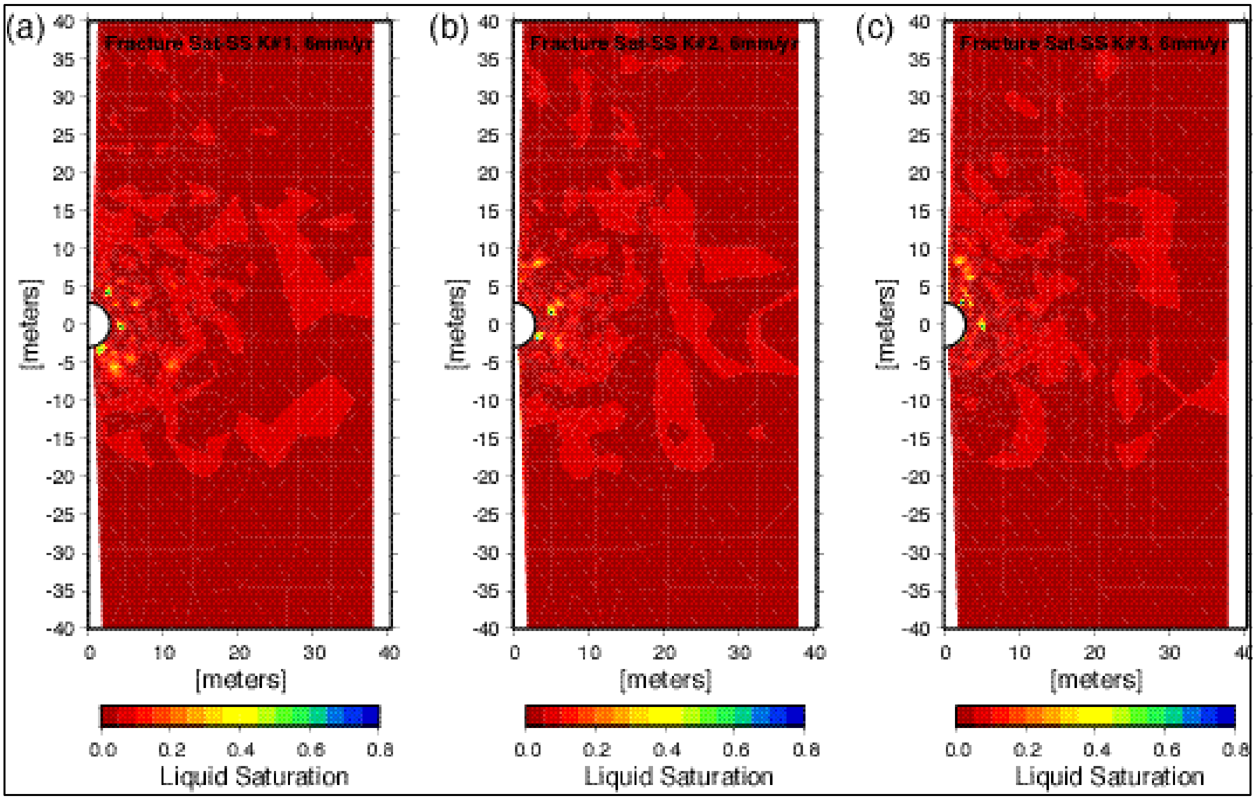

DTN: LB0011DSTTHCR1.002

Figure 73. Steady-State Fracture Liquid Saturations (Infiltration Rate = 6 mm/yr) for Permeability Realizations #1 (a), #2 (b), and #3 (c).

6.5.2.2 Thermal-Hydrological Effects of Fracture Permeability Heterogeneity

Heterogeneity in fracture permeability can have varied effects on thermohydrology, including flow-focusing and irregularity in isotherms and liquid saturations. Thermohydrological simulations were performed for the three heterogeneous fracture permeability realizations under the mean infiltration climate change scenario. Fracture liquid saturation at approximately the maximum extent of the dryout zone (600 years) for the three permeability realizations are shown in Figures 74a–c. This time is just prior to an increase in infiltration rate from 6mm/yr to 16 mm/yr. Regions of higher fracture liquid saturation are evident within the zone that is predominantly dry, with a maximum penetration of no more than one meter. Strong local differences in fracture liquid saturations are much greater than the more disperse overall effect of condensate shedding, although it is clear that the higher saturation areas are concentrated above and to the side of the drift, with the zone below the drift significantly drier.

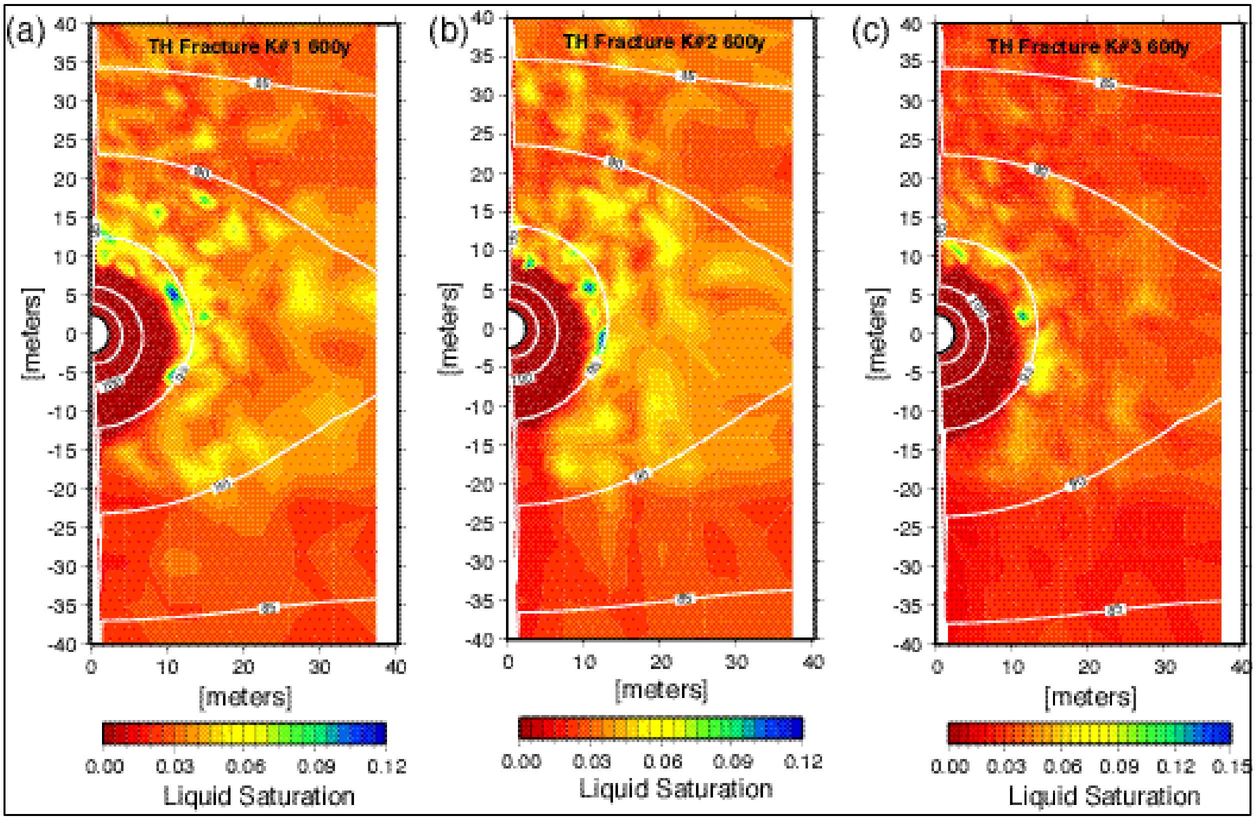

DTN: LB0011DSTTHCR1.002

Figure 74. Fracture Liquid Saturations at 600 Years from Thermohydrological Simulations (Infiltration Rate = 6 mm/yr) for Permeability Realizations #1 (a), #2 (b), and #3 (c).

Matrix liquid saturations were not affected significantly by the variations in fracture permeability, and their distribution is similar to those for the simulations employing a homogeneous Tptpmn unit.

6.5.2.3 THC Effects of Fracture Permeability Heterogeneity

The two most important questions regarding the effect of fracture permeability heterogeneity on THC processes are (1) the effect on flow owing to localized mineral precipitation or dissolution, and (2) the effect on water chemistry that may seep into drifts.

6.5.2.3.1 THC Effects on Permeability and Liquid Flow in a Heterogeneous Medium

The conceptual model for fracture permeability changes employed in the THC simulations of the heterogeneous Tptpmn THC Model (and those in Sections 6.2.8, 6.4, and 6.6) is based on changes to the hydraulic aperture, resulting from mineral precipitation or dissolution, as described in Section 6.1.6.2 Eq. 19-22. Therefore, changes in fracture permeability are much more sensitive to changes in porosity than the cubic law formulation dependent directly on porosity changes (Eq. 18) used for the simulations in Section 6.3.

Changes in fracture permeability after 20,000 years are shown as the ratio of the permeability to its initial value in Figure 75 for the extended and base-case geochemical systems (Realization

#1). Areas of highest initial liquid saturation, also having lower permeability and generally residing above the drift, tend to show the greatest reduction in fracture permeability, reaching a minimum of about 25% of the initial value. The effect of this localized permeability reduction tends to cause some additional flow focusing. However, the permeability changes are considerably less than the initial range in permeability. The corresponding maximum fracture porosity reductions are approximately 5% of the initial value. Porosity reductions for the extended geochemical system are slightly greater than those for the base-case system, owing to more mineral species precipitating and somewhat higher silica concentrations in the former.

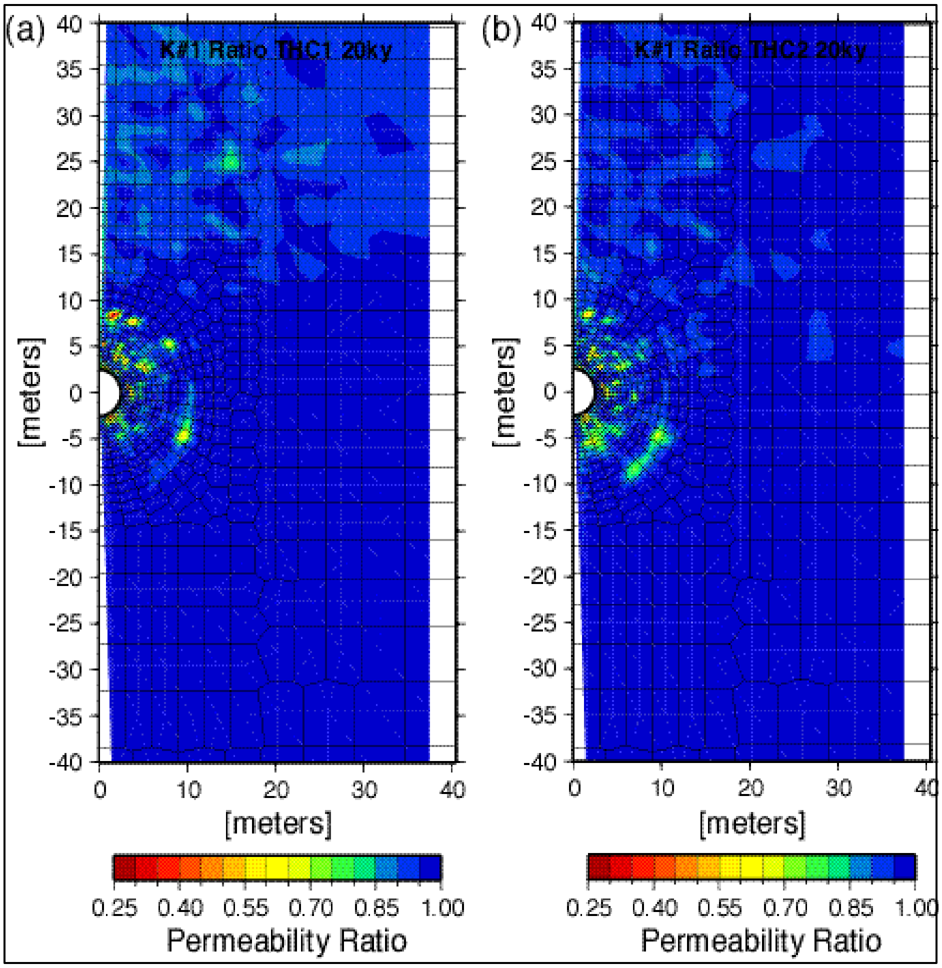

DTN: LB0011DSTTHCR1.002

Figure 75. Fracture Permeability Ratio after 20,000 Years for Realization #1. (a) Extended Geochemical System. (b) Base-Case Geochemical System

Spatial variations in fracture liquid saturation as a result of permeability reduction from mineral precipitation are little different from the effect of the initial heterogeneity. Fracture saturations after 20,000 years show a similar distribution to the steady-state pattern, although somewhat higher overall because of a larger infiltration rate (at 600 years and 2,000 years) than those of the 6 mm/yr steady-state simulation (Figure 76). This similarity implies that liquid fluxes to the drift wall are not dramatically modified. Otherwise, significant changes in liquid saturation near the drift wall would be evident.

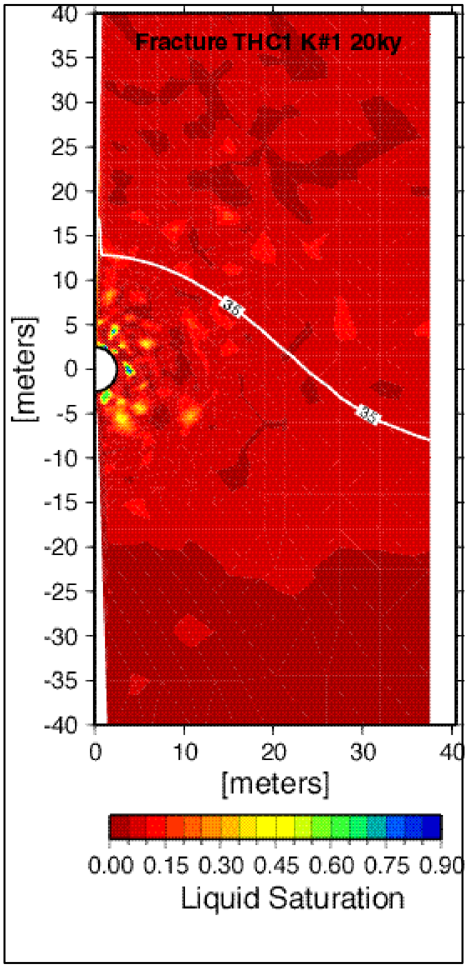

DTN: LB0011DSTTHCR1.002

Figure 76. Fracture Liquid Saturation for Realization #1. THC Simulation (Extended Case) after 20,000 Years

6.5.2.3.2 THC Effects on Geochemistry in a Heterogeneous Medium

Spatial differences in liquid saturation within fractures, resulting from variations in capillary suction, affect geochemical reactions in a number of ways. Reactive surface areas increase with increasing saturation via the modified active fracture model (Eq. 16). Given roughly uniform concentrations, higher liquid saturation results in a greater amount of precipitate formed during complete evaporation. Higher liquid saturations also lead to an increase in the liquid relative permeability, which tends to reduce the effect of lower absolute permeability on flow and transport in these same fractures. Relatively small variations in aqueous-species concentrations at a particular time may lead to much larger differences in mineral abundances, owing to a cumulative effect over time.

Quantitatively, minerals such as amorphous silica and calcite may be the most important for changing permeability and affecting flow (although clays and to a lesser extent zeolites have the potential for reducing permeability at smaller degrees of alteration due to their higher surface area and/or lower density than the primary minerals). Amorphous silica is undersaturated in the ambient pore water at Yucca Mountain and thus precipitates only when the silica concentration in the water increases significantly, which usually occurs during evaporation or boiling. Up to the point of boiling, silica tends to increase in heated waters because of its increased solubility and the increased reaction rate of such minerals as cristobalite, tridymite, quartz, and feldspars. As temperatures decline to below the boiling point and rewetting occurs, amorphous silica tends to redissolve slowly because percolating waters eventually trend to the ambient composition.

The distribution of amorphous silica after 20,000 years is shown for both geochemical cases in Figure 77. The precipitation patterns in the two cases are similar, with maximum amounts in the high saturation zones near the drift. The maximum amount of amorphous silica precipitated is about 2% (volume % of fracture) in the extended case and somewhat less in the base case. This overall behavior is consistent with the results of the DST validation studies, which showed the extended case giving higher silica concentrations in refluxing waters. Because the higher silica concentrations in the DST extended-case simulations are closer to the measured concentrations in waters sampled from boreholes (Figure 24), the extended case likely produces more justifiable amounts of precipitated silica in the Tptpmn THC model simulations.

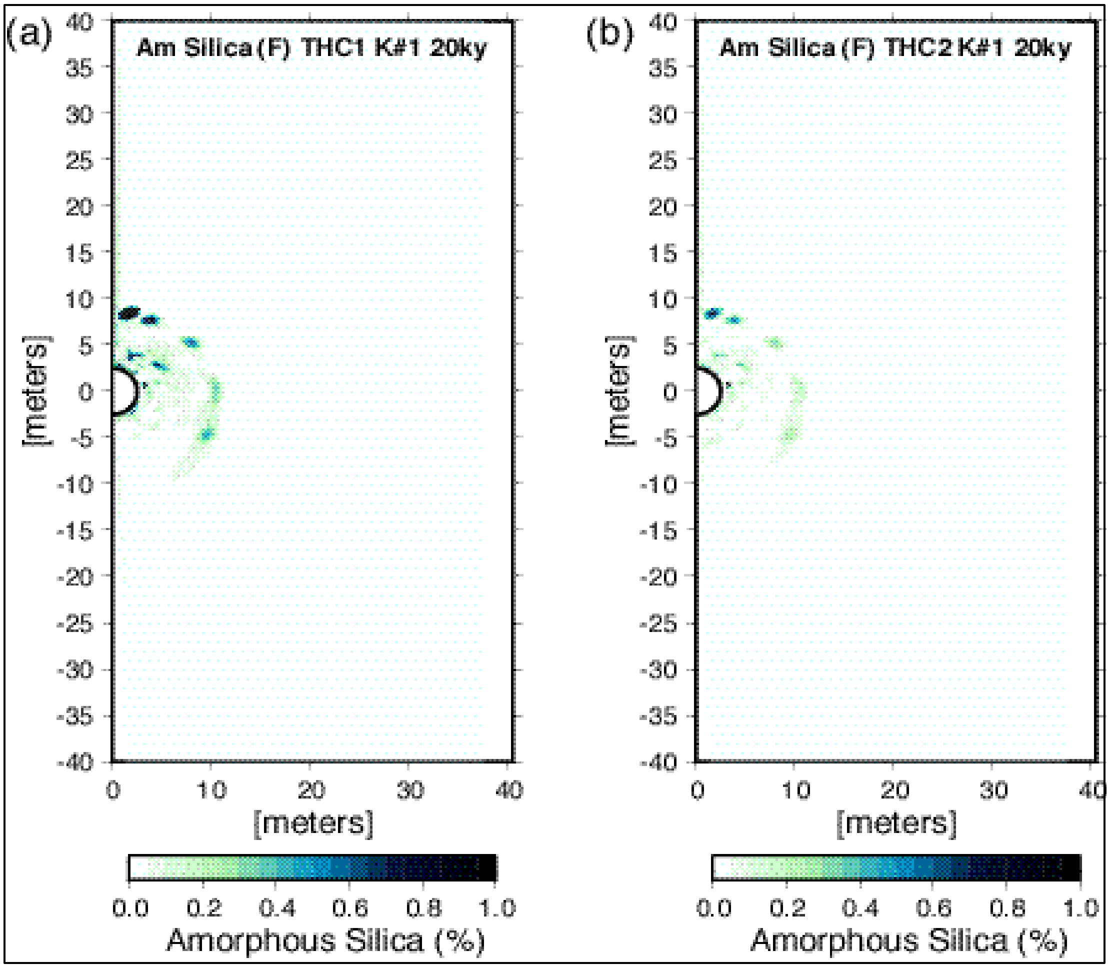

DTN: LB0011DSTTHCR1.002

Figure 77. Amorphous Silica Changes (Volume %) in Fractures after 20,000 Years for Realization #1: (a) Extended Geochemical System; (b) Base-Case Geochemical System

Calcite is an important phase because it provides a strong buffer for preventing the formation of acidic waters and is the major source of calcium and carbonate in the rock. The extended case considers calcite as an equilibrium mineral for Tptpmn THC simulations. Calcite becomes less soluble with increasing temperature and pH and therefore shows a broader area of precipitation (Figure 78) than for amorphous silica (Figure 79). In the vicinity of the drift, calcite is more abundant in the base-case simulations, whereas in the extended case more calcite is deposited in the Topopah Spring Upper lithophysal unit (Tptpul) above the drift, leading to less precipitation around the drift. Maximum calcite abundances are about 1.4% (volume % of fracture).

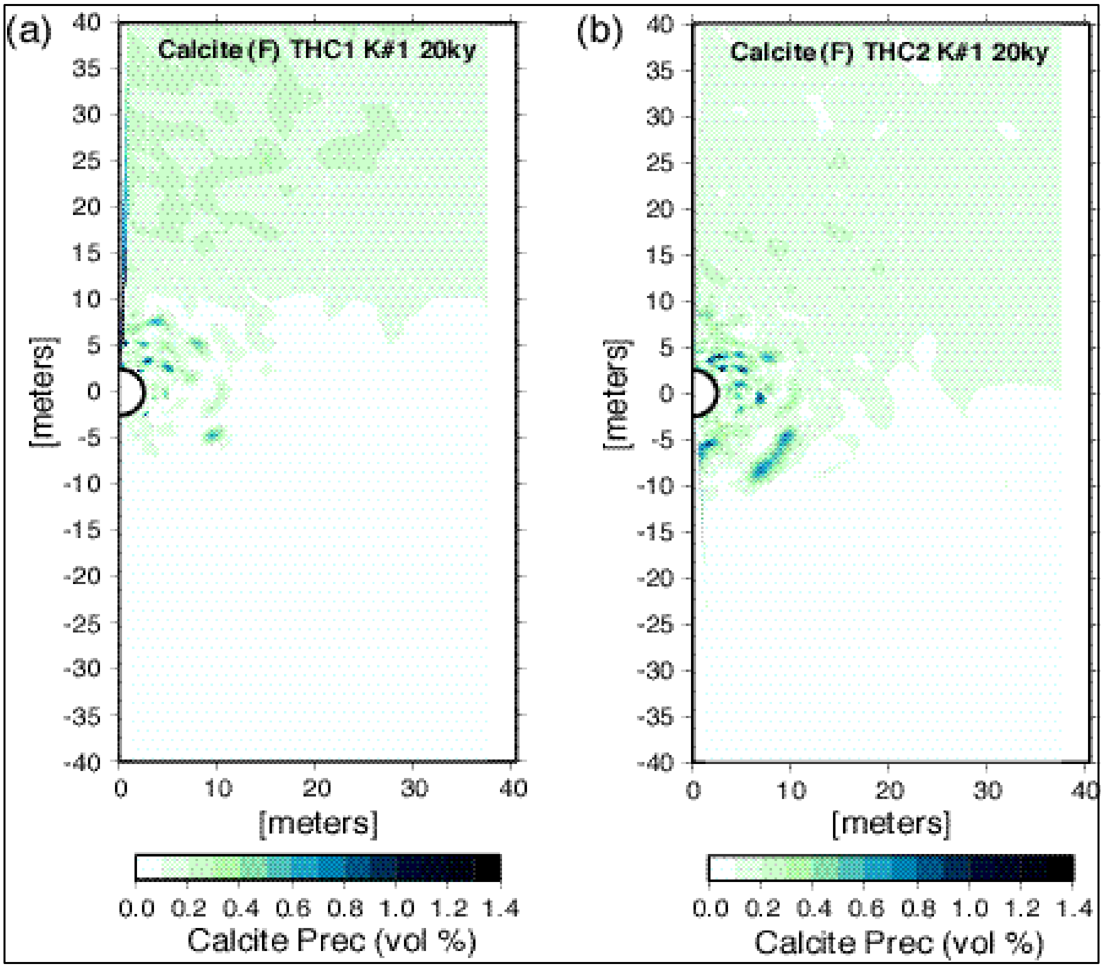

DTN: LB0011DSTTHCR1.002

Figure 78. Calcite Changes (Volume %) in Fractures after 20,000 Years for Realization #1: (a) Extended Geochemical System; (b) Base-Case Geochemical System

Clays are important because of their greater potential for reducing permeability and as potential sorbers of radionuclides. Precipitated clay phases are very low in abundance with a maximum illite volume percent of less than 0.0001 after 20,000 years (Figure 79). In zones of low permeability and high fracture saturation, the largest quantities of illite form, with the homogeneous Tptpmn showing a much more uniform band of illite around the drift and at the contact of the Tptpul with the Tptpmn.

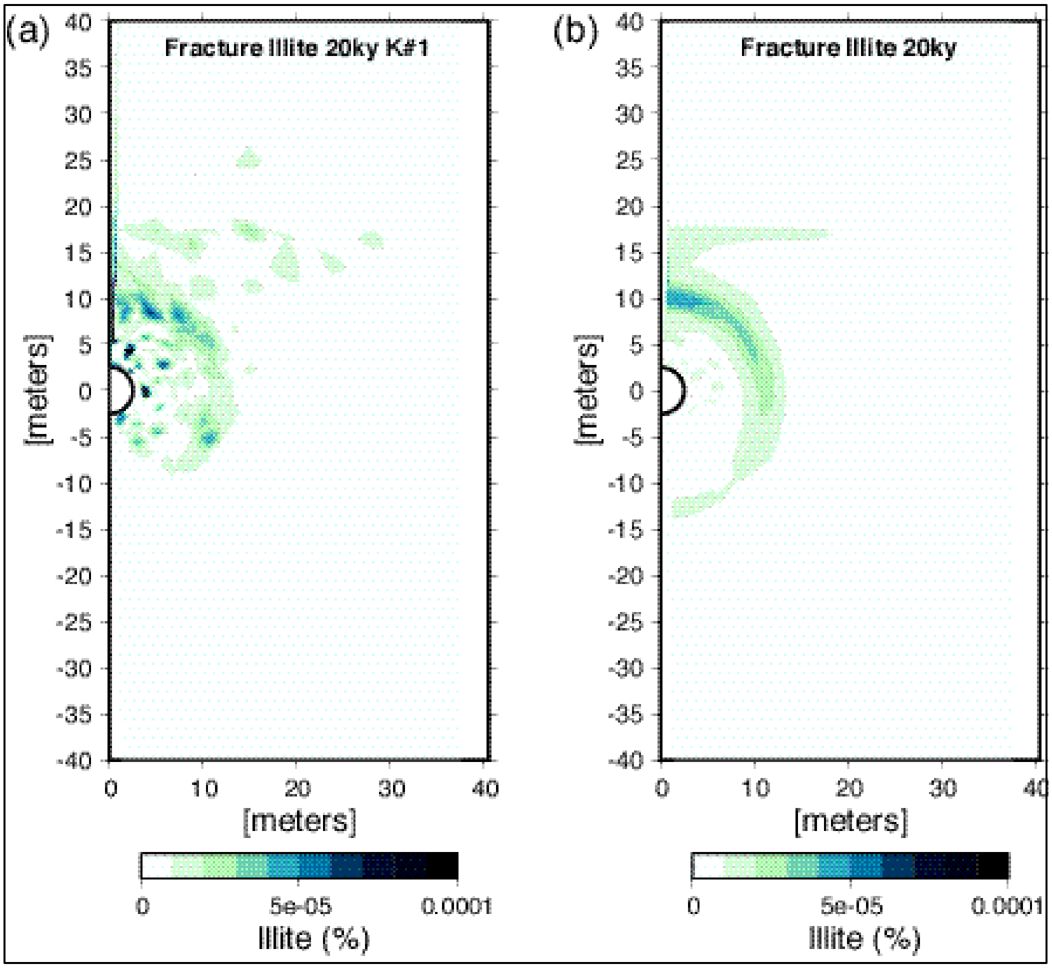

DTN: LB0011DSTTHCR1.002

Figure 79. Illite Changes (Volume %) in Fractures after 20,000 Years for Realization #1: (a) Extended Geochemical System–Permeability Realization #1; (b) Extended Geochemical System–Initially Homogeneous Tptpmn

The distribution of pH in fracture water near the time of maximum dryout (600 years) is shown in Figure 80, using the extended geochemical case for Permeability Realization #1. White areas are zones of dryout. For comparison to the model without locally heterogeneous permeability initial conditions, the pH for that simulation is shown in Figure 80b for the extended geochemical system. Small local variations appear in the pH of water in fractures due to the permeability heterogeneities, but otherwise the distribution is similar to the system without heterogeneities. A large plume of higher pH (maximum about pH 9) fracture water formed around the drift and is transported below the drift via percolation. At the approximate time of crown rewetting at 1400 years (Figure 81), the pH of fracture water around the drift is in the range of 8 to 8.5 for the extended case, similar to the initial pore water and 0.5 to 1 unit higher than for the base case. The higher pH water near the drift at 600 years is well below the drift after 1,400 years. (Recall that the infiltration rate increased to 16 mm/yr from 6 mm/yr at 600 years.) The pH increase is due to CO_2 degassing from the pore water upon heating and to the alteration of feldspars to clays (extended case), which consumes H^+.

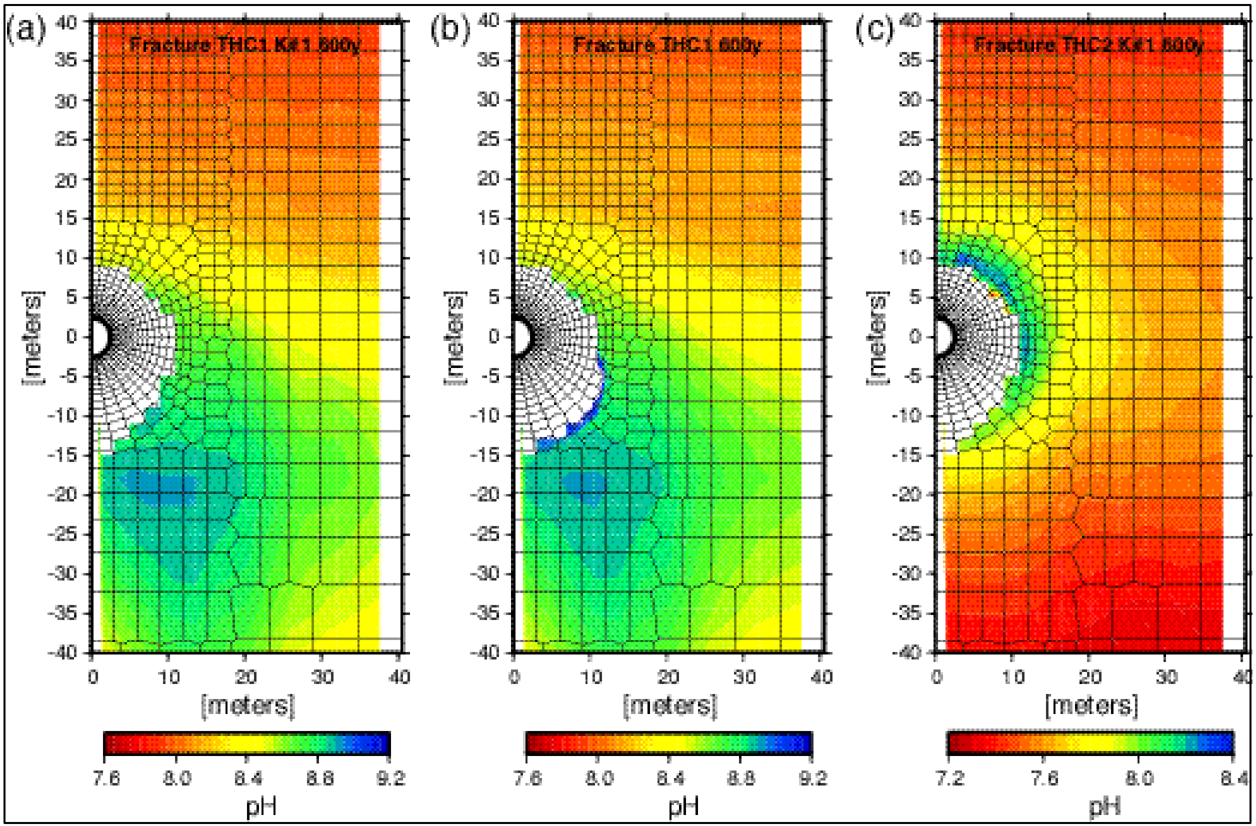

DTN: LB0011DSTTHCR1.002

Figure 80. Fracture Water pH after 600 Years (white area is dry): (a) Extended Geochemical System–Permeability Realization #1; (b) Extended Geochemical System–Initially Homogeneous Tptpmn; (c) Base-Case Geochemical System

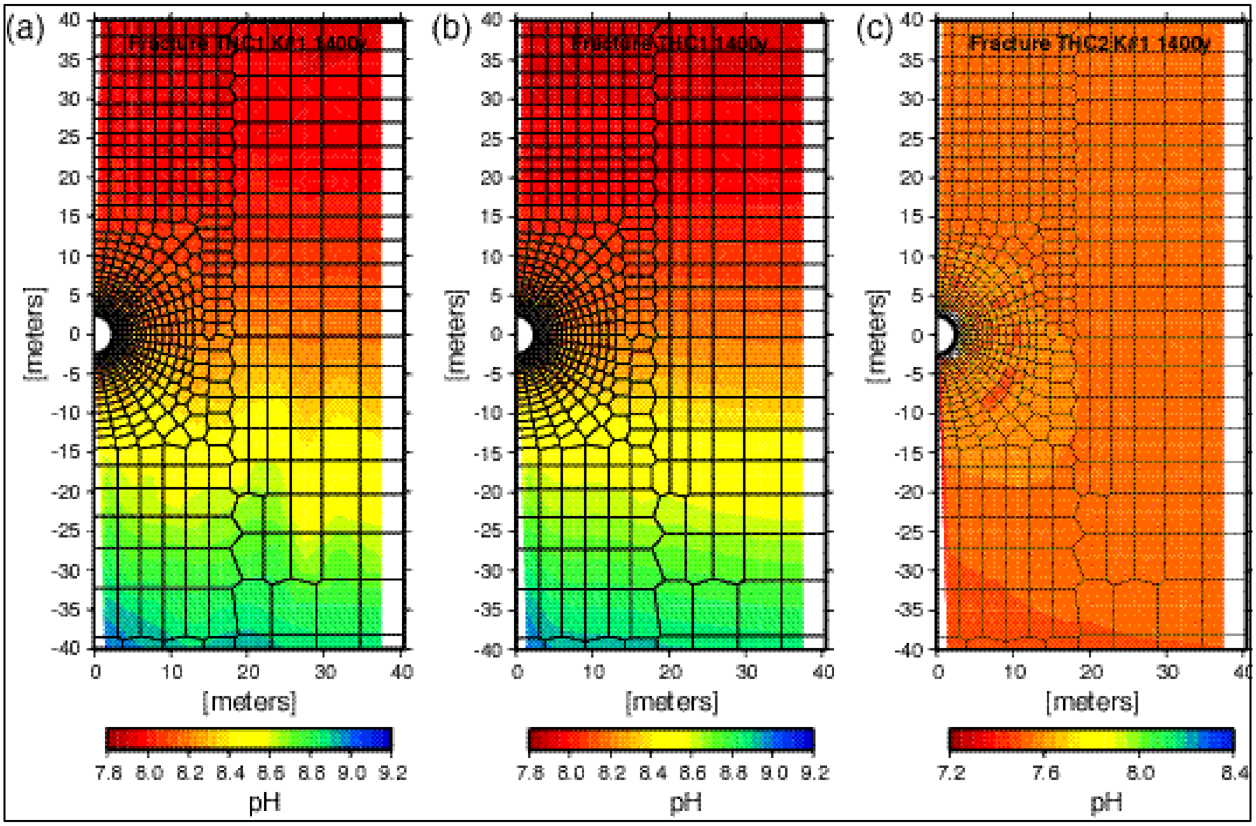

DTN: LB0011DSTTHCR1.002

Figure 81. Fracture Water pH after 1,400 Years (white area is dry): (a) Extended Geochemical System–Permeability Realization #1; (b) Extended Geochemical System–Initially Homogeneous Tptpmn; (c) Base-Case Geochemical System

Chloride is an important indicator of salt-concentration effects, because the solubility of sodium chloride is very high and chloride is essentially conservative up to the limit of halite saturation. Chloride concentrations after 600 years (log scale) are shown in Figure 82 and show a very narrow region of higher concentrations at the edge of the boiling zone surrounded by a much larger zone of dilute concentrations. An extensive, more dilute drainage zone is prominent for several tens of meters below the drift. This zone reflects the processes of strong dilution resulting from condensate formation, with limited fracture-matrix interaction, fracture drainage, and condensate shedding around the drift. The lowest concentrations are below the drift, where condensate formation in the shadow zone has experienced the least amount of mixing with the ambient percolation flux. The highest concentrations tend to be above the drift, where reflux and boiling of the ambient percolation flux is greatest.

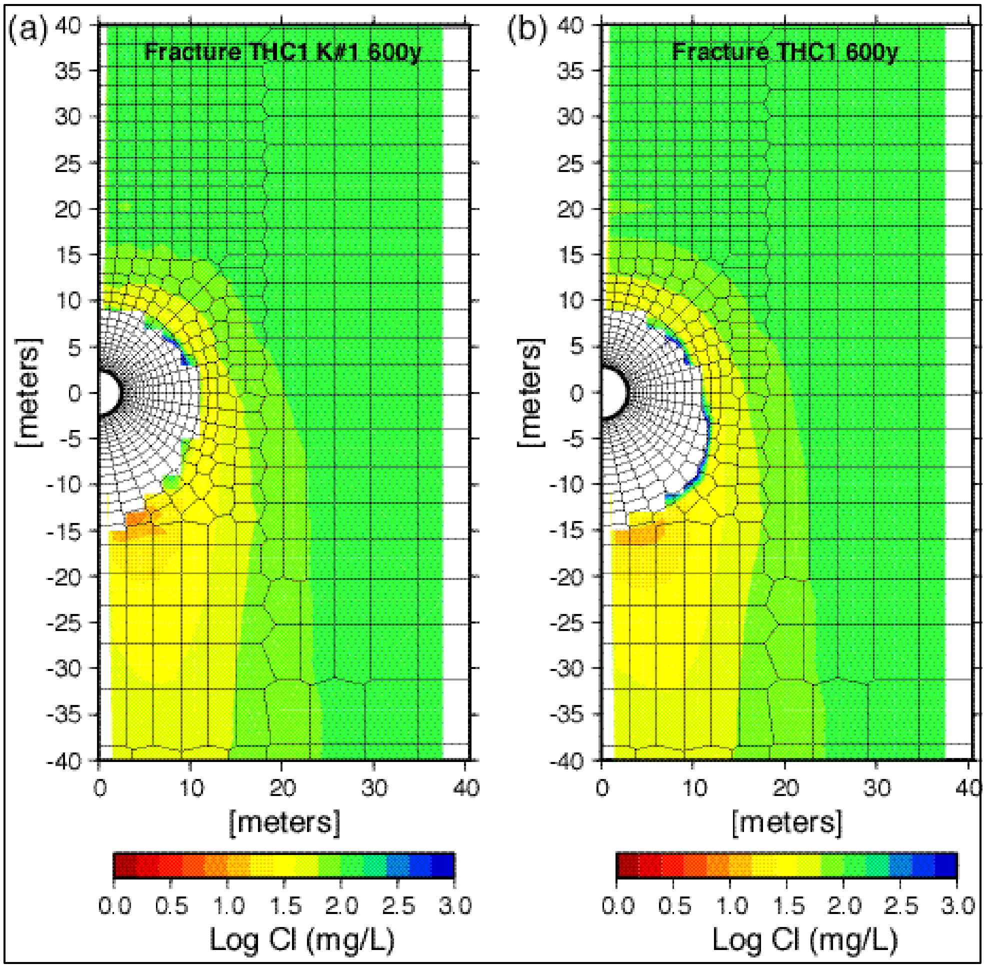

DTN: LB0011DSTTHCR1.002

Figure 82. Chloride (Cl) Concentrations in Fracture Water after 600 Years: (a) Extended Geochemical System–Permeability Realization #1; (b) Extended Geochemical System–Initially Homogeneous Tptpmn

Fluoride is a minor constituent in the aqueous phase, but is important from the standpoint of waste package corrosion. Fluoride (F) concentrations after 600 years are shown in Figure 83 and show a similar pattern as Cl, except for at the very edge of the dryout zone where fluorite precipitation has somewhat buffered any increases in F concentrations. Because there are no fluorine-bearing minerals in the initial mineral assemblage, these results may be a lower range of the fluoride concentration in the seepage flux. Further studies in the following section employ fluorite as a initial phase in the rock and therefore bound the upper limit of fluoride addition to refluxing waters.

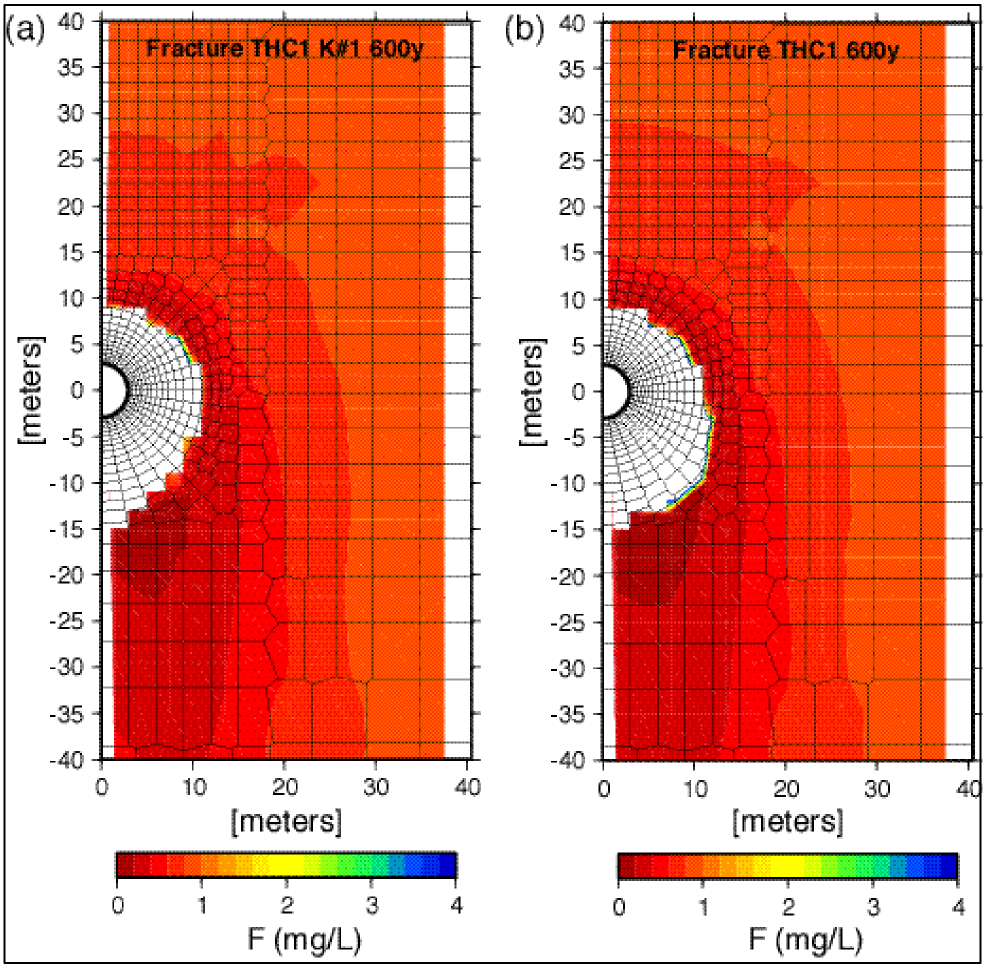

DTN: LB0011DSTTHCR1.002

Figure 83. Fluoride (F) Concentrations in Fracture Water after 600 Years: (a) Extended Geochemical System–Permeability Realization #1; (b) Extended Geochemical System–Initially Homogeneous Tptpmn

6.6 Tptpll THC MODEL

The Tptpll THC model presented in this section is similar to the model presented in Sections 6.4 and 6.5, with an almost identical drift design (no backfill), identical heat load, and drift thermal properties. The main difference is that the drift is located in the Topopah Spring Tuff lower lithophysal geologic unit (Tptpll unit, which corresponds to model layer tsw35, DTN: LB990501233129.004 [111475]). Most of the potential repository is planned to be located in the Tptpll unit. The stratigraphy of this model was taken at a location near the center of the potential repository (at approximately Nevada State Plane coordinates E170572, N233195), close to the area of the proposed CDTT.

The main differences between the Tptpll model described here and the Tptpmn model described in Sections 6.4 and 6.5 are the following:

- The drift is located in the Tptpll unit.

- The invert thickness was increased from 0.6 to 0.8 m (Section 4.1.7.3).
- Updated hydrological properties were calculated, including fracture permeabilities for most units of the Topopah Spring Tuff, capillary properties of the Tptpll, and fracture porosities of all units (except Tptpmn) (Section 4.1.2.2).
- Updated rock mineralogy, volume fractions, and mineral surface areas have been calculated for all units (Section 4.1.2.2, Attachments II and IV), with the addition of an opal phase in both the base-case and extended-case geochemical system (Table 8).

Although calibrated hydrological properties for this unit are used, lithophysae are not directly incorporated in the model, and therefore thermohydrological processes and associated chemical processes may be different from those in areas of high lithophysal porosities.

6.6.1 Numerical Mesh (Tptpll)

Simulations were performed on a vertical 2-D mesh based on the same drift spacing and diameter as for the Tptpmn THC Backfill Model (Section 6.3.1). Rock properties are assumed laterally homogeneous between drifts (Section 5, Assumption A-18) and, as in the Tptpmn THC models, the mesh is reduced to a 2-D half-drift model with a width of 40.5 m, corresponding to the midpoint between drifts (Figure 84). Geologic data from column “j34” of the UZ99_2_3D calibration model (DTN: LB990501233129.004 [111475]) were used to map geologic contacts into the 2-D mesh, and the mesh coordinate system was set with reference to the center of the drift (Table 17).

In an attempt to diminish grid orientation effects, the mesh design is mostly orthogonal, with a small radially gridded area in the immediate vicinity of the drift (Figure 84). The area extending approximately 40 m above the drift is more finely gridded than other areas to capture THC effects potentially affecting seepage into the drift. Outside the drift, the smallest grid spacing was specified at the drift wall (20 cm), and increasing outward. A constant square cell size of 50 cm was used from approximately 5 m to 7 m above drift center, increased to a 1-meter size until 15 m above drift center, then a 2-meter size from 15 to 30 m above drift center. Unlike the Tptpmn THC models, all geologic layers down to the water table below the modeled drift were incorporated into the numerical mesh (Table 17). Cell sizes increase significantly 100 m above and below the drift to increase computing efficiency. The mesh consists of 3202 gridblocks, including those representing matrix, fracture, and in-drift design elements.

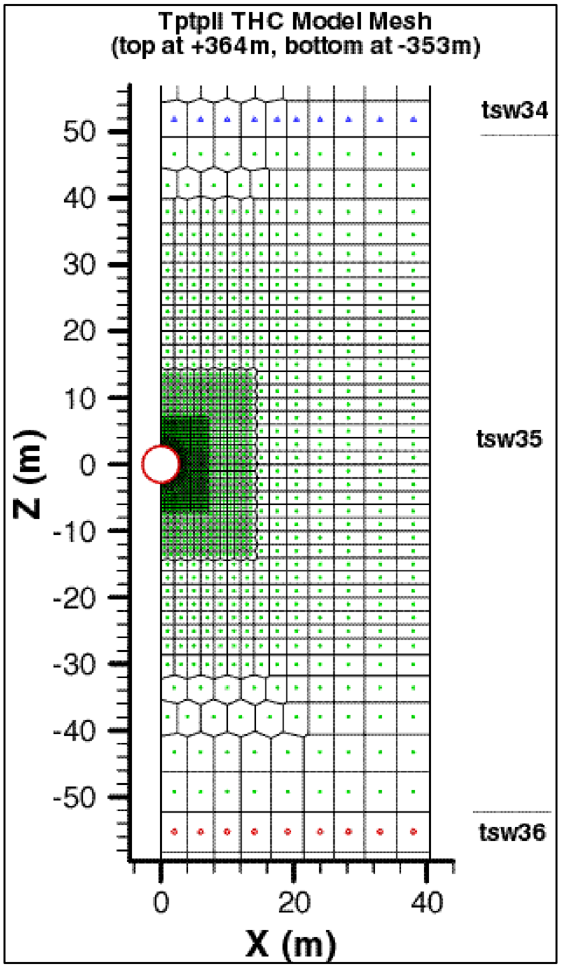

DTN: LB0011DSTTHCR1.002

NOTE: Grid detail around (0, 0) is shown in Figure 85.

Figure 84. Tptpll THC Model Mesh with Hydrogeologic Units Shown in the Vicinity of the Drift: Topopah Spring Tuff Middle Non-Lithophysal (tsw34 - triangles), Lower Lithophysal (tsw35 - dots), and Lower Non-Lithophysal (tsw36 - diamonds) Units.

Table 17. Vertical Mesh Dimensions and Geologic Contacts in the Tptpll THC Model

Model Layer	Top of Layer Elevation (masl)	Mesh Top of Layer Z Coordinate (m)
Top	1446.603	363.8
tcw11	1446.603	363.8
tcw12	1419.207	336.4
tcw13	1342.069	259.3
ptn21	1326.522	243.7
ptn22	1323.124	240.3
ptn23	1321.025	238.2
ptn24	1318.155	235.4
ptn25	1312.685	229.9
ptn26	1303.632	220.8
tsw31	1294.066	211.3
tsw32	1279.722	196.9
tsw33	1249.282	166.5
tsw34	1169.183	86.4
tsw35	1131.994	49.2
Drift center	1082.786	0.0
tsw36	1030.606	-52.2
tsw37	997.393	-85.4
tsw38	980.786	-102.0
tsw39	966.954	-115.8
ch1v	956.871	-125.9
ch2v	945.213	-137.6
ch3v	931.902	-150.9
ch4z	919.160	-163.6
ch5z	906.417	-176.4
ch6	892.394	-190.4
pp4	878.488	-204.3
pp3	865.850	-216.9
pp2	833.243	-249.5
pp1	818.227	-264.6
bf3	756.684	-326.1
Bottom	730.00	-352.8

DTN: LB0011DSTTHCR1.002 (model)
LB990501233129.004 [111475] (geologic column)

The drift discretization was unchanged from the Tptpmn model. However, node designations were changed to account for the absence of backfill and a thicker invert (0.8 m) reflecting a more recent drift design (CRWMS M&O 2000 [150953], p. 22). As in the Tptpmn THC no-backfill model, the invert was divided into an "upper invert" and a "lower invert" (Figure 85) for assignment of different thermal conductivities (Section 4.1.7.3) in these zones. The pre-closure and post-closure configurations implemented in this model are otherwise similar to those implemented previously (Section 4.1.7.2 and 6.4.1).

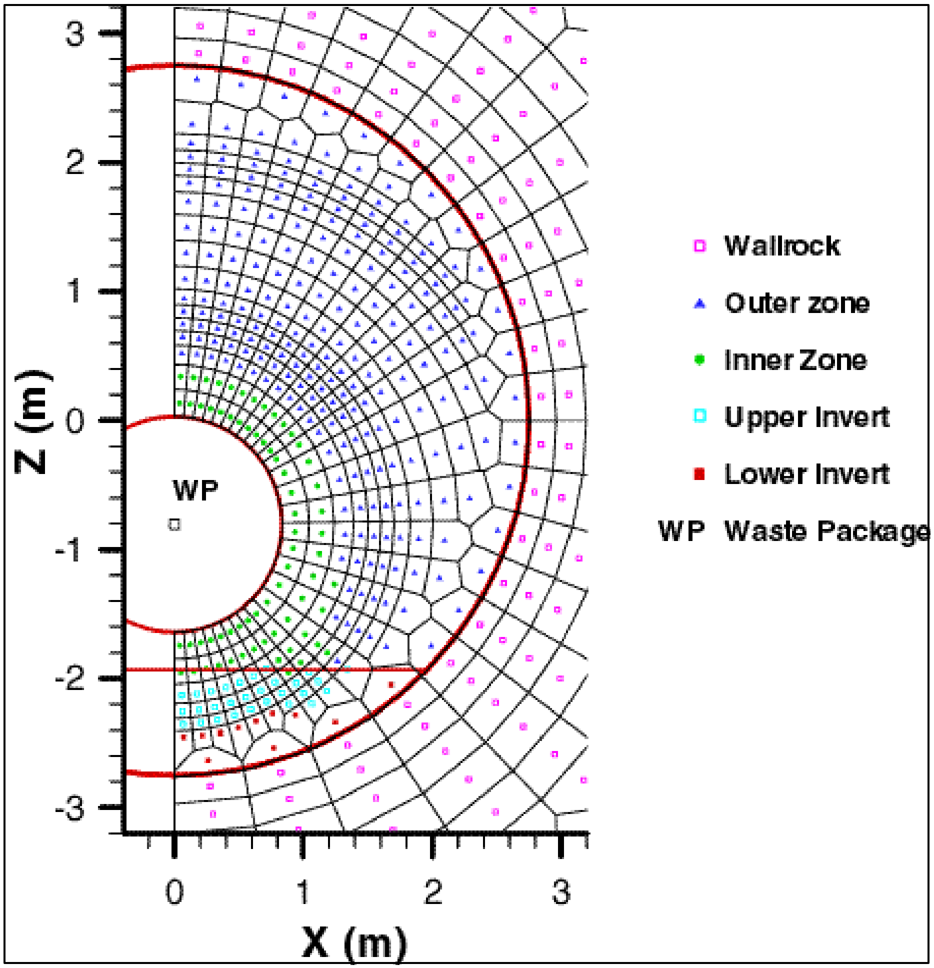

DTN: LB0011DSTTHCR1.002

Figure 85. Discretization of the Repository Drift in the Tptpll THC Model

6.6.2 Boundary Conditions

Boundary conditions were set according to those appropriate for the column location near the repository center (DTN: LB990701233129.002 [125604]). The pressure and temperatures are constant at the top and bottom boundaries. The exception that the initial CO_2 partial pressure in the drift was set to the ambient CO_2 partial pressure in the adjacent wallrock, instead of near-atmospheric (a difference having essentially no effect on model results). As for the Tptpmn THC No-Backfill Model, only the mean infiltration regime was implemented (Table 12).

6.6.3 Input Data and Modeling Procedure

The Tptpll THC model was run using TOUGHREACT V2.3 [153101] and similar input data as discussed in Section 6.4.3 for the Tptpmn THC No-Backfill Model. Exceptions are revised rock properties (Section 4.1.1.2), revised mineralogy and mineral surface areas (Section 4.1.2.2, Attachments II and IV), and an opal phase added to the base-case and extended-case geochemical systems (Table 8). Calcite was also considered as an equilibrium mineral, with the same precipitation gap as discussed in Section 6.4.3. The time-stepping scheme was also identical to the scheme used for the Tptpmn THC No-Backfill Model.

Revisions to rock properties included new fracture permeability, porosity, and capillary properties for the Tptpll, calibrated in part using recent data from field tests conducted in the Tptpll unit (Section 4.1.1.2). These properties, compared to Tptpmn properties, reflect a higher fracture porosity (0.018 vs. 0.01), and permeability (2.4×10^{-12} vs. 3.7×10^{-13} m^2) and higher capillarity (van Genuchten $\alpha = 8.23 \times 10^{-5}$ vs. 5.16×10^{-4} Pa^{-1}). The revised Tptpll properties in this model, however, do not reflect possible increased storage due to the presence of lithophysae, as these effects are still being investigated.

6.6.4 Model Runs

Five simulations were performed and are summarized in Table 18.

Table 18. Tptpll THC Model Runs

Infiltration-Property Set (Table 12)	Geochemical System (Table 8)	Simulation Type	Run ID (used in DTN: LB0011DSTTHCR1.001; Attachment XI)
Mean Infiltration	None	TH	th6_16_25_g4
Mean Infiltration	Base Case	THC	thc6_16_25_2g4
	Base Case	THC - Ambient	thc6_16_25 _2g4_amb
	Extended Case	THC	thc6_16_25_g4
	Extended Case	THC - Ambient	thc6_16_25_g4_amb

6.6.5 Simulation Results

Model results are presented below in Figures 86 through 107. As for the Tptpmn THC models, the focus is given to areas in the vicinity of the drift. Profiles of various predicted THC parameters through time are examined at three locations around the modeled drift: crown (model nodes F121 and M 121, side (nodes F 44 and M 44) and base (nodes F 128 and M 128). The locations correspond to the same locations, relative to drift center, to those in the Tptpmn THC models. These output results were tabulated and submitted to the technical database under DTN: LB0011DSTTHCR1.001 and are further discussed below.

6.6.5.1 Thermohydrology Simulation Results (Tptpll versus Tptpmn)

Calculated trends of thermohydrologic parameters in the Tptpll unit (Figures 86 to 92) are similar to those modeled previously in the Tptpmn unit. Nevertheless, several differences in the actual values of these parameters are noteworthy. Peak temperatures (shortly after ending ventilation) are higher by approximately 20°C in the Tptpll (Figures 86 and 88). Both dry and wet thermal conductivities of the Tptpll are lower than in the Tptpmn (by 23 and 13 %, respectively). The maximum size of the dryout zone, despite the higher temperatures, decreases slightly (approximately 12 m below, 9 m to the side and 8 m above drift center) (Figure 87) compared to the dryout extent in the Tptpmn (Figure 55), because of the higher fracture capillarity in the Tptpll. The time at which maximum dryout is calculated to occur remains near

600 years, as for the Tptpmn model simulations. (This is also the time at which the model infiltration rate increases from 6 to 16 mm/yr).

At the base of the drift, fracture saturations in the Tptpll (Figure 89) are larger than in the Tptpmn, and remain non-zero for a large part of the pre-closure period (compared to zero values in the Tptpmn model). This results from the thicker invert combined with the higher fracture capillarity in this model. In fractures at locations not shadowed by the drift, and in the matrix, predicted liquid saturations are smaller than in the Tptpmn (Figures 89 and 90). In fractures at the drift crown, these saturations are approximately 60% smaller because of the larger fracture and matrix permeabilities in the Tptpll. Calculated air mass fractions before and after dryout are also lower (higher water vapor content) than in the Tptpmn (Figure 91), because of the higher temperatures (thus greater evaporation) in the Tptpll (Figure 88).

The steady state (pre- and post-thermal load) vertical liquid flux at the drift crown in the Tptpll is close to half that in the Tptpmn (Figure 92). This is because fracture and matrix permeabilities in the Tptpll are larger (by approximately one order of magnitude) than in the Tptpmn, allowing for more lateral flow around the drift than if the permeabilities were lower. The drift crown remains well below full saturation and therefore, the drift acts as a capillary barrier due to the air entry pressure. For both the Tptpll and Tptpmn cases, the flux peak at rewetting (Figure 92) may not be fully resolved. More output points over smaller time intervals may be required for a better definition.

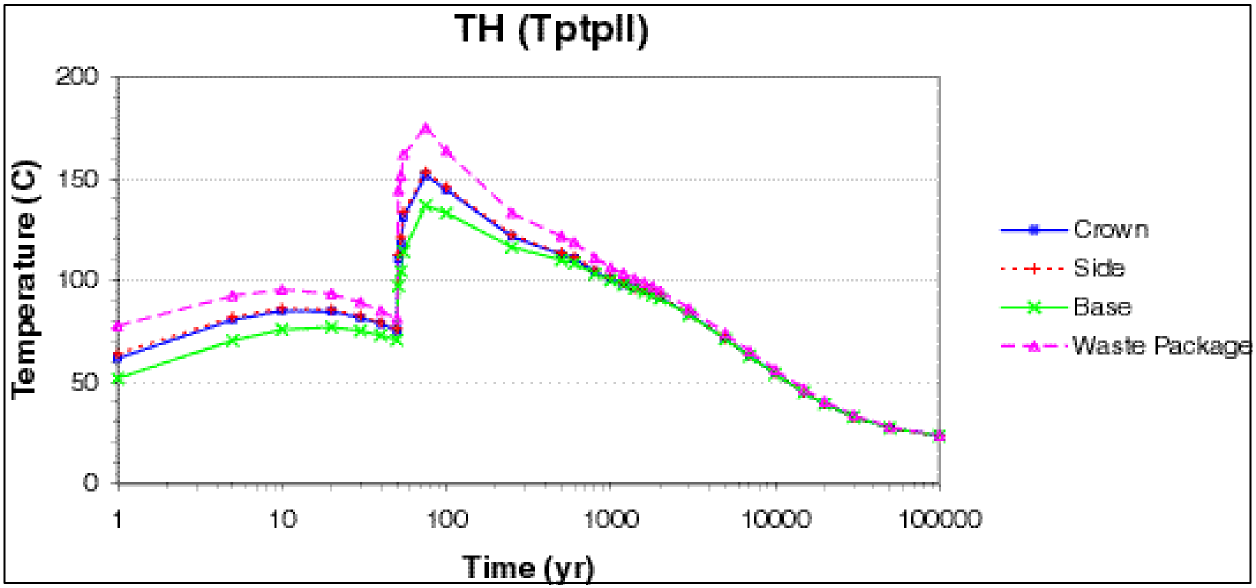

DTN: LB0011DSTTHCR1.001

Figure 86. TH Simulation (Tptpll). Time Profiles of Modeled Temperatures in Fractures (Similar in Matrix) at Three Drift-Wall Locations and in the Waste Package.

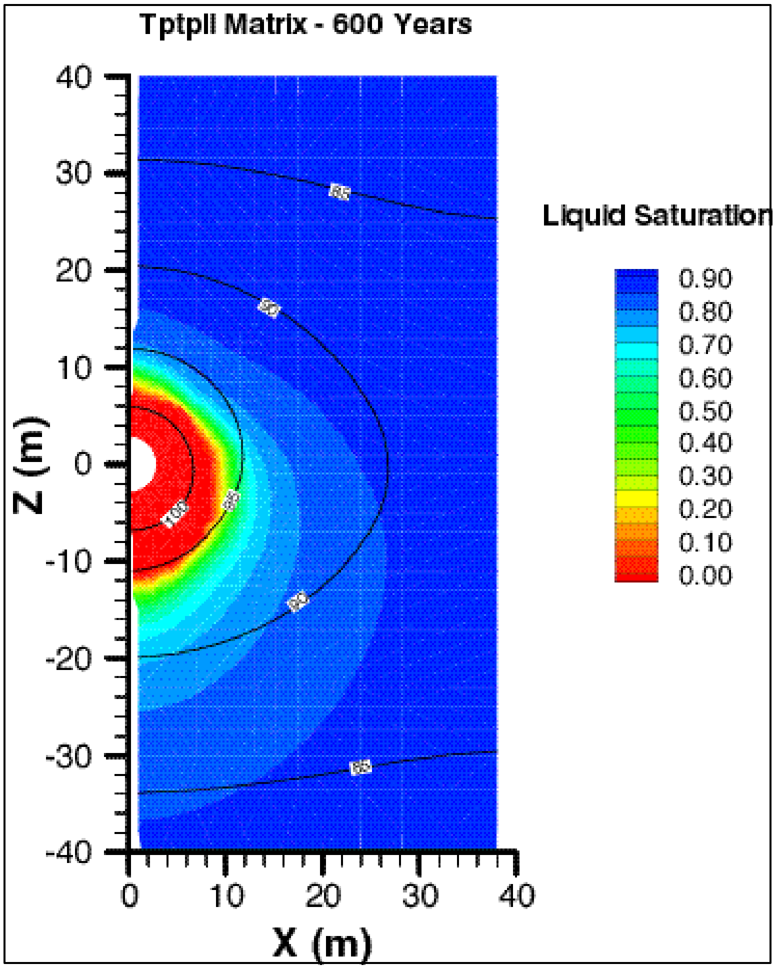

DTN: LB0011DSTTHCR1.002

Figure 87. TH Simulation (Tptpll). Contour Plot of Modeled Temperatures and Liquid Saturations in the Matrix at 600 Years (Near Maximum Dryout-Mean Infiltration).

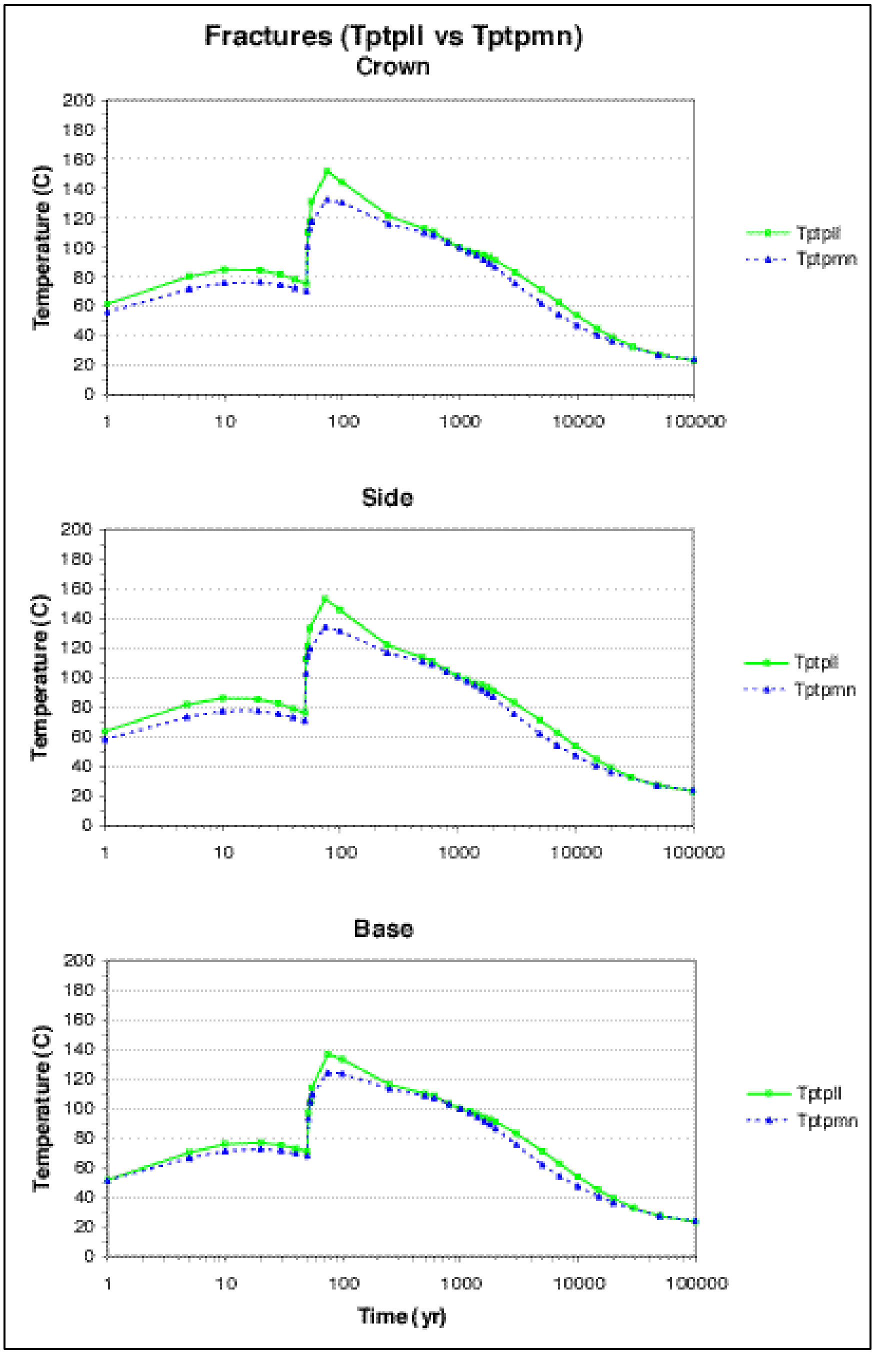

DTN: LB0011DSTTHCR1.001

Figure 88. TH Simulation (Tptpll versus Tptpmn). Time Profiles of Modeled Temperatures in Fractures at Three Drift-Wall Locations.

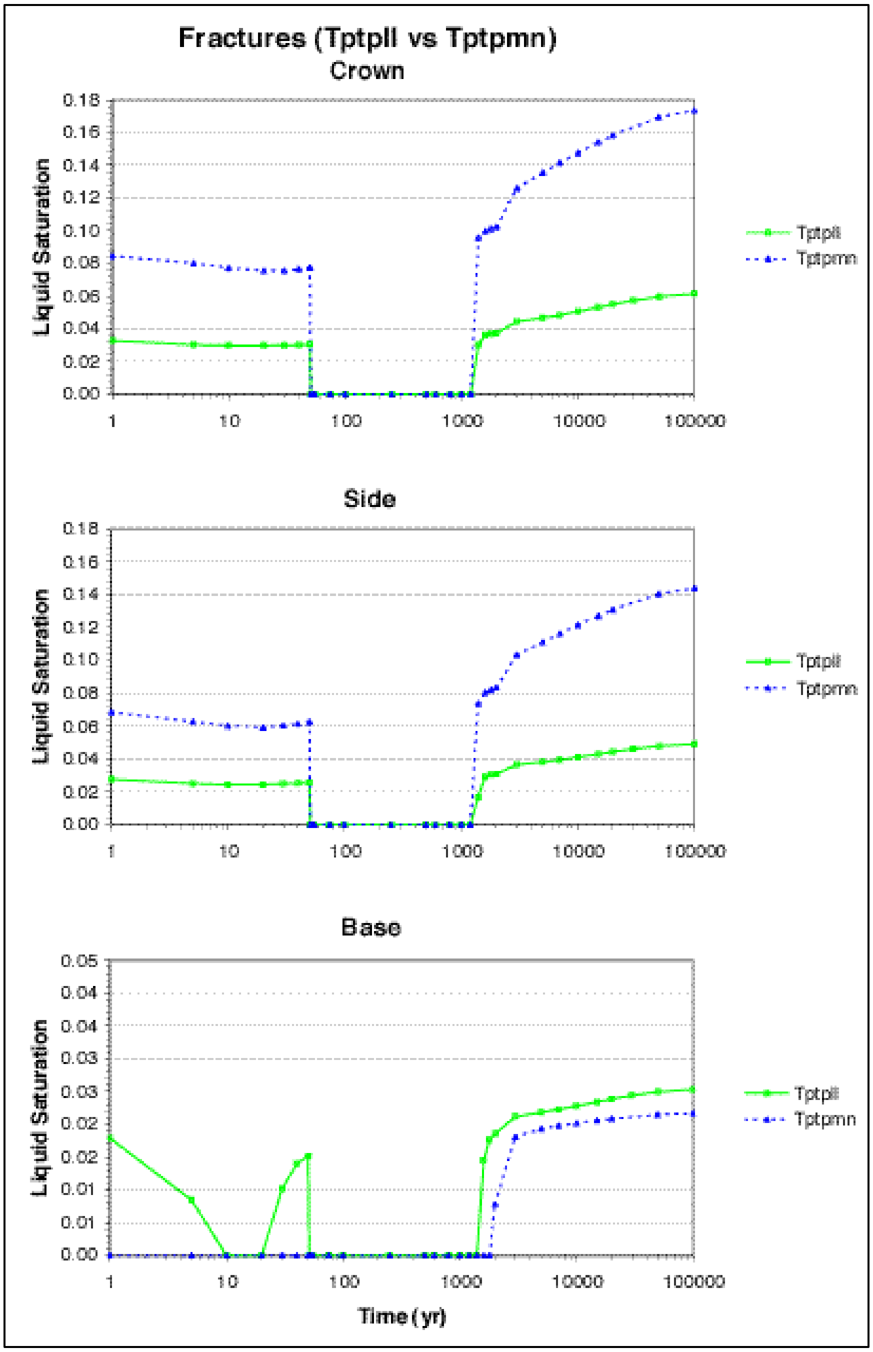

DTN: LB0011DSTTHCR1.001

Figure 89. TH Simulation (Tptpll versus Tptpmn). Time Profiles of Modeled Liquid Saturations in Fractures at Three Drift-Wall Locations.

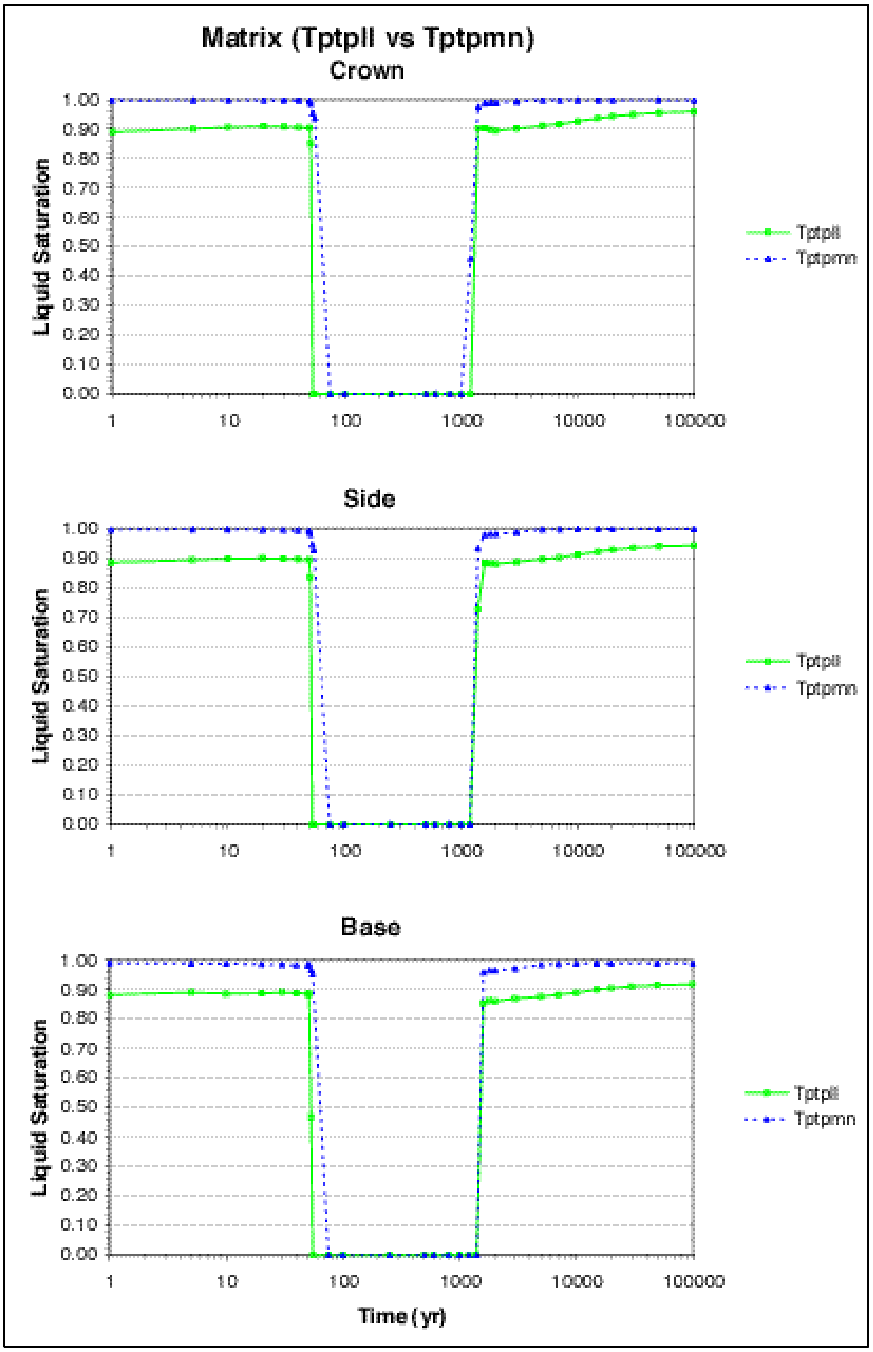

DTN: LB0011DSTTHCR1.001

Figure 90. TH Simulation (Tptpll versus Tptpmn). Time Profiles of Modeled Liquid Saturations in Matrix at Three Drift-Wall Locations.

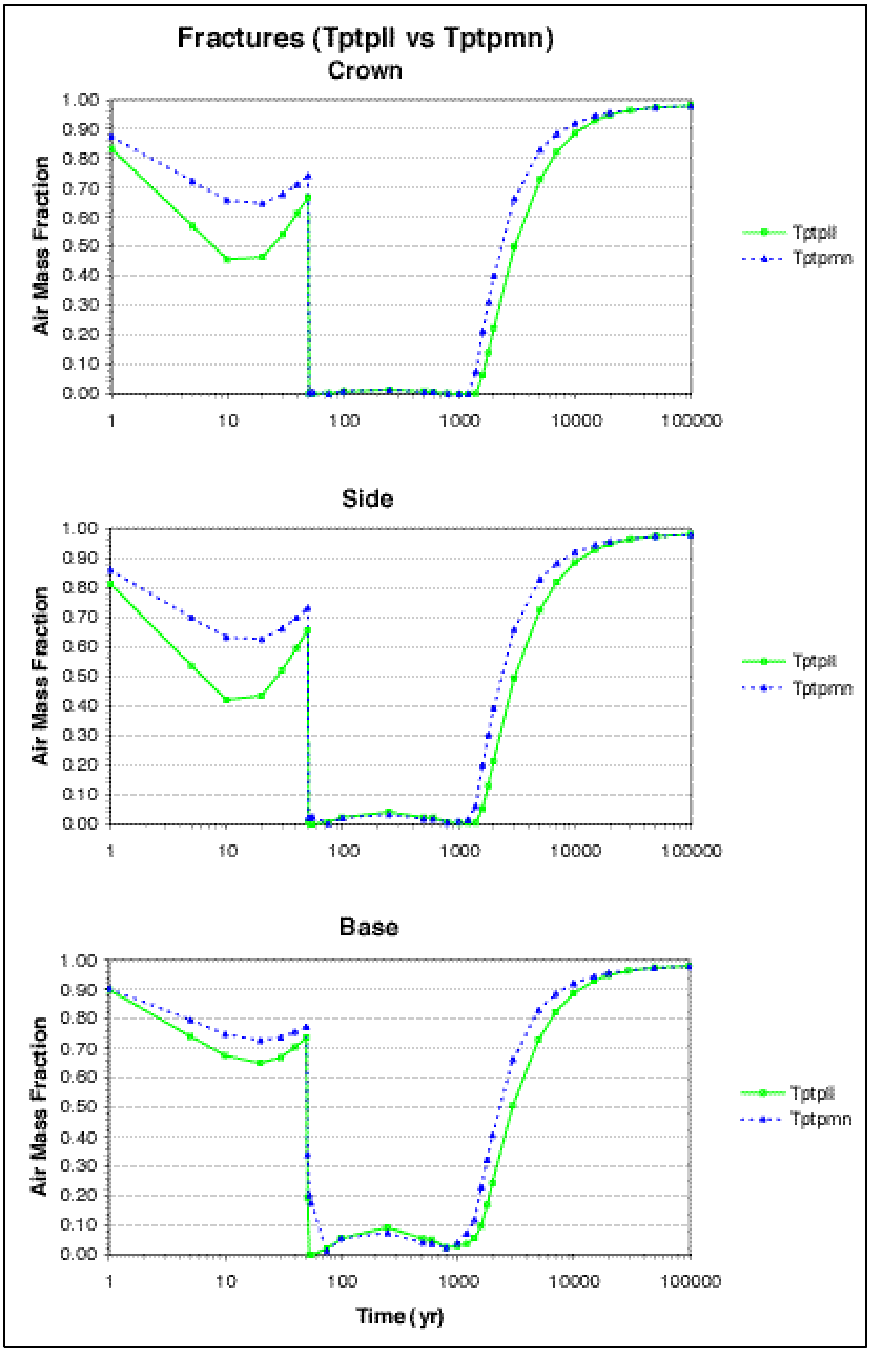

DTN: LB0011DSTTHCR1.001

Figure 91. TH Simulation (Tptpll versus Tptpmn). Time Profiles of Modeled Air Mass Fractions in the Gas Phase in Fractures at Three Drift-Wall Locations.

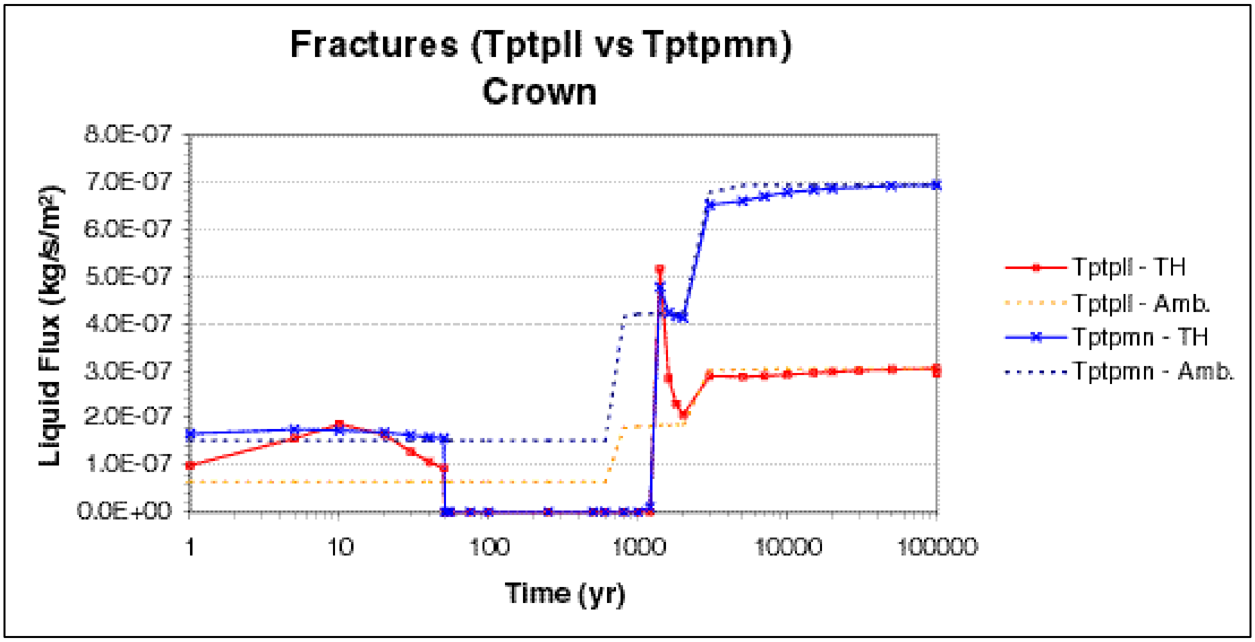

DTN: LB0011DSTTHCR1.001

Figure 92. TH Simulation (Tptpll versus Tptpmn). Time Profiles of Modeled Water Flux at the Drift Crown.

6.6.5.2 THC Simulation Results (Tptpll)

Time profiles of predicted CO_2 and various aqueous species concentrations in fractures are shown in Figures 93 to 100. As for the Tptpmn no-backfill model, results of ambient and heat-load calculations for both the base-case and extended-case geochemical systems are shown on these figures. Ambient trends are fairly steady, with some fluctuations resulting mostly from changes in infiltration rates, and indicate that the ambient geochemical system for this Tptpll model is also fairly well constrained. Consequently, the minor differences in input mineralogic data and mineral surface areas between the Tptpmn no-backfill model and this Tptpll model have only a small effect on modeled ambient water compositions, at least within the 100,000-year time period investigated. The same can be said for the effect of differences in hydrologic properties between both units.

Under thermal loading, modeled concentration trends in fractures for the chemical species in the Tptpll model are similar to those modeled in the Tptpmn. Discussions of model results in addition to those provided below can be found in Sections 6.3.5.2 and 6.4.5.2.

The base of the drift does not dry out during the entire time span of the pre-closure period shown on time profiles (contrary to the Tptpmn model results). Pre-closure concentrations are thus displayed (Figure 94 to 100) for this location (they are not in the Tptpmn model profiles). Evaporation at the base of the drift, combined with the "shadow" effect of the drift, generally results in increased concentrations at this location in both the Tptpmn and Tptpll models. However, because of the higher fracture capillarity in the Tptpll model, evaporative concentration below the drift occurs to a larger degree than in the Tptpmn model. Also, noteworthy differences exist in pH and CO_2, total carbonate (as HCO_3^-), and calcium concentrations at the side of the drift when modeled with the extended system (Figures 93 to

Main Menu

EXIT

96). These concentrations do not return to ambient values after rewetting because of significant calcite precipitation at this location.

Before and after dryout, the greater evaporation due to higher temperatures result in somewhat higher predicted concentrations of most aqueous species, compared to the Tptpmn model. Note that peak concentrations shown at the time of rewetting in both models (for example, sodium and chloride on Figures 97 and 99) reflect mostly the small values of the first, non-zero, liquid saturations output by the model at a preselected time value. These "first output" saturations differ between simulations, and therefore differences (between simulations) in "first output" concentrations must be evaluated with respect to these saturations. In any case, elevated concentrations are predicted only for small liquid saturations that should reflect essentially immobile water.

Predicted fluoride concentrations in the Tptpll model under ambient and thermal loading conditions (Figure 100) are higher than in the Tptpmn model (Figure 68) because of fluorite (CaF_2) dissolution. This mineral is included as one of the mineral constituents of the Tptpll (and of other units to a lesser extent), while it was not included as a primary mineral in the Tptpmn model. Ambient fluoride concentrations tend toward equilibrium with fluorite (5 to 6 mg/L for the modeled ambient geochemical conditions) because of the fast reaction rate of this mineral. With the extended-case geochemical system, under ambient and thermal loading conditions, modeled calcium concentrations (Figure 96) are generally smaller than predicted with the base-case system. Therefore, more fluorite is dissolved and higher fluoride concentrations are predicted with the extended-case system. This is most noticeable during the cooling period when, as noted earlier, calcium concentrations drop below ambient values (because of calcite precipitation) and fluoride concentrations remain above ambient concentrations.

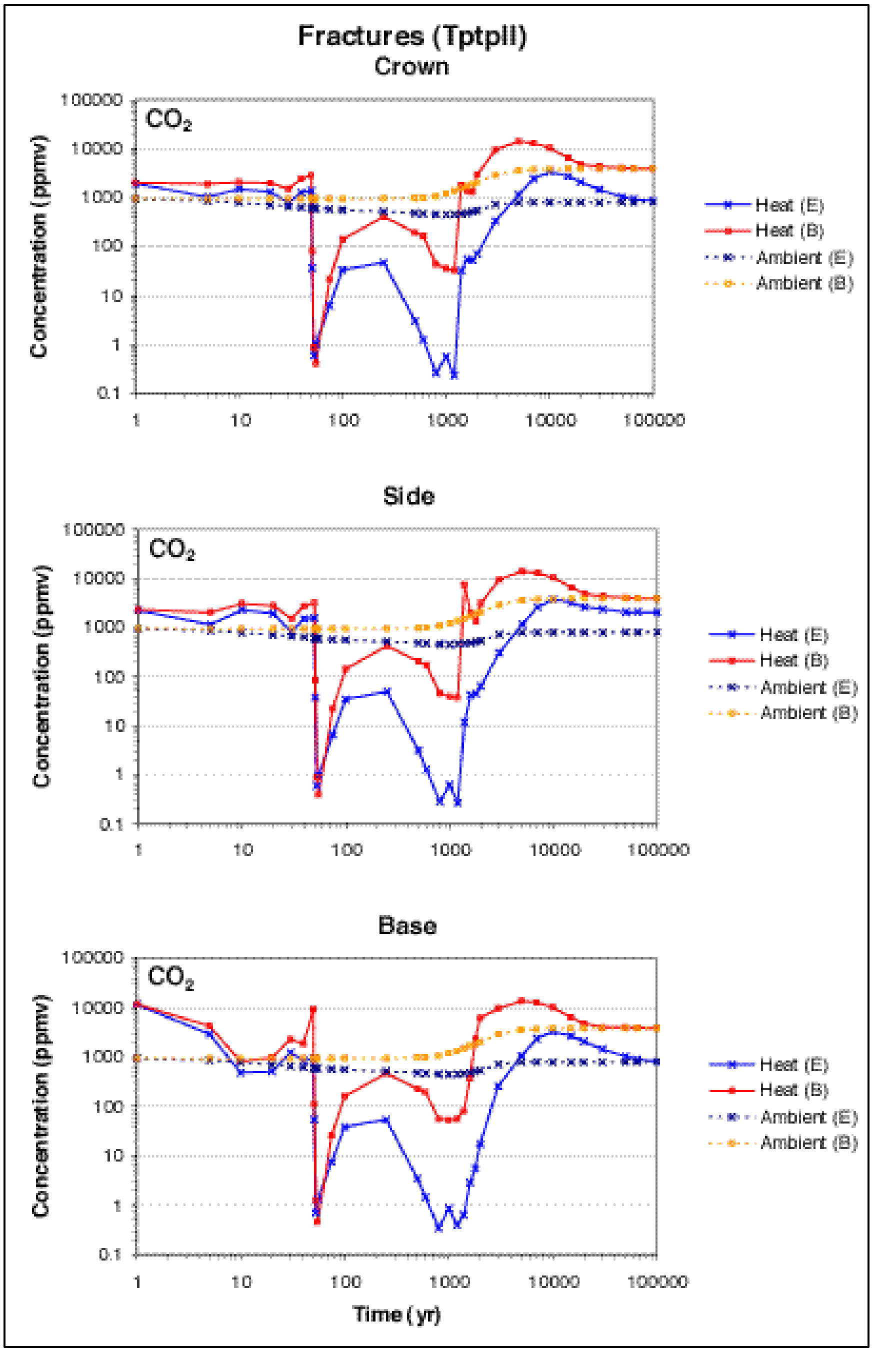

DTN: LB0011DSTTHCR1.001

Figure 93. THC Simulation (Tptpll). Time Profiles of Modeled CO_2 Concentrations in the Gas Phase in Fractures at Three Drift-wall Locations under Heat Load (Heat) and No Heat Load (Ambient) Conditions for the Extended (E) and Base-Case (B) Geochemical Systems.

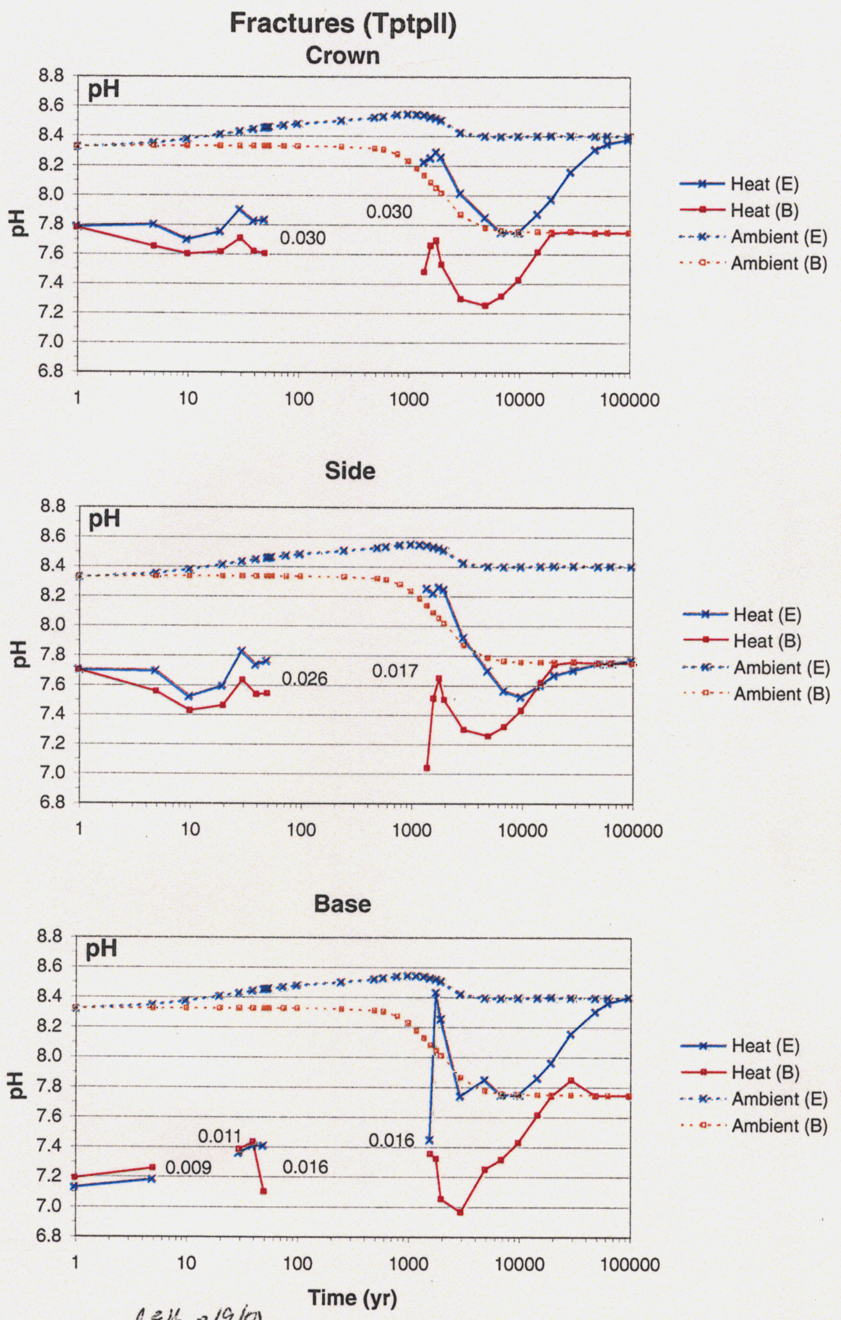

Fractures (Tptpll)

Crown

Side

Base

JEH 2/9/01

DTN: LB0011DSTTHCR1.001

Figure 94. THC Simulation (Tptp~~mn~~ll). Time Profiles of the Modeled pH of Fracture Water at Three Drift-Wall Locations under Heat Load (Heat) and No Heat Load (Ambient) Conditions for the Extended-Case (E) and Base-Case (B) Geochemical Systems. The dryout period is left blank. Numbers by each curve indicate the last output liquid saturation before dryout and the first output liquid saturation during rewetting.

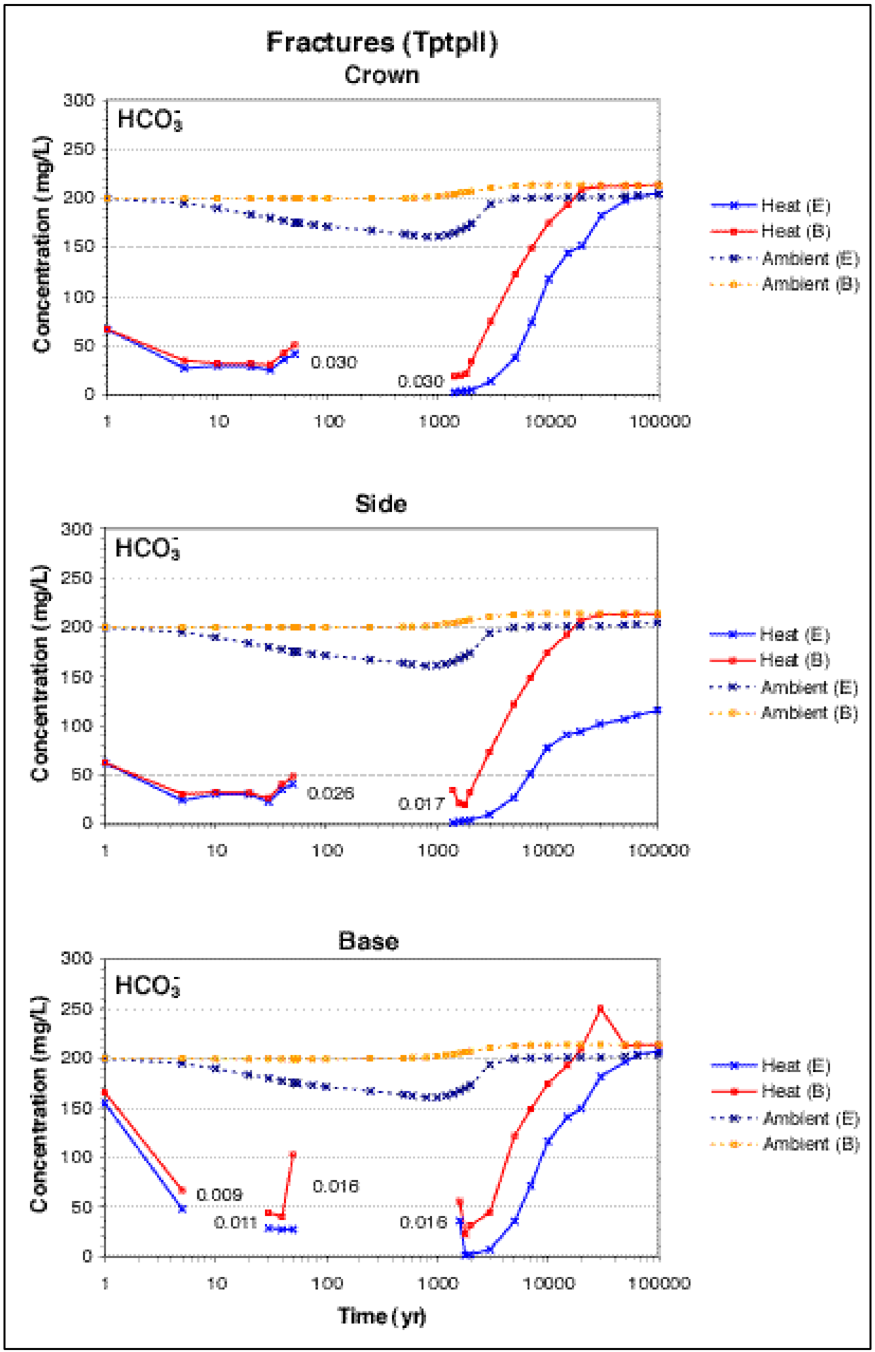

DTN: LB0011DSTTHCR1.001

Figure 95. THC Simulation (Tptpll). Time Profiles of Modeled Total Aqueous Carbonate Concentrations (as HCO_3^-) in Fracture Water at Three Drift-Wall Locations (designations denoted in Figure 94).

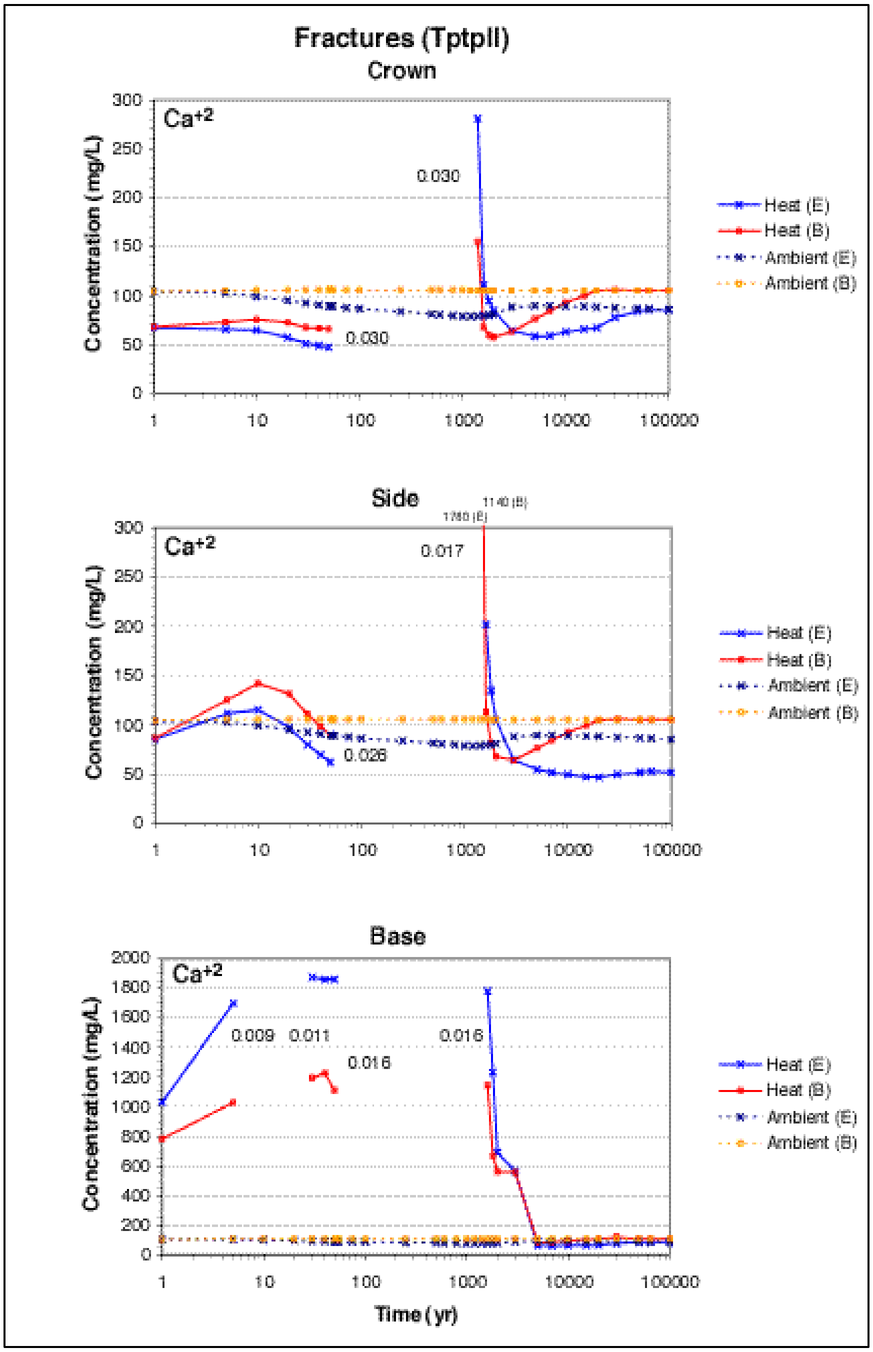

DTN: LB0011DSTTHCR1.001

Figure 96. THC Simulation (Tptpll). Time Profiles of Modeled Total Aqueous Calcium Concentrations in Fracture Water at Three Drift-Wall Locations (designations denoted in Figure 94).

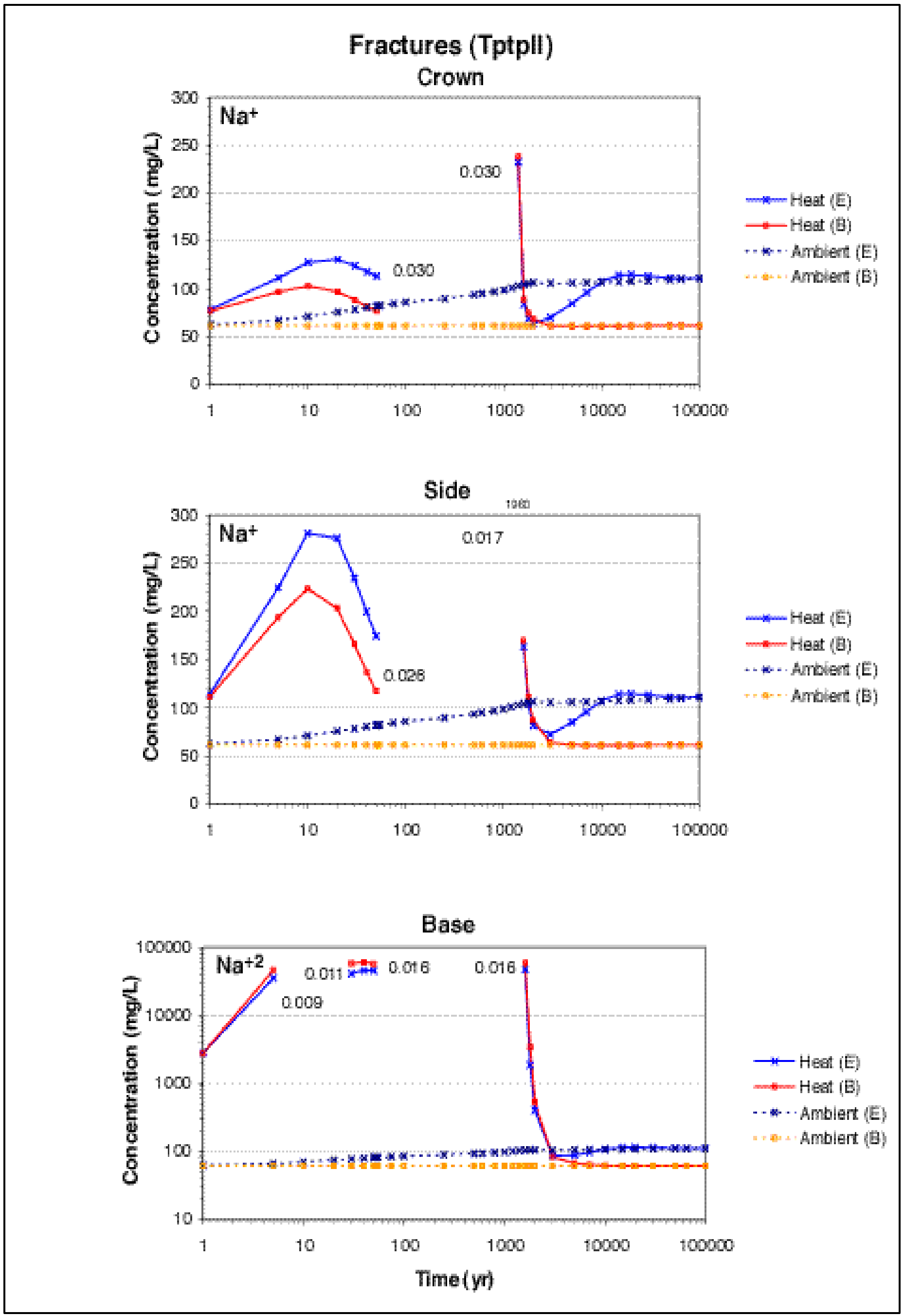

DTN: LB0011DSTTHCR1.001

Figure 97. THC Simulation (Tptpll). Time Profiles of Modeled Total Aqueous Sodium Concentrations in Fracture Water at Three Drift-Wall Locations (designations denoted in Figure 94).

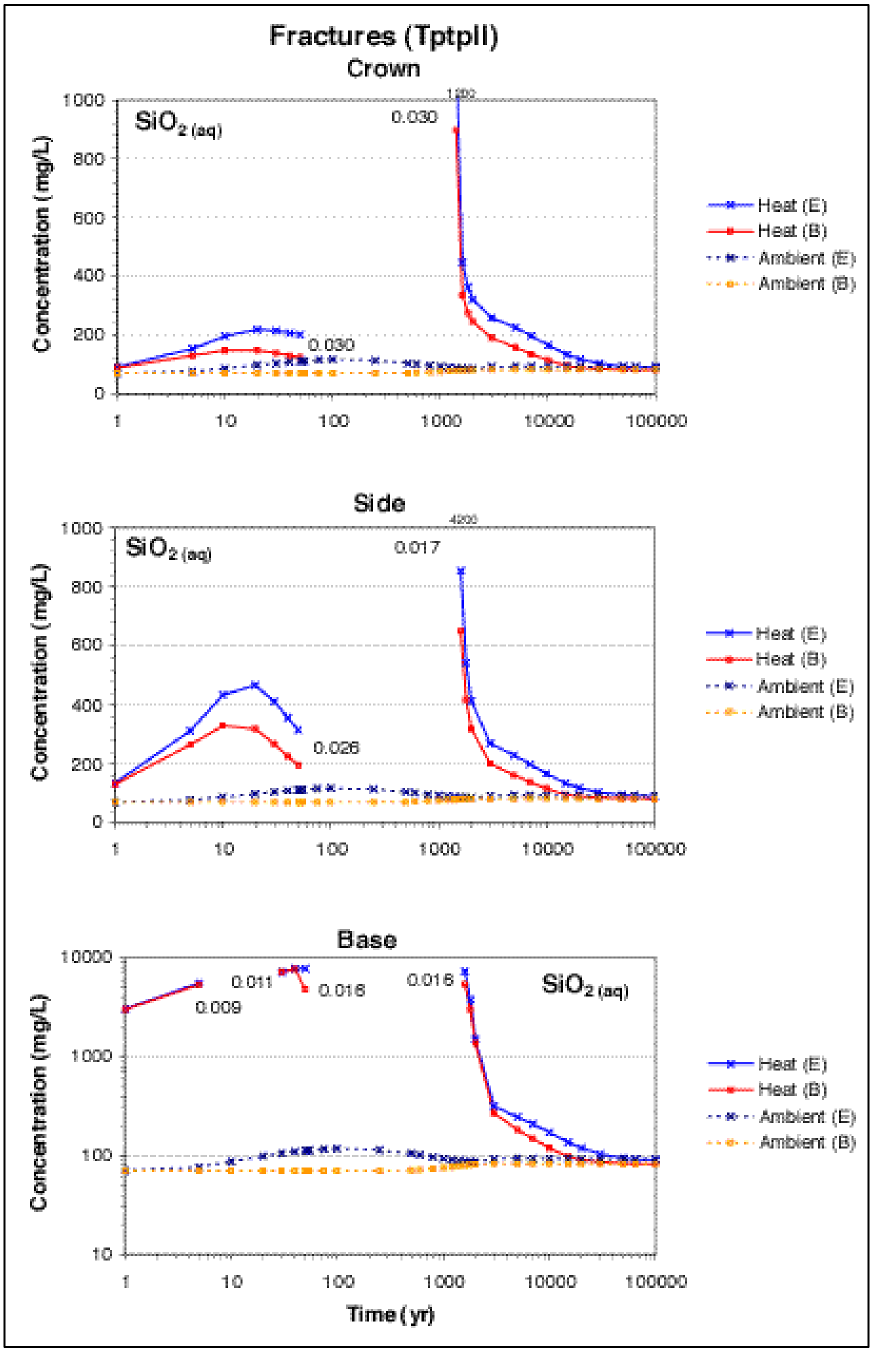

DTN: LB0011DSTTHCR1.001

Figure 98. THC Simulation (Tptpll). Time Profiles of Modeled Total Aqueous Silica Concentrations in Fracture Water at Three Drift-Wall Locations (designations denoted in Figure 94).

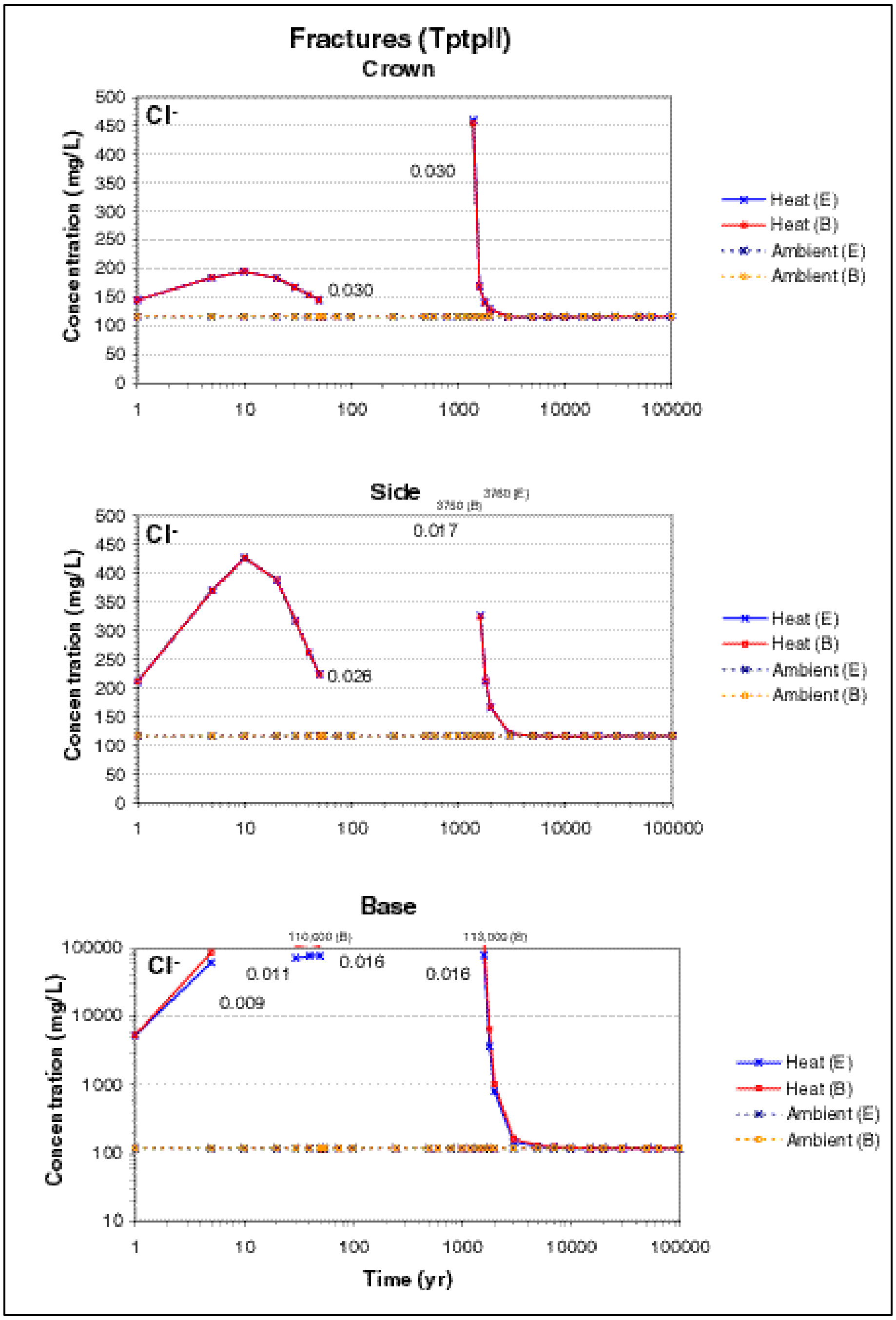

DTN: LB0011DSTTHCR1.001

Figure 99. THC Simulation (Tptpll). Time Profiles of Modeled Total Aqueous Chloride Concentrations in Fracture Water at Three Drift-Wall Locations (designations denoted in Figure 94).

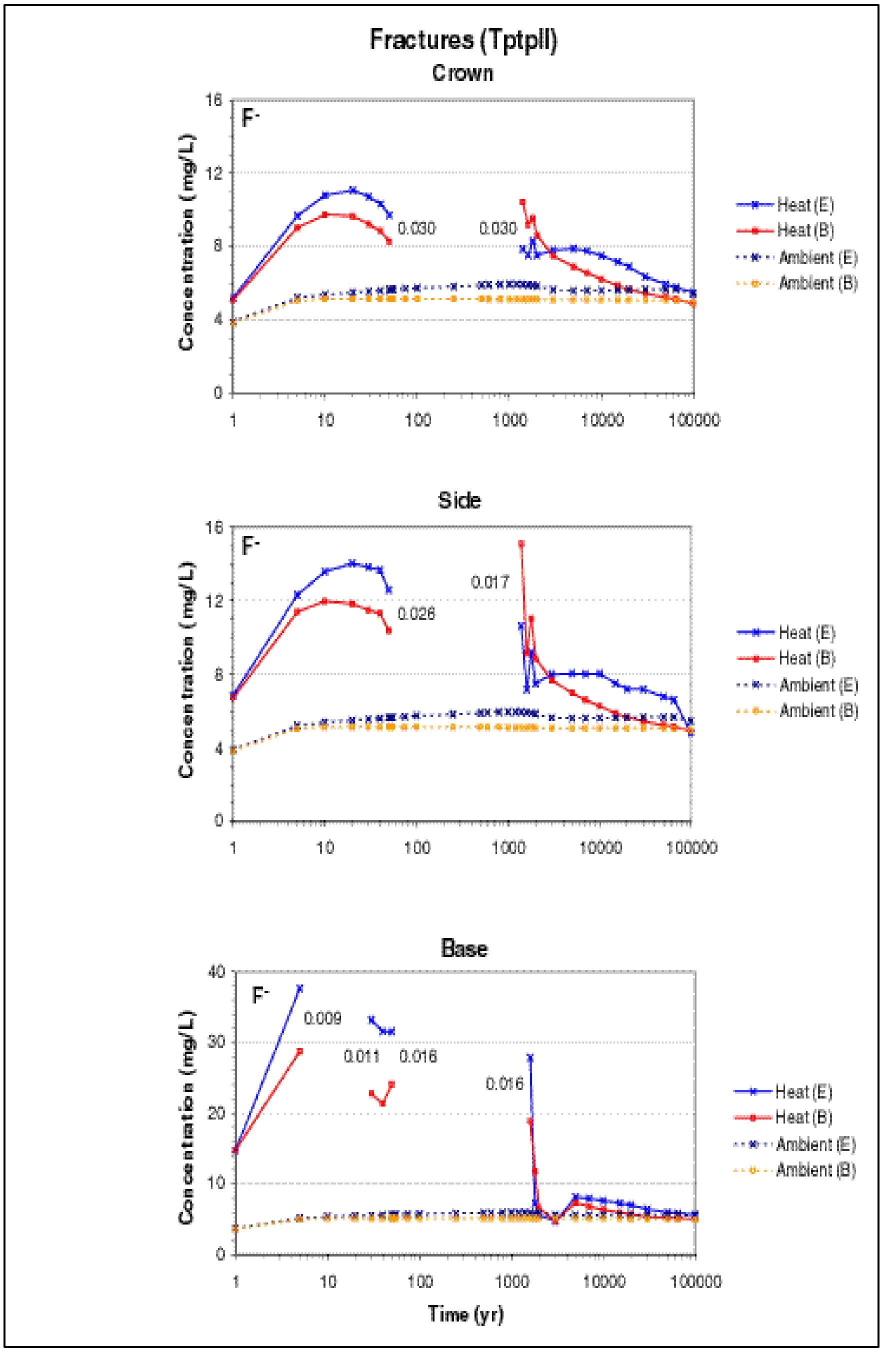

DTN: LB0011DSTTHCR1.001

Figure 100. THC Simulation (Tptpll). Time Profiles of Modeled Total Fluoride Concentrations in Fracture Water at Three Drift-Wall Locations (designations denoted in Figure 94).

The pattern in fracture porosity change around the drift is similar to that predicted in the Tptpmn models, with a decrease concentrated in a zone approximately 9 m above drift center, coinciding with the maximum extent of the dryout zone (Figures 101 to 105). Note that irregular patterns on these figures result, in part, from numerical effects.

A larger fracture porosity decrease occurs at the base of the drift (near 1%) than predicted with the Tptpmn model. This decrease results from higher evaporative concentration from higher fracture capillarity than in the Tptpmn. As in the Tptpmn no-backfill simulations, amorphous silica accounts for most of the porosity decrease between approximately 600 and 2,000 years (mostly near or below 0.3%), followed by calcite precipitation at later stages of cooling accounting for the remaining bulk of the porosity decrease (up to 1% after 100,000 years) (Figure 103). Late calcite precipitation is caused by the warming of percolating waters as they flow back towards the drift in zones that have not completely cooled. As in the Tptpmn model, the porosity decrease predicted with the base-case and extended-case geochemical systems are similar, with generally more late calcite precipitation predicted using the extended-case system.

Clays, and to the greatest extent illite (Figure 104) precipitate in very small quantities. As in the no-backfill Tptpmn model, stellerite (a calcium zeolite) is predicted to mostly dissolve in fractures (Figures 105a and b). Relatively minor and short-lived stellerite precipitation does occur below the drift in fractures and matrix during the initial cooling stage (Figure 105a). Precipitation of other zeolites is negligible in the vicinity of the drift.

The method to couple fracture permeability to fracture porosity is the same here as implemented in the no-backfill Tptpmn simulations (Section 6.4). Mineral precipitation is predicted to sufficiently decrease the fracture permeability around the drift to have a small effect on liquid saturations (Figure 106), but not enough to affect the general thermohydrology around the drift. A similar conclusion was reached for the Tptpmn model using both homogeneous (Section 6.4) and heterogeneous (Section 6.5) fracture permeability distributions. Some flux reduction at the drift crown, mostly after 20,000 years, is predicted using the extended geochemical system (Figure 107), because more calcite precipitates at this location than with the base-case system. However, the mineral precipitation pattern around the drift is artificially irregular, due in part to numerical effects, and therefore calculated flux variations may be exaggerated.

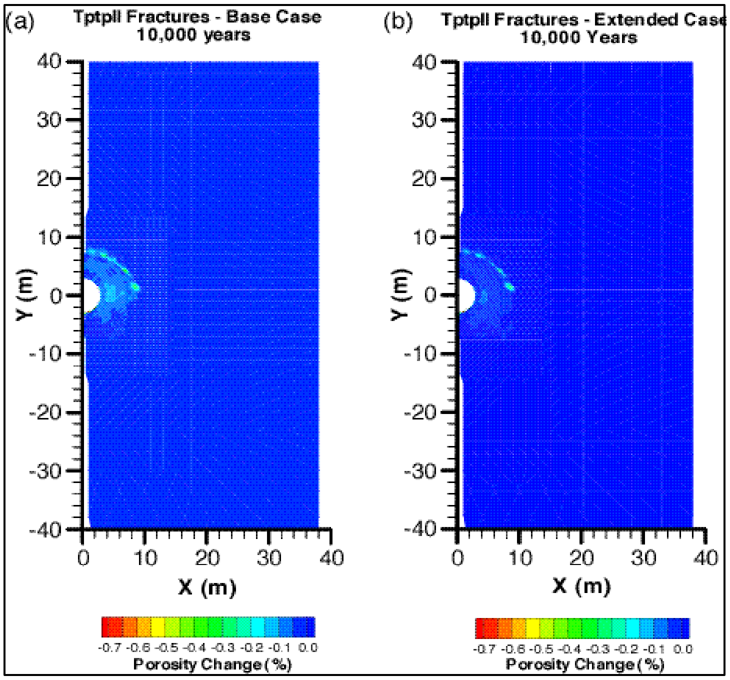

DTN: LB0011DSTTHCR1.002

Figure 101. THC Simulation (Tptpll). Contour Plot of Modeled Fracture Porosity Change at 10,000 Years. (a) Base-Case Geochemical System. (b) Extended-Case System. Red areas indicate maximum decrease in porosity (up to 1%) due to the precipitation of primarily amorphous silica between 600 and 2,000 years.

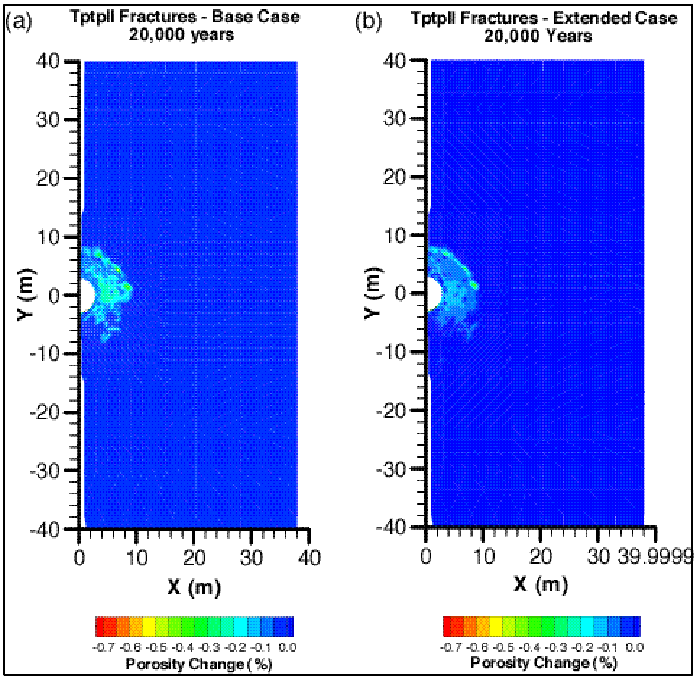

DTN: LB0011DSTTHCR1.002

Figure 102. THC Simulation (Tptpll). Contour Plot of Modeled Fracture Porosity Change at 20,000 Years. (a) Base-Case Geochemical System. (b) Extended-Case System. Red areas indicate maximum decrease in porosity (up to 1%) due primarily to deposition of calcite in addition to earlier precipitated amorphous silica.

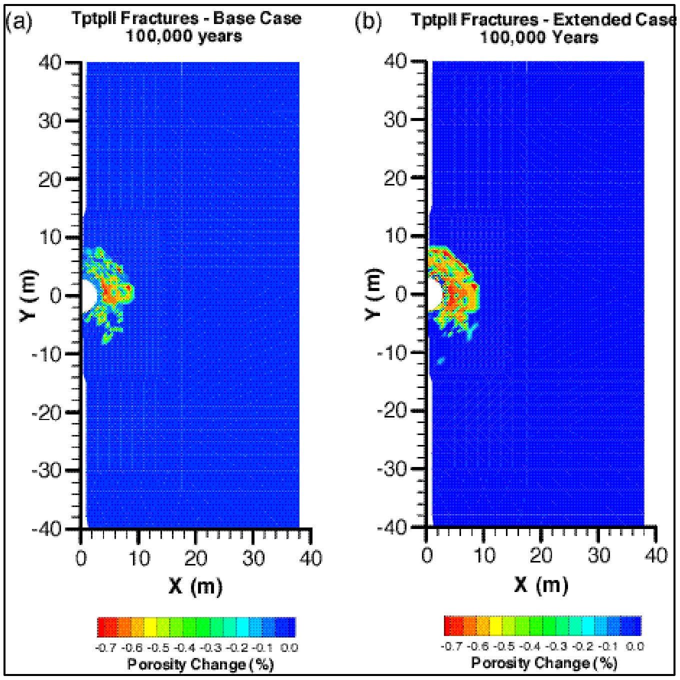

DTN: LB0011DSTTHCR1.002

Figure 103. THC Simulation (Tptpll). Contour Plot of Modeled Fracture Porosity Change at 100,000 Years. (a) Base-Case Geochemical System. (b) Extended-Case System. Red areas indicate maximum decrease in porosity (up to 1%) due primarily to late deposition of calcite in addition to earlier precipitated amorphous silica.

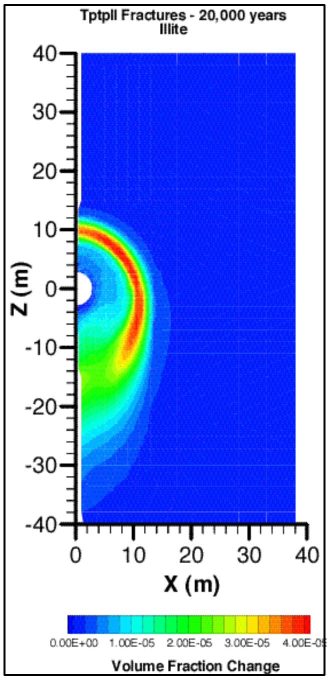

DTN: LB0011DSTTHCR1.002

Figure 104. THC Simulation (Tptpll). Contour Plot of Modeled Illite Volume Fraction Change in Fractures at 20,000 Years. Pattern and amounts do not vary significantly after the time of maximum dryout around 600 years.

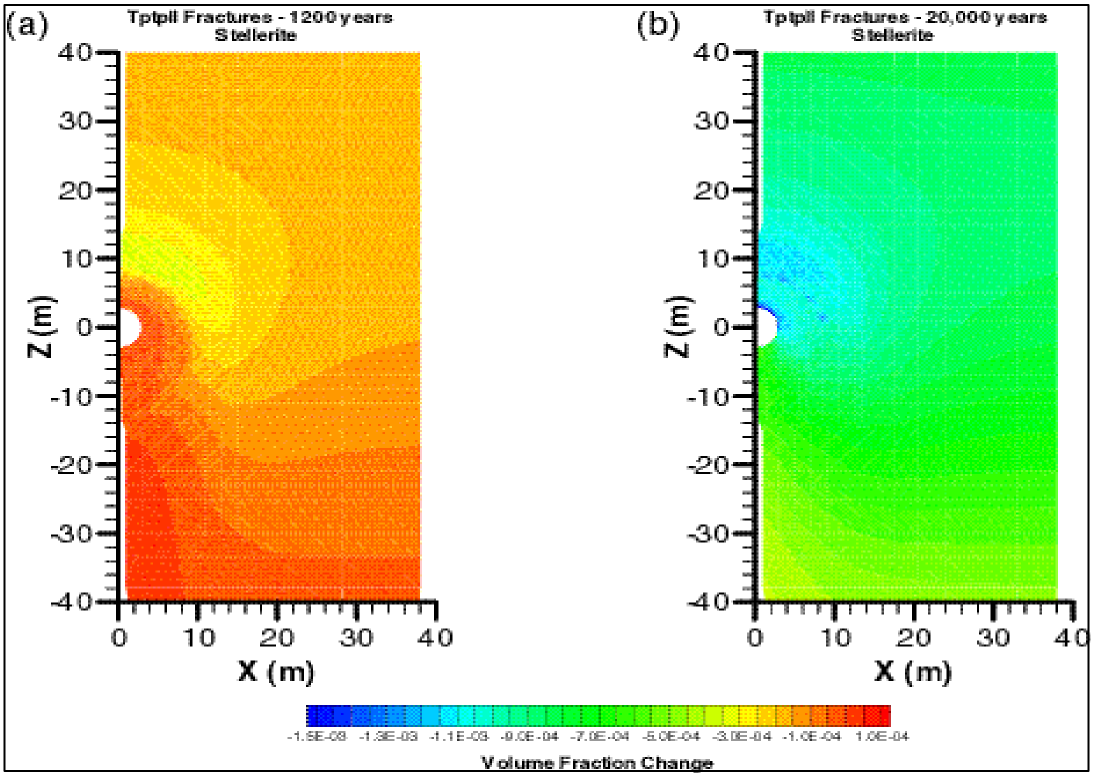

DTN: LB0011DSTTHCR1.002

Figure 105. THC Simulation (Tptpll). Contour Plot of Modeled Stellerite (Ca-Zeolite) Volume Fraction Change in Fractures at (a) 1,200 Years (some precipitation below the drift) and (b) at 20,000 Years (dissolution). Precipitation of other zeolites is negligible .

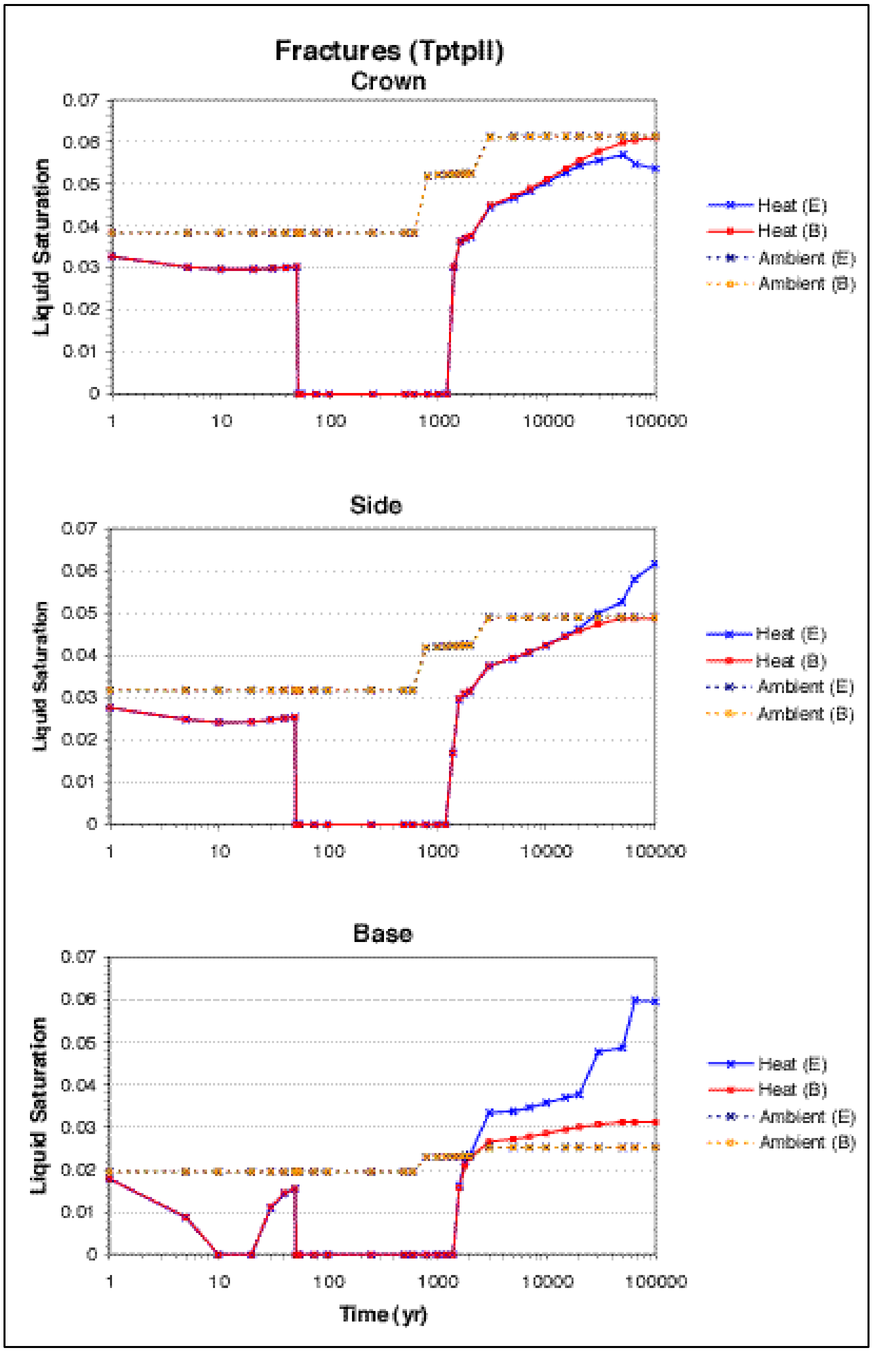

DTN: LB0011DSTTHCR1.001

Figure 106. TH and THC Simulations (Tptpll). Comparison of Modeled Liquid Saturations in Fractures at Three Drift-Wall Locations under Heat-Load (Heat) and No-Heat-Load (Ambient) Conditions for the Extended-Case (E) and Base-Case (B) Geochemical Systems.

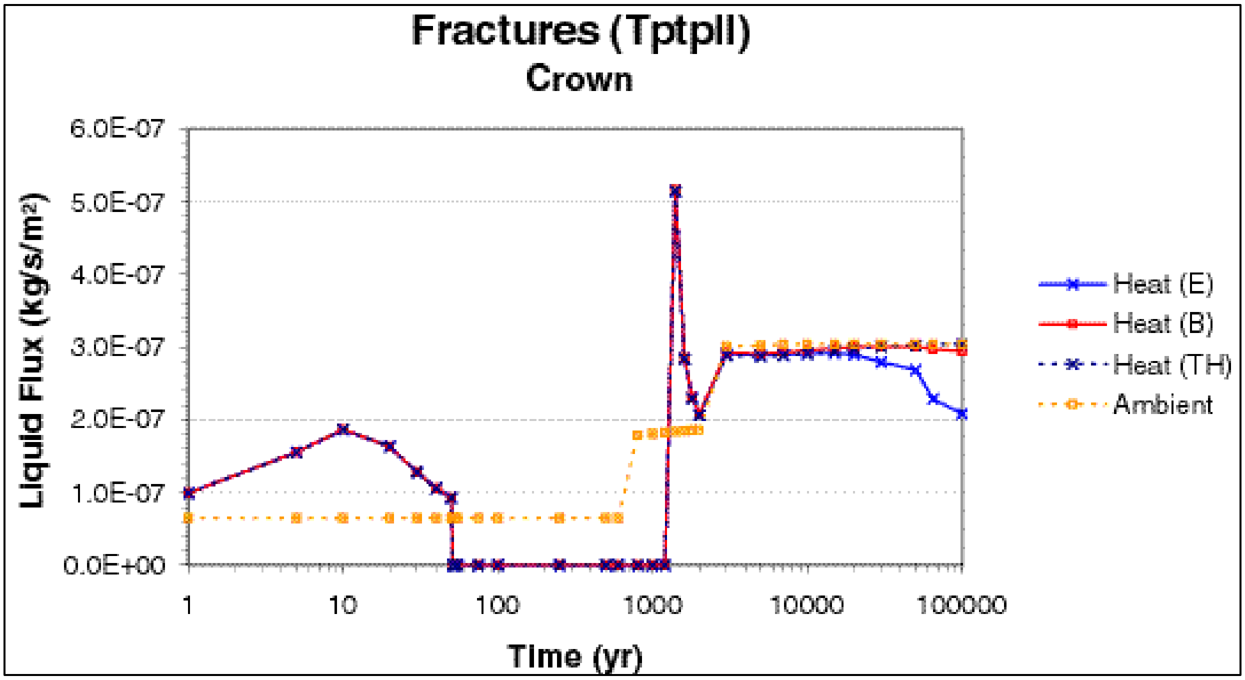

DTN: LB0011DSTTHCR1.001

Figure 107. TH and THC Simulations (Tptpll). Comparison of Modeled Liquid Flux at the Drift Crown in Fractures under Heat-Load (Heat) and No-Heat-Load (Ambient) Conditions for the Extended-Case (E) and Base-Case (B) Geochemical Systems, and without Chemical Reactions (TH). Flux variations after 20,000 years may be exaggerated (see text).

6.7 KINETIC SIMULATIONS OF PLUG-FLOW REACTOR EXPERIMENT

A tuff dissolution experiment conducted in 1999 was used to test geochemical models that were developed for the DST THC and the Tptpmn and Tptpll THC models. This experiment was performed under isothermal conditions with well-constrained initial water and rock compositions. Measured water compositions of samples obtained during the duration of the experiment also allowed the evaluation of kinetically controlled reactions with time. A number of simulations were run to evaluate the sensitivity of the geochemical models to the mineral surface area, rock composition, mineral thermodynamic data, and changes to the TOUGHREACT code.

A plug-flow reactor experiment was performed as part of a study investigating mineral dissolution and precipitation (Figure 108). Topopah Spring tuff (Tptpmn) obtained from overcores from borehole ESF-TMA-TC-H-1 was crushed, sieved, and washed, and material was selected from the 75–150 µm (89%) and 150–212 µm (11%) fractions (DTN: LB0011THCDISSX.001 [153380]). Scanning Electron Microscope (SEM) images of the tuff (Fig. 109) indicate that the actual grain sizes are smaller than the nominal sieve size fractions, with values ranging from 30–180 µm (DTN: LB0011THCDISSX.001 [153380]). Tuff fragments were added to a 29.8 cm long by 7.5 cm diameter polypropylene tube. The filled tube had a measured porosity of 37.5%.

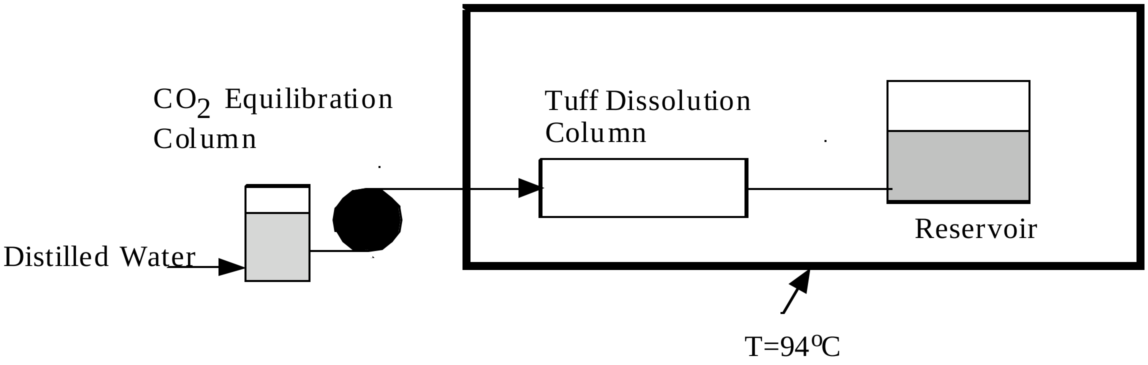

Figure 108. Schematic Diagram of the Tuff Plug-Flow Experiment.

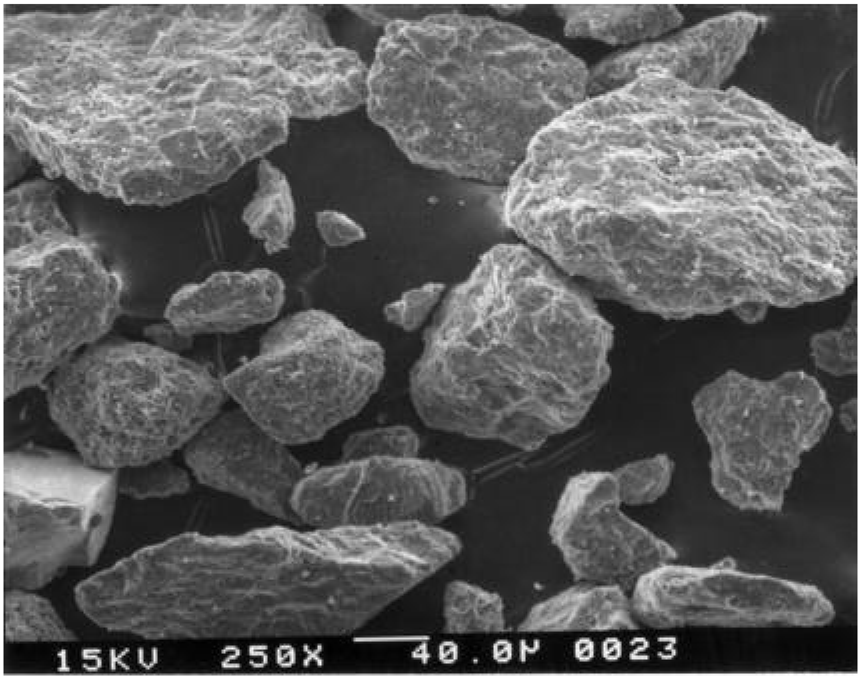

DTN: LB0011THCDISSX.001 [153380]

Figure 109. SEM Image of Topopah Spring Tuff Grains Used for Plug-Flow Experiment. Note that the grains have a fairly wide range in diameter (30-180 µm), and that they have irregular shapes and rough surfaces, contributing to a larger surface area per unit weight value.

The inlet fluid consisted of deionized water that was initially equilibrated with a CO_2/N_2 gas mixture with a 50,200 ppm CO_2 at 17°C. The resulting water had a measured pH of 4.58 (DTN: LB0011THCDISSX.001 [153380]). This water was heated to 94°C, and then introduced into the tuff column (also at 94°C) at a rate of 25 mL/h. Water exiting the tuff column was collected in a reservoir and sampled periodically for analysis over the length of the experiment (63.8 days). A fraction of the water exiting the tuff column was directly used in an experiment evaluating the effects of boiling on mineral dissolution and precipitation and fluid flow in a fracture. The sampled waters for the plug-flow reactor experiment were allowed to cool and equilibrate with the atmosphere at room temperature. These sampling conditions resulted in changes to the pH and bicarbonate values, due to the loss of CO_2 gas.

A series of isothermal 1-D TOUGHREACT V2.2 [153219] and V2.3 [153101] simulations were performed to model this dissolution using a 149-element mesh with dimensions and interface areas identical to those of the plug-flow experiment, plus one additional boundary element to obtain the appropriate outlet conditions (Bodvarsson 2001 [153816], YMP-LBNL-DSM-ELS-PD-1, p. 8). The goals of these simulations were to validate the geochemical model developed for the THC models presented in this AMR and test the sensitivity of the simulations to changes in input parameters such as reactive surface area and mineralogy.

Initial mineralogy used for plug flow simulations was obtained from the Tptpmn (tsw34) matrix composition reported in Attachments I and II. K-smectite was not considered in simulations run using TOUGHREACT V2.3 [153101], consistent with the revised "extended" mineralogical system used for the Tptpll THC simulations in Section 6.6.5.2 (Table 8). The corresponding volume fraction of K-smectite was either added to illite or disregarded, as noted for each sensitivity run. An initial fluid composition was calculated (Table 19) using SOLVEQ V1.0 [153217] and the measured pH and CO_2 concentration (Bodvarsson 2001 [153816], YMP-LBNL-DSM-ELS-PD-1, pp. 18-22). Trace amounts of other dissolved constituents were used in the simulation to reduce computational problems caused by zero values. The column was assumed to be liquid-saturated with no separate gas phase present.

Table 19. Initial Water Composition For Tuff Plug-Flow Simulations. Bicarbonate concentrations represent sum of all carbonate species present.

Species	Abundance (moles/liter)	Abundance (mg/liter)
Na^+	1.000E-10	2.299E-06
K^+	1.000E-10	3.910E-06
Ca^{+2}	1.000E-10	4.008E-06
HCO_3^-	1.943E-03	1.186E+02
SiO_2	1.000E-10	6.008E-06
Cl^-	1.000E-10	3.545E-06
SO_4^{-2}	1.000E-10	9.606E-06
F^-	1.000E-10	1.900E-06
AlO_2^-	1.000E-10	5.898E-06
$HFeO_2$	1.000E-10	8.885E-06
pH (20°C)	4.58	

DTN: LB0011THCDISSM.001 [153381]

A total column flow-through time of 19.75 hours was determined using the calculated pore volume of 493.7 cm^3 and the flow rate of 25 mL/h; this corresponds to a flow-through time of 477 seconds per element block (Bodvarsson 2001 [153816], YMP-LBNL-DSM-ELS-PD-1, pp. 10-11). The maximum time step (360 seconds) for each of the simulations was chosen to be smaller than this value. The temperature of the simulation was fixed at 94°C.

Two simulations were performed using TOUGHREACT V2.2 [153219], and three additional simulations were made with TOUGHREACT V2.3 [153101] (Table 20). Two different grain size models were used for the TOUGHREACT V2.2 [153219] simulations to evaluate the sensitivity of surface-area values on kinetic mineral reactions (Bodvarsson 2001 [153816], YMP-LBNL-DSM-ELS-PD-1, pp. 17-18). The first simulation employed mineral surface areas calculated using spherical grains with a diameter of 60 µm, with clay minerals represented by rectangular plates with dimensions 60 × 60 × 1.2 µm. The second simulation used spherical grains with diameters of 120 µm and clay minerals with dimensions 120 × 120 × 2.4 µm. The results of these simulations are depicted in Figures 110 (a-f).

Table 20. Summary Table of Tuff Dissolution Simulations

Run #	TOUGHREACT version	Thermodynamic database	Grain size surface area model	Thermodynamic representation of potassium feldspar	Thermodynamic representation of k-smectite
1	V2.2 [153219]	thermokapps2.05.dat*	60 µm dia.	microcline	k-smectite
2	V2.2 [153219]	thermokapps2.05.dat*	120 µm dia.	microcline	k-smectite
3	V2.3 [153101]	thermok2.07.dat†	60 µm dia.	microcline	ignored
4	V2.3 [153101]	thermok2.07.dat†	60 µm dia.	k-feldspar	ignored
5	V2.3 [153101]	thermok2.07.dat†	60 µm dia.	k-feldspar	illite

* Attachment V

† Attachment VI

6.7.1 Validation Criteria

The criteria for model validation are as follows: 1) The predicted concentrations for the major (>1 mg/L) dissolved species are within a factor of 2 of the measured average steady-state concentrations. Because the experimental alkalinity and pH values were significantly affected by degassing during collection, these values were not considered as primary factors in the model validation process. 2) The calculated fluid compositions over time should exhibit similar steady-state trends to those observed in the experiment. The early stages (0–11 days) of the experiment were not used for this comparison.

6.7.2 Results of Simulations and Comparison to Measured Data

Good matches were obtained between some of the simulation runs and the measured results of the plug-flow experiment (Bodvarsson 2001 [153816], YMP-LBNL-DSM-ELS-PD-1, pp. 30-34). Large (up to 100%) differences were observed between the two grain size models for Na, SiO_2, and Ca concentrations. These variations result from the two-fold difference in calculated initial surface areas that affect the kinetic mineral reactions controlling the concentrations of these species in solution. There is a close match between the measured and calculated concentrations of Na and SiO_2 for the 60 µm grain size (larger surface area/unit volume) simulation. As a result, the surface areas corresponding to this grain size model were used for subsequent TOUGHREACT V2.3 [153101] simulations of the plug-flow experiment.

Main Menu

EXIT

None of the simulation results fit directly the measured values of pH and total alkalinity. This discrepancy can be attributed to the exposure of the plug-flow effluent to air and the subsequent cooling and degassing of the outflow solution before analysis. The outflow compositions match the simulated results closely after they have been corrected for these processes (using SOLVEQ V1.0 [153217]) (Bodvarsson 2001 [153816], YMP-LBNL-DSM-ELS-PD-1, pp. 35-38).

A second set of simulations was conducted using TOUGHREACT V2.3 [153101] (Bodvarsson 2001 [153816], YMP-LBNL-DSM-ELS-PD-1, pp. 39-44). The revised version of the code uses temperature-pressure-corrected density values of water in surface-area calculations, resulting in a small change in calculated surface areas for the new series of simulations. This version also utilized a thermodynamic database (thermok2.07.dat; Attachment VI) that differs in several respects from the database (thermokapps2.05.dat; Attachment V) used in the TOUGHREACT V2.2 [153219] simulations. Other changes included modified activity coefficients, the removal of K-smectite as a mineral phase, and the incorporation of a smectite solid-solution model. Several changes were made for the TOUGHREACT V2.3 [153101] simulations. For all runs, smectite end members were considered as a solid solution. Different initial surface areas for minerals that are not initially present were used for the V2.3 [153101] runs as a sensitivity study on this parameter (Bodvarsson 2001 [153816], YMP-LBNL-DSM-ELS-PD-1, pp. 16, 39). For two of the runs, thermodynamic data for microcline were substituted by k-spar for the potassium feldspar. The simulations also evaluated the removal of the K-smectite component from the new thermodynamic database. One simulation added the K-smectite mineral fraction to the illite component. In the other two simulations, the K-smectite fraction was simply removed from the initial composition. The 60 µm grain size model was used for all of the TOUGHREACT V2.3 [153101] simulations.

Several important observations can be obtained from the TOUGHREACT V2.3 [153101] simulations. First, TOUGHREACT V2.3 [153101] and its thermodynamic database produced results similar to those generated using V2.2 [153219]. Most of the concentration profiles have steady-state compositions slightly higher than the corresponding values obtained from the TOUGHREACT V2.2 [153219] runs. These higher compositions results from the incorporation of the change in water density to the mineral surface area calculations in the new version of the code. Some of the fluid concentration profiles are more abrupt with the new simulations perhaps due to changes in the initial precipitation rate of new secondary phases.

The model does not appear to be sensitive to small changes in illite contents. This insensitivity suggests that this phase is not being dissolved during the experiment and thus does not contribute to the outflow fluid composition. However, major differences were observed for K when microcline was replaced by k-spar. It is, therefore, critical to select the proper thermodynamic data for the key mineral phases that buffer the main chemical constituents in the fluid.

A number of important observations and conclusions can be derived from the tuff dissolution experiment and simulations:

- A good match was obtained between the water compositions for the observed and simulated plug flow reactions.

- The simulations are sensitive to a number of parameters, including the initial mineral assemblage, the thermodynamic database used, and most importantly the mineral surface area.

- Minor differences in model results obtained using two versions (V2.2 [153219] and V2.3 [153101]) of the TOUGHREACT code result primarily from the temperature-pressure corrected density values of water used in the mineral surface area calculations incorporated in V2.3 [153101].

- Differences between the modeled and measured values in pH and alkalinity result from cooling and degassing of the experimental samples after exiting the tuff dissolution column. This illustrates the potential for fluid-chemistry changes during collection in samples obtained from the DST experiment (Sections 6.2.7 and 6.2.8).

- Results of the model simulations show that the model validation criteria have been met, as outlined in Section 6.7.1.

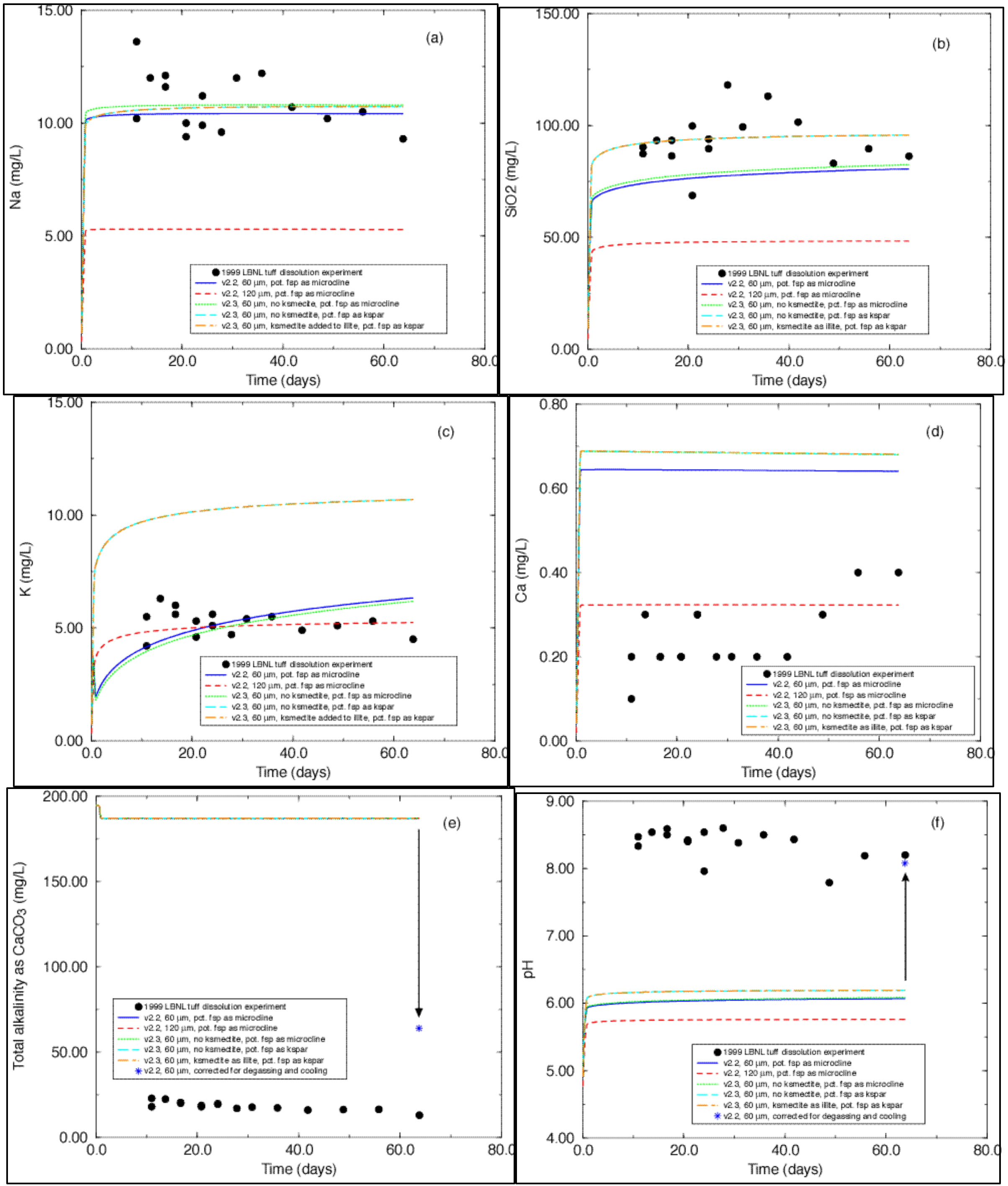

DTN: LB0011THCDISSM.002

Figure 110. (a)-(f). Comparison of Measured and Simulated Results of Tuff Dissolution Plug-Flow Experiment. Plots show variations with time for Na (a), SiO_2 (b), K (c), Ca (d), total alkalinity as $CaCO_3$ (e), and pH (f).

7. CONCLUSIONS

This AMR describes the conceptual model for the numerical simulation of coupled thermal-hydrological-chemical (THC) processes in the near-field environment (NFE), the Drift Scale Test (DST) THC Model, the Tptpmn THC Models (backfill and no backfill), and the Tptpll THC Model. Model results associated with this AMR have been submitted to the Technical Data Management System (TDMS) as output under DTNs listed in Section 8.4 of this AMR. The conceptual model provides a comprehensive basis for modeling the pertinent mineral-water-gas reactions in the host rock, under thermal loading conditions, as they influence the NFE water and gas chemistry that may enter potential waste-emplacement drifts over 100,000 years. Data are incorporated from the calibrated thermohydrological property sets, the three-dimensional mineralogical model, the UZ Flow and Transport Model, thermal test geochemical data (fracture and matrix mineralogy, aqueous geochemistry, and gas chemistry), thermodynamic data (minerals, gases, and aqueous species), data for mineral-water reaction kinetics, and transport data. Simulations of THC processes include coupling between heat, water, and vapor flow, aqueous and gaseous species transport, kinetic and equilibrium mineral-water reactions, and feedback of mineral precipitation/dissolution on porosity, permeability, and capillary pressure (hydrologic properties) for a dual permeability (fracture-matrix) system. The effect of these coupled THC processes on the time evolution of flow fields in the NFE has been investigated for different climate change scenarios, calibrated property sets, and initial mineralogy. Aqueous species included in the model are H^+, Ca^{2+}, Na^+, K^+, SiO_2 (aq), Mg^{2+}, Al^{3+}, Fe^{3+}, SO_4^{2-}, HCO_3^-, Cl^-, and F^-. Twenty-four minerals are considered, including several silica phases (α-cristobalite, quartz, tridymite, amorphous silica, and opal-CT), calcite, feldspars, smectites, illite, kaolinite, sepiolite, zeolites, fluorite, hematite, goethite, gypsum, and volcanic glass. Treatment of CO_2 included gas-water equilibration, gaseous diffusion and advection.

Numerous sensitivity studies were performed, including comparison of:

1. Different in-drift designs (backfill vs. no-backfill).
2. Potential repository host rock units (Tptpmn vs. Tptpll).
3. Alternative conceptual models of pertinent geochemical systems (base case vs. extended).
4. Effects of uncertainty in thermodynamic data (free energies and activity coefficient models).
5. Treatment of mineral-water reactions (kinetic rate constants, reactive surface areas, and equilibrium vs. kinetic conceptual models).
6. Fracture permeability-porosity relations during mineral precipitation-dissolution.
7. Realizations of strong initial spatial heterogeneity in fracture permeability with accompanying effects on THC processes in the NFE.
8. Different infiltration rates for different climate scenarios.

Given the many possible analyses of uncertainty in THC models, this list is by no means exhaustive. However, it covers a wide range of the most important uncertainties from the standpoint of model validation, bounding analyses, and conservatism. Validation of alternative geochemical systems was accomplished through analysis of the DST and a recent plug-flow reactor experiment performed under temperature-pressure-geochemical conditions appropriate to the near-boiling reflux zone.

The most realistic validation of the overall approach and data embodied in the Drift Scale THC conceptual model described in this AMR is the comparison of measured gas and water chemistry from the Drift Scale Test (DST) to the results of simulations using the DST THC Model. In particular, simulation results were compared to measured gas-phase CO_2 concentrations and the chemistry of waters collected from hydrology boreholes collected during the test. These comparisons of the model results to the measured changes in CO_2 concentrations over nearly three years show that the model captures the initial rise in concentration in all of the borehole intervals where comparisons were made, in areas having very different thermal histories. In those intervals closer to the heaters where an earlier peak in concentration was observed, the model also captured this behavior. However, a second larger peak was observed in those intervals, which was not predicted by the simulations. This discrepancy resulted from the fact that sample cooling during collection removed condensed water vapor from gas samples before analysis, whereas simulation results include water vapor. Because of a sharp reduction in the air mass fraction of the gas phase, it appears that this second peak was a result of the shift in the CO_2/air ratio in the initial boiling phase, which also undergoes a large spike at the early stages of boiling. Therefore, analysis of dry gas samples are very different from the model data in this time period only.

Comparisons between observed and modeled water chemistry (pH) and CO_2 concentrations in the gas phase from the DST indicate that a limited set of aqueous species (base case), minerals (calcite, silica phases, gypsum), and gases (H_2O, air, and CO_2) can describe the general evolution of DST waters with respect to pH, CO_2, and conservative anions. A more complete geochemical system (extended case), including a wide range of aluminosilicates (such as feldspars, clays and zeolites), yields modeled aqueous silica concentrations closer to those observed plus added information on additional species (i.e., Al, Fe, F). However, such a system also causes shifts in the pH to values slightly higher than those observed and correspondingly lower gas-phase CO_2 concentrations. By revision of poorly constrained thermodynamic data for smectites and zeolites, decreasing the reaction rate of anorthite, and making some other minor changes in the minerals included in the geochemical system, simulation results with this extended system yielded results more consistent with observations during the DST.

Confidence in the overall approach and input data used in all the Drift Scale THC models is also based on a comparison of modeled and measured water compositions from a laboratory plug flow dissolution experiment using volcanic tuff from the Tptpmn unit at Yucca Mountain. In this case also, the model reproduces fairly well concentrations measured during this experiment.

THC seepage models were developed that incorporated the elements of the Enhanced Design Alternative (EDA) II design to represent waste-package heating over time, changes in heat load due to ventilation, the effective heat transfer within the drift, the effect of adding backfill (or not) over the waste packages after 50 years of ventilation, and the THC processes in the NFE.

Four models for predicting drift-scale coupled THC processes over 100,000 years were considered. One included backfill and heat load in the Tptpmn geologic unit, for which a number of cases were evaluated with different calibrated property sets, climate change scenarios, and geochemical systems. Another similar model (also with heat load in the Tptpmn unit, but without backfill) incorporated better-constrained thermodynamic and kinetic data, improved consideration of initial mineral precipitation, larger reactive surface areas in fractures, and more sensitive coupling of permeability to porosity changes. A similar third model also evaluated the effect of heterogeneous permeability distributions around the drift. A fourth model considered heat load in the Tptpll geologic unit (without backfill), which was used for comparing prediction results with the other models. These 2-D THC models incorporated the initial vertical heterogeneity in hydrologic and thermal properties and mineralogy from the near-surface to the water table, along with different initial mineralogy and reactive surface areas in fractures and matrix.

Predictions are presented of the water and gas chemistry that may enter the potential waste-emplacement drifts, and data have been submitted that document the temporal frequency of potential seepage based on the times of rewetting around the drifts, along with the net fluxes of water and gas to the drift wall. These predictions are provided for a period of 100,000 years, including a pre-closure period of 50 years with 70% heat removal by ventilation. General trends of CO_2 gas and aqueous species concentrations around the drifts did not differ significantly between the various models. Water and gas composition trends predicted around waste-emplacement drifts using the THC seepage models, during the early phase of heating and during the dryout period of the models, were generally similar to trends observed in the DST and predicted with the DST THC simulations. The rewetting period has not yet been observed in the DST, and therefore no field data can be used to evaluate water and gas compositions at the time of rewetting. The THC simulations indicate that there may be an increase in the CO_2 gas concentrations around the drifts during rewetting (relative to ambient values). The predicted extent of the dryout zone and the time of rewetting are different for each modeled climate history and calibrated rock property set. Simulations of a no-backfill design predict a smaller dryout zone (particularly below the drift) and somewhat shorter time of rewetting than when backfill is considered. For all simulations, the time of maximum dryout is predicted to occur near 600 years (also the time of the modeled climate change and increase in infiltration rate). Depending on the modeled scenario, the maximum extent of the dryout zone is predicted to be between 6 and 10 m above drift center, and the predicted time of rewetting at the drift crown varies between 800 and 1,200 years.

THC simulations of the Drift Scale Test in Rev00 of this AMR, as well as for the Tptpmn THC Backfill THC Model, predicted notable differences in pH and CO_2 concentrations depending on which geochemical systems (base case or extended case) were considered in these simulations. However, a good part of this effect appears to result from higher rate of dissolution of feldspars to form clays and zeolites, which was predicted to occur under ambient conditions and increase under a heat load. Once input thermodynamic and kinetic data were revised to yield fairly steady water compositions under ambient conditions, the predicted water compositions, pH, and CO_2 concentrations under heat loading were better constrained, and differences between predictions using the two geochemical systems were reduced significantly. In general, with the base case, predicted pH values were smaller and CO_2 concentrations higher than with the extended case. The latter may overestimate the effect of mineral-water reactions on the geochemistry of waters and gases, and may therefore provide an upper limit on the extent of changes in chemical and hydrological properties around waste emplacement drifts. In both cases, fairly dilute and near-neutral to moderately alkaline water compositions are predicted around drifts, with pH values in the 7–9 range, and gas phase CO_2 concentrations generally below 10,000 ppmv. Elevated concentrations of aqueous species (relative to background values) predicted to occur only at small liquid saturations, that are conditions characterized by essentially no fluid movement. Similar water and gas composition trends were predicted in seepage models with heat load in the Tptpmn and in the Tptpll geologic units.

Predicted porosity changes due to water-rock interaction around waste emplacement drifts are small and show mostly a reduction due to mineral precipitation, with essentially no effect on predicted thermohydrological conditions around drifts. The Tptpmn THC Backfill Model predicted small porosity changes due to mineral precipitation and a small effect of porosity changes on permeability. The predicted reduction in porosity and permeability in the NFE over 100,000 years for the Tptpmn THC No-Backfill Model (homogeneous permeability) is less than 3% (of the initial fracture porosity) and less than one order of magnitude, respectively. This is somewhat greater than for the Tptpmn THC Backfill Model (< 1% change in fracture porosity), but still relatively minor. These results are based on uniform areas of precipitation in plane parallel fractures, with the actual effects in heterogeneous fractures with rough surfaces and nonuniform mineral precipitation possibly being greater. Comparison of the results of purely thermohydrologic simulations to those including coupled THC processes show only small differences in predicted water and gas fluxes, liquid saturations, and permeability around the drift. The porosity reduction well after rewetting of the drift wall is predicted to be due almost entirely to calcite and amorphous silica. The latter contributes to most of the initial precipitation during the initial cooling stage, with maximum deposition spreading above the drift in a zone roughly coinciding with the maximum extent of the dryout zone (8 to 10 m from drift center). Calcite is predicted to precipitate mostly during later cooling stages.

Heterogeneity in fracture permeability can have varied effects on thermohydrology, including flow focusing and irregularity in isotherms and liquid saturations. Thermohydrological simulations were performed for three heterogeneous fracture permeability realizations (4 orders of magnitude range in permeability), under the mean infiltration climate change scenario, for the Tptpmn unit. Areas of highest initial liquid saturation, also having lower permeability and generally residing above the drift, tend to show the greatest reduction in fracture permeability, down to about 25% of the initial value in some regions. The effect of this localized permeability reduction tends to cause some additional flow focusing, but the permeability changes are considerably less than the initial range in permeability. The corresponding maximum fracture porosity reductions are approximately 5% of the initial value. Porosity reductions for the extended geochemical system are slightly greater than those for the base-case system, owing to more mineral species precipitating and somewhat higher silica concentrations in the former. The maximum amount of amorphous silica precipitated is about 2% (volume % of fracture) in the extended case and somewhat less in the base case, with maximum amounts in the high saturation zones near the drift. Spatial differences in water chemistry are not affected significantly by permeability heterogeneities for these simulations.

Many uncertainties exist in modeling coupled THC processes, because of the large amount of data needed and the complexity of natural systems. These data range from the fundamental thermodynamic properties of minerals, aqueous species, and gases; the kinetic data for mineral-water reactions; and the representation of the unsaturated hydrologic system for fractured tuffs. In addition, a wealth of site-specific thermohydrologic, geologic, and geochemical data are necessary to describe the initial and boundary conditions. For these reasons, it may not be possible to assign a model uncertainty based on the uncertainties of the data themselves, and therefore model validation gives a true test of whether the system can be described sufficiently well for the intended purposes of the model. Simulated THC processes occurring during the DST captured the important changes in pH, aqueous species concentrations, and gas-phase CO_2 concentrations at specific locations over time. This provides sufficient validation of the model's capability to predict spatial and temporal variation in water and gas chemistry.

This document may be affected by technical product input information that requires confirmation. Any changes to the document that may occur as a result of completing the confirmation activities will be reflected in subsequent revisions. The status of the technical input information quality may be confirmed by review of the DIRS database.

The impact of TBVs (to-be-verified), associated with input data, on model predictions would not be significant, because the model is validated against measured data. However, TBVs associated with the measured water and gas chemistry from the DST are much more significant. Changes in these data could result in a re-evaluation of the model if deviations from the simulation results were much greater. Because of very limited field testing data, the Tptpll THC model did not consider the local effects of lithophysae on seepage chemistry, but instead used a drift-scale property set that included such effects as they influence the calibration to matrix saturation. Under transient TH conditions, high lithophysal densities may change the extent of the dryout and reflux zones, as well as gas transport. Yet, the overall trends in the geochemistry of the system should not be markedly altered. The presence of lithophysae could, however, cause some additional flow focusing akin to that observed in the Tptpmn THC Model with heterogeneous permeability simulations. Once additional field-testing data is reported, including associated lithophysal densities, characteristics, and local heterogeneity, sensitivity studies on these effects could be added to future revisions of this document.

INTENTIONALLY LEFT BLANK

8. REFERENCES AND INPUTS

The following is a list of the references cited in this document. Column 1 represents the unique six digit numerical identifier, which is placed in the text following the reference callout (e.g., CRWMS M&O 2000 [144054]). The purpose of these numbers is to assist the reader in locating a specific reference. Within the reference list, multiple sources by the same author (e.g., CRWMS M&O 2000) are ordered numerically by the unique identifier.

8.1 DOCUMENTS CITED

124208 Apps, J.A. 1970. *The Stability Field of Analcime.* Ph.D. thesis. Cambridge, Massachusetts: Harvard University. TIC: 247233.

124211 Apps, J.A. and Chang, G.M. 1992. "Correlation of the Na/K Ratio in Geothermal Well Waters with the Thermodynamic Properties of Low Albite and Potash Feldspar." *Proceedings of the 7th International Symposium on Water-Rock Interaction, Park City, Utah, July 13-18, 1992*. Kharaka, Y.K. and Maest, A.S., eds. 2, 1437-1440. Rotterdam, The Netherlands: A.A. Balkema. TIC: 208527.

153329 Arnórsson, S. and Stefánsson, A. 1999. "Assessment of Feldspar Solubility Constants in Water in the Range 0° to 350°C at Vapor Saturation Pressures." *American Journal of Science*, *299*, (3), 173-209. New Haven, Connecticut: Kline Geology Laboratory, Yale University. TIC: 249258.

101379 Bear, J. 1988. *Dynamics of Fluids in Porous Media*. New York, New York: Dover Publications. TIC: 217568.

104905 Berman, R.G. 1988. "Internally Consistent Thermodynamic Data for Minerals in the System Na2O-K2O-CaO-MgO-FeO-Fe2O3-Al2O3-SiO2-TiO2-H2O-CO2." *Journal of Petrology*, *29*, (2), 445-522. Oxford, England: Oxford University Press. TIC: 236892.

101430 Bish, D.L.; Carey, J.W.; Levy, S.S.; and Chipera, S.J. 1996. *Mineralogy-Petrology Contribution to the Near-Field Environment Report*. Milestone LA3668. Los Alamos, New Mexico: Los Alamos National Laboratory. ACC: MOL.19971111.0588.

126590 Blum, A.E. and Stillings, L.L. 1995. "Feldspar Dissolution Kinetics." Chapter 7 of *Chemical Weathering Rates of Silicate Minerals*. White, A.F. and Brantley, S.L., eds. Reviews in Mineralogy Volume 31. Washington, D.C.: Mineralogical Society of America. TIC: 222496.

153816 Bodvarsson, G.S. 2001. "Scientific Notebooks Referenced in AMR N0120/U0110, Drift-Scale Coupled Processes (Drift-Scale Test and THC Seepage) Models DI: MDL-NBS-HS-000001 Rev01." Interoffice correspondence from G.S. Bodvarsson (CRWMS M&O) to File, February 1, 2001, with attachments. ACC: MOL.20010202.0152.

124275 Carroll, S.; Mroczek, E.; Alai, M.; and Ebert, M. 1998. "Amorphous Silica Precipitation (60 to 120°C): Comparison of Laboratory and Field Rates." *Geochimica et Cosmochimica Acta, 62*, (8), 1379-1396. New York, New York: Elsevier Science. TIC: 243029.

105073 Chermak, J.A. and Rimstidt, J.D. 1989. "Estimating the Thermodynamic Properties (Delta G and Delta H) of Silicate Minerals at 298 K from the Sum of Polyhedral Contributions." *American Mineralogist, 74*, 1023-1031. Washington, D.C.: Mineralogical Society of America. TIC: 237564.

105079 Chipera, S.J. and Bish, D.L. 1997. "Equilibrium Modeling of Clinoptilolite-Analcime Equilibria at Yucca Mountain, Nevada." *Clays and Clay Minerals, 45*, (2), 226-239. Long Island City, New York: Pergamon Press. TIC: 233948.

124263 CRWMS M&O (Civilian Radioactive Waste Management System Management and Operating Contractor) 1999. *Performance Assessment Operations-Thermal Hydrology and Coupled Processes Abstraction Core Team*. Input Transmittal PA-SSR-99241.T. Las Vegas, Nevada: CRWMS M&O. ACC: MOL.19991027.0159.

150953 CRWMS M&O 2000. *Emplacement Drift System Description Document*. SDD-EDS-SE-000001 REV 01. Las Vegas, Nevada: CRWMS M&O. ACC: MOL.20000803.0348.

151804 CRWMS M&O 2000. *Engineered Barrier System Degradation, Flow, and Transport Process Model Report*. TDR-EBS-MD-000006 REV 00 ICN 01. Las Vegas, Nevada: CRWMS M&O. ACC: MOL.20000724.0479.

142736 CRWMS M&O 2000. *Invert Effective Thermal Conductivity Calculation*. CAL-WIS-TH-000004 REV 00. Las Vegas, Nevada: CRWMS M&O. ACC: MOL.20000317.0593.

153225 CRWMS M&O 2000. *Repository Safety Strategy: Plan to Prepare the Safety Case to Support Yucca Mountain Site Recommendation and Licensing Considerations*. TDR-WIS-RL-000001 REV 04 ICN 01. Two volumes. Las Vegas, Nevada: CRWMS M&O. ACC: MOL.20001122.0186.

149137 CRWMS M&O 2000. *Repository Subsurface Design Information to Support TSPA-SR*. Input Transmittal PA-SSR-99218.Tc. Las Vegas, Nevada: CRWMS M&O. ACC: MOL.20000424.0690.

151014 CRWMS M&O 2000. *Tabulated In-Drift Geometric and Thermal Properties Used in Drift-Scale Models for TSPA-SR*. CAL-EBS-HS-000002 REV 00. Las Vegas, Nevada: CRWMS M&O. ACC: MOL.20000718.0219.

151467 CRWMS M&O 2000. *Subsurface Facility System Description Document*. SDD-SFS-SE-000001 REV 01. Las Vegas, Nevada: CRWMS M&O. ACC: MOL.20000807.0078.

153309 CRWMS M&O 2000. *Technical Work Plan for Nearfield Environment Thermal Analyses and Testing*. TWP-NBS-TH-000001 REV 00. Las Vegas, Nevada: CRWMS M&O. ACC: MOL.20001201.0026.

153447 CRWMS M&O 2000. *Technical Work Plan for Unsaturated Zone (UZ) Flow and Transport Process Model Report*. TWP-NBS-HS-000001 REV 00 ICN 2. Las Vegas, Nevada: CRWMS M&O. ACC: MOL.20010115.0311.

153814 CRWMS M&O 2001. *Updated CO2 Analysis of Gas Samples Collected from the Drift Scale Test*. Input Transmittal 00423.T. Las Vegas, Nevada: CRWMS M&O. ACC: MOL.20010202.0170.

100439 de Marsily, G. 1986. *Quantitative Hydrogeology: Groundwater Hydrology for Engineers*. San Diego, California: Academic Press. TIC: 208450.

149540 DOE (U.S. Department of Energy) 2000. *Quality Assurance Requirements and Description*. DOE/RW-0333P, Rev. 10. Washington, D.C.: U.S. Department of Energy, Office of Civilian Radioactive Waste Management. ACC: MOL.20000427.0422.

135997 Doughty, C. 1999. “Investigation of Conceptual and Numerical Approaches for Evaluating Moisture, Gas, Chemical, and Heat Transport in Fractured Unsaturated Rock.” *Journal of Contaminant Hydrology, 38*, (1-3), 69-106. New York, New York: Elsevier. TIC: 244160.

140067 Drever, J.I. 1997. *Geochemistry of Natural Waters*. 3rd Edition. Upper Saddle River, New Jersey: Prentice Hall. TIC: 246732.

105655 Dyer, J.R. 1999. “Revised Interim Guidance Pending Issuance of New U.S. Nuclear Regulatory Commission (NRC) Regulations (Revision 01, July 22, 1999), for Yucca Mountain, Nevada.” Letter from J.R. Dyer (DOE/YMSCO) to D.R. Wilkins (CRWMS M&O), September 3, 1999, OL&RC:SB-1714, with enclosure, “Interim Guidance Pending Issuance of New NRC Regulations for Yucca Mountain (Revision 01).” ACC: MOL.19990910.0079.

117799 Ehrlich, R.; Etris, E.L.; Brumfield, D.; Yuan, L.P.; and Crabtree, S.J. 1991. “Petrography and Reservoir Physics III: Physical Models for Permeability and Formation Factor.” *AAPG Bulletin, 75*, (10), 1579-1592. Tulsa, Oklahoma: American Association of Petroleum Geologists. TIC: 246294.

153464 Fournier, R.O. 1973. “Silica in Thermal Waters: Laboratory and Field Investigations.” *Proceedings of Symposium on Hydrogeochemistry and Biogeochemistry, Tokyo, Japan, September 7-9, 1970. Volume I - Hydrogeochemistry, 122-139*. Washington, D.C.: The Clarke Company. TIC: 235117.

124282 Fournier, R.O. and Rowe, J.J. 1962. “The Solubility of Cristobalite Along the Three-Phase Curve, Gas Plus Liquid Plus Cristobalite.” *The American Mineralogist, 47*, 897-902. Washington, D.C.: Mineralogical Society of America. TIC: 235380.

105797 Garrels, R.M. and Christ, C.L. 1965. *Solutions, Minerals and Equilibria*. Boston, Massachusetts: Jones and Bartlett. TIC: 223483.

106024 Helgeson, H.C.; Kirkham, D.H.; and Flowers, G.C. 1981. “Theoretical Prediction of the Thermodynamic Behavior of Aqueous Electrolytes at High Pressures and Temperatures: IV. Calculation of Activity Coefficients, Osmotic Coefficients, and Apparent Molal and Standard and Relative Partial Molal Properties to 600ºC and 5 kb.” *American Journal of Science, 281*, (10), 1249-1516. New Haven, Connecticut: Yale University, Kline Geology Laboratory. TIC: 238264.

106044 Holland, T.J.B. 1989. “Dependence of Entropy on Volume for Silicate and Oxide Minerals: A Review and a Predictive Model.” *American Mineralogist, 74*, 5-13. Washington, D.C.: Mineralogical Society of America. TIC: 235381.

128129 Inskeep, W.P. and Bloom, P.R. 1985. “An Evaluation of Rate Equations for Calcite Precipitation Kinetics at pCO2 Less than 0.01 atm and pH Greater than 8.” *Geochimica et Cosmochimica Acta, 49*, 2165-2180. New York, New York: Pergamon Press. TIC: 241125.

101630 Johnson, J.W.; Knauss, K.G.; Glassley, W.E.; DeLoach, L.D.; and Thompson, A.F.B 1998. “Reactive Transport Modeling of Plug-Flow Reactor Experiments: Quartz and Tuff Dissolution at 240°C.” *Journal of Hydrology, 209*, 81-111. Amsterdam, The Netherlands: Elsevier Science. TIC: 240986.

101632 Johnson, J.W.; Oelkers, E.H.; and Helgeson, H.C. 1992. “SUPCRT92: A Software Package for Calculating the Standard Molal Thermodynamic Properties of Minerals, Gases, Aqueous Species, and Reactions from 1 to 5000 Bar and 0 to 1000°C.” *Computers & Geosciences, 18*, (7), 899-947. New York, New York: Pergamon Press. TIC: 234273.

153700 Klein, C. and Hurlbut, C.S., Jr. 1993. *Manual of Mineralogy*. 21st Edition. New York, New York: John Wiley & Sons. TIC: 249368.

124300 Knauss, K.G. and Wolery, T.J. 1989. “Muscovite Dissolution Kinetics as a Function of pH and Time at 70°C.” *Geochimica et Cosmochimica Acta, 53*, 1493-1501. Elmsford, New York: Pergamon Press. TIC: 236215.

124306 Knowles-Van Cappellan, V.; Van Cappellan, P.; and Tiller, C. 1997. "Probing the Charge of Reactive Sites at the Mineral-Water Interface: Effect of Ionic Strength on Crystal Growth Kinetics of Fluorite." *Geochimica et Cosmochimica Acta, 61*, (9), 1871-1877. New York, New York: Pergamon Press. TIC: 246450.

128132 Kulik, D.A. and Aja, S.U. 1997. "The Hydrothermal Stability of Illite: Implications of Empirical Correlations and Gibbs Energy Minimization." *Proceedings of the Fifth International Symposium on Hydrothermal Reactions, Gatlinburg, Tennessee, July 20-24, 1997*. Palmer, D.A. and Wesolowski, D.J., eds. Pages 288-292. Oak Ridge, Tennessee: Oak Ridge National Laboratory. TIC: 247217.

100051 Langmuir, D. 1997. *Aqueous Environmental Geochemistry*. Upper Saddle River, New Jersey: Prentice Hall. TIC: 237107.

117091 Lasaga, A.C. 1998. *Kinetic Theory in the Earth Sciences*. Princeton, New Jersey: Princeton University Press. TIC: 246279.

126599 Levy, S.S.; Fabryka-Martin, J.T.; Dixon, P.R.; Liu, B.; Turin, H.J.; and Wolfsberg, A.V. 1997. "Chlorine-36 Investigations of Groundwater Infiltration in the Exploratory Studies Facility at Yucca Mountain, Nevada." *Scientific Basis for Nuclear Waste Management XX, Symposium held December 2-6, 1996, Boston, Massachusetts.* Gray, W.J. and Triay, I.R., eds. 465, 901-908. Pittsburgh, Pennsylvania: Materials Research Society. TIC: 238884.

105729 Liu, H.H.; Doughty, C.; and Bodvarsson, G.S. 1998. "An Active Fracture Model for Unsaturated Flow and Transport in Fractured Rocks." *Water Resources Research, 34*, (10), 2633-2646. Washington, D.C.: American Geophysical Union. TIC: 243012.

124354 Mazer, J.J.; Bates, J.K.; Bradley, J.P.; Bradley, C.R.; and Stevenson, C.M. 1992. "Alteration of Tektite to Form Weathering Products." *Nature, 357*, 573-576. London, England: Macmillan Magazines. TIC: 246479.

153292 NRC (U.S. Nuclear Regulatory Commission) 2000. *Issue Resolution Status Report Key Technical Issue: Evolution of the Near-Field Environment*. Rev. 3. [Washington, D.C.]: U.S. Nuclear Regulatory Commission. TIC: 249134.

126601 Ragnarsdottir, K.V. 1993. "Dissolution Kinetics of Heulandite at pH 2-12 and 25°C." *Geochimica et Cosmochimica Acta*, *57*, (11), 2439-2449. New York, New York: Pergamon Press. TIC: 243920.

117901 Reed, M.H. 1982. "Calculation of Multicomponent Chemical Equilibria and Reaction Processes in Systems Involving Minerals, Gases and an Aqueous Phase." *Geochimica et Cosmochimica Acta, 46*, (4), 513-528. New York, New York: Pergamon Press. TIC: 224159.

107088 Renders, P.J.N.; Gammons, C.H.; and Barnes, H.L. 1995. “Precipitation and Dissolution Rate Constants for Cristobalite from 150 to 300°C.” *Geochimica et Cosmochimica Acta*, *59*, 77-85. New York, New York: Elsevier Science. TIC: 226987.

101709 Rimstidt, J.D. 1997. “Quartz Solubility at Low Temperatures.” *Geochimica et Cosmochimica Acta*, *61*, (13), 2553-2558. New York, New York: Pergamon Press. TIC: 239020.

101708 Rimstidt, J.D. and Barnes, H.L. 1980. “The Kinetics of Silica–Water Reactions.” *Geochimica et Cosmochimica Acta, 44*, 1683-1699. [New York, New York]: Pergamon Press. TIC: 219975.

153683 Robie, R.A. and Hemingway, B.S. 1995. *Thermodynamic Properties of Minerals and Related Substances at 298.15 K and 1 Bar (105 Pascals) Pressure and at Higher Temperatures*. U.S. Geological Survey Bulletin 2131. Reston, Virginia: U.S. Geological Survey. On Order Library Tracking Number-230505

108567 Robinson, R.A. and Stokes, R.H. 1965. *Electrolyte Solutions, the Measurement and Interpretation of Conductance, Chemical Potential and Diffusion in Solutions of Simple Electrolytes*. 2nd Edition. London, England: Butterworths & Company. TIC: 242575.

127953 Shock, E.L.; Sassani, D.C.; Willis, M.; and Sverjensky, D.A. 1997. “Inorganic Species in Geologic Fluids: Correlations Among Standard Molal Thermodynamic Properties of Aqueous Ions and Hydroxide Complexes.” *Geochimica et Cosmochimica Acta*, *61*, (5), 907-950. [New York, New York]: Pergamon Press. TIC: 246451.

128146 Slider, H.C. 1976. *Practical Petroleum Reservoir Engineering Methods, An Energy Conservation Science*. Tulsa, Oklahoma: Petroleum Publishing Company. TIC: 247798.

133216 Smyth, J.R. and Bish, D.L. 1988. *Crystal Structures and Cation Sites of the Rock-Forming Minerals*. 332. Boston, Massachusetts: Allen & Unwin, Inc. On Order Library Tracking Number-235071

117914 Sonnenthal, E. and Ortoleva, P.J. 1994. “Numerical Simulations of Overpressured Compartments in Sedimentary Basins.” *Basin Compartments and Seals*. Ortoleva, P.J., ed. AAPG Memoir 61. 403-416. Tulsa, Oklahoma: American Association of Petroleum Geologists. TIC: 235940.

117127 Sonnenthal, E.L. and Bodvarsson, G.S. 1999. “Constraints on the Hydrology of the Unsaturated Zone at Yucca Mountain, NV from Three-Dimensional Models of Chloride and Strontium Geochemistry.” *Journal of Contaminant Hydrology, 38*, (1-3), 107-156. New York, New York: Elsevier. TIC: 244160.

153571 Spycher, N. 1998. First Exploratory Study Facility Thermal Test. Scientific Notebook YMP-LBNL-YWT-NS-1. ACC: MOL.20000413.0673.

153572 Spycher, N. 2000. First Exploratory Study Facility Thermal Test. Scientific Notebook YMP-LBNL-YWT-NS-1.1. ACC: MOL.20000829.0068.

101480 Steefel, C.I. and Lasaga, A.C. 1994. "A Coupled Model for Transport of Multiple Chemical Species and Kinetic Precipitation/Dissolution Reactions with Application to Reactive Flow in Single Phase Hydrothermal Systems." *American Journal of Science*, *294*, (5), 529-592. New Haven, Connecticut: Kline Geology Laboratory, Yale University. TIC: 235372.

153578 Stefansson, A. and Arnorsson, S. 2000. "Feldspar Saturation State in Natural Waters." *Geochimica et Cosmochimica Acta, 64*, (15), 2567-2584. New York, New York: Elsevier Science. TIC: 249336.

127964 Stoessell, R.K. 1988. "25°C and 1 Atm Dissolution Experiments of Sepiolite and Kerolite." *Geochimica et Cosmochimica Acta, 52*, 365-374. [New York, New York]: Pergamon Press. TIC: 246452.

127978 Svensson, U. and Dreybrodt, W. 1992. "Dissolution Kinetics of Natural Calcite Minerals in CO2-Water Systems Approaching Calcite Equilibrium." *Chemical Geology*, *100*, 129-145. Amsterdam, The Netherlands: Elsevier Science. TIC: 246497.

101732 Tester, J.W.; Worley, G.W.; Robison, B.A.; Grigsby, C.O.; and Feerer, J.L. 1994. "Correlating Quartz Dissolution Kinetics in Pure Water from 25° to 625°C." *Geochimica et Cosmochimica Acta*, *58*, (11), 2407-2420. New York, New York: Elsevier Science. TIC: 236776.

117170 Xu, T. and Pruess, K. 1998. *Coupled Modeling of Non-Isothermal Multi-Phase Flow, Solute Transport and Reactive Chemistry in Porous and Fractured Media: 1. Model Development and Validation.* LBNL-42050. Berkeley, California: Lawrence Berkeley National Laboratory. TIC: 243735.

101751 Xu, T.; Pruess, K.; and Brimhall, G. 1998. *An Improved Equilibrium-Kinetics Speciation Algorithm for Redox Reactions in Variably Saturated Subsurface Flow Systems.* LBNL-41789. Berkeley, California: Lawrence Berkeley National Laboratory. TIC: 240019.

100194 Yang, I.C.; Rattray, G.W.; and Yu, P. 1996. *Interpretation of Chemical and Isotopic Data from Boreholes in the Unsaturated Zone at Yucca Mountain, Nevada*. Water-Resources Investigations Report 96-4058. Denver, Colorado: U.S. Geological Survey. ACC: MOL.19980528.0216.

149733 YMP (Yucca Mountain Site Characterization Project) 2000. *Q-List*. YMP/90-55Q, Rev. 6. Las Vegas, Nevada: Yucca Mountain Site Characterization Office. ACC: MOL.20000510.0177.

Software Cited

146496 Lawrence Berkeley National Laboratory 1/14/2000. *Software Code: TOUGH2 V1.4*. V1.4. Sun Workstation and DEC/ALPHA. 10007-1.4-01.

153100 Lawrence Berkeley National Laboratory 2000. *Software Code: GSLIB*. V1.0SISIMV1.204. SUN w/Unix OS. STN: 10397-1.0SISIMV1.204-00.

153217 LBNL (Lawrence Berkeley National Laboratory) 08/29/1999. *Software Code: SOLVEQ/CHILLER*. V1.0. PC w/Windows OS. STN: 10057-1.0-00.

153216 LBNL (Lawrence Berkeley National Laboratory) 09/17/1999. *Software Code: AMESH*. V1.0. DEC and SUN w/Unix OS. STN: 10045-1.0-00.

153219 LBNL (Lawrence Berkeley National Laboratory) 09/21/1999. *Software Code: TOUGHREACT*. V2.2. DEC and SUN w/Unix OS. STN: 10154-2.2-00.

153090 LBNL (Lawrence Berkeley National Laboratory) 09/22/2000. *Software Routine Report: assign.f*. V1.0. SUN w/Unix OS. STN: 10315-1.0-00.

153089 LBNL (Lawrence Berkeley National Laboratory) 09/22/2000. *Software Routine Report: exclude.f*. V1.0. SUN w/Unix OS. STN: 10316-1.0-00.

153087 LBNL (Lawrence Berkeley National Laboratory) 09/22/2000. *Software Routine Report: kswitch*. V1.0. SUN w/Unix OS. STN: 10319-1.0-00.

153091 LBNL (Lawrence Berkeley National Laboratory) 09/22/2000. *Software Routine Report: merggrid2.f*. V1.0. SUN w/Unix OS. STN: 10314-1.0-00.

153092 LBNL (Lawrence Berkeley National Laboratory) 09/22/2000. *Software Routine Report: mk_circ2*. V1.0. SUN w/Unix OS. STN: 10312-1.0-00.

153093 LBNL (Lawrence Berkeley National Laboratory) 09/22/2000. *Software Routine Report: mk_rect2.f*. V1.0. SUN w/Unix OS. STN: 10313-1.0-00.

152883 LBNL (Lawrence Berkeley National Laboratory) 09/22/2000. *Software Routine: flipk*. V1.0. SUN w/Unix OS. STN: 10320-1.0-00.

152902 LBNL (Lawrence Berkeley National Laboratory) 09/22/2000. *Software Routine: kreg*. V1.0. SUN w/Unix OS. STN: 10318-1.0-00.

152901 LBNL (Lawrence Berkeley National Laboratory) 09/22/2000. *Software Routine: mk_incon*. V1.0. SUN w/Unix OS. STN: 10350-1.0-00.

152900 LBNL (Lawrence Berkeley National Laboratory) 09/22/2000. *Software Routine: regress*. V1.0. PC w/Windows OS. STN: 10321-1.0-00.

152899 LBNL (Lawrence Berkeley National Laboratory) 09/22/2000. *Software Routine: switch*. V1.0. PC w/Windows OS. STN: 10322-1.0-00.

153068 LBNL (Lawrence Berkeley National Laboratory) 11/03/2000. *Software Routine Report: mk_grav2.f*. V1.0. SUN w/Unix OS. STN: 10379-1.0-00.

153082 LBNL (Lawrence Berkeley National Laboratory) 11/03/2000. *Software Routine Report: mrgdrift.f*. V1.0. SUN w/Unix OS. STN: 10380-1.0-00.

153083 LBNL (Lawrence Berkeley National Laboratory) 11/03/2000. *Software Routine Report: sav1d_dst2d.f*. V1.0. SUN w/Unix OS. STN: 10381-1.0-00.

153218 LBNL (Lawrence Berkeley National Laboratory) 1999. *Software Code: SUPCRT92*. V1.0. PC w/Windows OS and MAC w/MAC OS. STN: 10058-1.0-00.

153101 LBNL (Lawrence Berkeley National Laboratory) 2000. *Software Code*: *TOUGHREACT*. V2.3. SUN and DEC w/Unix OS. STN: 10396-2.3-00. URN-0730

153067 LBNL (Lawrence Berkeley National Laboratory) 2000. *Software Routine Report: 2kgridv1a.for*. V1.0. PC w/Windows OS. STN: 10382-1.0-00.

153085 LBNL (Lawrence Berkeley National Laboratory) 2000. *Software Routine Report: avgperm.f*. V1.0. DEC & SUN w/UNIX OS. STN: 10378-1.0-00.

126891 LLNL (Lawrence Livermore National Laboratory) 1999. *Software Code: EQ3/6 V7.2b*. V7.2b. PC. LLNL: UCRL-MA-110662.

8.2 CODES, STANDARDS, REGULATIONS, AND PROCEDURES

AP-2.21Q, Rev. 1, ICN 0. *Quality Determinations and Planning for Scientific, Engineering, and Regulatory Compliance Activities*. [Washington, D.C.]: U.S. Department of Energy, Office of Civilian Radioactive Waste Management. ACC: MOL.20010129.0145.

AP-3.10Q, Rev. 2, ICN 3. *Analyses and Models*. Washington, D.C.: U. S. Department of Energy, Office of Civilian Radioactive Waste Management. ACC: MOL.20000918.0282.

AP-3.15Q, Rev. 2, ICN 0. *Managing Technical Product Inputs*. Washington, D.C: U.S. Department of Energy, Office of Civilian Radioactive Waste Management. ACC: MOL.20001109.0051.

AP-SI.1Q, Rev. 2, ICN 4, ECN 1. *Software Management*. Washington, D.C.: U.S. Department of Energy, Office of Civilian Radioactive Waste Management. ACC: MOL.20001019.0023.

AP-SV.1Q, Rev. 0, ICN 2. *Control of the Electronic Management of Information*. Washington, D.C.: U.S. Department of Energy, Office of Civilian Radioactive Waste Management. ACC: MOL.20000831.0065.

QAP-2-3, Rev. 10. *Classification of Permanent Items*. Las Vegas, Nevada: CRWMS M&O. ACC: MOL.19990316.0006.

YMP-LBNL-QIP-SV.0 Rev. 2, Mod. 0. *Management of YMP-LBNL Electronic Data.* Berkeley, California: Lawrence Berkeley National Laboratory. ACC: MOL.20001113.0014.

8.3 SOURCE DATA, LISTED BY DATA TRACKING NUMBER

145617 GS950608312272.001. Chemical Data for Pore Water from Tuff Cores of USW NRG-6, NRG7/7a, UZ-14 and UZ-N55, and UE-25 UZ#16. Submittal date: 05/30/1995.

153637 LA000000000071.001. Chemistry of Diagenetically Altered Tuffs at Yucca Mountain. Submittal date: 10/21/1993.

153386 LA0008SC12213N.001. Calculated Zeolite Thermodynamic Properties. Submittal date: 08/16/2000.

153485 LA0009SL831151.001. Fracture Mineralogy of the ESF Single Heater Test Block, Alcove 5. Submittal date: 09/28/2000.

113495 LA9908JC831321.001. Mineralogic Model “MM3.0” Version 3.0. Submittal date: 08/16/1999.

146447 LA9912SL831151.001. Fracture Mineralogy of Drill Core ESF-HD-TEMP-2. Submittal date: 01/05/2000.

146449 LA9912SL831151.002. Percent Coverage by Fracture-Coating Minerals in Core ESF-HD-TEMP-2. Submittal date: 01/05/2000.

146451 LB000121123142.003. Isotope Data for CO2 Gas Samples Collected From the Hydrology Holes of the ESF Drift Scale Test for the Period August 9, 1999 through November 30, 1999. Submittal date: 01/21/2000.

153460 LB0011CO2DST08.001. Isotope Data for CO2 from Gas Samples Collected from Hydrology Holes in Drift-Scale Test. Submittal date: 12/09/2000. Submit to RPC URN-0801

153470 LB0011DSTFRAC1.001. Drift-Scale Properties Update: 1. Updated Drift-Scale Properties. This is Input Data for AMR U0110 (MDL-NBS-HS-000001 REV 01). Submittal date: 12/06/2000. Submit to RPC URN-0802

153381 LB0011THCDISSM.001. Comparison Modeling for Tptpmn Tuff Dissolution Experiment: 1. Input Data for AMR U0110 REV01. Submittal date: 12/07/2000. Submit to RPC URN-0800

153380 LB0011THCDISSX.001. Summary of Results from Tptpmn Tuff Dissolution Experiment. Submittal date: 12/07/2000. Submit to RPC URN-0799

153687 LB0101DSTTHGRD.001. 2D Finite Element Mesh used for DST THC Model Simulations (AMR U0110 REV 01). Submittal date: 01/05/2001. Submit to RPC URN-0803

111475 LB990501233129.004. 3-D UZ Model Calibration Grids for AMR U0000, “Development of Numerical Grids of UZ Flow and Transport Modeling”. Submittal date: 09/24/1999.

105888 LB990601233124.001. Seepage Data Feed to UZ Drift-Scale Flow Model for TSPA-SR. Submittal date: 06/18/1999.

111476 LB990630123142.003. Fourth, Fifth, and Sixth Quarters TDIF Submission for the Drift Scale Test, September 1998 to May 1999. Submittal date: 06/30/1999.

125604 LB990701233129.002. 3-D Model Calibration Grid for Calculation of Flow Fields Using #3 Perched Water Conceptual Model (Non-Perched Water Model) for AMR U0050, “UZ Flow Models and Submodels”. Submittal date: 03/11/2000.

110226 LB990861233129.001. Drift Scale Calibrated 1-D Property Set, FY99. Submittal date: 08/06/1999.

109899 LB990861233129.002. Drift Scale Calibrated 1-D Property Set, FY99. Submittal date: 08/06/1999.

111479 LB990861233129.003. Drift Scale Calibrated 1-D Property Set, FY99. Submittal date: 08/06/1999.

125868 LB991091233129.001. One-Dimensional, Mountain-Scale Calibration for AMR U0035, “Calibrated Properties Model”. Submittal date: 10/22/1999.

128157 LB991215123142.001. CO2 Analysis of Gas Samples Collected from the Drift Scale Test. Submittal date: 02/17/2000.

1040555 LB997141233129.001. Calibrated Basecase Infiltration 1-D Parameter Set for the UZ Flow and Transport Model, FY99. Submittal date: 07/21/1999.

142884 LL000114004242.090. TSPA-SR Mean Calculations. Submittal date: 01/28/2000.

153288 LL001100931031.008. Aqueous Chemistry of Water Sampled from Boreholes of the Drift Scale Test (DST). Submittal date: 11/10/2000.

153616 LL001200231031.009. Aqueous Chemistry of Water Sampled from Boreholes of the Drift Scale Test (DST). Submittal date: 12/04/2000.

144922 LL990702804244.100. Borehole and Pore Water Data. Submittal date: 7/13/1999.

150930 MO0005PORWATER.000. Perm-Sample Pore Water Data. Submittal date: 05/04/2000.

153707 MO0007SEPDSTPC.001. Drift Scale Test (DST) Temperature, Power, Current, and Voltage Data for November 1, 1999 through May 31, 2000. Submittal date: 07/13/2000. Submit to RPC URN-0804

153742 MO0008THRMODYN.000. Data Qualification Report: Data Qualification Report for Thermodynamic Data File, DATA0.YMP.R0 for Geochemical Code, EQ3/6. Submittal date: 08/03/2000. Submit to RPC URN-0807

153708 MO0012SEPDSTPC.002. Drift Scale Test (DST) Temperature, Power, Current, and Voltage Data for June 1, 2000 through November 30, 2000. Submittal date: 12/19/2000. Submit to RPC URN-0805

153711 MO0101SEPFDDST.000. Field Measured Data of Water Samples from the Drift Scale Test. Submittal date: 01/03/2001. Submit to RPC URN-0806

153364 SN0002T0872799.009. Effective Thermal Conductivity Parameter for the No Backfill Case Implemented in the Drift-Scale Models used in TSPA-SR. Submittal date: 02/10/2000.

111485 SN9907T0872799.001. Heat Decay Data and Repository Footprint for Thermal-Hydrologic and Conduction-Only Models for TSPA-SR (Total System Performance Assessment-Site Recommendation). Submittal date: 07/27/1999.

124205 SN9907T0872799.002. Effective Thermal Conductivity for Drift-Scale Models Used in TSPA-SR (Total System Performance Assessment-Site Recommendation). Submittal date: 07/27/1999.

8.4 OUTPUT DATA, LISTED BY DATA TRACKING NUMBER

LB991200DSTTHC.003. Attachment II – Mineral Initial Volume Fractions of AMR N0120/U0110, “Drift-Scale Coupled Processes (Drift-Scale and THC Seepage) Models Rev00.” Submittal date: 03/11/2000. (Now referred to as Attachment I in Rev01)

LB991200DSTTHC.006. Waste Package Average Heat Transfer: Attachment V of AMR

U0110/N0120, “Drift-Scale Coupled Processes (DST and THC Seepage) Models Rev 00.” Submittal date: 3/11/00. (Now referred to as Attachment VII in Rev01)

LB0011DSTTHCR1.001. Tables showing Geochemical and Drift-Scale Seepage Model Data which are presented in AMR N0120, “Drift-Scale Coupled Processes (DST and THC Seepage) Models Rev01.” Submittal date: submitted with this AMR.

LB0011DSTTHCR1.002. Model Input and Output Files, Excel Spreadsheets and Resultant Figures which are presented in AMR N0120, “Drift-Scale Coupled Processes (DST and THC Seepage) Models Rev 01.” Submittal date: submitted with this AMR.

LB0101DSTTHCR1.001. Pore Water Composition and CO2 Partial Pressure Input to Thermal-Hydrological-Chemical (THC) Simulations: Table 3 of AMR N0120/U0110 Rev01, “Drift-Scale Coupled Processes (Drift-Scale Test And Thc Seepage) MODELS.” Submittal date: submitted with this AMR.

LB0101DSTTHCR1.002. Attachment II - Mineral Initial Volume Fractions: Tptpll THC Model for AMR N0120/U0110 Rev01, “Drift-Scale Coupled Processes (Drift-Scale Test And THC Seepage) Models.” Submittal date: submitted with this AMR.

LB0101DSTTHCR1.003. Attachment III – Mineral Reactive Surface Areas: Tptpmn And DST THC Models for AMR N0120/U0110 Rev01, “Drift-Scale Coupled Processes (Drift-Scale Test And THC Seepage) Models.” Submittal date: submitted with this AMR.

LB0101DSTTHCR1.004. Attachment IV - Mineral Reactive Surface Areas: Tptpll THC Model for AMR N0120/U0110 Rev01, “Drift-Scale Coupled Processes (Drift-Scale Test and THC Seepage) Models.” Submittal date: submitted with this AMR.

LB0101DSTTHCR1.005. Attachment V – Thermodynamic Database: Tptpmn THC Backfill and DST THC Rev00 Models for AMR N0120/U0110 Rev01, “Drift-Scale Coupled Processes (Drift-Scale Test and THC Seepage) Models.” Submittal date: submitted with this AMR.

LB0101DSTTHCR1.006. Attachment VI – Thermodynamic Database: Tptpmn THC Backfill and DST THC Rev01 Models for AMR N0120/U0110 Rev01, “Drift-Scale Coupled Processes (Drift-Scale Test and THC Seepage) Models.” Submittal date: submitted with this AMR.

LB0101DSTTHCR1.007. Attachment VIII – Waste Package Average Heat Transfer: Tptpmn No-Backfill and Tptpll THC Models for AMR N0120/U0110 Rev01, “Drift-Scale Coupled Processes (Drift-Scale Test and THC Seepage) Models.” Submittal date: submitted with this AMR.

INTENTIONALLY LEFT BLANK

9. ATTACHMENTS

ATTACHMENT I – MINERAL INITIAL VOLUME FRACTIONS: Tptpmn and DST THC Models

ATTACHMENT II - MINERAL INITIAL VOLUME FRACTIONS: Tptpll THC Model

ATTACHMENT III – MINERAL REACTIVE SURFACE AREAS: Tptpmn and DST THC Models

ATTACHMENT IV - MINERAL REACTIVE SURFACE AREAS: Tptpll THC Model

ATTACHMENT V – THERMODYNAMIC DATABASE: Tptpmn THC Backfill and DST THC Rev00 Models

ATTACHMENT VI – THERMODYNAMIC DATABASE: Tptpmn THC No-Backfill and DST THC Rev01 Models

ATTACHMENT VII – WASTE PACKAGE AVERAGE HEAT TRANSFER: Tptpmn THC Backfill Model

ATTACHMENT VIII – WASTE PACKAGE AVERAGE HEAT TRANSFER: Tptpmn No-Backfill and Tptpll THC Models

ATTACHMENT IX – EFFECTIVE THERMAL CONDUCTIVITY FOR IN-DRIFT OPEN SPACES: Tptpmn THC Backfill Model

ATTACHMENT X – EFFECTIVE THERMAL CONDUCTIVITY FOR IN-DRIFT OPEN SPACES: Tptpmn No-Backfill and Tptpll THC Models

ATTACHMENT XI – LIST OF MODEL INPUT AND OUTPUT FILES

3/5/01

INTENTIONALLY LEFT BLANK

JSH 3/5/01

Main Menu

EXIT

ATTACHMENT I – MINERAL INITIAL VOLUME FRACTIONS: Tptpmn and DST THC Models

(DTN: LB991200DSTTHC.003).

Unit	Rock Name	Zone	K-feldspar	Albite	Anorthite	Ca-Smectite	Na-Smectite	Mg-Smectite	K-Smectite	Illite	Tridymite
Tcw3	tcwm3	1	0.0946	0.0699	0.0024	0.0407	0.0175	0.0407	0.0175	0.0129	0.0000
	tcwf3	2	0.0946	0.0699	0.0024	0.0407	0.0175	0.0407	0.0175	0.0129	0.0000
Ptn1	ptnm1	3	0.0377	0.0279	0.0009	0.0643	0.0276	0.0643	0.0276	0.0204	0.0000
	ptnf1	4	0.0377	0.0279	0.0009	0.0643	0.0276	0.0643	0.0276	0.0204	0.0000
Ptn2	ptnm2	5	0.0449	0.0332	0.0011	0.0568	0.0244	0.0568	0.0244	0.0180	0.0000
	ptnf2	6	0.0449	0.0332	0.0011	0.0568	0.0244	0.0568	0.0244	0.0180	0.0000
Ptn3	ptnm3	7	0.0156	0.0116	0.0004	0.0095	0.0041	0.0095	0.0041	0.0030	0.0000
	ptnf3	8	0.0156	0.0116	0.0004	0.0095	0.0041	0.0095	0.0041	0.0030	0.0000
Ptn4	ptnm4	9	0.0806	0.0595	0.0020	0.0209	0.0090	0.0209	0.0090	0.0066	0.0000
	ptnf4	10	0.0806	0.0595	0.0020	0.0209	0.0090	0.0209	0.0090	0.0066	0.0000
Ptn5	ptnm5	11	0.0965	0.0712	0.0024	0.0090	0.0039	0.0090	0.0039	0.0029	0.0000
	ptnf5	12	0.0965	0.0712	0.0024	0.0090	0.0039	0.0090	0.0039	0.0029	0.0000
Ptn6	ptnm6	13	0.0855	0.0631	0.0021	0.0329	0.0141	0.0329	0.0141	0.0104	0.0000
	ptnf6	14	0.0855	0.0631	0.0021	0.0329	0.0141	0.0329	0.0141	0.0104	0.0000
Tsw31	tswm1	15	0.2358	0.1741	0.0059	0.0001	0.0001	0.0001	0.0001	0.0000	0.0000
	tswf1	16	0.2358	0.1741	0.0059	0.0001	0.0001	0.0001	0.0001	0.0000	0.0000
Tsw32	tswm2	17	0.4025	0.2973	0.0100	0.0027	0.0012	0.0027	0.0012	0.0009	0.0919
	tswf2	18	0.2435	0.1798	0.0061	0.0174	0.0074	0.0174	0.0074	0.0055	0.0556
Tsw33	tswm3	19	0.3051	0.2253	0.0076	0.0131	0.0056	0.0131	0.0056	0.0042	0.1071
	tswf3	20	0.1846	0.1363	0.0046	0.0237	0.0102	0.0237	0.0102	0.0075	0.0648
Tsw34	tswm4	21	0.3096	0.2286	0.0077	0.0081	0.0035	0.0081	0.0035	0.0026	0.0489
	tswf4	22	0.1873	0.1383	0.0047	0.0207	0.0089	0.0207	0.0089	0.0066	0.0296
Tsw35	tswm5	23	0.3051	0.2253	0.0076	0.0082	0.0035	0.0082	0.0035	0.0026	0.0597
	tswf5	24	0.1846	0.1363	0.0046	0.0207	0.0089	0.0207	0.0089	0.0066	0.0361
Tsw36	tswm6	25	0.3094	0.2285	0.0077	0.0074	0.0032	0.0074	0.0032	0.0024	0.0137
	tswf6	26	0.1872	0.1382	0.0047	0.0202	0.0087	0.0202	0.0087	0.0064	0.0083
Tsw37	tswm7	27	0.3057	0.2257	0.0076	0.0079	0.0034	0.0079	0.0034	0.0025	0.0077
	tswf7	28	0.1849	0.1366	0.0046	0.0205	0.0088	0.0205	0.0088	0.0065	0.0047
Tsw38	tswm8	29	0.0878	0.0648	0.0022	0.0180	0.0077	0.0180	0.0077	0.0057	0.0054
	tswf8	30	0.0878	0.0648	0.0022	0.0180	0.0077	0.0180	0.0077	0.0057	0.0054
Ch2	ch2mz	31	0.0370	0.0273	0.0009	0.0060	0.0026	0.0060	0.0026	0.0019	0.0000
	ch2fz	32	0.0370	0.0273	0.0009	0.0060	0.0026	0.0060	0.0026	0.0019	0.0000

Main Menu

EXIT

Unit	Rock Name	Zone	Cristobalite	Quartz	Glass	Hematite	Calcite	Stellerite	Heulandite	Mordenite	Clinoptilolite
Tcw3	tcwm3	1	0.1323	0.0037	0.4580	0.0000	0.0000	0.0000	0.0329	0.0110	0.0659
	tcwf3	2	0.1323	0.0037	0.4580	0.0000	0.0000	0.0000	0.0329	0.0110	0.0659
Ptn1	ptnm1	3	0.0000	0.0009	0.7283	0.0000	0.0000	0.0000	0.0000	0.0000	0.0000
	ptnf1	4	0.0000	0.0009	0.7283	0.0000	0.0000	0.0000	0.0000	0.0000	0.0000
Ptn2	ptnm2	5	0.0350	0.0157	0.6895	0.0002	0.0000	0.0000	0.0000	0.0000	0.0000
	ptnf2	6	0.0350	0.0157	0.6895	0.0002	0.0000	0.0000	0.0000	0.0000	0.0000
Ptn3	ptnm3	7	0.0763	0.0009	0.8652	0.0000	0.0000	0.0000	0.0000	0.0000	0.0000
	ptnf3	8	0.0763	0.0009	0.8652	0.0000	0.0000	0.0000	0.0000	0.0000	0.0000
Ptn4	ptnm4	9	0.0524	0.0139	0.7254	0.0000	0.0000	0.0000	0.0000	0.0000	0.0000
	ptnf4	10	0.0524	0.0139	0.7254	0.0000	0.0000	0.0000	0.0000	0.0000	0.0000
Ptn5	ptnm5	11	0.0214	0.0094	0.7679	0.0024	0.0000	0.0000	0.0000	0.0000	0.0000
	ptnf5	12	0.0214	0.0094	0.7679	0.0024	0.0000	0.0000	0.0000	0.0000	0.0000
Ptn6	ptnm6	13	0.0083	0.0142	0.7129	0.0024	0.0070	0.0000	0.0000	0.0000	0.0000
	ptnf6	14	0.0083	0.0142	0.7129	0.0024	0.0070	0.0000	0.0000	0.0000	0.0000
Tsw31	tswm1	15	0.0915	0.0047	0.4550	0.0050	0.0276	0.0000	0.0000	0.0000	0.0000
	tswf1	16	0.0915	0.0047	0.4550	0.0050	0.0276	0.0000	0.0000	0.0000	0.0000
Tsw32	tswm2	17	0.1516	0.0079	0.0152	0.0044	0.0095	0.0011	0.0000	0.0001	0.0000
	tswf2	18	0.0917	0.0048	0.0092	0.0027	0.0257	0.3257	0.0000	0.0001	0.0000
Tsw33	tswm3	19	0.2336	0.0760	0.0000	0.0036	0.0000	0.0000	0.0000	0.0000	0.0000
	tswf3	20	0.1413	0.0460	0.0000	0.0022	0.0200	0.3250	0.0000	0.0000	0.0000
Tsw34	tswm4	21	0.2588	0.1202	0.0000	0.0004	0.0000	0.0000	0.0000	0.0000	0.0000
	tswf4	22	0.1566	0.0727	0.0000	0.0002	0.0200	0.3250	0.0000	0.0000	0.0000
Tsw35	tswm5	23	0.1660	0.2037	0.0000	0.0017	0.0050	0.0000	0.0000	0.0000	0.0000
	tswf5	24	0.1004	0.1232	0.0000	0.0010	0.0230	0.3250	0.0000	0.0000	0.0000
Tsw36	tswm6	25	0.1509	0.2643	0.0000	0.0020	0.0000	0.0000	0.0000	0.0000	0.0000
	tswf6	26	0.0913	0.1599	0.0000	0.0012	0.0200	0.3250	0.0000	0.0000	0.0000
Tsw37	tswm7	27	0.2273	0.2004	0.0000	0.0005	0.0000	0.0000	0.0000	0.0000	0.0000
	tswf7	28	0.1375	0.1212	0.0000	0.0003	0.0200	0.3250	0.0000	0.0000	0.0000
Tsw38	tswm8	29	0.1557	0.0244	0.5629	0.0000	0.0000	0.0000	0.0119	0.0040	0.0238
	tswf8	30	0.1557	0.0244	0.5629	0.0000	0.0000	0.0000	0.0119	0.0040	0.0238
Ch2	ch2mz	31	0.1609	0.0326	0.0000	0.0000	0.0000	0.0000	0.2166	0.0722	0.4333
	ch2fz	32	0.1609	0.0326	0.0000	0.0000	0.0000	0.0000	0.2166	0.0722	0.4333

Main Menu

EXIT

ATTACHMENT II - MINERAL INITIAL VOLUME FRACTIONS:
Tptpll THC Model

(DTN: LB0101DSTTHCR1.002).

Rock	Zone	K-Feldspar	Albite	Anorthite	Ca-Smectite	Na-Smectite	Mg-Smectite	Illite	Tridymite	Cristobalite	Quartz
tcwm1	1	0.36911	0.27257	0.00917	0.00198	0.00085	0.00198	0.00148	0.10285	0.21294	0.00942
tcwf1	2	0.36911	0.27257	0.00917	0.00198	0.00085	0.00198	0.00148	0.10285	0.21294	0.00942
tcwm2	3	0.36911	0.27257	0.00917	0.00198	0.00085	0.00198	0.00148	0.10285	0.21294	0.00942
tcwf2	4	0.36911	0.27257	0.00917	0.00198	0.00085	0.00198	0.00148	0.10285	0.21294	0.00942
tcwm3	5	0.16239	0.11992	0.00403	0.04403	0.01887	0.04403	0.03284	0.00000	0.12577	0.00744
tcwf3	6	0.16239	0.11992	0.00403	0.04403	0.01887	0.04403	0.03284	0.00000	0.12577	0.00744
ptnm1	7	0.05149	0.03802	0.00128	0.02441	0.01046	0.02441	0.01821	0.00015	0.01460	0.00702
ptnf1	8	0.05149	0.03802	0.00128	0.02441	0.01046	0.02441	0.01821	0.00015	0.01460	0.00702
ptnm2	9	0.05148	0.03802	0.00128	0.02441	0.01046	0.02441	0.01821	0.00015	0.01460	0.00702
ptnf2	10	0.05148	0.03802	0.00128	0.02441	0.01046	0.02441	0.01821	0.00015	0.01460	0.00702
ptnm3	11	0.05149	0.03802	0.00128	0.02441	0.01046	0.02441	0.01821	0.00015	0.01460	0.00702
ptnf3	12	0.05149	0.03802	0.00128	0.02441	0.01046	0.02441	0.01821	0.00015	0.01460	0.00702
ptnm4	13	0.05149	0.03802	0.00128	0.02441	0.01046	0.02441	0.01821	0.00015	0.01460	0.00702
ptnf4	14	0.05149	0.03802	0.00128	0.02441	0.01046	0.02441	0.01821	0.00015	0.01460	0.00702
ptnm5	15	0.05136	0.03793	0.00128	0.02435	0.01044	0.02435	0.01817	0.00015	0.01460	0.00702
ptnf5	16	0.05136	0.03793	0.00128	0.02435	0.01044	0.02435	0.01817	0.00015	0.01460	0.00702
ptnm6	17	0.05137	0.03794	0.00128	0.02436	0.01044	0.02436	0.01817	0.00015	0.01457	0.00701
ptnf6	18	0.05137	0.03794	0.00128	0.02436	0.01044	0.02436	0.01817	0.00015	0.01457	0.00701
tswm1	19	0.10362	0.07652	0.00257	0.00213	0.00091	0.00213	0.00159	0.00112	0.01999	0.00118
tswf1	20	0.10362	0.07652	0.00257	0.00213	0.00091	0.00213	0.00159	0.00112	0.01999	0.00118
tswm2	21	0.38312	0.28291	0.00952	0.00343	0.00147	0.00343	0.00256	0.15942	0.13313	0.00473
tswf2	22	0.23179	0.17116	0.00576	0.01767	0.00757	0.01767	0.01318	0.09645	0.08054	0.00286
tswm3	23	0.36306	0.26810	0.00902	0.00777	0.00333	0.00777	0.00580	0.05630	0.23767	0.02695
tswf3	24	0.21965	0.16220	0.00546	0.02029	0.00870	0.02029	0.01514	0.03406	0.14379	0.01630
tswm4	25	0.32265	0.23826	0.00802	0.00517	0.00221	0.00517	0.00385	0.02310	0.35588	0.02526
tswf4	26	0.19520	0.14415	0.00485	0.01872	0.00802	0.01872	0.01396	0.01397	0.21530	0.01529
tswm5	27	0.34968	0.25822	0.00869	0.00686	0.00294	0.00686	0.00512	0.02321	0.18589	0.14046
tswf5	28	0.21155	0.15622	0.00526	0.01974	0.00846	0.01974	0.01473	0.01404	0.11247	0.08498
tswm6	29	0.36268	0.26782	0.00901	0.00327	0.00140	0.00327	0.00244	0.00195	0.16651	0.16845
tswf6	30	0.21942	0.16203	0.00545	0.01757	0.00753	0.01757	0.01311	0.00118	0.10074	0.10191
tswm7	31	0.36322	0.26822	0.00902	0.00328	0.00140	0.00328	0.00244	0.00195	0.16676	0.16870
tswf7	32	0.21975	0.16227	0.00546	0.01758	0.00753	0.01758	0.01311	0.00118	0.10089	0.10206
tswm8	33	0.11030	0.08145	0.00274	0.04279	0.01834	0.04279	0.03192	0.00000	0.09981	0.00790
tswf8	34	0.11030	0.08145	0.00274	0.04279	0.01834	0.04279	0.03192	0.00000	0.09981	0.00790
tswm9	35	0.06105	0.04508	0.00152	0.02739	0.01174	0.02739	0.02044	0.00000	0.06216	0.01481
tswf9	36	0.06105	0.04508	0.00152	0.02739	0.01174	0.02739	0.02044	0.00000	0.06216	0.01481
ch1mv	37	0.07829	0.05781	0.00195	0.00747	0.00320	0.00747	0.00557	0.00586	0.06920	0.03831
ch1fv	38	0.07829	0.05781	0.00195	0.00747	0.00320	0.00747	0.00557	0.00586	0.06920	0.03831

Main Menu

EXIT

Rock	Zone	Glass	Hematite	Calcite	Stellerite	Heulandite	Mordenite	Clinoptilolite	Kaolinite	Am. Silica	Opal	Fluorite
tcwm1	1	0.00139	0.00000	0.00358	0.00000	0.00083	0.00028	0.00167	0.00000	0.00000	0.00990	0.00000
tcwf1	2	0.00139	0.00000	0.00358	0.00000	0.00083	0.00028	0.00167	0.00000	0.00000	0.00990	0.00000
tcwm2	3	0.00139	0.00000	0.00358	0.00000	0.00083	0.00028	0.00167	0.00000	0.00000	0.00990	0.00000
tcwf2	4	0.00139	0.00000	0.00358	0.00000	0.00083	0.00028	0.00167	0.00000	0.00000	0.00990	0.00000
tcwm3	5	0.43046	0.00000	0.00032	0.00000	0.00000	0.00000	0.00000	0.00000	0.00000	0.00990	0.00000
tcwf3	6	0.43046	0.00000	0.00032	0.00000	0.00000	0.00000	0.00000	0.00000	0.00000	0.00990	0.00000
ptnm1	7	0.78888	0.00000	0.01086	0.00000	0.00008	0.00003	0.00017	0.00000	0.00000	0.00990	0.00000
ptnf1	8	0.78888	0.00000	0.01086	0.00000	0.00008	0.00003	0.00017	0.00000	0.00000	0.00990	0.00000
ptnm2	9	0.78876	0.00015	0.01086	0.00000	0.00008	0.00003	0.00017	0.00000	0.00000	0.00990	0.00000
ptnf2	10	0.78876	0.00015	0.01086	0.00000	0.00008	0.00003	0.00017	0.00000	0.00000	0.00990	0.00000
ptnm3	11	0.78888	0.00000	0.01086	0.00000	0.00008	0.00003	0.00017	0.00000	0.00000	0.00990	0.00000
ptnf3	12	0.78888	0.00000	0.01086	0.00000	0.00008	0.00003	0.00017	0.00000	0.00000	0.00990	0.00000
ptnm4	13	0.78888	0.00000	0.01086	0.00000	0.00008	0.00003	0.00017	0.00000	0.00000	0.00990	0.00000
ptnf4	14	0.78888	0.00000	0.01086	0.00000	0.00008	0.00003	0.00017	0.00000	0.00000	0.00990	0.00000
ptnm5	15	0.78694	0.00239	0.01083	0.00000	0.00008	0.00003	0.00017	0.00000	0.00000	0.00990	0.00000
ptnf5	16	0.78694	0.00239	0.01083	0.00000	0.00008	0.00003	0.00017	0.00000	0.00000	0.00990	0.00000
ptnm6	17	0.78707	0.00228	0.01084	0.00000	0.00008	0.00003	0.00017	0.00000	0.00000	0.00990	0.00000
ptnf6	18	0.78707	0.00228	0.01084	0.00000	0.00008	0.00003	0.00017	0.00000	0.00000	0.00990	0.00000
tswm1	19	0.75630	0.00485	0.01693	0.00000	0.00005	0.00002	0.00009	0.00000	0.00000	0.00990	0.00010
tswf1	20	0.75630	0.00485	0.01693	0.00000	0.00005	0.00002	0.00009	0.00000	0.00000	0.00990	0.00010
tswm2	21	0.00070	0.00439	0.00110	0.00010	0.00000	0.00001	0.00000	0.00000	0.00000	0.00990	0.00010
tswf2	22	0.00042	0.00265	0.02046	0.32181	0.00000	0.00001	0.00000	0.00000	0.00000	0.00990	0.00010
tswm3	23	0.00000	0.00353	0.00067	0.00000	0.00001	0.00000	0.00003	0.00000	0.00000	0.00990	0.00010
tswf3	24	0.00000	0.00214	0.02020	0.32175	0.00001	0.00000	0.00002	0.00000	0.00000	0.00990	0.00010
tswm4	25	0.00000	0.00036	0.00007	0.00000	0.00000	0.00000	0.00000	0.00000	0.00000	0.00990	0.00010
tswf4	26	0.00000	0.00022	0.01984	0.32175	0.00000	0.00000	0.00000	0.00000	0.00000	0.00990	0.00010
tswm5	27	0.00000	0.00162	0.00038	0.00000	0.00002	0.00001	0.00005	0.00000	0.00000	0.00990	0.00010
tswf5	28	0.00000	0.00098	0.02003	0.32175	0.00001	0.00000	0.00003	0.00000	0.00000	0.00990	0.00010
tswm6	29	0.00000	0.00194	0.00007	0.00000	0.00035	0.00012	0.00071	0.00000	0.00000	0.00990	0.00010
tswf6	30	0.00000	0.00118	0.01984	0.32175	0.00021	0.00007	0.00043	0.00000	0.00000	0.00990	0.00010
tswm7	31	0.00000	0.00049	0.00007	0.00000	0.00035	0.00012	0.00071	0.00000	0.00000	0.00990	0.00010
tswf7	32	0.00000	0.00029	0.01984	0.32175	0.00021	0.00007	0.00043	0.00000	0.00000	0.00990	0.00010
tswm8	33	0.49522	0.00000	0.00039	0.00000	0.01691	0.00564	0.03381	0.00000	0.00000	0.00990	0.00010
tswf8	34	0.49522	0.00000	0.00039	0.00000	0.01691	0.00564	0.03381	0.00000	0.00000	0.00990	0.00010
tswm9	35	0.69427	0.00000	0.00005	0.00000	0.00723	0.00241	0.01446	0.00000	0.00000	0.00990	0.00010
tswf9	36	0.69427	0.00000	0.00005	0.00000	0.00723	0.00241	0.01446	0.00000	0.00000	0.00990	0.00010
ch1mv	37	0.50592	0.00000	0.00024	0.00000	0.06265	0.02088	0.12529	0.00000	0.00000	0.00990	0.00000
ch1fv	38	0.50592	0.00000	0.00024	0.00000	0.06265	0.02088	0.12529	0.00000	0.00000	0.00990	0.00000

Main Menu

EXIT

Rock	Zone	K-Feldspar	Albite	Anorthite	Ca-Smectite	Na-Smectite	Mg-Smectite	Illite	Tridymite	Cristobalite	Quartz
ch2mv	39	0.09836	0.07263	0.00244	0.00691	0.00296	0.00691	0.00515	0.00079	0.05704	0.04824
ch2fv	40	0.09836	0.07263	0.00244	0.00691	0.00296	0.00691	0.00515	0.00079	0.05704	0.04824
ch3mv	41	0.04708	0.03477	0.00117	0.00216	0.00093	0.00216	0.00161	0.00001	0.04663	0.02747
ch3fv	42	0.04708	0.03477	0.00117	0.00216	0.00093	0.00216	0.00161	0.00001	0.04663	0.02747
ch4mz	43	0.04820	0.03559	0.00120	0.00058	0.00025	0.00058	0.00043	0.00000	0.03726	0.02878
ch4fz	44	0.04820	0.03559	0.00120	0.00058	0.00025	0.00058	0.00043	0.00000	0.03726	0.02878
ch5mz	45	0.04551	0.03361	0.00113	0.00046	0.00020	0.00046	0.00035	0.00000	0.02171	0.02707
ch5fz	46	0.04551	0.03361	0.00113	0.00046	0.00020	0.00046	0.00035	0.00000	0.02171	0.02707
ch6mv	47	0.09931	0.07334	0.00247	0.00620	0.00266	0.00620	0.00463	0.00000	0.05861	0.09735
ch6fv	48	0.09931	0.07334	0.00247	0.00620	0.00266	0.00620	0.00463	0.00000	0.05861	0.09735
pp4m	49	0.08283	0.06116	0.00206	0.00829	0.00355	0.00829	0.00619	0.00003	0.06691	0.01512
pp4f	50	0.08283	0.06116	0.00206	0.00829	0.00355	0.00829	0.00619	0.00003	0.06691	0.01512
pp3m	51	0.36843	0.27207	0.00915	0.00332	0.00142	0.00332	0.00248	0.00590	0.07075	0.24829
pp3f	52	0.36843	0.27207	0.00915	0.00332	0.00142	0.00332	0.00248	0.00590	0.07075	0.24829
pp2m	53	0.36843	0.27207	0.00915	0.00332	0.00142	0.00332	0.00248	0.00590	0.07075	0.24829
pp2f	54	0.36843	0.27207	0.00915	0.00332	0.00142	0.00332	0.00248	0.00590	0.07075	0.24829
pp1m	55	0.09931	0.07334	0.00247	0.00620	0.00266	0.00620	0.00463	0.00000	0.05861	0.09735
pp1f	56	0.09931	0.07334	0.00247	0.00620	0.00266	0.00620	0.00463	0.00000	0.05861	0.09735
bf3m4	57	0.36843	0.27207	0.00915	0.00332	0.00142	0.00332	0.00248	0.00590	0.07075	0.24829
bf3f4	58	0.36843	0.27207	0.00915	0.00332	0.00142	0.00332	0.00248	0.00590	0.07075	0.24829

Main Menu

EXIT

Rock	Zone	Glass	Hematite	Calcite	Stellerite	Heulandite	Mordenite	Clinoptilolite	Kaolinite	Am. Silica	Opal	Fluorite
ch2mv	39	0.60921	0.00000	0.00000	0.00000	0.02384	0.00795	0.04768	0.00000	0.00000	0.00990	0.00000
ch2fv	40	0.60921	0.00000	0.00000	0.00000	0.02384	0.00795	0.04768	0.00000	0.00000	0.00990	0.00000
ch3mv	41	0.73775	0.00000	0.00000	0.00000	0.02651	0.00884	0.05302	0.00000	0.00000	0.00990	0.00000
ch3fv	42	0.73775	0.00000	0.00000	0.00000	0.02651	0.00884	0.05302	0.00000	0.00000	0.00990	0.00000
ch4mz	43	0.73310	0.00000	0.00003	0.00000	0.03123	0.01041	0.06246	0.00000	0.00000	0.00990	0.00000
ch4fz	44	0.73310	0.00000	0.00003	0.00000	0.03123	0.01041	0.06246	0.00000	0.00000	0.00990	0.00000
ch5mz	45	0.77556	0.00000	0.00004	0.00000	0.02520	0.00840	0.05040	0.00000	0.00000	0.00990	0.00000
ch5fz	46	0.77556	0.00000	0.00004	0.00000	0.02520	0.00840	0.05040	0.00000	0.00000	0.00990	0.00000
ch6mv	47	0.32953	0.00000	0.00150	0.00000	0.09249	0.03083	0.18497	0.00000	0.00000	0.00990	0.00000
ch6fv	48	0.32953	0.00000	0.00150	0.00000	0.09249	0.03083	0.18497	0.00000	0.00000	0.00990	0.00000
pp4m	49	0.49175	0.00000	0.00163	0.00000	0.07269	0.02423	0.14538	0.00000	0.00000	0.00990	0.00000
pp4f	50	0.49175	0.00000	0.00163	0.00000	0.07269	0.02423	0.14538	0.00000	0.00000	0.00990	0.00000
pp3m	51	0.00003	0.00474	0.00000	0.00000	0.00005	0.00002	0.00010	0.00000	0.00000	0.00990	0.00000
pp3f	52	0.00003	0.00474	0.00000	0.00000	0.00005	0.00002	0.00010	0.00000	0.00000	0.00990	0.00000
pp2m	53	0.00003	0.00474	0.00000	0.00000	0.00005	0.00002	0.00010	0.00000	0.00000	0.00990	0.00000
pp2f	54	0.00003	0.00474	0.00000	0.00000	0.00005	0.00002	0.00010	0.00000	0.00000	0.00990	0.00000
pp1m	55	0.32953	0.00000	0.00150	0.00000	0.09249	0.03083	0.18497	0.00000	0.00000	0.00990	0.00000
pp1f	56	0.32953	0.00000	0.00150	0.00000	0.09249	0.03083	0.18497	0.00000	0.00000	0.00990	0.00000
bf3m4	57	0.00003	0.00474	0.00000	0.00000	0.00005	0.00002	0.00010	0.00000	0.00000	0.00990	0.00000
bf3f4	58	0.00003	0.00474	0.00000	0.00000	0.00005	0.00002	0.00010	0.00000	0.00000	0.00990	0.00000

Main Menu

EXIT

ATTACHMENT III – MINERAL REACTIVE SURFACE AREAS: Tptpmn and DST THC Models

(DTN: LB0101DSTTHCR1.003)

Unit	Rock Name	Zone	K-Feldspar	Albite	Anorthite	Ca-Smectite	Na-Smectite	Mg-Smectite	K-Smectite	Illite	Tridymite
Tcw3	tcwm3	1	98.0	98.0	98.0	1516.3	1516.3	1516.3	1516.3	1516.3	98.0
	tcwf3	2	394.8	394.8	394.8	394.8	394.8	394.8	394.8	394.8	394.8
Ptn1	ptnm1	3	7.6	7.6	7.6	2253.3	2253.3	2253.3	2253.3	2253.3	7.6
	ptnf1	4	142.8	142.8	142.8	142.8	142.8	142.8	142.8	142.8	142.8
Ptn2	ptnm2	5	8.6	8.6	8.6	2484.8	2484.8	2484.8	2484.8	2484.8	8.6
	ptnf2	6	184.6	184.6	184.6	184.6	184.6	184.6	184.6	184.6	184.6
Ptn3	ptnm3	7	7.1	7.1	7.1	1721.5	1721.5	1721.5	1721.5	1721.5	7.1
	ptnf3	8	1099.6	1099.6	1099.6	1099.6	1099.6	1099.6	1099.6	1099.6	1099.6
Ptn4	ptnm4	9	9.3	9.3	9.3	2356.2	2356.2	2356.2	2356.2	2356.2	9.3
	ptnf4	10	44.5	44.5	44.5	44.5	44.5	44.5	44.5	44.5	44.5
Ptn5	ptnm5	11	11.0	11.0	11.0	2666.7	2666.7	2666.7	2666.7	2666.7	11.0
	ptnf5	12	276.2	276.2	276.2	276.2	276.2	276.2	276.2	276.2	276.2
Ptn6	ptnm6	13	10.0	10.0	10.0	2666.7	2666.7	2666.7	2666.7	2666.7	10.0
	ptnf6	14	1553.3	1553.3	1553.3	1553.3	1553.3	1553.3	1553.3	1553.3	1553.3
Tsw31	tswm1	15	57.0	57.0	57.0	694.3	694.3	694.3	694.3	694.3	57.0
	tswf1	16	1102.4	1102.4	1102.4	1102.4	1102.4	1102.4	1102.4	1102.4	1102.4
Tsw32	tswm2	17	109.2	109.2	109.2	1317.4	1317.4	1317.4	1317.4	1317.4	109.2
	tswf2	18	530.8	530.8	530.8	530.8	530.8	530.8	530.8	530.8	530.8
Tsw33	tswm3	19	105.6	105.6	105.6	1303.3	1303.3	1303.3	1303.3	1303.3	105.6
	tswf3	20	1056.7	1056.7	1056.7	1056.7	1056.7	1056.7	1056.7	1056.7	1056.7
Tsw34	tswm4	21	89.8	89.8	89.8	1086.6	1086.6	1086.6	1086.6	1086.6	89.8
	tswf4	22	2126.9	2126.9	2126.9	2126.9	2126.9	2126.9	2126.9	2126.9	2126.9
Tsw35	tswm5	23	98.2	98.2	98.2	1195.3	1195.3	1195.3	1195.3	1195.3	98.2
	tswf5	24	1382.3	1382.3	1382.3	1382.3	1382.3	1382.3	1382.3	1382.3	1382.3
Tsw36	tswm6	25	90.8	90.8	90.8	1098.1	1098.1	1098.1	1098.1	1098.1	90.8
	tswf6	26	1289.1	1289.1	1289.1	1289.1	1289.1	1289.1	1289.1	1289.1	1289.1
Tsw37	tswm7	27	82.4	82.4	82.4	996.5	996.5	996.5	996.5	996.5	82.4
	tswf7	28	1289.1	1289.1	1289.1	1289.1	1289.1	1289.1	1289.1	1289.1	1289.1
Tsw38	tswm8	29	40.4	40.4	40.4	526.7	526.7	526.7	526.7	526.7	40.4
	tswf8	30	1746.2	1746.2	1746.2	1746.2	1746.2	1746.2	1746.2	1746.2	1746.2
Ch2	ch2mz	31	44.5	44.5	44.5	2024.7	2024.7	2024.7	2024.7	2024.7	44.5
	ch2fz	32	1570.8	1570.8	1570.8	1570.8	1570.8	1570.8	1570.8	1570.8	1570.8

Main Menu

EXIT

Unit	Rock Name	Zone	Cristobalite	Quartz	Glass	Hematite	Calcite	Stellerite	Heulandite	Mordenite	Clinoptilolite
Tcw3	tcwm3	1	98.0	98.0	98.0	128.7	128.7	128.7	128.7	128.7	128.7
	tcwf3	2	394.8	394.8	394.8	394.8	394.8	394.8	394.8	394.8	394.8
Ptn1	ptnm1	3	7.6	7.6	7.6	9.6	9.6	9.6	9.6	9.6	9.6
	ptnf1	4	142.8	142.8	142.8	142.8	142.8	142.8	142.8	142.8	142.8
Ptn2	ptnm2	5	8.6	8.6	8.6	10.5	10.5	10.5	10.5	10.5	10.5
	ptnf2	6	184.6	184.6	184.6	184.6	184.6	184.6	184.6	184.6	184.6
Ptn3	ptnm3	7	7.1	7.1	7.1	7.3	7.3	7.3	7.3	7.3	7.3
	ptnf3	8	1099.6	1099.6	1099.6	1099.6	1099.6	1099.6	1099.6	1099.6	1099.6
Ptn4	ptnm4	9	9.3	9.3	9.3	10.0	10.0	10.0	10.0	10.0	10.0
	ptnf4	10	44.5	44.5	44.5	44.5	44.5	44.5	44.5	44.5	44.5
Ptn5	ptnm5	11	11.0	11.0	11.0	11.3	11.3	11.3	11.3	11.3	11.3
	ptnf5	12	276.2	276.2	276.2	276.2	276.2	276.2	276.2	276.2	276.2
Ptn6	ptnm6	13	10.0	10.0	10.0	11.3	11.3	11.3	11.3	11.3	11.3
	ptnf6	14	1553.3	1553.3	1553.3	1553.3	1553.3	1553.3	1553.3	1553.3	1553.3
Tsw31	tswm1	15	57.0	57.0	57.0	59.0	59.0	59.0	59.0	59.0	59.0
	tswf1	16	1102.4	1102.4	1102.4	1102.4	1102.4	1102.4	1102.4	1102.4	1102.4
Tsw32	tswm2	17	109.2	109.2	109.2	111.9	111.9	111.9	111.9	111.9	111.9
	tswf2	18	530.8	530.8	530.8	530.8	530.8	530.8	530.8	530.8	530.8
Tsw33	tswm3	19	105.6	105.6	105.6	110.7	110.7	110.7	110.7	110.7	110.7
	tswf3	20	1056.7	1056.7	1056.7	1056.7	1056.7	1056.7	1056.7	1056.7	1056.7
Tsw34	tswm4	21	89.8	89.8	89.8	92.3	92.3	92.3	92.3	92.3	92.3
	tswf4	22	2126.9	2126.9	2126.9	2126.9	2126.9	2126.9	2126.9	2126.9	2126.9
Tsw35	tswm5	23	98.2	98.2	98.2	101.5	101.5	101.5	101.5	101.5	101.5
	tswf5	24	1382.3	1382.3	1382.3	1382.3	1382.3	1382.3	1382.3	1382.3	1382.3
Tsw36	tswm6	25	90.8	90.8	90.8	93.2	93.2	93.2	93.2	93.2	93.2
	tswf6	26	1289.1	1289.1	1289.1	1289.1	1289.1	1289.1	1289.1	1289.1	1289.1
Tsw37	tswm7	27	82.4	82.4	82.4	84.6	84.6	84.6	84.6	84.6	84.6
	tswf7	28	1289.1	1289.1	1289.1	1289.1	1289.1	1289.1	1289.1	1289.1	1289.1
Tsw38	tswm8	29	40.4	40.4	40.4	44.7	44.7	44.7	44.7	44.7	44.7
	tswf8	30	1746.2	1746.2	1746.2	1746.2	1746.2	1746.2	1746.2	1746.2	1746.2
Ch2	ch2mz	31	44.5	44.5	44.5	171.9	171.9	171.9	171.9	171.9	171.9
	ch2fz	32	1570.8	1570.8	1570.8	1570.8	1570.8	1570.8	1570.8	1570.8	1570.8

Main Menu

EXIT

ATTACHMENT IV - MINERAL REACTIVE SURFACE AREAS: Tptpll THC Model

(DTN: LB0101DSTTHCR1.004)

Rock	Zone	K-Feldspar	Albite	Anorthite	Ca-Smectite	Na-Smectite	Mg-Smectite	Illite	Tridymite	Cristobalite	Quartz
tcwm1	1	110.5	110.5	110.5	1516.3	1516.3	1516.3	1516.3	110.5	110.5	110.5
tcwf1	2	394.8	394.8	394.8	394.8	394.8	394.8	394.8	394.8	394.8	394.8
tcwm2	3	110.5	110.5	110.5	1516.3	1516.3	1516.3	1516.3	110.5	110.5	110.5
tcwf2	4	394.8	394.8	394.8	394.8	394.8	394.8	394.8	394.8	394.8	394.8
tcwm3	5	110.5	110.5	110.5	1516.3	1516.3	1516.3	1516.3	110.5	110.5	110.5
tcwf3	6	394.8	394.8	394.8	394.8	394.8	394.8	394.8	394.8	394.8	394.8
ptnm1	7	8.7	8.7	8.7	2253.3	2253.3	2253.3	2253.3	8.7	8.7	8.7
ptnf1	8	142.8	142.8	142.8	142.8	142.8	142.8	142.8	142.8	142.8	142.8
ptnm2	9	9.6	9.6	9.6	2484.8	2484.8	2484.8	2484.8	9.6	9.6	9.6
ptnf2	10	184.6	184.6	184.6	184.6	184.6	184.6	184.6	184.6	184.6	184.6
ptnm3	11	6.7	6.7	6.7	1721.5	1721.5	1721.5	1721.5	6.7	6.7	6.7
ptnf3	12	1099.6	1099.6	1099.6	1099.6	1099.6	1099.6	1099.6	1099.6	1099.6	1099.6
ptnm4	13	9.1	9.1	9.1	2356.2	2356.2	2356.2	2356.2	9.1	9.1	9.1
ptnf4	14	44.5	44.5	44.5	44.5	44.5	44.5	44.5	44.5	44.5	44.5
ptnm5	15	10.3	10.3	10.3	2666.7	2666.7	2666.7	2666.7	10.3	10.3	10.3
ptnf5	16	276.2	276.2	276.2	276.2	276.2	276.2	276.2	276.2	276.2	276.2
ptnm6	17	10.3	10.3	10.3	2666.7	2666.7	2666.7	2666.7	10.3	10.3	10.3
ptnf6	18	1553.3	1553.3	1553.3	1553.3	1553.3	1553.3	1553.3	1553.3	1553.3	1553.3
tswm1	19	57.2	57.2	57.2	694.3	694.3	694.3	694.3	57.2	57.2	57.2
tswf1	20	1102.4	1102.4	1102.4	1102.4	1102.4	1102.4	1102.4	1102.4	1102.4	1102.4
tswm2	21	110.0	110.0	110.0	1317.4	1317.4	1317.4	1317.4	110.0	110.0	110.0
tswf2	22	530.8	530.8	530.8	530.8	530.8	530.8	530.8	530.8	530.8	530.8
tswm3	23	107.4	107.4	107.4	1303.3	1303.3	1303.3	1303.3	107.4	107.4	107.4
tswf3	24	1056.7	1056.7	1056.7	1056.7	1056.7	1056.7	1056.7	1056.7	1056.7	1056.7
tswm4	25	90.7	90.7	90.7	1086.6	1086.6	1086.6	1086.6	90.7	90.7	90.7
tswf4	26	2126.9	2126.9	2126.9	2126.9	2126.9	2126.9	2126.9	2126.9	2126.9	2126.9
tswm5	27	99.0	99.0	99.0	1195.3	1195.3	1195.3	1195.3	99.0	99.0	99.0
tswf5	28	844.7	844.7	844.7	844.7	844.7	844.7	844.7	844.7	844.7	844.7
tswm6	29	92.0	92.0	92.0	1098.1	1098.1	1098.1	1098.1	92.0	92.0	92.0
tswf6	30	1289.1	1289.1	1289.1	1289.1	1289.1	1289.1	1289.1	1289.1	1289.1	1289.1
tswm7	31	83.6	83.6	83.6	996.5	996.5	996.5	996.5	83.6	83.6	83.6
tswf7	32	1289.1	1289.1	1289.1	1289.1	1289.1	1289.1	1289.1	1289.1	1289.1	1289.1
tswm8	33	36.0	36.0	36.0	526.7	526.7	526.7	526.7	36.0	36.0	36.0
tswf8	34	1746.2	1746.2	1746.2	1746.2	1746.2	1746.2	1746.2	1746.2	1746.2	1746.2
tswm9	35	36.0	36.0	36.0	526.7	526.7	526.7	526.7	36.0	36.0	36.0
tswf9	36	1007.4	1007.4	1007.4	1007.4	1007.4	1007.4	1007.4	1007.4	1007.4	1007.4
ch1mv	37	152.6	152.6	152.6	2024.7	2024.7	2024.7	2024.7	152.6	152.6	152.6
ch1fv	38	683.0	683.0	683.0	683.0	683.0	683.0	683.0	683.0	683.0	683.0

Main Menu

EXIT

Rock	Zone	Glass	Hematite	Calcite	Stellerite	Heulandite	Mordenite	Clinoptilolite	Kaolinite	Am. Silica	Opal	Fluorite
tcwm1	1	110.5	128.7	128.7	128.7	128.7	128.7	128.7	1516.3	1516.3	1516.3	128.7
tcwf1	2	394.8	394.8	394.8	394.8	394.8	394.8	394.8	394.8	394.8	394.8	394.8
tcwm2	3	110.5	128.7	128.7	128.7	128.7	128.7	128.7	1516.3	1516.3	1516.3	128.7
tcwf2	4	394.8	394.8	394.8	394.8	394.8	394.8	394.8	394.8	394.8	394.8	394.8
tcwm3	5	110.5	128.7	128.7	128.7	128.7	128.7	128.7	1516.3	1516.3	1516.3	128.7
tcwf3	6	394.8	394.8	394.8	394.8	394.8	394.8	394.8	394.8	394.8	394.8	394.8
ptnm1	7	8.7	9.6	9.6	9.6	9.6	9.6	9.6	2253.3	2253.3	2253.3	9.6
ptnf1	8	142.8	142.8	142.8	142.8	142.8	142.8	142.8	142.8	142.8	142.8	142.8
ptnm2	9	9.6	10.5	10.5	10.5	10.5	10.5	10.5	2484.8	2484.8	2484.8	10.5
ptnf2	10	184.6	184.6	184.6	184.6	184.6	184.6	184.6	184.6	184.6	184.6	184.6
ptnm3	11	6.7	7.3	7.3	7.3	7.3	7.3	7.3	1721.5	1721.5	1721.5	7.3
ptnf3	12	1099.6	1099.6	1099.6	1099.6	1099.6	1099.6	1099.6	1099.6	1099.6	1099.6	1099.6
ptnm4	13	9.1	10.0	10.0	10.0	10.0	10.0	10.0	2356.2	2356.2	2356.2	10.0
ptnf4	14	44.5	44.5	44.5	44.5	44.5	44.5	44.5	44.5	44.5	44.5	44.5
ptnm5	15	10.3	11.3	11.3	11.3	11.3	11.3	11.3	2666.7	2666.7	2666.7	11.3
ptnf5	16	276.2	276.2	276.2	276.2	276.2	276.2	276.2	276.2	276.2	276.2	276.2
ptnm6	17	10.3	11.3	11.3	11.3	11.3	11.3	11.3	2666.7	2666.7	2666.7	11.3
ptnf6	18	1553.3	1553.3	1553.3	1553.3	1553.3	1553.3	1553.3	1553.3	1553.3	1553.3	1553.3
tswm1	19	57.2	59.0	59.0	59.0	59.0	59.0	59.0	694.3	694.3	694.3	59.0
tswf1	20	1102.4	1102.4	1102.4	1102.4	1102.4	1102.4	1102.4	1102.4	1102.4	1102.4	1102.4
tswm2	21	110.0	111.9	111.9	111.9	111.9	111.9	111.9	1317.4	1317.4	1317.4	111.9
tswf2	22	530.8	530.8	530.8	530.8	530.8	530.8	530.8	530.8	530.8	530.8	530.8
tswm3	23	107.4	110.7	110.7	110.7	110.7	110.7	110.7	1303.3	1303.3	1303.3	110.7
tswf3	24	1056.7	1056.7	1056.7	1056.7	1056.7	1056.7	1056.7	1056.7	1056.7	1056.7	1056.7
tswm4	25	90.7	92.3	92.3	92.3	92.3	92.3	92.3	1086.6	1086.6	1086.6	92.3
tswf4	26	2126.9	2126.9	2126.9	2126.9	2126.9	2126.9	2126.9	2126.9	2126.9	2126.9	2126.9
tswm5	27	99.0	101.5	101.5	101.5	101.5	101.5	101.5	1195.3	1195.3	1195.3	101.5
tswf5	28	844.7	844.7	844.7	844.7	844.7	844.7	844.7	844.7	844.7	844.7	844.7
tswm6	29	92.0	93.2	93.2	93.2	93.2	93.2	93.2	1098.1	1098.1	1098.1	93.2
tswf6	30	1289.1	1289.1	1289.1	1289.1	1289.1	1289.1	1289.1	1289.1	1289.1	1289.1	1289.1
tswm7	31	83.6	84.6	84.6	84.6	84.6	84.6	84.6	996.5	996.5	996.5	84.6
tswf7	32	1289.1	1289.1	1289.1	1289.1	1289.1	1289.1	1289.1	1289.1	1289.1	1289.1	1289.1
tswm8	33	36.0	44.7	44.7	44.7	44.7	44.7	44.7	526.7	526.7	526.7	44.7
tswf8	34	1746.2	1746.2	1746.2	1746.2	1746.2	1746.2	1746.2	1746.2	1746.2	1746.2	1746.2
tswm9	35	36.0	44.7	44.7	44.7	44.7	44.7	44.7	526.7	526.7	526.7	44.7
tswf9	36	1007.4	1007.4	1007.4	1007.4	1007.4	1007.4	1007.4	1007.4	1007.4	1007.4	1007.4
ch1mv	37	152.6	171.9	171.9	171.9	171.9	171.9	171.9	2024.7	2024.7	2024.7	171.9
ch1fv	38	683.0	683.0	683.0	683.0	683.0	683.0	683.0	683.0	683.0	683.0	683.0

Main Menu

EXIT

Rock	Zone	K-Feldspar	Albite	Anorthite	Ca-Smectite	Na-Smectite	Mg-Smectite	Illite	Tridymite	Cristobalite	Quartz
ch2mv	39	152.6	152.6	152.6	2024.7	2024.7	2024.7	2024.7	152.6	152.6	152.6
ch2fv	40	758.9	758.9	758.9	758.9	758.9	758.9	758.9	758.9	758.9	758.9
ch3mv	41	152.6	152.6	152.6	2024.7	2024.7	2024.7	2024.7	152.6	152.6	152.6
ch3fv	42	758.9	758.9	758.9	758.9	758.9	758.9	758.9	758.9	758.9	758.9
ch4mz	43	152.6	152.6	152.6	2024.7	2024.7	2024.7	2024.7	152.6	152.6	152.6
ch4fz	44	1570.8	1570.8	1570.8	1570.8	1570.8	1570.8	1570.8	1570.8	1570.8	1570.8
ch5mz	45	152.6	152.6	152.6	2024.7	2024.7	2024.7	2024.7	152.6	152.6	152.6
ch5fz	46	1570.8	1570.8	1570.8	1570.8	1570.8	1570.8	1570.8	1570.8	1570.8	1570.8
ch6mv	47	152.6	152.6	152.6	2024.7	2024.7	2024.7	2024.7	152.6	152.6	152.6
ch6fv	48	1016.4	1016.4	1016.4	1016.4	1016.4	1016.4	1016.4	1016.4	1016.4	1016.4
pp4m	49	152.6	152.6	152.6	2024.7	2024.7	2024.7	2024.7	152.6	152.6	152.6
pp4f	50	1570.8	1570.8	1570.8	1570.8	1570.8	1570.8	1570.8	1570.8	1570.8	1570.8
pp3m	51	152.6	152.6	152.6	2024.7	2024.7	2024.7	2024.7	152.6	152.6	152.6
pp3f	52	871.1	871.1	871.1	871.1	871.1	871.1	871.1	871.1	871.1	871.1
pp2m	53	152.6	152.6	152.6	2024.7	2024.7	2024.7	2024.7	152.6	152.6	152.6
pp2f	54	871.1	871.1	871.1	871.1	871.1	871.1	871.1	871.1	871.1	871.1
pp1m	55	152.6	152.6	152.6	2024.7	2024.7	2024.7	2024.7	152.6	152.6	152.6
pp1f	56	1570.8	1570.8	1570.8	1570.8	1570.8	1570.8	1570.8	1570.8	1570.8	1570.8
bf3m4	57	152.6	152.6	152.6	2024.7	2024.7	2024.7	2024.7	152.6	152.6	152.6
bf3f4	58	2228.3	2228.3	2228.3	2228.3	2228.3	2228.3	2228.3	2228.3	2228.3	2228.3

Main Menu

EXIT

Rock	Zone	Glass	Hematite	Calcite	Stellerite	Heulandite	Mordenite	Clinoptilolite	Kaolinite	Am. Silica	Opal	Fluorite
ch2mv	39	152.6	171.9	171.9	171.9	171.9	171.9	171.9	2024.7	2024.7	2024.7	171.9
ch2fv	40	758.9	758.9	758.9	758.9	758.9	758.9	758.9	758.9	758.9	758.9	758.9
ch3mv	41	152.6	171.9	171.9	171.9	171.9	171.9	171.9	2024.7	2024.7	2024.7	171.9
ch3fv	42	758.9	758.9	758.9	758.9	758.9	758.9	758.9	758.9	758.9	758.9	758.9
ch4mz	43	152.6	171.9	171.9	171.9	171.9	171.9	171.9	2024.7	2024.7	2024.7	171.9
ch4fz	44	1570.8	1570.8	1570.8	1570.8	1570.8	1570.8	1570.8	1570.8	1570.8	1570.8	1570.8
ch5mz	45	152.6	171.9	171.9	171.9	171.9	171.9	171.9	2024.7	2024.7	2024.7	171.9
ch5fz	46	1570.8	1570.8	1570.8	1570.8	1570.8	1570.8	1570.8	1570.8	1570.8	1570.8	1570.8
ch6mv	47	152.6	171.9	171.9	171.9	171.9	171.9	171.9	2024.7	2024.7	2024.7	171.9
ch6fv	48	1016.4	1016.4	1016.4	1016.4	1016.4	1016.4	1016.4	1016.4	1016.4	1016.4	1016.4
pp4m	49	152.6	171.9	171.9	171.9	171.9	171.9	171.9	2024.7	2024.7	2024.7	171.9
pp4f	50	1570.8	1570.8	1570.8	1570.8	1570.8	1570.8	1570.8	1570.8	1570.8	1570.8	1570.8
pp3m	51	152.6	171.9	171.9	171.9	171.9	171.9	171.9	2024.7	2024.7	2024.7	171.9
pp3f	52	871.1	871.1	871.1	871.1	871.1	871.1	871.1	871.1	871.1	871.1	871.1
pp2m	53	152.6	171.9	171.9	171.9	171.9	171.9	171.9	2024.7	2024.7	2024.7	171.9
pp2f	54	871.1	871.1	871.1	871.1	871.1	871.1	871.1	871.1	871.1	871.1	871.1
pp1m	55	152.6	171.9	171.9	171.9	171.9	171.9	171.9	2024.7	2024.7	2024.7	171.9
pp1f	56	1570.8	1570.8	1570.8	1570.8	1570.8	1570.8	1570.8	1570.8	1570.8	1570.8	1570.8
bf3m4	57	152.6	171.9	171.9	171.9	171.9	171.9	171.9	2024.7	2024.7	2024.7	171.9
bf3f4	58	2228.3	2228.3	2228.3	2228.3	2228.3	2228.3	2228.3	2228.3	2228.3	2228.3	2228.3

ATTACHMENT V – THERMODYNAMIC DATABASE: Tptpmn THC Backfill and DST THC Rev00 Models

(DTN: LB0101DSTTHCR1.005)

(Data from database thermokapps2.05.dat)				***log (k)***						
Mineral	**Molecular Weight (g/mol)**	**Molecular Volume (cm^3/mol)**	**Reaction Stoichiometry**[1]	0 (^{o}C)	25 (^{o}C)	60 (^{o}C)	100 (^{o}C)	150 (^{o}C)	200 (^{o}C)	**ref**
albite-low	262.223	100.07	(1)alo2-, (1)na+, (3)sio2(aq)	-21.694	-20.177	-18.362	-16.684	-15.094	-13.986	4
anorthite	278.207	100.79	(2)alo2-, (1)ca+2, (2)sio2(aq)	-20.398	-19.188	-18.333	-17.852	-17.629	-17.703	1,14
calcite	100.087	36.934	(1)ca+2, (-1)h+, (1)hco3-	2.226	1.849	1.333	0.774	0.1	-0.584	1,14
SiO2(amor.)	60.084	29	(1)sio2(aq)	-2.871	-2.663	-2.423	-2.205	-1.99	-1.82	7
cristobalite-a	60.084	25.74	(1)sio2(aq)	-3.63	-3.332	-2.99	-2.678	-2.371	-2.129	6
fluorite	78.075	24.542	(1)ca+2, (2)f-	-10.31	-10.037	-9.907	-9.967	-10.265	-10.784	1,14
goethite	88.854	20.82	(1)hfeo2	-12.78	-11.483	-10.202	-9.208	-8.407	-7.92	1
glass1	56.588	23.978	(-0.0362)h2o, (0.15)alo2-, (0.0021)ca+2,(0.0654)h+, (0.0042)k+,(0.0003)mg+2, (0.0756)na+,(0.7608)sio2(aq), (0.0070)hfeo2	-4.7	-4.54	-4.35	-4.16	-3.98	-3.86	13
glass	60.084	29	(1)sio2(aq)	-2.871	-2.663	-2.423	-2.205	-1.99	-1.82	12
gypsum	172.172	74.69	(2)h2o, (1)ca+2, (1)so4-2	-4.533	-4.482	-4.609	-4.903	-5.41	-6.127	1,14
hematite	159.692	30.274	(-1)h2o, (2)hfeo2	-26.439	-23.927	-21.485	-19.661	-18.293	-17.573	1,14
illite	378.963	135.08	(0.44)h2o, (2.06)alo2-, (1.12)h+,(0.5)k+, (0.22)mg+2,(3.72)sio2(aq)	-45.354	-41.926	-38.294	-34.994	-31.867	-29.606	4
microcline	278.332	108.741	(1)alo2-, (1)k+, (3)sio2(aq)	-24.861	-22.91	-20.619	-18.526	-16.549	-15.154	4
kaolinite	258.16	99.52	(1)h2o, (2)alo2-, (2)h+,(2)sio2(aq)	-43.073	-39.895	-36.336	-33.181	-30.212	-28.082	4
quartz	60.084	22.688	(1)sio2(aq)	-4.079	-3.739	-3.349	-2.992	-2.642	-2.365	5
sepiolite	323.913	142.83	(5.5)h2o, (-4)h+, (2)mg+2,(3)sio2(aq)	17.28	15.76	13.83	12.08	10.45	9.23	8
tridymite	60.084	26.586	(1)sio2(aq)	-3.872	-3.567	-3.193	-2.821	-2.394	-1.984	10
smectite-ca	365.394	132.51	(0.52)h2o, (1.77)alo2-, (0.145)ca+2,(0.96)h+, (0.26)mg+2,(3.97)sio2(aq)	-42.523	39.519	-36.156	-33.159	-30.303	-28.219	9
smectite-na	366.25	132.51	(0.52)h2o, (1.77)alo2-, (0.96)h+,(0.26)mg+2, (0.29)na+,(3.97)sio2(aq)	-42.628	-39.528	-36.049	-32.937	-29.956	-27.761	9
smectite-mg	363.107	132.51	(0.52)h2o, (1.77)alo2-, (0.96)h+,(0.405)mg+2, (3.97)sio2(aq)	-42.583	-39.613	-36.289	-33.325	-30.498	-28.435	9
smectite-k	370.921	132.51	(0.52)h2o, (1.77)alo2-, (0.96)h+,(0.29)k+, (0.26)mg+2,(3.97)sio2(aq)	-43.004	-39.829	-36.275	-33.11	-30.093	-27.885	4
steller/10	281.733	133.1	(2.8)h2o, (0.79)alo2-, (0.39)ca+2,(0.01)na+, (2.81)sio2(aq)	-20.918	-19.404	-17.676	-16.103	-14.564	-13.428	11
heuland/10	279.347	126.64	(2.6)h2o, (0.8)alo2-, (0.33)ca+2,(0.04)k+, (0.1)na+,(2.8)sio2(aq)	-20.872	-19.32	-17.55	-15.94	-14.365	-13.202	11
mordeni/10	269.631	127.35	(2.2)h2o, (0.6)alo2-, (0.15)ca+2,(0.09)k+, (0.21)na+,(3)sio2(aq)	-19	-17.51	-15.802	-14.238	-12.694	-11.523	11
clinopt/10	277.66	126.41	(2.6)h2o, (0.68)alo2-, (0.28)ca+2,(0.08)k+, (0.04)na+,(2.92)sio2(aq)	-19.999	-18.463	-16.704	-15.095	-13.52	-12.309	11
Gas:	**Molecular Weight (g/mol)**	**Molecular Diameter (m)**								
CO2(g)	44.01	2.50E-10	(-1)h2o, (1)h+, (1)hco3-	-7.677	-7.818	-8.053	-8.36	-8.77	-9.217	1,14

[1] Negative number in parenthesis indicate the species is on the left side of equation

Minerals names or abbreviations above are those used in the database and may not exactly match names used in the text of the report. Names ending by /10 indicate the stoichiometry , molecular weight, molar volume, and log(K) values for those minerals were divided by 10 compared to original data. Glass phases glass1 and glass were used in extended-case and base-case simulations, respectively.

(Data from database thermokapps2.05.dat)				**log (k)**						
Aqueous Species	**a_o**	**Charge**	**Reaction Stoichiometry**	0 (^{o}C)	25 (^{o}C)	60 (^{o}C)	100 (^{o}C)	150 (^{o}C)	200 (^{o}C)	**ref.**
CO2(aq)	3	0	(-1)h2o, (1)h+, (1)hco3-	-6.58	-6.345	-6.268	-6.388	-6.724	-7.197	1,14
CO3-2	5	-2	(-1)h+, (1)hco3-	10.624	10.329	10.13	10.084	10.2	10.465	1,14
OH-	3	-1	(1)h2o, (-1)h+	14.94	13.995	13.027	12.255	11.631	11.284	1,14
Al(OH)2+	4	1	(1)alo2-, (2)h+	-13.656	-12.289	-10.831	-9.6	-8.53	-7.823	1
$HAlO_2$	3	0	(1)alo2-, (1)h+	-7.08	-6.45	-5.846	-5.409	-5.121	-5.035	1
Al+3	9	3	(-2)h2o, (1)alo2-, (4)h+	-25.795	-22.883	-19.571	-16.582	-13.676	-11.409	1
AlOH+2	4.5	2	(-1)h2o, (1)alo2-, (3)h+	-20.069	-17.926	-15.568	-13.519	-11.624	-10.242	1
CaCl+	4	1	(1)ca+2, (1)cl-	0.673	0.696	0.589	0.357	-0.04	-0.533	1
CaCl2(aq)	0	0	(1)ca+2, (2)cl-	0.452	0.644	0.629	0.381	-0.159	-0.911	1,14
CaCO3(aq)	0	0	(1)ca+2, (-1)h+, (1)hco3-	7.502	7.002	6.452	5.964	5.468	5.018	1,14
CaHCO3+	4	1	(1)ca+2, (1)hco3-	-1.095	-1.047	-1.159	-1.418	-1.859	-2.4	1,14
CaSO4(aq)	0	0	(1)ca+2, (1)so4-2	-2.071	-2.111	-2.265	-2.511	-2.91	-3.433	1,14
CaF+	4	1	(1)ca+2, (1)f-	-0.655	-0.682	-0.862	-1.17	-1.649	-2.215	1,14
HSiO3-	4	-1	(1)h2o, (-1)h+, (1)sio2(aq)	10.323	9.953	9.468	9.084	8.85	8.839	1
HCl(aq)	3	0	(1)cl-, (1)h+	0.661	0.67	0.689	0.62	0.41	0.092	1
KCl(aq)	0	0	(1)cl-, (1)k+	1.71	1.495	1.216	0.924	0.575	0.215	1
KHSO4(aq)	0	0	(1)h+, (1)k+, (1)so4-2	-0.435	-0.814	-1.479	-2.294	-3.341	-4.431	1
KSO4-	4	-1	(1)k+, (1)so4-2	-0.885	-0.88	-0.99	-1.194	-1.52	-1.919	1,14
HF(aq)	3	0	(1)h+, (1)f-	-2.985	-3.168	-3.474	-3.848	-4.338	-4.859	1,14
MgCl+	4	1	(1)cl-, (1)mg+2	0.049	0.135	0.055	-0.182	-0.607	-1.139	1,14
MgCO3(aq)	0	0	(-1)h+, (1)hco3-, (1)mg+2	7.74	7.35	6.926	6.563	6.204	5.872	1,14
MgHCO3+	4	1	(1)hco3-, (1)mg+2	-1.08	-1.036	-1.164	-1.436	-1.88	-2.415	1,14
MgSO4(aq)	3	0	(1)mg+2, (1)so4-2	-2.139	-2.412	-2.837	-3.347	-4.073	-4.955	1
MgF+	4	1	(1)mg+2, (1)f-	-1.387	-1.352	-1.478	-1.739	-2.168	-2.688	1,14
NaCl(aq)	3	0	(1)cl-, (1)na+	0.829	0.777	0.651	0.473	0.214	-0.093	1
NaOH(aq)	3	0	(1)h2o, (-1)h+, (1)na+	15.645	14.795	13.8	12.885	11.971	11.221	1
NaCO3-	4	-1	(-1)h+, (1)hco3-, (1)na+	9.815	9.814	10.075	10.649	11.568	12.632	2
NaHCO3(aq)	3	0	(1)hco3-, (1)na+	-0.373	-0.154	0.11	0.411	0.793	1.213	1,14
NaHSiO3	0	0	(1)h2o, (-1)h+, (1)na+,(1)sio2(aq)	8.414	8.304	8.053	7.829	7.684	7.658	1
NaF(aq)	0	0	(1)na+, (1)f-	1.082	0.998	0.833	0.624	0.338	0.011	1,14
FeO2-	4	-1	(-1)h+, (1)hfeo2	10.231	9.602	8.839	8.111	7.38	6.821	3,14
FeO+	4	1	(-1)h2o, (1)h+, (1)hfeo2	-7.324	-6.368	-5.372	-4.561	-3.865	-3.393	3,14
Primary Aqueous Species:			**Mol. Wt. (g/mol)**							
H2O	3	0	18.015							1,14
AlO2-	4	-1	58.98							1,14
Ca+2	6	2	40.078							1,14
Cl-	3	-1	35.453							1,14
H+	9	1	1.008							1,14
HCO3-	4	-1	61.017							1,14
K+	3	1	39.098							1,14
Mg+2	8	2	24.305							1,14
Na+	4	1	22.99							1,14
SiO2(aq)	3	0	60.084							1,14
SO4-2	4	-2	96.064							1,14
F-	4	-1	18.998							1,14
HFeO2	3	0	88.854							3,14

ref. no	Reference
1	EQ3/6 V7.2b [126891] database data0.com.R2 Aug.2.1995 (STN: LLNL:UCRL-MA-110662). Mostly calculated with SUPCRT92 [153218] and associated databases (Johnson et al. 1992 [101632]). If two sources are cited, data are from the first source, and values are identical or differ by less than 0.05 units between sources.
2	EQ3/6 V7.2b [126891] database data0.com.R6 Dec.3.1996 (STN: LLNL:UCRL-MA-110662)
3	Log(K) calculated using SUPCRT92 [153218] (Johnson et al. 1992 [101632]) with Fe+3 and Fe(III)-OH data from Shock et al. (1997 [127953]) added to SPRONS.DAT version dated 3/14/96 (the latter is the database of SUPCRT92). See Scientific Notebook Spycher 2000 [153572], p. 104-110.
4	Log(K) calculated using SUPCRT92 [153218] (Johnson et al. 1992 [101632]) with thermodynamic properties from various sources (Berman 1988 [104905] for albite; Kulik and Aja 1997 [128132] for illite and k-smectite; Robie and Hemingway 1995 [153683] for kaolinite; Apps and Chang 1992 [124211] for microcline) added to SPRONS.DAT version dated 3/14/96 (the latter is the database of SUPCRT92), then corrected to reflect the quartz solubility data of Rimstidt (1997 [101709]). See Bodvarsson 2001 [153816], YMP-LBNL-YWT-JA-1A p. 28-39.
5	Rimstidt (1997 [101709])
6	Regression by Apps (1970 [124208]) of pressure-corrected cristobalite solubility data derived from measurements by Fournier and Rowe (1962 [124282]). See Bodvarsson 2001 [153816], YMP-LBNL-YWT-JA-1A p. 38.
7	Regression by Apps (1970 [124208]). See Bodvarsson 2001 [153816], YMP-LBNL-YWT-JA-1A p. 37.
8	Stoessell (1988 [127964])
9	Recalculated from log(K) data for montmor-k, montmor-ca, montmor-mg, and montmor-k in EQ3/6 V7.2b [126891] database (see ref. 1), as described in Bodvarsson 2001 [153816], YMP-LBNL-YWT-JA-1A p. 40-43.
10	From log(K) data for quartz and tridymite in ref.1 above, then corrected with the quartz solubility data of Rimstidt (1997 [101709]). See Scientific Notebook Spycher 2000 [153572], p. 113-114. Molar volume from molecular weight in ref.1 and density in Klein and Hurlbut (1993 [153700], p. 665).
11	Log(K) calculated using SUPCRT92 [153218] (Johnson et al. 1992 [101632]) with zeolite formulas and thermodynamic data from DTN: LA0008SC12213N.001 [153386] and data calculations from additional references (Smyth and Bish (1988 [133216]), Chermak and Rimstidt (1989 [105073]), Chipera and Bish (1997 [105079]), Holland (1989 [106044]) and DTN: LA000000000071.001 [153637]) in Bodvarsson 2001 [153816], YMP-LBNL-YWT-NS-1.2 p. 44-46, added to SPRONS.DAT version dated 3/14/96 (the latter is the database of SUPCRT92), then corrected to reflect the quartz solubility data of Rimstidt (1997 [101709]). See Bodvarsson 2001 [153816], YMP-LBNL-YWT-JA-1A p. 48-50, Spycher 1998 [153571], p.115, 136 and Spycher 2000 [153572], p. 111-113.
12	Same composition and log(K) as amorphous silica
13	Formula from composition by Bish et al. (1996 [101430]). Log(K) at 25^{o}C was calculated by equilibrating the glass with the initial water composition (Section 4.1.3) using SOLVEQ V1.0 [153217] and adjusting the log(K) value to yield approximately 100 ppm SiO2(aq.) in solution at 25^{o}C. Log(K) values at higher temperatures were then adjusted to maintain the same degree of amorphous silica undersaturation with the equilibrated glass at all temperatures. See Scientific Notebook Spycher 2000 [153572], p. 114-116.
14	Corroborated using SUPCRT92 [153218] (Johnson et al. 1992 [101632]) with original thermodynamic data from the database DATA0.YMP.R0 for the geochemical code EQ3/6 (DTN: MO0008THRMODYN.000 [153742]). If two sources are cited, data are from the first source, and values are identical or differ by less than 0.05 units between the first and second source.

ATTACHMENT VI – THERMODYNAMIC DATABASE:
Tptpmn THC No-Backfill and DST THC Rev01 Models

(DTN: LB0101DSTTHCR1.006)

(Data from database thermok2.07.dat)				***log (k)***						
Mineral	**Molecular Weight (g/mol)**	**Molecular Volume (cm^3/mol)**	**Reaction Stoichiometry[1]**	0 (^{o}C)	25 (^{o}C)	60 (^{o}C)	100 (^{o}C)	150 (^{o}C)	200 (^{o}C)	**ref**
albite-low	262.223	100.07	(1)alo2-, (1)na+, (3)sio2(aq)	-21.694	-20.177	-18.362	-16.684	-15.094	-13.986	4,14
anorthite	278.207	100.79	(2)alo2-, (1)ca+2, (2)sio2(aq)	-21.229	-20.484	-19.64	-18.96	-18.514	-18.485	14
calcite	100.087	36.934	(1)ca+2, (-1)h+, (1)hco3-	2.226	1.849	1.333	0.774	0.1	-0.584	1,16
SiO2(amor.)	60.084	29	(1)sio2(aq)	-2.871	-2.663	-2.423	-2.205	-1.99	-1.82	7
cristobalite-a	60.084	25.74	(1)sio2(aq)	-3.63	-3.332	-2.99	-2.678	-2.371	-2.129	6
fluorite	78.075	24.542	(1)ca+2, (2)f-	-10.31	-10.037	-9.907	-9.967	-10.265	-10.784	1,16
goethite	88.854	20.82	(1)hfeo2	-12.78	-11.483	-10.202	-9.208	-8.407	-7.92	1
glass1	56.588	23.978	(-0.0362)h2o, (0.15)alo2-, (0.0021)ca+2,(0.0654)h+, (0.0042)k+,(0.0003)mg+2, (0.0756)na+,(0.7608)sio2(aq),	-4.55	-4.39	-4.2	-4.01	-3.83	-3.71	13
glass	60.084	29	(1)sio2(aq)	-2.871	-2.663	-2.423	-2.205	-1.99	-1.82	12
gypsum	172.172	74.69	(2)h2o, (1)ca+2, (1)so4-2	-4.533	-4.482	-4.609	-4.903	-5.41	-6.127	1,16
hematite	159.692	30.274	(-1)h2o, (2)hfeo2	-26.439	-23.927	-21.485	-19.661	-18.293	-17.573	1,16
illite	378.963	135.08	(0.44)h2o, (2.06)alo2-, (1.12)h+,(0.5)k+, (0.22)mg+2,(3.72)sio2(aq)	-45.354	-41.926	-38.294	-34.994	-31.867	-29.606	4
k-spar	278.332	108.741	(1)alo2-, (1)k+, (3)sio2(aq)	-23.77	-21.82	-19.53	-17.44	-15.46	-14.06	4,15
kaolinite	258.16	99.52	(1)h2o, (2)alo2-, (2)h+,(2)sio2(aq)	-43.073	-39.895	-36.336	-33.181	-30.212	-28.082	4
quartz	60.084	22.688	(1)sio2(aq)	-4.079	-3.739	-3.349	-2.992	-2.642	-2.365	5
opal_proxy	60.084	29.000	(1)sio2(aq)	-3.501	-3.005	-2.627	-2.358	-2.118	-1.926	17
tridymite	60.084	26.586	(1)sio2(aq)	-3.872	-3.567	-3.193	-2.821	-2.394	-1.984	10
smectite-ca	365.394	132.51	(0.52)h2o, (1.77)alo2-, (0.145)ca+2,(0.96)h+, (0.26)mg+2,(3.97)sio2(aq)	-39.970	-36.970	-33.600	-30.610	-27.750	-25.670	9,15
smectite-na	366.25	132.51	(0.52)h2o, (1.77)alo2-, (0.96)h+,(0.26)mg+2, (0.29)na+,(3.97)sio2(aq)	-40.080	-36.980	-33.500	-30.380	-27.400	-25.210	9,15
smectite-mg	363.107	132.51	(0.52)h2o, (1.77)alo2-, (0.96)h+,(0.405)mg+2, (3.97)sio2(aq)	-40.030	-37.060	-33.730	-30.770	-27.940	-25.880	9,15
steller/10	281.733	133.1	(2.8)h2o, (0.79)alo2-, (0.39)ca+2,(0.01)na+, (2.81)sio2(aq)	-17.910	-16.400	-14.670	-13.100	-11.560	-10.420	11,15
heuland/10	279.347	126.64	(2.6)h2o, (0.8)alo2-, (0.33)ca+2,(0.04)k+, (0.1)na+,(2.8)sio2(aq)	-17.900	-16.350	-14.580	-12.970	-11.400	-10.230	11,15
mordeni/10	269.631	127.35	(2.2)h2o, (0.6)alo2-, (0.15)ca+2,(0.09)k+, (0.21)na+,(3)sio2(aq)	-16.150	-14.660	-12.950	-11.390	-9.840	-8.670	11,15
clinopt/10	277.66	126.41	(2.6)h2o, (0.68)alo2-, (0.28)ca+2,(0.08)k+, (0.04)na+,(2.92)sio2(aq)	-17.040	-15.500	-13.740	-12.130	-10.560	-9.350	11,15
Gas:	**Molecular Weight (g/mol)**	**Molecular Diameter (m)**								
CO2(g)	44.01	2.50E-10	(-1)h2o, (1)h+, (1)hco3-	-7.677	-7.818	-8.053	-8.36	-8.77	-9.217	1,16
NOTES:	[1] Negative number in parenthesis indicate the species is on the left side of equation									
	Minerals names or abbreviations above are those used in the database and may not exactly match names used in the text of the report. Names ending by /10 indicate the stoichiometry , molecular weight, molar volume, and log(K) values for those minerals were divided by 10 compared to original data. Glass phases glass1 and glass were used with the extended-case and base-case geochemical systems, respectively.									

(Data in input file thermok2.07.dat)				***log (k)***						
Aqueous Species	**$r_{ej}^{(19)}$**	**Charge**	**Reaction Stoichiometry**	0 (^{o}C)	25 (^{o}C)	60 (^{o}C)	100 (^{o}C)	150 (^{o}C)	200 (^{o}C)	**ref.**
CO2(aq)	$0.231^{(18)}$	0	(-1)h2o, (1)h+, (1)hco3-	-6.58	-6.345	-6.268	-6.388	-6.724	-7.197	1,16
CO3-2	2.81	-2	(-1)h+, (1)hco3-	10.624	10.329	10.13	10.084	10.2	10.465	1,16
OH-	1.4	-1	(1)h2o, (-1)h+	14.94	13.995	13.027	12.255	11.631	11.284	1,16
Al(OH)2+	2.31	1	(1)alo2-, (2)h+	-13.656	-12.289	-10.831	-9.6	-8.53	-7.823	1
HAlO$_2$	0	0	(1)alo2-, (1)h+	-7.08	-6.45	-5.846	-5.409	-5.121	-5.035	1
Al+3	3.33	3	(-2)h2o, (1)alo2-, (4)h+	-25.795	-22.883	-19.571	-16.582	-13.676	-11.409	1
AlOH+2	2.8	2	(-1)h2o, (1)alo2-, (3)h+	-20.069	-17.926	-15.568	-13.519	-11.624	-10.242	1
CaCl+	2.31	1	(1)ca+2, (1)cl-	0.673	0.696	0.589	0.357	-0.04	-0.533	1
CaCl2(aq)	0	0	(1)ca+2, (2)cl-	0.452	0.644	0.629	0.381	-0.159	-0.911	1,16
CaCO3(aq)	0	0	(1)ca+2, (-1)h+, (1)hco3-	7.502	7.002	6.452	5.964	5.468	5.018	1,16
CaHCO3+	2.31	1	(1)ca+2, (1)hco3-	-1.095	-1.047	-1.159	-1.418	-1.859	-2.4	1,16
CaSO4(aq)	0	0	(1)ca+2, (1)so4-2	-2.071	-2.111	-2.265	-2.511	-2.91	-3.433	1,16
CaF+	2.31	1	(1)ca+2, (1)f-	-0.655	-0.682	-0.862	-1.17	-1.649	-2.215	1,16
CaOH+	2.31	1	(1)h2o, (-1)h+, (1)ca+2	14.085	12.833	11.416	10.142	8.904	7.931	16
HSiO3-	1.81	-1	(1)h2o, (-1)h+, (1)sio2(aq)	10.323	9.953	9.468	9.084	8.85	8.839	1
HCl(aq)	$0.2^{(18)}$	0	(1)cl-, (1)h+	0.661	0.67	0.689	0.62	0.41	0.092	1
KCl(aq)	0	0	(1)cl-, (1)k+	1.71	1.495	1.216	0.924	0.575	0.215	1
KHSO4(aq)	0	0	(1)h+, (1)k+, (1)so4-2	-0.435	-0.814	-1.479	-2.294	-3.341	-4.431	1
KSO4-	1.81	-1	(1)k+, (1)so4-2	-0.885	-0.88	-0.99	-1.194	-1.52	-1.919	1,16
HF(aq)	$0.2^{(18)}$	0	(1)h+, (1)f-	-2.985	-3.168	-3.474	-3.848	-4.338	-4.859	1,16
MgCl+	2.31	1	(1)cl-, (1)mg+2	0.049	0.135	0.055	-0.182	-0.607	-1.139	1,16
MgCO3(aq)	0	0	(-1)h+, (1)hco3-, (1)mg+2	7.74	7.35	6.926	6.563	6.204	5.872	1,16
MgHCO3+	2.31	1	(1)hco3-, (1)mg+2	-1.08	-1.036	-1.164	-1.436	-1.88	-2.415	1,16
MgSO4(aq)	0	0	(1)mg+2, (1)so4-2	-2.139	-2.412	-2.837	-3.347	-4.073	-4.955	1
MgF+	2.31	1	(1)mg+2, (1)f-	-1.387	-1.352	-1.478	-1.739	-2.168	-2.688	1,16
MgOH+	2.31	1	(1)h2o, (-1)h+, (1)mg+2	12.674	11.682	10.502	9.399	8.291	7.398	16
NaOH(aq)	0	0	(1)h2o, (-1)h+, (1)na+	15.645	14.795	13.8	12.885	11.971	11.221	1
NaCO3-	1.81	-1	(-1)h+, (1)hco3-, (1)na+	9.815	9.814	10.075	10.649	11.568	12.632	2
NaHCO3(aq)	0	0	(1)hco3-, (1)na+	-0.373	-0.154	0.11	0.411	0.793	1.213	1,16
NaHSiO3	0	0	(1)h2o, (-1)h+, (1)na+,(1)sio2(aq)	8.414	8.304	8.053	7.829	7.684	7.658	1
NaF(aq)	0	0	(1)na+, (1)f-	1.082	0.998	0.833	0.624	0.338	0.011	1,16
NaSO4-	1.81	-1	(1)na+, (1)so4-2	-0.677	-0.700	-0.842	-1.063	-1.389	-1.772	16
FeO2-	1.81	-1	(-1)h+, (1)hfeo2	10.231	9.602	8.839	8.111	7.38	6.821	3,16
FeO+	2.31	1	(-1)h2o, (1)h+, (1)hfeo2	-7.324	-6.368	-5.372	-4.561	-3.865	-3.393	3,16
Primary Aqueous Species:			**Mol. Wt. (g/mol)**							
H2O	0	0	18.015							1,16
AlO2-	1.81	-1	58.98							1,16
Ca+2	2.87	2	40.078							1,16
Cl-	1.81	-1	35.453							1,16
H+	3.08	1	1.008							1,16
HCO3-	2.1	-1	61.017							1,16
K+	2.27	1	39.098							1,16
Mg+2	2.54	2	24.305							1,16
Na+	1.91	1	22.99							1,16
SiO2(aq)	$0.08^{(18)}$	0	60.084							1,16
SO4-2	3.15	-2	96.064							1,16
F-	1.33	-1	18.998							1,16
HFeO2	0	0	88.854							3,16

ref. no	Reference
1	EQ3/6 V7.2b [126891] database data0.com.R2 Aug.2.1995 (STN: LLNL:UCRL-MA-110662). Mostly calculated with SUPCRT92 [153218] and associated databases (Johnson et al. 1992 [101632]). If two sources are cited, data are from the first source, and values are identical or differ by less than 0.05 units between sources.
2	EQ3/6 V7.2b [126891] database data0.com.R6 Dec.3.1996 (STN: LLNL:UCRL-MA-110662)
3	Log(K) calculated using SUPCRT92 [153218] (Johnson et al. 1992 [101632]) with Fe+3 and Fe(III)-OH data from Shock et al. (1997 [127953]) added to SPRONS.DAT version dated 3/14/96 (the latter is the database of SUPCRT92). See Scientific Notebook Spycher 2000 [153572], p. 104-110.
4	Log(K) calculated using SUPCRT92 [153218] (Johnson et al. 1992 [101632]) with thermodynamic properties from various sources (Berman 1988 [104905] for albite; Kulik and Aja 1997 [128132] for illite and k-smectite; Robie and Hemingway 1995 [153683] for kaolinite; Apps and Chang 1992 [124211] for microcline) added to SPRONS.DAT version dated 3/14/96 (the latter is the database of SUPCRT92), then corrected to reflect the quartz solubility data of Rimstidt (1997 [101709]). See Bodvarsson 2001 [153816], YMP-LBNL-YWT-JA-1A p. 28-39.
5	Rimstidt (1997 [101709])
6	Regression by Apps (1970 [124208]) of pressure-corrected cristobalite solubility data derived from measurements by Fournier and Rowe (1962 [124282]). See Bodvarsson 2001 [153816], YMP-LBNL-YWT-JA-1A p. 38.
7	Regression by Apps (1970 [124208]). See Bodvarsson 2001 [153816], YMP-LBNL-YWT-JA-1A p. 37.
8	Number not used.
9	Recalculated from log(K) data for montmor-k, montmor-ca, montmor-mg, and montmor-k in EQ3/6 V7.2b database [126891] (see ref. 1), as described in Bodvarsson 2001 [153816], YMP-LBNL-YWT-JA-1A p. 40–43
10	From log(K) data for quartz and tridymite in ref.1 above, then corrected with the quartz solubility data of Rimstidt (1997 [101709]). See Scientific Notebook Spycher 2000 [153572], p. 113-114. Molar volume from molecular weight in ref.1 and density in Klein and Hurlbut (1993 [153700], p. 665).
11	Log(K) calculated using SUPCRT92 [153218] (Johnson et al. 1992 [101632]) with zeolite formulas and thermodynamic data from DTN: LA0008SC12213N.001 [153386] and data calculations from additional referenecs Smyth and Bish (1988 [133216]), Chermak and Rimstidt (1989 [105073]), Chipera and Bish (1997 [105079]), Holland (1989 [106044]), and DTN: LA000000000071.001 [153637]) in Bodvarsson 2001 [153816], YMP-LBNL-YWT-NS-1.2, pp. 44–46, added to SPRONS.DAT version dated 3/14/96 (the latter is the database of SUPCRT92), then corrected to reflect the quartz solubility data of Rimstidt (1997 [101709]). See Bodvarsson 2001 [153816], YMP-LBNL-YWT-JA-1A p. 48-50, Spycher 1998 [153571], p. 115, 136 and Spycher 2000 [153572], p. 111-113.
12	Same composition and log(K) as amorphous silica
13	Formula from composition by Bish et al. (1996 [101430]). Log(K) at 25^{o}C was calculated by equilibrating the glass with the initial water composition (Section 4.1.3) using SOLVEQ V1.0 [153217] and adjusting the log(K) value to yield approximately 100 ppm SiO2(aq.) in solution at 25^{o}C. Log(K) values at higher temperatures were then adjusted to maintain the same degree of amorphous silica undersaturation with the equilibrated glass at all temperatures. See Scientific Notebook Spycher 2000 [153572], p 156.
14	Arnórsson and Stefánsson (1999 [153329], p. 173)
15	Original data revised as described in Section 4.1.4.2
16	Calculated using SUPCRT92 [153218] (Johnson et al. 1992 [101632]) with original thermodynamic data from the database DATA0.YMP.R0 for the geochemical code EQ3/6 (DTN: MO0008THRMODYN.000). If two sources are cited, data are from the first source, and values are identical or differ by less than 0.05 units between the first and second source.
17	β-cristobalite from ref. 1. This is actually not β-cristobalite (see Section 4.1.4.2)
18	Neutral species: salting out coefficients from Table 4.5 in Langmuir (1997 [100051])
19	Effective electrostatic radius from Table 3 in Helegeson et al. (1981 [106024]). If unavailable, values for similar species are used (see Bodvarsson 2001 [153816], YMP-LBNL-YWT-NS-1.2 p. 18)

ATTACHMENT VII – WASTE PACKAGE AVERAGE HEAT TRANSFER: Tptpmn THC Backfill Model

(DTN: LB991200DSTTHC.006)

Time (years)	Total Heat (no ventilation) (W/meter)	Model Heat Load (W/meter)
0.01	1540.413	462.124
0.02	1538.978	461.693
0.03	1538.078	461.424
0.04	1537.190	461.157
0.05	1536.297	460.889
0.06	1535.411	460.623
0.07	1534.536	460.361
0.08	1533.632	460.090
0.09	1532.778	459.833
0.10	1531.892	459.568
0.15	1527.633	458.290
0.20	1523.418	457.025
0.25	1519.360	455.808
0.30	1515.371	454.611
0.35	1511.471	453.441
0.40	1507.662	452.299
0.45	1503.928	451.178
0.50	1500.288	450.087
0.55	1496.715	449.014
0.60	1493.234	447.970
0.65	1489.795	446.938
0.70	1486.453	445.936
0.75	1483.142	444.943
0.80	1479.935	443.981
0.85	1476.770	443.031
0.90	1473.664	442.099
0.95	1470.592	441.178
1.0	1467.611	440.283
1.5	1439.923	431.977
2.0	1415.942	424.783
2.5	1394.705	418.412
3.0	1375.415	412.624
3.5	1358.036	407.411
4.0	1341.878	402.563
4.5	1326.553	397.966
5.0	1312.104	393.631
5.5	1296.809	389.043
6.0	1282.270	384.681
6.5	1268.766	380.630
7.0	1255.846	376.754

DTN: SN9907T0872799.001 [111485] (Total Heat)

NOTE: Point at 50.001 years was interpolated between original data points at 50 and 55 years. From 0 to 50 years: Model Heat Load = Total Heat x 0.3 (70% heat removal)

Time (years)	Total Heat (no ventilation) (W/meter)	Model Heat Load (W/meter)
7.5	1242.619	372.786
8.0	1229.944	368.983
8.5	1217.624	365.287
9.0	1205.763	361.729
9.5	1193.723	358.117
10	1182.073	354.622
15	1074.598	322.379
20	983.485	295.045
25	901.588	270.476
30	829.938	248.981
35	767.015	230.104
40	710.239	213.072
45	659.213	197.764
50	614.555	184.367
50.001	614.547	614.547
55	574.043	574.043
60	537.708	537.708
65	504.775	504.775
70	476.139	476.139
75	449.277	449.277
80	425.849	425.849
85	404.184	404.184
90	385.201	385.201
95	367.303	367.303
100	351.814	351.814
150	253.283	253.283
200	208.867	208.867
250	182.764	182.764
300	164.855	164.855
350	150.949	150.949
400	139.546	139.546
450	129.712	129.712
500	121.251	121.251
550	113.640	113.640
600	107.056	107.056
650	101.089	101.089
700	95.546	95.546
750	90.641	90.641
800	85.985	85.985
850	81.688	81.688

DTN: SN9907T0872799.001 [111485] (Total Heat)

NOTE: Point at 50.001 years was interpolated between original data points at 50 and 55 years. From 0 to 50 years: Model Heat Load = Total Heat x 0.3 (70% heat removal).

Time (years)	Total Heat (no ventilation) (W/meter)	Model Heat Load (W/meter)
900	77.753	77.753
950	74.214	74.214
1000	71.169	71.169
1500	49.114	49.114
2000	38.723	38.723
2500	33.617	33.617
3000	30.482	30.482
3500	28.676	28.676
4000	27.425	27.425
4500	26.223	26.223
5000	25.254	25.254
5500	24.204	24.204
6000	23.596	23.596
6500	22.687	22.687
7000	21.910	21.910
7500	21.344	21.344
8000	20.553	20.553
8500	19.948	19.948
9000	19.308	19.308
9500	18.729	18.729
10000	18.144	18.144
15000	13.570	13.570
20000	10.633	10.633
25000	8.594	8.594
30000	7.027	7.027
35000	5.908	5.908
40000	5.071	5.071
45000	4.407	4.407
50000	3.868	3.868
55000	3.378	3.378
60000	3.041	3.041
65000	2.671	2.671
70000	2.425	2.425
75000	2.192	2.192
80000	1.985	1.985
85000	1.817	1.817
90000	1.692	1.692
95000	1.562	1.562
100000	1.457	1.457

DTN: SN9907T0872799.001 [111485] (Total Heat)

NOTE: Point at 50.001 years was interpolated between original data points at 50 and 55 years. From 0 to 50 years: Model Heat Load = Total Heat x 0.3 (70% heat removal).

ATTACHMENT VIII – WASTE PACKAGE AVERAGE HEAT TRANSFER: Tptpmn No-Backfill and Tptpll THC Models

(DTN: LB0101DSTTHCR1.007)

Time (years)	Total Heat (no ventilation) (W/meter)	Model Heat Load (W/meter)
0.01	1450.000	435.000
0.02	1448.649	434.595
0.03	1447.802	434.341
0.04	1446.966	434.090
0.05	1446.126	433.838
0.06	1445.292	433.587
0.07	1444.468	433.340
0.08	1443.617	433.085
0.09	1442.813	432.844
0.1	1441.979	432.594
0.15	1437.970	431.391
0.2	1434.003	430.201
0.25	1430.183	429.055
0.3	1426.428	427.928
0.35	1422.757	426.827
0.4	1419.171	425.751
0.45	1415.657	424.697
0.5	1412.230	423.669
0.55	1408.866	422.660
0.6	1405.590	421.677
0.65	1402.353	420.706
0.7	1399.207	419.762
0.75	1396.090	418.827
0.8	1393.072	417.922
0.85	1390.093	417.028
0.9	1387.169	416.151
0.95	1384.277	415.283
1.0	1381.471	414.441
1.5	1355.408	406.623
2.0	1332.834	399.850
2.5	1312.844	393.853
3.0	1294.686	388.406
3.5	1278.327	383.498
4.0	1263.118	378.935
4.5	1248.692	374.608
5.0	1235.091	370.527
5.5	1220.694	366.208
6.0	1207.008	362.102
6.5	1194.297	358.289
7.0	1182.135	354.641

DTN: SN9907T0872799.001 [111485] multiplied by 1450/1540.413 (Total Heat)

NOTE: Point at 50.001 years was interpolated between original data points at 50 and 55 years. From 0 to 50 years: Model Heat Load = Total Heat x 0.3 (70% heat removal)

Time (years)	Total Heat (no ventilation) (W/meter)	Model Heat Load (W/meter)
7.5	1169.685	350.905
8.0	1157.754	347.326
8.5	1146.156	343.847
9.0	1134.992	340.498
9.5	1123.659	337.098
10	1112.692	333.808
15	1011.525	303.458
20	925.760	277.728
25	848.670	254.601
30	781.226	234.368
35	721.996	216.599
40	668.553	200.566
45	620.521	186.156
50	578.485	173.545
50.001	578.477	578.477
55	540.350	540.350
60	506.148	506.148
65	475.148	475.148
70	448.192	448.192
75	422.908	422.908
80	400.854	400.854
85	380.461	380.461
90	362.592	362.592
95	345.744	345.744
100	331.164	331.164
150	238.417	238.417
200	196.608	196.608
250	172.037	172.037
300	155.179	155.179
350	142.089	142.089
400	131.355	131.355
450	122.099	122.099
500	114.135	114.135
550	106.970	106.970
600	100.772	100.772
650	95.156	95.156
700	89.938	89.938
750	85.321	85.321
800	80.938	80.938
850	76.894	76.894

DTN: SN9907T0872799.001 [111485] multiplied by 1450/1540.413 (Total Heat)

NOTE: Point at 50.001 years was interpolated between original data points at 50 and 55 years. From 0 to 50 years: Model Heat Load = Total Heat x 0.3 (70% heat removal)

Time (years)	Total Heat (no ventilation) (W/meter)	Model Heat Load (W/meter)
900	73.190	73.190
950	69.859	69.859
1000	66.992	66.992
1500	46.231	46.231
2000	36.450	36.450
2500	31.644	31.644
3000	28.693	28.693
3500	26.993	26.993
4000	25.815	25.815
4500	24.684	24.684
5000	23.772	23.772
5500	22.783	22.783
6000	22.211	22.211
6500	21.355	21.355
7000	20.624	20.624
7500	20.091	20.091
8000	19.347	19.347
8500	18.777	18.777
9000	18.174	18.174
9500	17.630	17.630
10000	17.079	17.079
15000	12.774	12.774
20000	10.009	10.009
25000	8.089	8.089
30000	6.615	6.615
35000	5.561	5.561
40000	4.774	4.774
45000	4.148	4.148
50000	3.641	3.641
55000	3.180	3.180
60000	2.862	2.862
65000	2.514	2.514
70000	2.282	2.282
75000	2.063	2.063
80000	1.869	1.869
85000	1.710	1.710
90000	1.593	1.593
95000	1.470	1.470
100000	1.372	1.372

DTN: SN9907T0872799.001 [111485] multiplied by 1450/1540.413 (Total Heat)

NOTE: Point at 50.001 years was interpolated between original data points at 50 and 55 years. From 0 to 50 years: Model Heat Load = Total Heat x 0.3 (70% heat removal)

ATTACHMENT IX – EFFECTIVE THERMAL CONDUCTIVITY FOR IN-DRIFT OPEN SPACES: Tptpmn THC Backfill Model

Pre-closure

Time (sec)	Time (year)	Factor
0.00000E+00	0.0	0.400
3.15360E+07	1.0	0.775
4.73040E+07	1.5	0.825
6.30720E+07	2	0.858
9.46080E+07	3	0.899
1.26144E+08	4	0.923
1.57680E+08	5	0.941
1.89216E+08	6	0.956
2.20752E+08	7	0.966
2.52288E+08	8	0.975
2.83824E+08	9	0.982
3.15360E+08	10	0.988
3.46896E+08	11	0.993
3.78432E+08	12	0.997
4.73040E+08	15	1.000
6.30720E+08	20	0.994
7.88400E+08	25	0.979
8.19936E+08	26	0.976
8.51472E+08	27	0.972
9.46080E+08	30	0.961
1.10376E+09	35	0.941
1.26144E+09	40	0.921
1.57680E+09	50	0.887

DTN: SN9907T0872799.002 [124205]

NOTE: $K_{thermal}$ is calculated as Max. $K_{thermal}$ x Factor

Maximum $K_{thermal}$ (W/m-K) = 10.443

Post-closure

Time		Factor	
(sec)	(year)	Inner	Outer
1.57680E+09	50	0.887	0.887
1.60834E+09	51	0.872	0.800
1.63987E+09	52	0.915	0.849
1.73448E+09	55	0.984	0.935
1.89216E+09	60	1.000	0.983
2.04984E+09	65	0.990	1.000
2.20752E+09	70	0.968	0.999
2.36520E+09	75	0.941	0.990
2.39674E+09	76	0.936	0.987
2.42827E+09	77	0.931	0.986
2.52288E+09	80	0.916	0.980
2.83824E+09	90	0.874	0.963
3.15360E+09	100	0.833	0.940
3.18514E+09	101	0.829	0.937
3.31128E+09	105	0.813	0.924
3.46896E+09	110	0.796	0.910
3.78432E+09	120	0.767	0.890
4.09968E+09	130	0.746	0.879
4.41504E+09	140	0.729	0.873
5.04576E+09	160	0.703	0.864
5.67648E+09	180	0.679	0.847
6.30720E+09	200	0.659	0.836
6.93792E+09	220	0.638	0.816
7.88400E+09	250	0.617	0.800
9.46080E+09	300	0.587	0.775
1.10376E+10	350	0.563	0.754
1.26144E+10	400	0.540	0.731
1.41912E+10	450	0.519	0.709
1.57680E+10	500	0.506	0.698
1.73448E+10	550	0.497	0.692
1.89216E+10	600	0.491	0.688
2.20752E+10	700	0.476	0.677
2.52288E+10	800	0.462	0.664
2.83824E+10	900	0.450	0.652

DTN: SN9907T0872799.002 [124205]

NOTE: $K_{\textbf{thermal}}$ is calculated as Max. $K_{\textbf{thermal}}$ x Factor

Maximum K_{thermal} (W/m-K) Inner=3.426,
Outer=9.068

Post-closure (Cont.)

Time		Factor	
(sec)	**(year)**	**Inner**	**Outer**
3.15360E+10	1000	0.439	0.642
3.46896E+10	1100	0.431	0.633
3.78432E+10	1200	0.423	0.624
4.09968E+10	1300	0.414	0.615
4.41504E+10	1400	0.406	0.606
4.73040E+10	1500	0.398	0.597
5.04576E+10	1600	0.392	0.590
5.67648E+10	1800	0.382	0.577
6.30720E+10	2000	0.370	0.563
6.93792E+10	2200	0.363	0.552
7.88400E+10	2500	0.353	0.540
9.46080E+10	3000	0.342	0.524
1.10376E+11	3500	0.334	0.512
1.26144E+11	4000	0.327	0.501
1.41912E+11	4500	0.321	0.493
1.57680E+11	5000	0.317	0.486
1.89216E+11	6000	0.308	0.474
2.20752E+11	7000	0.302	0.464
2.52288E+11	8000	0.296	0.455
3.15360E+11	10000	0.286	0.441
4.73040E+11	15000	0.267	0.413
6.30720E+11	20000	0.255	0.395
9.46080E+11	30000	0.237	0.371
1.26144E+12	40000	0.228	0.358
1.57680E+12	50000	0.222	0.350
1.89216E+12	60000	0.218	0.344
2.52288E+12	80000	0.212	0.337
3.15360E+12	100000	0.209	0.333

DTN: SN9907T0872799.002 [124205]

NOTE: $K_{\mathbf{thermal}}$ is calculated as Max. $K_{\mathbf{thermal}}$ x Factor

Maximum K_{thermal} (W/m-K) Inner=3.426,
Outer=9.068

ATTACHMENT X – EFFECTIVE THERMAL CONDUCTIVITY FOR IN-DRIFT OPEN SPACES: Tptpmn No-Backfill and Tptpll THC Models

Pre-closure

Time		Factor
(sec)	(year)	
3.15360E+03	0.0	0.395
3.15360E+07	1.0	0.777
4.73040E+07	1.5	0.825
6.30720E+07	2	0.856
9.46080E+07	3	0.898
1.26144E+08	4	0.921
1.57680E+08	5	0.939
1.89216E+08	6	0.955
2.20752E+08	7	0.966
2.52288E+08	8	0.975
2.83824E+08	9	0.982
3.15360E+08	10	0.988
3.46896E+08	11	0.993
3.78432E+08	12	0.997
4.73040E+08	15	1
6.30720E+08	20	0.993
7.88400E+08	25	0.977
8.19936E+08	26	0.974
8.51472E+08	27	0.97
9.46080E+08	30	0.958
1.10376E+09	35	0.936
1.26144E+09	40	0.915
1.57680E+09	50	0.879

DTN: SN0002T0872799.009 [153364]

NOTE: $K_{\mathbf{thermal}}$ is calculated as Max. $K_{\mathbf{thermal}}$ x Factor

Maximum $K_{thermal}$ (W/m-K) = 10.568

Post-closure (No Backfill)

Time		Factor	
(sec)	**(year)**	**Inner**	**Outer**
1.57680E+09	50	0.879	0.879
1.608336E+09	51	0.844	0.829
1.639872E+09	52	0.892	0.878
1.734480E+09	55	0.951	0.944
1.892160E+09	60	0.988	0.986
2.049840E+09	65	1	1
2.207520E+09	70	0.995	0.998
2.365200E+09	75	0.985	0.99
2.396736E+09	76	0.983	0.988
2.428272E+09	77	0.981	0.986
2.522880E+09	80	0.973	0.98
2.838240E+09	90	0.954	0.963
3.153600E+09	100	0.932	0.943
3.185136E+09	101	0.929	0.941
3.311280E+09	105	0.918	0.929
3.468960E+09	110	0.905	0.917
3.784320E+09	120	0.882	0.896
4.099680E+09	130	0.872	0.886
4.415040E+09	140	0.864	0.879
5.045760E+09	160	0.852	0.869
5.676480E+09	180	0.839	0.857
6.307200E+09	200	0.83	0.849
6.937920E+09	220	0.818	0.838
7.884000E+09	250	0.798	0.818
9.460800E+09	300	0.763	0.784
1.103760E+10	350	0.736	0.758
1.261440E+10	400	0.707	0.729
1.419120E+10	450	0.689	0.711
1.576800E+10	500	0.677	0.7
1.734480E+10	550	0.672	0.694
1.892160E+10	600	0.667	0.69
2.207520E+10	700	0.656	0.68
2.522880E+10	800	0.646	0.67
2.838240E+10	900	0.637	0.661

DTN: SN0002T0872799.009 [153364]

NOTE: $K_{thermal}$ is calculated as Max. $K_{thermal}$ x Factor

Maximum $K_{thermal}$ (W/m-K) Inner=2.298,

Outer=14.407

Post-closure (No Backfill) (Cont.)

Time		Factor	
(sec)	(year)	Inner	Outer
3.153600E+10	1000	0.627	0.651
3.468960E+10	1100	0.619	0.643
3.784320E+10	1200	0.611	0.635
4.099680E+10	1300	0.602	0.626
4.415040E+10	1400	0.592	0.616
4.730400E+10	1500	0.582	0.605
5.045760E+10	1600	0.574	0.597
5.676480E+10	1800	0.559	0.583
6.307200E+10	2000	0.543	0.566
6.937920E+10	2200	0.533	0.555
7.884000E+10	2500	0.519	0.541
9.460800E+10	3000	0.503	0.523
1.103760E+11	3500	0.491	0.51
1.261440E+11	4000	0.48	0.499
1.419120E+11	4500	0.472	0.491
1.576800E+11	5000	0.465	0.484
1.892160E+11	6000	0.453	0.471
2.207520E+11	7000	0.444	0.461
2.522880E+11	8000	0.436	0.452
3.153600E+11	10000	0.422	0.438
4.730400E+11	15000	0.395	0.411
6.307200E+11	20000	0.378	0.393
9.460800E+11	30000	0.354	0.367
1.261440E+12	40000	0.341	0.354
1.576800E+12	50000	0.333	0.346
1.892160E+12	60000	0.326	0.339
2.522880E+12	80000	0.318	0.33
3.153600E+12	100000	0.314	0.325

DTN: SN0002T0872799.009 [153364]

NOTE: $K_{thermal}$ is calculated as Max. $K_{thermal}$ x Factor
Maximum $K_{thermal}$ (W/m-K) Inner=2.298,
Outer=14.407

ATTACHMENT XI – LIST OF MODEL INPUT AND OUTPUT FILES

1.0 Rev00 Input and Output Files

The following types of files were submitted for Rev00 of this AMR to the TDMS under DTN: LB991200DSTTHC.002. They also support Rev01.

1. Input and output files of simulations with the reactive transport model TOUGHREACT V2.2 [153219]. For each simulation, these files were concatenated into one file using the Unix *tar* utility then compressed using the Unix *gzip* utility. Resulting concatenated/compressed files have the extension *.tar.gz*.

2. Summary Excel spreadsheets of seepage models output data at three locations adjacent to the drift wall (crown, side, and base).

<u>DST THC Model Rev00 Input and Output File Folders (Simulations in Section 6.2.7)</u>

dst99amr_8.tar.gz	DST simulations with base-case geochemical system
dst99amr_9.tar.gz	DST simulations with extended-case geochemical system

<u>Tptpmn THC Backfill Model Input and Output File Folders (Simulations in Table 13)</u>

thc1mm_amb1.tar.gz	THC simulation, 1 mm/year mean infiltration, base-case geochemical system - 0 to 50 years
thc1mm_amb1a.tar.gz	THC simulation, 1 mm/year mean infiltration, base-case geochemical system - 50 to 100,000 years
thc1mm_amb2.tar.gz	THC simulation, 1 mm/year mean infiltration extended-case geochemical system- 0 to 50 years
thc1mm_amb2a.tar.gz	THC simulation, 1 mm/year mean infiltration, extended-case geochemical system - 50 to 20,000 years
thc1mm_amb2b.tar.gz	THC simulation, 1 mm/year mean infiltration, extended-case geochemical system - 20,000 to100,000 years

Other file names have similar designations as shown in the examples below. The file name shows the infiltration rates used in each simulation (e.g., *6_16_25* refers to 6 mm/year from 0 to 600 years, 16 mm/year from 600 to 2000 years, and 25 mm/year from 2000 to 100,000 years). For THC simulations, the last digit in the file name is *3* for simulations with the base-case geochemical system, and *4* for the extended-case geochemical system (e.g., thc*6_16_25_3* refers to 6/16/25 mm/year with the base-case geochemical system). The last letters *a*, *b*, *c*, *or d* are used for time designations.

th6_16_25_3.tar.gz	TH Simulation - 0 to 50 years
th6_16_25_3a.tar.gz	TH Simulation - 50 to 600 years
th6_16_25_3b.tar.gz	TH Simulation - 600 to 2000 years
th6_16_25_3c.tar.gz	TH Simulation - 2000 to 100,000 years

thc0.6_6_3_4.tar.gz	THC simulation, extended-case - 0 to 50 years
thc0.6_6_3_4a.tar.gz	THC simulation, extended-case - 50 to 600 years
thc0.6_6_3_4b.tar.gz	THC simulation, extended-case - 600 to 2000 years
thc0.6_6_3_4c.tar.gz	THC simulation, extended-case - 2000 to 20,000 years
thc0.6_6_3_4d.tar.gz	THC simulation, extended-case - 20,000 to 100,000 years

.
.
.
etc...

2.0 Rev01 Input and Output Files

The following types of files were submitted for Rev01 of this AMR to the TDMS under DTN: LB0011DSTTHCR1.001 and LB0011DSTTHCR1.002.

1. Input and output files of simulations with the reactive transport model TOUGHREACT V2.3 [153101]. For each simulation, these files were concatenated into one file using the Unix *tar* utility then compressed using the Unix *gzip* utility. Resulting concatenated/compressed files have the extension *.tar.gz*.

2. Summary Excel spreadsheets of seepage models output data at three locations adjacent to the drift wall (crown, side, and base).

3. Spreadsheets containing calculations have been included as part of several DTNs in order to document the embedded calculations and supplement the Scientific Notebooks. READ.ME files are also included which outline the use of calculations in each spreadsheet. The calculations can be observed by clicking on the spreadsheet cells or selecting the “Tools\Options\View\Formulas” option in MS Excel. In addition, the cell references in the equations show all cells used as input to the calculation executed in the spreadsheet. The formulae in the submitted spreadsheets use the standard functions of MS Excel 97.

<u>DST THC Model Rev01 Input and Output File Folders (Simulations in Section 6.2.8)</u>

dst00_amr1	Base Case CC Kin
dst00_amr2	Extended CC Kin
dst00_amr3	Base Case CC Eq
dst00_amr4	Extended CC Eq
dst00_amr5	Extended An Full
dst00_amr6	Base Case No CC

More complete descriptions can be found in Section 6.2.8.

<u>Tptpmn THC No-Backfill Model Input and Output File Folders (Simulations in Table 15)</u>

th6_3_r (plus a-d)
th6_16_25_7 (plus a-d)
thc6_16_25_9 (plus a-d)
thc6_16_25_9_amb (plus a-d)
thc6_16_25_10 (plus a-d)
thc6_16_25_10_amb (plus a-d)

<u>Tptpmn Heterogeneous THC Model Input and Output File Folders (Simulations in Table 16)</u>

ds00ss_het1
ds00th_het1(plus a-c)
ds00amb1_het1 (plus a-d)
ds00amb2_het1 (plus a-d)
ds00thc1_het1 (plus a-d)
ds00thc2_het1 (plus a-d)
ds00ss_het2
ds00th_het2 (plus a-c)
ds00thc1_het2 (plus a-d)
ds00thc2_het2 (plus a-d)
ds00ss_het3
ds00th_het3 (plus a-c)
ds00thc1_het3 (plus a-d)
ds00thc2_het3 (plus a-d)

<u>Tptpll THC Model Input and Output File Folders (Simulations in Table 18)</u>

th6_16_25_g4 (plus a-d)
thc6_16_25_2g4 (plus a-d)
thc6_16_25_2g4_amb (plus a-d)
thc6_16_25_g4 (plus a-d)
thc6_16_25_g4_amb (plus a-d)

3.0 Contents of *.tar.gz* files

FLOW.INP	Rock thermal and hydrological properties, run flags and other specifications (input)
FLOW.OUT	Thermal and hydrological results (gas/liquid saturation, T, P, air mass fraction, etc.) (output)
GENER	Infiltration rates, heat load, and effective thermal conductivity (input)
INCON	Initial thermal and hydrological conditions (T, P, liquid saturation, etc.) (input)
MESH	Input numerical mesh (input)
SAVE	Thermal and hydrological conditions (T, P, liquid saturation, etc.) to use for restarting a run (output, same format as INCON file)
TABLE	Miscellaneous output data
VERS	Miscellaneous output data

LINEQ	Miscellaneous output data
CHEMICAL.INP	Water chemistry, mineralogy, and CO_2 partial pressure data (input)
CHEMICAL.OUT	Echo of data read in CHEMICAL.INP
SOLUTE.INP	Run flags and other data relating to reactive transport (input)
SOLUTE.OUT	Echo of data read in SOLUTE.INP
thermokapps2.05.dat	Thermodynamic database (input)
thermok2.07.dat	Thermodynamic database for Rev01 (input)
TEC_CONC.DAT	Calculated concentrations of aqueous species (moles/liter) at each grid node (two records for each node - first record for fractures and second record for matrix) (output)
TEC_MIN.DAT	Calculated volume fraction change for minerals at each grid node (two records for each node - first record for fractures and second record for matrix) (output)
TEC_GAS.DAT	Calculated CO_2 volume fraction at each grid node (two records for each node - first record for fractures and second record for matrix) (output)
TIME.DAT	Chemical data at selected grid nodes (output)
chdump.dat	Chemical speciation of initial water (output) and nodes with convergence problems
INCHEM	Chemistry data at all grid nodes to use for restarting a run (input)
SAVECHEM	Chemistry data at all grid nodes to use for restarting a run (output, same format as INCHEM file)
ITER.DAT	Iteration information (output)
run_log.dat	Miscellaneous run-time information. Note: mass balances may not be printed out correctly in this file for runs that have been restarted (i.e., starting at times different than zero).

4.0 Summary Spreadsheets of THC Seepage Models Output Data (also used for plotting time profiles)

The data in these files were extracted from output files FLOW.OUT, TEC_CONC.DAT, TEC_MIN.DAT, and TEC_GAS.DAT for each simulation.

Tptpmn THC Backfill Model (TOUGHREACT V2.2 [153219]):

case1_0.6.xls	THC, extended-case, 0.6/6/3 mm/year infiltration
case1_6.xls	THC, extended-case, 6/16/25 mm/year infiltration
case1_15.xls	THC, extended-case, 15/25/47 mm/year infiltration
case2_0.6.xls	THC, base-case, 0.6/6/3 mm/year infiltration
case2_6.xls	THC, base-case, 6/16/25 mm/year infiltration
case2_15.xls	THC, base-case, 15/25/47 mm/year infiltration
case1_1amb.xls	THC, no heat load, extended-case, 1 mm/year infiltration
case2_1amb.xls	THC, no heat load, base-case, 1 mm/year infiltration
th_only_6.xls	TH, 6/16/25 mm/year infiltration

Tptpmn THC Backfill Model (TOUGHREACT V2.3 [153101]):

th6_3_r.xls	TH, 6/16/25 mm/year infiltration

Tptpmn THC No-Backfill Model (TOUGHREACT V2.3 [153101]):

th6_7.xls	TH, 6/16/25 mm/year infiltration
thc6_9base.xls	THC, base-case, 6/16/25 mm/year infiltration
thc6_9base_amb.xls	THC, no heat load, base-case, 6/16/25 mm/year infiltration
thc6_10ext.xls	THC, extended-case, 6/16/25 mm/year infiltration
thc6_10ext_amb.xls	THC, no heat load, extended-case, 6/16/25 mm/year infiltration

Tptpll THC Model (TOUGHREACT V2.3 [153101]):

th6_g4.xls	TH, 6/16/25 mm/year infiltration
thc6_2g4base.xls	THC, base-case, 6/16/25 mm/year infiltration
thc6_2g4base_amb.xls	THC, no heat load, base-case, 6/16/25 mm/year infiltration
thc6_2g4ext.xls	THC, extended-case, 6/16/25 mm/year infiltration
thc6_2g4ext_amb.xls	THC, no heat load, extended-case, 6/16/25 mm/year infiltration

5.0 Rev01 Input and Output Files for Section 6.7 (Plug Flow Reactor Experiment)

Input and output files for this section were submitted to the TDMS as DTN: LB0011THCDISSM.001 [153381] and DTN: LB0011THCDISSM.002, respectively. The input files (for DTN: LB0011THCDISSM.001 [153381]) consist of SOLVEQ V1.0 [153217] files used to calculate the initial water composition for the simulations, along with the input files for two TOUGHREACT V2.2 [153219] simulations and three TOUGHREACT V2.3 [153101] simulations. The output files (for DTN: LB0011THCDISSM.002) consist of the output files for the TOUGHREACT V2.2 [153219] and V2.3 [153101] simulations, and SOLVEQ V1.0 [153217] files used to correct for degassing and cooling. The files for each of the DTNs were grouped into folders (one for each simulation, plus additional folders for the SOLVEQ runs), and these were compressed using the Windows *Winzip* V7.0 utility. A Word 97 document (LB0011THCDISSM.00# notes.doc) describing the information contained in each DTN file was included in the compressed master file for each DTN.

5.1 DTN: LB0011THCDISSM.001 (INPUT FILES FOR PLUG FLOW SIMULATIONS)

SOLVEQ V1.0 [153217] was used to calculate the inlet water composition used for all of the simulations. The following files are grouped in the folder *starting_hco3_20C*.

solrun_s1.dat	Input file for SOLVEQ V1.0
solout_s1.dat	Output file for SOLVEQ V1.0
soltherm.dat	Thermodynamic database

A common model mesh was used for all of the simulations. The mesh was generated using the file *plugmesh* and TOUGH2 V1.4 [146496], resulting in the output file *plugmesh.mes*. This file was edited and incorporated in the FLOW.INP file used in each simulation.

Each of the TOUGHREACT simulations is grouped in a distinct folder. These are as follows:

simulation1input	TOUGHREACT V2.2, 60 µm diameter grain size surface area model, potassium feldspar as microcline

simulation2input	TOUGHREACT V2.2, 120 μm diameter grain size surface area model, potassium feldspar as microcline
simulation3input	TOUGHREACT V2.3, 60 μm diameter grain size surface area model, potassium feldspar as microcline, no K-smectite phase
simulation4input	TOUGHREACT V2.3, 60 μm diameter grain size surface area model, potassium feldspar as k-spar, no K-smectite phase
simulation5input	TOUGHREACT V2.3, 60 μm diameter grain size surface area model, potassium feldspar as k-spar, illite substituted for K-smectite phase

Each simulation folder contains the following files:

CHEMICAL.INP	Water chemistry, mineralogy, and CO_2 partial pressure data
FLOW.INP	Rock thermal and hydrological properties, run flags and other specifications
SOLUTE.INP	Run flags and other data relating to reactive transport
thermokapps.2.05.dat or thermok2.07.dat	Thermodynamic database (the first was used with V2.2 simulations, while the second was used with V2.3 simulations)

5.2 DTN: LB0011THCDISSM.002 (OUTPUT FILES FOR PLUG FLOW SIMULATIONS)

Each of the TOUGHREACT simulations resulted in a number of output files, which are grouped into five folders, one for each of the simulations described above. The folders are named using the format *simulation#output*, with the subdirectories *TOUGHREACTfiles* and *extracteddatafiles*. These folders each contain the following files:

TOUGHREACTfiles:

TEC_CONC.DAT
TEC_GAS.DAT
TEC_MIN.DAT
TIME.DAT
ITER.DAT

Extracteddatafiles:

Xna.dat
Xsio2.dat
Xk.dat
Xca.dat
Xhco3.dat
Xph.dat

Main Menu

EXIT

where *X* is *60um* for simulation 1, *120um* for simulation2, *microrev* for simulation3, *0.26illrev* for simulation4, and *0.61illrev* for simulation5. Two additional data files, *60umcorrhco3.dat* and *60umcorrph.dat* (generated from the SOLVEQ V1.0 [153217] runs described below), were also generated for simulation1.

The resulting values for simulation1 were modeled using SOLVEQ V1.0 [153217] to evaluate the effects of degassing and cooling that were experienced by the analyzed samples from the actual tuff dissolution experiment. The files used for these calculations (listed below) are grouped in the folder *effluent_corr*.

slr_eff2.2_60um.dat	SOLVEQ V1.0 input file for degassing
slt_eff2.2_60um.dat	SOLVEQ V1.0 output file for degassing
slr_eff2.2_60um_cool.dat	SOLVEQ V1.0 input file for cooling
slt_eff2.2_60um_cool.dat	SOLVEQ V1.0 output file for cooling

The data files generated from the results of the tuff dissolution experiment are grouped in the folder *tuffdissexptoutput*, and include the following files:

kneafna.dat	Sodium concentration data for effluent water (mg/L)
kneafsio2.dat	Silica concentration data for effluent water (mg/L)
kneafk.dat	Potassium concentration data for effluent water (mg/L)
kneafca.dat	Calcium concentration data for effluent water (mg/L)
kneafcaco3.dat	Total alkalinity data for effluent water (mg of $CaCO_3$/L)
kneafph.dat	pH of effluent water